ISSN
2712-8172

Magazine of Civil Engineering

102(2), 2021

Федеральное государственное автономное образовательное учреждение высшего образования
Санкт-Петербургский политехнический университет Петра Великого

ПОЛИТЕХ
Санкт-Петербургский политехнический университет Петра Великого

Инженерно-строительный институт
Центр дополнительных профессиональных программ

195251, г. Санкт-Петербург, Политехническая ул., 29, тел/факс: 552-94-60, www.stroikursi.spbstu.ru, stroikursi@mail.ru

Приглашает специалистов организаций, вступающих в СРО, на курсы повышения квалификации (72 часа)

Код	Наименование программы	Виды работ*
	Курсы по строительству	
БС-01-04	«Безопасность и качество выполнения общестроительных работ»	**п.1,2, 3, 5, 6, 7, 9, 10, 11, 12, 13, 14**
БС-01	«Безопасность и качество выполнения геодезических, подготовительных и земляных работ, устройства оснований и фундаментов»	**1,2,3,5**
БС-02	«Безопасность и качество возведения бетонных и железобетонных конструкций»	**6,7**
БС-03	«Безопасность и качество возведения металлических, каменных и деревянных конструкций»	**9,10,11**
БС-04	«Безопасность и качество выполнения фасадных работ, устройства кровель, защиты строительных конструкций, трубопроводов и оборудования»	**12,13,14**
БС-05	«Безопасность и качество устройства инженерных сетей и систем»	**15,16,17,18,19**
БС-06	«Безопасность и качество устройства электрических сетей и линий связи»	**20,21**
БС-08	«Безопасность и качество выполнения монтажных и пусконаладочных работ»	**23,24**
БС-12	«Безопасность и качество устройства мостов, эстакад и путепроводов»	**29**
БС-13	«Безопасность и качество выполнения гидротехнических, водолазных работ»	**30**
БС-14	«Безопасность и качество устройства промышленных печей и дымовых труб»	**31**
БС-15	«Осуществление строительного контроля»	**32**
БС-16	«Организация строительства, реконструкции и капитального ремонта. Выполнение функций технического заказчика и генерального подрядчика»	**33**
	Курсы по проектированию	
БП-01	«Разработка схемы планировочной организации земельного участка, архитектурных решений, мероприятий по обеспечению доступа маломобильных групп населения»	**1,2,11**
БП-02	«Разработка конструктивных и объемно-планировочных решений зданий и сооружений»	**3**
БП-03	«Проектирование внутренних сетей инженерно-технического обеспечения»	**4**
БП-04	«Проектирование наружных сетей инженерно-технического обеспечения»	**5**
БП-05	«Разработка технологических решений при проектировании зданий и сооружений»	**6**
БП-06	«Разработка специальных разделов проектной документации»	**7**
БП-07	«Разработка проектов организации строительства»	**8**
БП-08	«Проектные решения по охране окружающей среды»	**9**
БП-09	«Проектные решения по обеспечению пожарной безопасности»	**10**
БП-10	«Обследование строительных конструкций и грунтов основания зданий и сооружений»	**12**
БП-11	«Организация проектных работ. Выполнение функций генерального проектировщика»	**13**
Э-01	«Проведение энергетических обследований с целью повышения энергетической эффективности и энергосбережения»	
	Курсы по инженерным изысканиям	
И-01	«Инженерно-геодезические изыскания в строительстве»	**1**
И-02	«Инженерно-геологические изыскания в строительстве»	**2,5**
И-03	«Инженерно-гидрометеорологические изыскания в строительстве»	**3**
И-04	«Инженерно-экологические изыскания в строительстве»	**4**
И-05	«Организация работ по инженерным изысканиям»	**7**

***(согласно приказам Минрегионразвития РФ N 624 от 30 декабря 2009 г.)**

По окончании курса слушателю выдается удостоверение о краткосрочном повышении квалификации установленного образца (72 ак. часа)

Для регистрации на курс необходимо выслать заявку на участие, и копию диплома об образовании по телефону/факсу: 8(812) 552-94-60, 535-79-92, , e-mail: stroikursi@mail.ru.

Magazine of Civil Engineering
SCHOLAR JOURNAL

ISSN 2712-8172

Свидетельство о государственной регистрации:
Эл № ФС77-77906 от 19.02.2020,
выдано Роскомнадзором

Специализированный научный журнал.

Выходит с 09.2008.

Включен в Перечень ВАК РФ

Индексируется в БД Scopus

Периодичность: 8 раз в год

Учредитель и издатель:

Санкт-Петербургский политехнический университет Петра Великого

Адрес редакции:

195251, СПб, ул. Политехническая, д. 29

Главный редактор:
Екатерина Александровна Линник

Научный редактор:
Виталий Владимирович Сергеев

Заместитель главного научного редактора:
Галина Леонидовна Козинец

Редакционная коллегия:
PhD, проф. Т. Аввад;
д.т.н., проф. М.И. Бальзанников
д.т.н., проф. А.И. Белостоцкий;
к.т.н., проф. А.И. Боровков;
д.т.н., проф. А. Бородинец;
PhD, проф. М. Велькович;
PhD, проф. Р.Д. Гарг;
PhD, М.Р. Гарифуллин;
Dr.-Ing, проф. Т. Грис;
д.т.н., проф. Т.А. Дацюк;
д.т.н., проф. В.В. Елистратов;
Dr.-Ing., проф. Т. Кэрки;
д.т.н., проф. Д.В. Козлов;
д.т.н., доцент С.В. Корниенко;
д.т.н., проф. Ю.Г. Лазарев;
д.т.н., проф. М.М. Мухаммадиев;
Dr.-Ing. Habil., проф. Х. Пастернак;
Dr.-Ing., проф. Ф. Рёгинер;
д.т.н., проф. Т.З. Султанов;
д.т.н., проф. М.Г. Тягунов;
акад. РАН, д.т.н., проф. М.П. Федоров;
Dr.-Ing., проф. Д. Хецк;
д.г.-м.н. А.Г. Шашкин;
д.т.н. В.Б. Штильман

Дата выхода: 19.03.2021

© ФГАОУ ВО СПбПУ, 2021
© Иллюстрация на обложке: Илья Смагин

Magazine of Civil Engineering
SCHOLAR JOURNAL

ISSN 2712-8172

Peer-reviewed scientific journal

Start date: 2008/09

8 issues per year

Publisher:

Peter the Great St. Petersburg Polytechnic University

Indexing:

Scopus, Russian Science Citation Index (WoS), Compendex, EBSCO, Google Academia, Index Copernicus, ProQuest, Ulrich's Serials Analysis System, CNKI

Corresponding address:

29 Polytechnicheskaya st., Saint-Petersburg, 195251, Russia

Editor-in-chief:

Ekaterina A. Linnik

Science editor:

Vitaly V. Sergeev

Deputy chief science editor:

Galina L. Kozinetc

Editorial board:

T. Awwad, PhD, professor
M.I. Balzannikov, D.Sc., professor
A.I. Belostotsky, D.Sc., professor
A.I. Borovkov, PhD, professor
A. Borodinecs, Dr.Sc.Ing., professor
M. Veljkovic, PhD, professor
R.D. Garg, PhD, professor
M. Garifullin, PhD, postdoctorant
T. Gries, Dr.-Ing., professor
T.A. Datsyuk, D.Sc., professor
V.V. Elistratov, D.Sc., professor
T. Kärki, Dr.-Ing., professor
D.V. Kozlov, D.Sc., professor
S.V. Korniyenko, D.Sc., professor
Yu.G. Lazarev, D.Sc., professor
M.M. Muhammadiev, D.Sc., professor
H. Pasternak, Dr.-Ing.habil., professor
F. Rögener, Dr.-Ing., professor
T.Z. Sultanov, D.Sc., professor
M.G. Tyagunov, D.Sc., professor
M.P. Fedorov, D.Sc., professor
D. Heck, Dr.-Ing., professor
A.G. Shashkin, D.Sc.
V.B. Shtilman, D.Sc.

Date of issue: 19.03.2021

© Peter the Great St. Petersburg Polytechnic University. All rights reserved.
© Coverpicture – Ilya Smagin

Contacts:
E-mail: mce@spbstu.ru
Web: http://www.engstroy.spbstu.ru

Contents

Evtushenko, S.I., Petrov, I.A., Shutova, M.N., Chernykhovsky, B.A. Bearing capacity of eccentrically compressed bisteel columns 10201

Erofeev, V.T., Rodin, A.I., Bochkin, V.S., Ermakov, A.A. Properties of porous glass ceramics based on siliceous rocks 10202

Konstantinova, N.I., Smirnov, N.V., Shebeko, A.Y., Tanklevsky, L.T. Flammability of polymeric materials used in construction 10203

Chahal, S., Baalbaki, O., Temsah, Y., Ghanem, H., Abu Saleh, Z. Performance of two-way hinges in reinforced concrete structures 10204

Tarasov, V., Lalin V.V., Radaev, A.E., Mentishinov, A. Methodology for calculation and design of earthquake-resistant vibroisolated turbine foundations 10205

Mukhametrakhimov, R.Kh., Lukmanova, L.V. Structure and properties of mortar printed on a 3D printer 10206

Do, T.M.D, Lam, T.Q.K. Design parameters of steel fiber concrete beams 10207

Haji, M., Azarhomayun, F., Ghiami Azad, A.R. Numerical investigation of truss-shaped braces in eccentrically braced steel frames 10208

Prokopovich, S.V., Uzdin, A.M., Ivanova, T.V. Setting seismic input characteristics required for designing 10209

Usanova, K., Barabanshchikov, Yu.G., Pakrastins, L., Akimov, S.V., Belyaeva, S.V. Heat release and thermal conductivity of expanded-clay concrete for 3D printer 10210

Kirsanov, M.N. Analytical calculation of deflection of a planar truss with a triple lattice 10211

Sainov, M.P., Kotov, F.V. Tendencies in developing structural designs of non-soil seepage-control structures of embankment dams 10212

Smirnova, O.M. Low-heat steaming treatment of concrete with polycarboxylate superplasticizers 10213

Fialko, S.Yu., Kabantsev, O.V., Perelmuter, A.V. Elasto-plastic progressive collapse analysis based on the integration of the equations of motion 10214

Mehdipanah, H.R., Fanaie, N. Dynamic response of structures located in near-field and far-field regions using IDA and MIDA 10215

Magazine of Civil Engineering

ISSN 2712-8172

journal homepage: http://engstroy.spbstu.ru/

DOI: 10.34910/MCE.102.1

Bearing capacity of eccentrically compressed bisteel columns

S.I. Evtushenko[a*], I.A. Petrov[b], M.N. Shutova[b], B.A. Chernykhovsky[b]
[a] *Moscow State University of Civil Engineering (National Research University), Moscow, Russia*
[b] *Platov South-Russian State Polytechnic University (NPI), Novocherkassk, Russia*
[*]*E-mail: evtushenkosi@mgsu.ru*

Keywords: ultimate load, eccentric compression, numerical analysis, structural analysis, finite element, thin-walled rod, thin-walled bar, bisteel column

Abstract. Article is devoted to calculation the bisteel non-central compressed columns from I-shaped profile. The web of I-shaped profile is made of structural steel, the flanges is made from increased-durability steel. The analytical decision used the system of the equations was applied. Also, physical tests of prototypes on the prof. Korobov's testing machine were carried out. Loading is applied eccentrically to a steel plate, the hinge support applied to the lower plate, plates are fixed by screws from rotational translations. Displacements on axes are measured in the plane of the section in middle of rack and also occurs tilt angles. Calculation in ANSYS software taking into account physical and geometrical nonlinearity is carried out. It is established that analytical calculation gives the results close to experimental values (the maximum divergence of 15 %), the configuration of schedule of ANSYS simulation results repeats the schedule of experience data, and a divergence of results is insignificant (to 9 %).

1. Introduction

In sections with non-central loaded buildings constructions arise various tension, at the same time a part of section is used ineffectively. The idea to use in the loaded parts of section high-strength metal is effective as it allows using optimum sections – in places with big tension steel with a high durability is applied.

The possibility of application the bisteel constructions were analyzed by several scientists in Russia and abroad.

Authors [1] made using comparison of bridges load-bearing element working in seismic zones. A part of constructions it was executed as bisteel.

In a [2] research of a bend of the two-layers steel beam (steel with normal and high-strength durability) shown, that the normal stresses in multilayer beams depend on the bending stiffness's relative to the principal axes of cross sections of the beams.

A similar analysis with bisteel profile was made with bisteel beam (a composition of high-strength steel inclusions for the flanges in the region of maximum stresses and of low-strength steel for remaining volume of the beam) [3].

In the [4] article analyzes the stability of bisteel beams taking into account the development of plastic deformation in one or more cross-sectional elements.

Calculation of section of bisteel beams was carried out also using ANSYS complex [5]. Quantitative assessment of the phenomenon of a delay of the beginning of fluidity of the elastic-plastic zones of a wall adjoining elastic belts is received.

The authors of [6] performed experimental and numerical modeling of bending and torsion behavior and bearing capacity of columns from an equal-angle L-shape column of hot-rolled austenitic steel with a fixed end.

The authors of [7] conducted a comprehensive experimental and numerical study of the behavior of welded stainless-steel beam-columns. Twenty test specimens were made of duplex plates; they were tested

This work is licensed under a CC BY-NC 4.0

for bending with compression. Tensile tests and geometric defects were also conducted. Numerical models were developed, calibrated according to test results and subsequently used in parametric studies, taking into account a wider range of sample geometries.

The authors of [8] studied the properties of a rack made of square steel pipes filled with concrete with a cross section in the L-shape. Using two eccentric compression experiments, the fracture mode, load displacement curves for the entire element, and deflection curves for the rack were obtained.

The authors of [9] experimentally and numerically investigated the bending behavior of welded steel I-beams under eccentric compression.

The authors of [10] studied the mechanical properties of a steel L-shape column rigidly fixed with one support. The influence of the plate thickness and the number of bolts on the bearing capacity was analyzed.

The authors of [11] performed an experimental study to assess the effect of vertical soil movement on steel columns with wide flanges in the lower floors of steel frames. Three cyclic side load tests were performed.

The authors of [12] conducted a numerical study of columns made of high-strength steel plates. The study included 4 reference models, confirmed by test data, and parametric research models.

The authors of [13] tested 28 steel L-shape specimens to study their reaction when it is necessary to withstand the axial compressive load at different end eccentricities.

The authors of [14] investigated the stability and design of laser-welded stainless-steel I-beam columns.

In [15], the authors conducted an experimental study on the ultimate strength of welded I-beams made of steel using laser cutting under axial compression.

The methodology for calculating centrally and eccentrically compressed non-ideal rods of a rectangular profile in critical and supercritical states is described in the [16], in which the principle of possible displacements was used as the calculation method.

The authors of [17] proposed variants of linearized differential equations of “geometrically” and “physically” nonlinear problems on bending-torsional deformations of thin-walled open-profile rods. Two “step-by-step” methods for solving the original nonlinear problem are considered. General expressions are obtained for the formation of sequentially refined stiffness matrices of rods as systems with 14 degrees of freedom with the possibility of introducing them into the finite element method programs when calculating bar nonlinearly deformable structures.

The solution of the problem of determining the bearing capacity and stability of compressed rods is urgent. Many authors offer various methods, some of which use the calculus of variations [18−19].

Many scientific works provide examples of determining the bearing capacity of beam and column structures by analytical and numerical methods [20−24].

The purpose of this study is to compare the results (the dependence of the axial displacements of the mid-section) of the calculation of the eccentrically loaded bisteel column using the analytical and numerical method of solution, and also to prove their comparability with the experimental results.

2. Methods

2.1. Analytical method

Bisteel columns are effective constructions in comparison with traditional monosteel standard structures: the bearing capacity of section increases due to elastic-plastic work and a favorable combination of various durability of steel.

At production welded I-shaped profiles residual tension influence were arisen. Their influence on the intense deformed condition of thin-walled elements of metal designs is studied insufficiently. Calculation methods were developed for bisteel elements of metal constructions beyond an elasticity limit.

Algorithms of finding of maximum loads of non-central compressed welded the bisteel columns are developed, considering residual welding tension and elastic-plastic deformations.

According to project codes calculation of the compressed elements of steel metal structures consists of:

- selection of the sizes of cross section providing the set service conditions at and minimum cost;
- check of durability;
- check of rigidity;
- check of general stability and also stability of elements of cross section.

Feature of work of non-central compressed columns with two-axis eccentricity is the development of all three characteristic deformations (deflections in two planes and the angles of twisting).

For the analysis of the intense deformed condition of thin-walled elements at elastic-plastic deformations used the charts of balance conditions connecting the internal forces of a profile with its displacements.

Searching of the limit parameter of the load N (loss of bearing capacity) provides by step method. $N_{\lim}$ is a load from requirement of first and second group of limiting condition.

The conducted researches are based on the system of the differential equations of a bend and torsion of thin-walled cores of open profile with the geometrical and physical nonlinearity, offered by A.Z. Zarifyan [25]. The decision of a boundary-value problem based on method of "elastic solution", developed by A.A. Ilyushin.

For analyses pendulum column (H-shape form), compressed by longitudinal force N, having an eccentricity e_x, e_y (shown on Fig. 1) using system of the differential equations (1):

$$\begin{cases} EA\zeta_t^{II} = q_{z\psi,t}; \\ EI_y\xi_t^{IV} + (1-\dfrac{I_y}{I_x})(M_x\theta_t)'' + N\xi_t'' = q_{x\psi,t} \\ EI_x\eta_t^{IV} + (1-\dfrac{I_x}{I_y})(M_y\theta_t)'' + N\eta_t'' = q_{y\psi,t}; \\ EI_\omega\theta_t^{IV} - GI_{tor}\theta_t'' + M_x\xi_t'' + M_y\eta_t'' + \dfrac{I_y+I_x}{A}N = m_{\psi,t} \end{cases} \quad (1)$$

where $q_{z\psi,t}$, $q_{x\psi,t}$, $q_{y\psi,t}$, $m_{\psi t}$ are intensity of additional distributed loading in the plasticity zone, which depends on the propagation of the plastic strain zones along the cross section and the length of the rod. The additional load functions were determined from the formulas:

$$q_{z\psi} = N_\psi;\ q_{x\psi} = (M_{y\psi})'';\ q_{y\psi} = -(M_{x\psi})'';\ m_\psi = B_\psi, \quad (2)$$

where N_ψ, $M_{x\psi}$, $M_{y\psi}$, B_ψ are partial values of internal forces in the zones of plastic deformations of the rod's cross sections, arising from the difference between the elastic and effective stresses, according to the actual diagrams of deformation of the materials of the column elements ($\sigma_i - \varepsilon_i$). In the absence of plastic deformations in the sections, we consider these quantities to be equal to zero. A detailed description of the algorithm for determining the bearing capacity for eccentrically compressed rods, taking into account the geometric and physical nonlinearity, is given in [26].

In the general case, the algorithm for solving the system of nonlinear differential equations was implemented as follows:

- at the first step, the plasticity function $\psi_1(\varepsilon_i)$, the intensity of the additional loads $q_{x\psi,1}$, ..., as well as the additional forces in the boundary sections $M_{x\psi,1}$, ... are set equal to zero and a system of linearized ordinary differential equations was solved. At the next stage, the values of the displacement functions ζ_1, ξ_1, η_1, θ_1 were determined, the strain intensities $\varepsilon_{i,1}$ were calculated, the zones of plasticity propagation over the cross sections and the length of the thin-walled rod were found.
- taking into account the nature of the diagrams $\sigma_{if} = \sigma_{if}(\varepsilon_i)$ for the shelf and $\sigma_{iw} = \sigma_{iw}(\varepsilon_i)$ for the column wall, the stress intensities σ_i, the plasticity function $\psi_2(\varepsilon_i)$ were found and the quantities the development of plastic areas, the values $q_{x\psi,2}$, ... and $M_{x\psi,2}$, ... The rod, in addition to the given external forces, was loaded with additional distributed loads $q_{x\psi,2}$, ... in the span along the elastoplastic region and additional forces $M_{x\psi,2}$, ... at the ends. Since the expressions $q_{x\psi,2}$, ..., $M_{x\psi,2}$, ... were determined by substituting the corresponding formulas for the displacement functions of the previous approximation into nonlinear terms, a system of linear differential equations was obtained.

The calculation in the third and following approximations was reduced to the sequential solution of linear equations.

The system of differential equations (1) for calculating elastoplastic thin-walled rods of an open profile is obtained on the basis of the following premises:

- the projection of the contour of the cross section on the accompanying plane normal to the deformed axis of the centers of bending of the rod is not distorted;
- shear deformations of the middle surface are insignificant, and their influence on the law of distribution of longitudinal displacements along the midline of the contour can be neglected;
- normal stresses in the cross section are considered uniformly distributed over the thickness;
- tangential stresses τ_{zs} are directed parallel to the tangent to the midline and along the thickness of the profile elements and vary linearly.
- for rods made of elastoplastic materials, under simple loading, the dependence between the stress intensity σ_i and the strain rate ε_i is taken in the form $\sigma_i = E\,[1-\psi(\varepsilon_i)]\;\varepsilon_z$, where $\psi(\varepsilon_i)$ is a function depending on the achieved level of strain intensity and determined from the diagram $\sigma_i - \varepsilon_i$ of the material;
- with simple loading in the rods of elastoplastic materials, there is a continuous increase in the strain intensity;
- the relationship between deformations and components of the displacement vector has the form

$$\varepsilon_z = \zeta' - (\xi'' + \theta\,\eta'')\,x - (\eta'' - \theta\,\xi'')\,y - \theta''\omega.$$

- to determine the boundaries of the distribution of plastic zones over cross sections and the length of a thin-walled rod, the Mises plasticity condition was adopted. The transition of the rod to the elastoplastic state occurs when the stress intensity value in the most stressed fibers becomes equal to the yield strength of the material $\sigma_i = \sigma_y$.

At non-central compression with the two-axis eccentricity identical on both ends, kinematic boundary conditions for ξ, η, θ do not change and depend on a way of fixing of a core. Internal efforts in the case of the development of plastic deformations in the main sections when the force N is transmitted to the ends of the rod through diaphragms that are rigid from their plane (the absence of an external bimoment at the ends) have the form:

$$\xi = \eta = \theta = 0,\;\; M_x = Ne_y - M_{x\psi},\;\; M_y = -Ne_x - M_{y\psi},\;\; B = Ne_xe_y - B_\psi.$$

The calculation results using formulas (1), (2) are shown on diagram, Fig. 6, denote by green color.

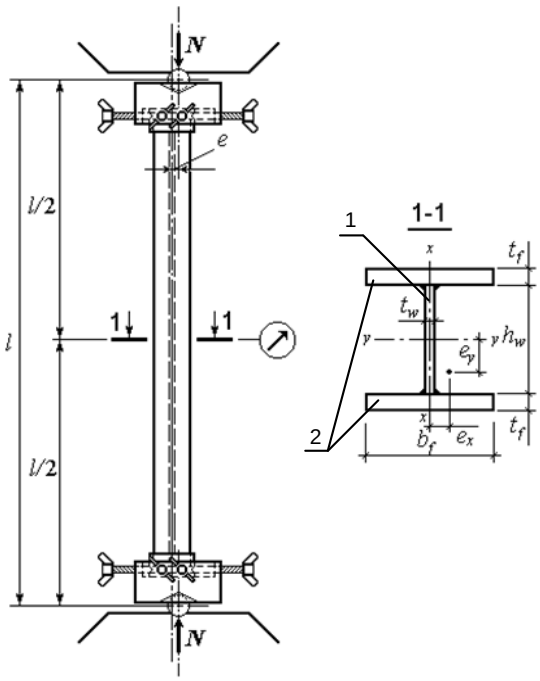

Figure 1. The design scheme of column and cross section:
1 – normal-strength steel; 2 – high-strength steel.

Table 1. Parameters of the studied specimens.

№ of rack	Name	Geometrical values h_w, mm	b_f, mm	t_w, mm	t_f, mm	Design loadings N, kN	Slenderness λ_y	Length l, cm
1	2	8	9	10	11	13	14	15
1	KM 1-01	62	61	2	2	34.0	60	85.5
2	KM 1-02	63	60	2	2		61	--
3	KB 1-03	42	38	2	4.5	23.0	96	94
4	KB 1-04	41	39	2	4.5		94	--
5	KB 2-01	26	45	2	4.5	24.5	85	105
6	KB 2-02	27	44	2	4.6		88	--
7	KB 2-03	25	45	2	4.5		85	--
8	KB 2-04	27	45	2	4.6		86	--

Note: KM is monosteel rack; KB is bisteel rack.

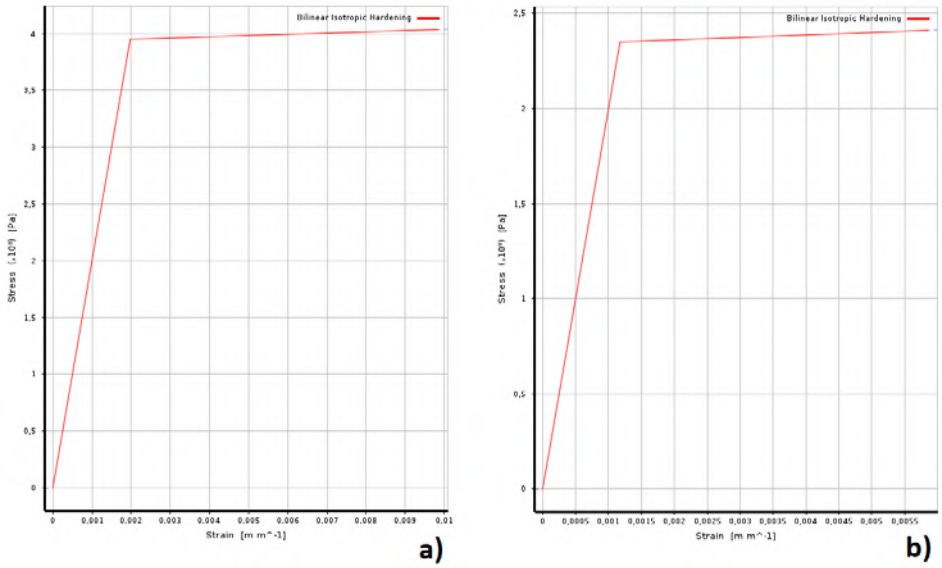

Figure 2. Bilinear isotropic hardening chart: a – 09G2; b – VSt3sp5.

2.2. Experimental method

Testing of welded I-shaped rack by compression with an eccentricity [27] relative to both main axes were carried out on special test unit based on 10-ton unit used prof. Korobov's system (Fig. 3).

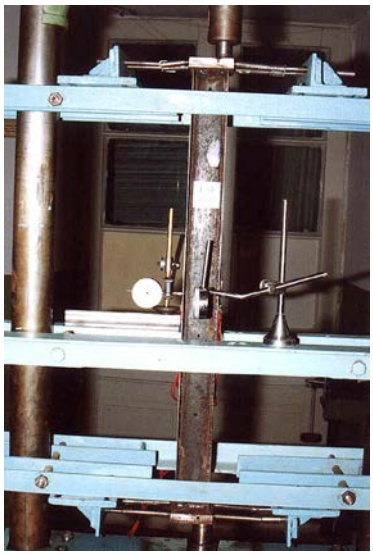

Figure 3. Overall view of test unit.

The optimal sizes of the experimental bisteel pillar columns were calculated using the multicriteria multiparameter optimization of the cross-sectional dimensions of eccentrically compressed rods, the material of which works in the elastoplastic stage [17].

The following materials were used for the rack:

- webs of the I-beam profile were made from sheet broadband universal hire of the brand VSt3sp5 (Russian State Standard GOST 27772-88*) with design resistance $R_{y,\,w}$ = 235 MPa,
- flanges of the I-beam profile were made from high-strength steel of the brand 09G2 (Russian State Standard GOST 19282-73*) and 14G2 with design resistance $R_{y,\,f}$ = 355 MPa.

The columns were welded by semi-automatic welding in carbon dioxide. To make the shape and dimensions of the posts after welding consistent with the design, a number of measures were taken during their manufacture, which were reduced to compensate for the plastic deformation that develops during welding. These included the following:

- increase in stiffness by means of special fastenings of the elements being welded (use of a conductor);
- application of a rational order of welding.

The ends of the strut elements were milled to obtain a flat supporting surface.

It was made 8 racks of two series. Each series consisted of 4 samples. After manufacturing, each rod was measured in three sections along the length using a caliper. The scatter of measurements was no more than 1.6 %, which made it possible to use all the characteristics.

To obtain a diagram σ–ε of the material of the shelves and walls, flat samples were made, which were subjected to tension up to fracture. In the elements (wall and shelves) of the H-shaped profile of sheet metal, the samples were oriented in the direction of the greatest compressive stresses in the column. Production of samples and their tensile tests were carried out according to Russian State Standard GOST 1497-84*.

Testing of all rods for eccentric compression was carried out according to a single method. The full test cycle of each rod in the elastic and elastoplastic stages included the preparatory stage and the test phase. At the preparatory stage, after the final centering, the rod was installed in the supporting devices of the machine with the specified eccentricities of the load application and the measuring devices were mounted.

The eccentricities e_x, e_y of the application of the load were created due to the displacement of the axis of the rack relative to the axes of the loading device of the testing machine. The magnitude and sign of the eccentricities at both ends of the rod were assumed to be the same. After obtaining the specified eccentricity of the load application, eccentric loading was performed by the applied force.

The following measurements were made on the tests:

- displacement of the center of a bend (ξ, η) in the direction of axes *OX* and *OY* in the central section of the column (were installed dial indicators with an increment of 0.01 mm);
- deformation in the middle of the rack using strain gauges with a base of 10 mm and strain gauge station VST-6. The device provided measurement of longitudinal deformations with an accuracy of $1 \cdot 10^{-5}$ and allowed to define relative deformations up to 2 %;
- bearing capacity (it was fixed according to indications of a dynamometer).

The tests results are shown on diagram, Fig. 7, denoted by red color.

2.3. Finite element modelling method

Finite element model of rack was calculated by ANSYS software. Authors found that the divergence between the calculation and experimental results for the tested rack in the linearity zone is on average 3.39 % [28]. Computer analysis of the data allows obtaining the results of deformation of an eccentrically compressed column without full-scale experiment.

The model consists of: steel plate with design resistance $R_{y,w}$ = 235 MPa (web of I-beam); steel plates with design resistance $R_{y,f}$ = 355 MPa (flange of I-beam); prisms (welded seams); heavy plate (upper plate has a load, lower plate has a fixing surface); constraints by side screws (Fig. 4).

The finite element model consists of tetrahedral (lower and upper plates) and hexahedral (the rest of the model) elements with a minimum size of 1−2 mm near the boundary conditions or contact interaction. For extended and geometrically unchanged sections of the structure, a bias modifier is used, which allows to reduce the number of elements in the model without losing the accuracy of the calculation results (Fig. 5).

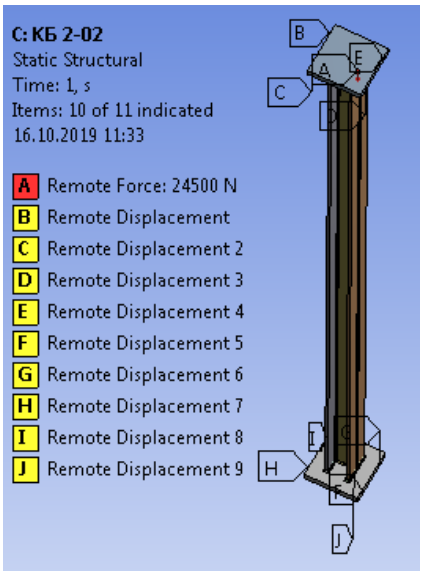

Figure 4. The design model of I-shape form profiles.

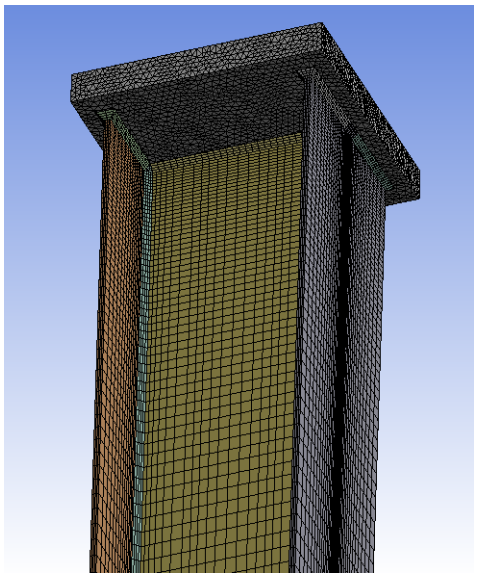

Figure 5. Biased mesh.

The calculation was carried out in a nonlinear formulation. Such a statement implies an iterative type of solution. This means that the conditional loading time is divided into substeps, in each of which the load applied to the structure increases sequentially to the nominal value, the design scheme changes due to deformations (geometric non-linearity), and the elastic properties of the material also change when the stresses leave the proportional band (physical nonlinearity).

3. Results and Discussion

The resulting contours of the values of the directional deformations are represented in Fig. 6.

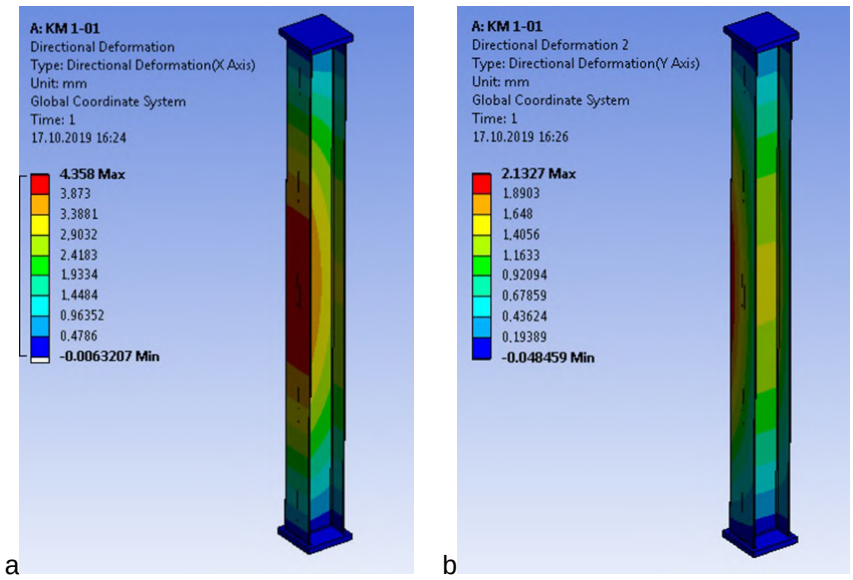

a b

Figure 6. Directional deformation:
a – in the direction of ax *Ox*, b – in the direction of ax *Oy*.

All results are represented in Table 1 and on the Fig. 7.

Table 2. Results of analytical solution, tests and computer simulation.

Loading, kN	5	10	15	20	25	30	32
Deformation in the direction of axis *OX*							
Tests results	0.052	0.114	0.179	0.271	0.486	0.75	0.84
Results of calculation by (1), (2)	0.052	0.103	0.164	0.244	0.4	0.63	0.79
Nonlinear Finite Element Analysis	0.051	0.102	0.154	0.206	0.257	0.308	–
Deformation in the direction of axis *OY*							
Tests results	0.06	0.126	0.196	0.269	0.371	0.56	0.61
Results of calculation by (1), (2)	0.06	0.126	0.205	0.298	0.44	0.662	0.79
Nonlinear Finite Element Analysis	0.059	0.12	0.18	0.24	0.299	0.36	0.382

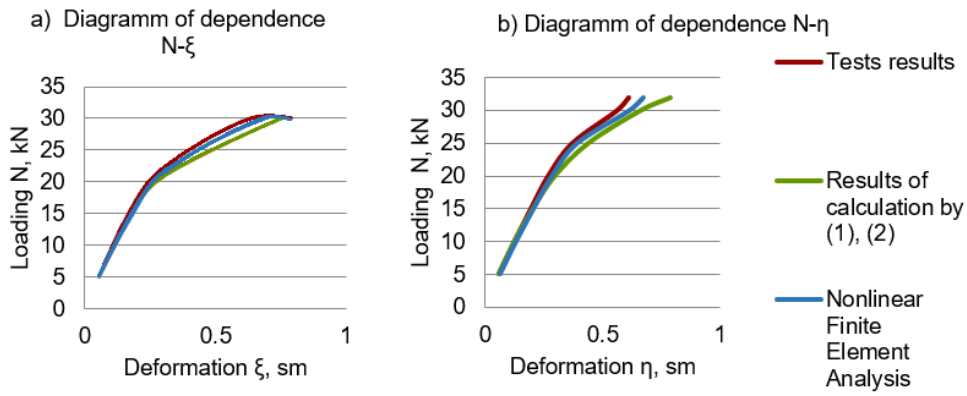

Figure 7. Diagramms of results: a – diagramm of dependence N-ξ (in the direction of axis *OX*), b – diagramm of dependence N-η (in the direction of axis *OY*).

Analytical calculation for formulas (1) and (2) gives the results close to experimental values (the maximum divergence of 15 %), the configuration of schedule of ANSYS simulation results repeats the schedule of experience data, and a divergence of results insignificant (to 9 %). In the analytical calculation, linear displacements in the direction of the main axes of inertia of the cross section and angular displacements relative to the axis of the column were taken into account. Linear deformations are given in the results of the analytical solution. Under the given boundary conditions corresponding to the parameters of the physical model, total angular displacements in the numerical experiment were less than 0.1 degrees. In a physical experiment, torsional strains were not measured [26]. Thus, it is possible to draw a conclusion on adequacy of computer calculation for the solution of a difficult nonlinear problem. Methods for determining bearing capacity were used to optimize the cross-sectional size of thin-walled rods.

The calculation module for determining the bearing capacity was used to solve the problem of multicriteria optimization of the parameters of the cross section of the bisteel column, taking into account geometric and physical nonlinearity. Optimization was carried out at given values of the column length and compressive force, which was applied with eccentricities. The solution to the optimization problem was based on a search method in a uniformly distributed sequence. The following parameters were taken as varied: design resistance of the material, wall and shelf dimensions. Regulatory (local stability of the wall and shelf profiles of the column) and structural limitations (the possibility of using welding equipment in the manufacture of the column) were taken into account. The following criteria were taken as criteria of the objective function: the cross-sectional area of the column, the moment of inertia of the cross-section in the plane of least rigidity, and the manufacturing cost.

Based on the solution of the problem of determining the bearing capacity, a technique is developed for optimizing the cross-sectional dimensions of a composite H-shaped eccentrically compressed welded bisteel columns, taking into account the elastoplastic properties of the material, initial defects and residual stresses in a geometrically and physically nonlinear setting under a given load [29].

4. Conclusion

1. A theoretical and experimental study of the operation of columns of steel of two grades with different yield strengths under static load was carried out. The method for determining the maximum loads makes it possible to rationally select economical sections in the form of a welded I-beam taking into account the required regulatory restrictions.

2. The results of analytical and numerical modeling of the stress-strain state and ultimate loads of the bisteel columns are in satisfactory agreement with the data of experimental studies.

3. The developed technique was used to solve the problem of multi-criteria, multi-parameter optimization of the cross-sectional dimensions of H-shaped columns with a high degree of sampling of the dimensions of the structure.

5. Acknowledgements

The reported study was funded by RFBR, project number 20-38-90056\20.

References

1. Bruneau, M., El-Bahey, S., Fujikura, S., Keller, D. Structural fuses and concrete-filled steel shapes for seismic and multi-hazard resistant design. Bulletin of the New Zealand Society for Earthquake Engineering. 2011. DOI: 10.5459/bnzsee.44.1.45-52
2. Bareišis, J., Kleiza, V. Effect of layer geometry and stiffness on the fields of normal stresses in multilayer beams under asymmetric bending. Mechanics of Composite Materials. 2009. DOI: 10.1007/s11029-009-9093-6

3. Jaras, A., Kačianauskas, R. Elastic-plastic analysis of bisteel i-section beams. Statyba. 2001. DOI: 10.1080/13921525.2001.10531713
4. Moiseev, V.I. Analysis of the stability of webs and flanges in bisteel beams with consideration of plastic deformation. Journal of Constructional Steel Research. 1992. DOI: 10.1016/0143-974X(92)90029-E
5. Dmitriev, V.G., Krasnovskiy, E.E., Salatov, E.K. Research of features of nonlinear deformation the bisteel beams using a finite element method. Engineering physics. 2009.
6. Liang, Y., Jeyapragasam, V.V.K., Zhang, L., Zhao, O. Flexural-torsional buckling behaviour of fixed-ended hot-rolled austenitic stainless steel equal-leg angle section columns. Journal of Constructional Steel Research. 2019. DOI: 10.1016/j.jcsr.2018.11.019
7. Yang, L., Zhao, M., Gardner, L., Ning, K., Wang, J. Member stability of stainless steel welded I-section beam-columns. Journal of Constructional Steel Research. 2019. DOI: 10.1016/j.jcsr.2018.12.022
8. Liu, J., Zhou, T., Lei, Z., Chen, X., Chen, Z. Eccentric compression performance of slender L-shaped column composed of concrete-filled steel tubes connected by steel linking plates. Journal of Constructional Steel Research. 2019. DOI: 10.1016/j.jcsr.2019.06.012
9. Yang, B., Shen, L., Kang, S.B., Elchalakani, M., Nie, S.D. Load bearing capacity of welded Q460GJ steel H-columns under eccentric compression. Journal of Constructional Steel Research. 2018. DOI: 10.1016/j.jcsr.2018.01.011
10. Liu, Y., Chantel, S. Experimental study of steel single unequal-leg angles under eccentric compression. Journal of Constructional Steel Research. 2011. DOI: 10.1016/j.jcsr.2011.02.005
11. Sun, Y.B., Cao, T.J., Xiao, Y. Full-scale steel column tests under simulated horizontal and vertical earthquake loadings. Journal of Constructional Steel Research. 2019. DOI: 10.1016/j.jcsr.2019.105767
12. Jiang, J., Ye, Z.J., Bao, W., Wang, X., Wang, Y.B., Dai, X.H. Flexural buckling behaviour of 690 MPa high strength steel H-section columns. Engineering Structures. 2019. DOI: 10.1016/j.engstruct.2019.109718
13. Liu, Y., Hui, L. Experimental study of beam-column behaviour of steel single angles. Journal of Constructional Steel Research. 2008. DOI: 10.1016/j.jcsr.2007.11.002
14. Bu, Y., Gardner, L. Finite element modelling and design of welded stainless steel I-section columns. Journal of Constructional Steel Research. 2019. DOI: 10.1016/j.jcsr.2018.03.026
15. Wang, Y.B., Li, G.Q., Chen, S.W., Sun, F.F. Experimental and numerical study on the behavior of axially compressed high strength steel columns with H-section. Engineering Structures. 2012. DOI: 10.1016/j.engstruct.2012.05.018
16. Iljashenko, A.V. About eccentric compression of thin-walled bars composed of initially curved finned elements. International Journal for Computational Civil and Structural Engineering. 2008. Vol. 4. Issue 1. Pp. 71–74.
17. Vorontsov, G.V., Petrov, I.A., Alekseev, S.A. Stiffness matrices of spatially loaded non-linearly deformable rods. Part 2. News of higher educational institutions. North Caucasus region. Series: Engineering. 2008. No. 4. Pp. 68–72.
18. Lalin, V.V., Rozin, L.A., Kushova, D.A. Variational functionals for two-dimensional equilibrium and stability problems of Cosserat-Timoshenko elastic rods. Magazine of Civil Engineering. 2013. 36(1). Pp. 87–96. DOI: 10.5862/MCE.36.11
19. Lalin, V.V., Zdanchuk, E.V., Kushova, D.A., Rozin, L.A. Variational formulations for non-linear problems with independent rotational degrees of freedom. Magazine of Civil Engineering. 2015. 56(4). Pp. 54–65. (rus). DOI: 10.5862/MCE.56.7
20. Przybylski, J., Kuliński, K. Shape enhancement of an eccentrically loaded column using piezoelectric actuator. Engineering Structures. 2019. DOI: 10.1016/j.engstruct.2018.07.014
21. Pastor, M.M., Roure, F. Open cross-section beams under pure bending II. Finite element simulation. Thin-Walled Structures. 2009. DOI: 10.1016/j.tws.2008.10.021
22. Bu, Y., Gardner, L. Laser-welded stainless steel I-section beam-columns: Testing, simulation and design. Engineering Structures. 2019. DOI: 10.1016/j.engstruct.2018.09.075
23. Volkova, V.E., Makarova, A.A. Numerical modeling of the stress-strain state of a beam with a flexible wall. Metal constructions. 2012. No. 4(17). Pp. 261–269.
24. Sokolovsky, Z.N., Kholkin, E.G. Determination of the bearing capacity of thin-walled structures taking into account local stability loss. Bulletin of the Siberian State Automobile and Highway Academy. 2013. No. 3(31). Pp. 93–96.
25. Zarifyan, A.Z., Petrov, I.A. Determination of the optimum sizes of cross section compressed H-shaped bisteel columns. Easy building constructions. 1999.
26. Petrov, I.A. Optimization of sections of eccentrically compressed bistal columns: dissertation of a candidate of technical sciences: 05.23.17. Novocherkassk, 2000. 175 p.
27. Petrov, I.A., Shkurakov, L.V. Bearing capacity of is central-compressed double-T column. Improvement of calculation, design and production of building constructions. 1995.
28. Skibin, G.M., Shutova, M.N., Evtushenko, S.I., Chutchenko, I.A. Reliability increase of running gears elements of mining traction locomotives using finite-element analysis package. IOP Conference Series: Earth and Environmental Science. 2017. DOI: 10.1088/1755-1315/87/2/022021
29. Evtushenko, S.I., Petrov, I.A., Alexeev, S.A. Optimization task when calculating the bi-steel thin-walled rod. AIP Conference Proceedings. 2019. DOI: 10.1063/1.5138445

Contacts:

Sergej Evtushenko, evtushenkosi@mgsu.ru

Igor Petrov, iap6691@gmail.com

Marina Shutova, shutovapublish@mail.ru

Boris Chernykhovsky, cbotms@gmail.com

© Evtushenko, S.I., Petrov, I.A., Shutova, M.N., Chernykhovsky, B.A., 2021

Magazine of Civil Engineering

ISSN 2712-8172

journal homepage: http://engstroy.spbstu.ru/

DOI: 10.34910/MCE.102.2

Properties of porous glass ceramics based on siliceous rocks

V.T. Erofeev[a], A.I. Rodin[a]*, V.S. Bochkin[b], A.A. Ermakov[a]

[a] Ogarev Mordovia State University, Saransk, Respublika Mordoviya, Russia

[b] LLC "Kombinat teploizolyacionnyh izdelij", Saransk, Respublika Mordoviya, Russia

** E-mail: al_rodin@mail.ru*

Keywords: glass ceramics, thermal insulating materials, mechanical properties, compressive strength, water absorption, acid resistance

Abstract. Porous glass ceramic materials are widely used in the construction industry. Foam glass ceramics are obtained from industrial wastes, rocks of various chemical and mineralogical composition and other raw materials. Samples of foam glass ceramic materials obtained by burning the mechanically activated charge were studied. Siliceous rocks from six deposits were ground together with thermonatrite ($Na_2CO_3 \cdot H_2O$). The resulting charge was burned at a temperature of 850 °C. The following properties were determined experimentally: bulk density, compressive strength, water absorption, sorption humidity, thermal conductivity, application limit temperature, thermal and chemical stability of samples. In order to obtain glass ceramic materials with a uniform porous structure, the total amount of cristobalite and the amorphous phase in the composition of siliceous rock has to be more than 44.5 %. The amount of quartz, calcite and muscovite in the rock should not exceed 12 %. The bulk density of the samples decreases with an increase of heilandite share in the charge composition. The maximum compressive strength of the developed materials is 6 MPa with a bulk density of samples equal to 290 kg/m^3. The water absorption of samples decreases to 2.5 % (by volume) with an increase of diatomite share in the charge composition for more than 39.5 %. The minimum thermal conductivity of glass ceramics (0.0583 W/m °C) was revealed at a sample density of 180 kg/m^3. Insufficiently high values of thermal stability index (167–183 °C) are associated with the presence of both amorphous phase and crystalline minerals in the material, which have different thermal expansion coefficients. The application limit temperature of the material reaches 850 °C. The developed materials demonstrated high chemical stability after boiling in water, an aqueous HCl solution, as well as in an alkaline solution. Regarding a number of indicators, porous glass ceramic materials based on siliceous rocks are superior to foam glass and can be used as thermal insulation of pipelines, industrial plants (melting furnaces, boiler equipment), etc.

1. Introduction

Porous glass ceramic materials are widely used in the construction industry. Glass ceramic materials have high strength, low heat conductivity, high stability to harsh chemical environments, a wide range of operating temperatures, etc. They are used as insulators in the construction of industrial and civil facilities, nuclear power plants, gas and oil industry enterprises [1–3].

In industrial and civil engineering, foam glass ceramic materials from glass waste are widely used [4–6]. Glass ceramics based on industrial wastes, such as slag from metallurgical production [7–9], lead-zinc mine tailings [10], red mud [11], etc., possess decent physical, mechanical, thermal and physical properties. A large number of researches are devoted to developing the compositions and studying the properties of porous glass ceramic materials from siliceous rocks (diatomite, tripoli, opoka) [12–19]. Technologies for the production of porous glass ceramics are also diverse. Materials are obtained by the method of co-melting the components [20], by method of mixing the components in the molten state [21], by foaming a colloidal suspension [22], etc. Porous glass ceramic from siliceous rock is obtained mainly in the form of bulk materials [13–19]. Diatomite, opoka, zeolite-containing rocks are activated with aqueous solutions of alkalis, then they are granulated and burned after that. The equipment deteriorates rapidly with this production technology, as a result of exposure to alkalis. Burning the charge is accompanied with the release of harmful substances (NaOH) into the atmosphere [23]. This issue is resolved by replacing the alkaline solution with an alkaline component (for example, $Na_2CO_3 \cdot H_2O$) in dry form. The components have to be mixed using joint grinding method (mechanochemical activation). Structural defects accumulate in the particles of a solid body during

This work is licensed under a CC BY-NC 4.0

intense grinding, phase transformations occur, as well as amorphization of minerals in the crystal structure [24, 25]. The practice of obtaining block porous glass ceramic materials by burning joint ground siliceous rock (tripoli) and an alkaline component (Na_2CO_3) is described in the research [26].

Siliceous rocks from various deposits have significant differences regarding chemical and mineralogical composition. The impact of chemical composition of raw materials on the physical, mechanical, thermal, physical and other properties of glass ceramic materials is described in detail in scientific literature. It was determined that the strength characteristics of glass ceramics increase with increasing the amount of Al_2O_3 in the mixture up to 18 % [27]. According to the studies [28, 29], the increase in the alumina amount in the mixture to a certain extent reduces the thermal conductivity and thermal expansion coefficient of porous glass ceramic samples. The impact of CaO content in the material composition on various properties of glass ceramic samples from glass wastes and fly ash was described in detail in article [30]. Their obtained results indicate a density increase and a simultaneous decrease in compressive strength of samples. The calcium oxide content in the material composition increases and is more than 4.25 %. An increase in the density of glass ceramic materials, which are based on slag from copper production, with an increase of calcium oxide in the composition was also noted in the study [31]. The positive effect of Fe_2O_3 in the material composition on increase in the strength characteristics of glass ceramics was determined [32]. Almost all of the above mentioned results were obtained while studying glass ceramic samples based on artificially created glasses or industrial wastes. There are only few studies describing the impact of chemical and mineralogical composition of siliceous rocks on the properties of porous glass ceramic materials obtained by burning a mechanochemically activated charge (siliceous rock + fluxing agent).

The research goal is to determine the impact of chemical and mineralogical composition of siliceous rocks on the physical, mechanical, hydrophysical and thermophysical properties. The chemical stability of the foamed glass ceramic samples obtained by burning a mechanochemically activated charge needs to be determined as well.

Objectives:

- to determine the impact of chemical and mineralogical composition of siliceous rocks on the bulk density, compressive strength, as well as on water absorption and sorption humidity of foam glass ceramic samples;
- to determine the thermal conductivity, thermal stability and application limit temperature of the production samples of foam glass ceramic materials;
- to determine the stability of developed material samples in water or aqueous solutions of acids and alkalis.

2. Methods

2.1. Materials

In order to obtain foamed glass ceramic samples, siliceous rocks from six deposits were used, five species of tripoli and one diatomite (humidity ≤ 1 %). The chemical and mineralogical composition of the rocks is given in Table 1 and 2, respectively.

Table 1. The chemical composition of the rocks.

Comp. number	Chemical composition, % mass									
	SiO_2	CaO	Al_2O_3	Fe_2O_3	K_2O	MgO	TiO_2	Na_2O	SO_3	Other
R1	69.6	6.9	7.1	2.0	1.5	1.0	0.3	0.0	0.1	11.5
R2	68.5	6.8	6.8	1.8	1.5	1.0	0.3	0.2	0.1	13.0
R3	67.9	7.7	7.6	2.0	1.6	1.1	0.3	0.2	0.1	11.5
R4	56.4	12.5	8.7	2.7	2.0	1.2	0.4	0.2	0.1	15.8
R5	62.3	11.3	6.7	2.0	1.4	0.9	0.3	0.1	0.0	15.0
R6	81.5	1.5	5.3	2.1	1.0	0.9	0.2	0.2	1.8	5.5

Table 2. The mineralogical composition of the rocks.

Comp. number	Mineralogical composition, %						
	Quartz	Calcite	Heulandite	Muscovite	Cristobalite	Tridymite	Amorphous phase
R1	11.6	12.3	16.8	12.6	24.7	2.0	20.0
R2	11.4	12.1	19.0	10.8	24.6	2.1	20.0
R3	10.8	12.8	19.2	14.4	21.1	1.7	20.0
R4	11.1	22.4	19.8	14.3	11.4	1.0	20.0
R5	8.5	21.3	19.6	9.9	19.2	1.5	20.0
R6	14.3	0.0	0.0	10.7	0.0	0.0	75.0

Thermonatrite with a main substance mass fraction of at least 99 % was used as fluxing agent. The chemical formula is $Na_2CO_3 \cdot H_2O$.

2.2. Compositions and manufacturing technology of samples

Samples of foamed glass materials were produced according to the technology described below. First, the siliceous rock was ground together with fluxing agent ($Na_2CO_3 \cdot H_2O$). The grinding was carried out in a Retsch PM 400 planetary ball mill for 90 minutes (the rotation speed of the grinding jars was 250 rpm). Then, the resulting charge was poured into metal molds and burned in a muffle furnace (the molds were pre-treated with kaolin paste). The charge burning program is as follows: heating to a temperature of 600 °C at a rate of 4.5 °C/min, holding at 600 °C for 1 hour, heating to 850 °C at a speed of 4.5 °C/min, holding at 850 °C for 30 minutes. Holding at a temperature of 600 °C is necessary in order to remove excess gases formed due to the decomposition of individual minerals from the charge's composition (calcite, muscovite, etc.). After cooling the mold with the obtained material together with the furnace to 40 °C, the mold was disassembled, and the samples were removed for further testing.

The studied charge compositions are presented in Table 3. The compositions are selected based on previously conducted experimental studies of obtaining glass ceramic materials with an optimal porous structure (pore diameter not more than 2 mm). The results are partially described in the study [26].

Table 3. Compositions studied in the research.

Composition number	Charge composition, %						
	Siliceous rock (chemical composition see Table 1)						Thermonatrite
	R1	R2	R3	R4	R5	R6	
C1	79	–	–	–	–	–	
C2	75.05	–	–	–	–	3.95	
C3	71.10	–	–	–	–	7.90	
C4	67.15	–	–	–	–	11.85	
C5	–	79.00	–	–	–	–	
C6	–	75.05	–	–	–	3.95	
C7	–	71.10	–	–	–	7.90	
C8	–	67.15	–	–	–	11.85	
C9	–	–	79.00	–	–	–	21.00
C10	–	–	75.05	–	–	3.95	
C11	–	–	71.10	–	–	7.90	
C12	–	–	67.15	–	–	11.85	
C13	–	–	–	39.50	–	39.50	
C14	–	–	–	34.00	–	45.00	
C15	–	–	–	–	44.40	34.60	
C16	–	–	–	–	42.00	37.00	
C17	–	–	–	–	39.50	39.50	

2.3. Analytical techniques

2.3.1. Physical and mechanical properties

The density and compressive strength of foamed glass ceramic materials were determined using dry cubic samples with a face size of 90±5 mm. The maximum destructive force when determining the compressive strength was adopted as the value, at which the sample collapsed with cracking or crumpled in the surface layers by 10 % of the initial height value. The final result was the average value of the test results of five samples for each composition.

2.3.2. Hydrophysical properties

Water absorption (W_V) of foamed glass ceramic materials by volume was determined by measuring the water mass adsorbed by a dry sample when completely immersed in water for 24 hours. The tests were carried out on cubic samples with a face size of 50±5 mm. Before testing, the samples were dried to constant weight at a temperature of 105±5 °C. The formula for determining water absorption (W_V, %) is as follows:

$$W_V = \frac{m_1 - m}{V \cdot \rho_W} \cdot 100 , \quad (1)$$

where m is mass of the sample, previously dried to constant weight, g;

m_1 is mass of the sample saturated with water, g;

V is volume of the sample, cm³;

ρ_W is the density of water, g/cm³.

The sorption humidity (W_S) of foamed glass ceramic materials was determined for samples with the mass of 5±0.5 g. The samples were placed in glass beaker and dried to constant weight. Then the glasses with samples were placed in artificially created steam-air medium (relative air humidity: 40 %, 80 %, 97 %, temperature is 20±2 °C). Every 5 days within 1 month, the moisture content of the samples was determined by weighing. The temperature of the room, in which the samples were weighed, was 20±2 °C; the relative air humidity was 60±10 %. The formula for determining the sorption humidity (W_S, %) of the samples is as follows:

$$W_S = \frac{m_1 - m}{m - m_2} \cdot 100 , \quad (2)$$

where m is mass of the dried sample in a glass beaker, g;

m_1 is the mass of the sample in a glass beaker after the end of the sorption process, g;

m_2 is mass of dry glass beaker, g.

When determining the hydrophysical properties, the average value of the test results for three samples of each composition was taken as the final result.

2.3.3. Thermophysical properties

The thermal conductivity (λ) of samples was determined by the probe method using the MIT–1 device (probe diameter 6 mm). The studies were carried out on dry cubic samples with a face of 90±5 mm at a temperature of 25±2 °C. In the center of cube face a hole was drilled with a diameter of 6 mm and a depth from 50 to 60 mm, into which the probe was immersed.

The application limit temperature of foamed glass ceramic materials was determined by the residual change in sample size (90×40×40 mm) after aging at a given temperature. Dry samples were placed in a muffle furnace in one row in height. The temperature in the furnace was increased at a rate of 10 °C/min to a temperature, which is 50 °C less than maximum. Then it was increased at a rate of 2 °C/min for the last 50 °C before holding. The samples were kept at the testing temperature for 2 hours. The samples were cooled together with the furnace down to room temperature. Linear temperature shrinkage ($-\Delta l$) or growth thermal expansion ($+\Delta l$) during sample heating was calculated in percent by the following formula:

$$\Delta l = \frac{l - l_1}{l} \cdot 100 , \quad (3)$$

where l is the sample height before heating, cm;

l_1 is the sample height after heating, cm.

The thermal stability (ΔT) of the samples was determined according to the temperature difference of the alternately heated and cooled samples, at which cracks occurred. Dry cubic samples (face length equals 50±5 mm) were kept for 30 minutes in a thermostat at a temperature of 110 °C. Then, the samples were removed from the thermostat after no more than 10 seconds and immersed in a water tank (water temperature is 20±2 °C). The immerse duration of samples in water is 65±5 seconds. The experiment was repeated with an increase in the thermostat temperature by 10 °C until cracks appeared on all samples. The thermal stability (ΔT, °C) of each sample was calculated by the following formula:

$$\Delta T = T_T - T_W - T_t , \quad (4)$$

where T_T is thermostat temperature, at which a crack on the sample appeared, °C;

T_W is temperature of the coolant in the tank, °C;

T_t is thermostat temperature difference between the subsequent and previous tests, 10 °C.

The average value of test results for three samples of each composition was taken as the final result, when determining the thermophysical properties.

2.3.4. Chemical stability

The chemical stability (X) of foamed glass ceramic materials was determined using powder samples (fraction 0.315–0.630 mm). The weight loss of the samples was determined after boiling for 3 hours in distilled water, in aqueous solution of 6N HCl, and in a mixture of equal volumes of 1N solutions of Na_2CO_3 and NaOH. 5±0.0005 g of the prepared sample were placed in a flask and filled with 100 cm^3 of reagent. The flask was connected to a reflux condenser. After boiling the contents of the flask for 3 hours, an aggressive liquid was drained from it, and the sample was washed with distilled water. The washed sample was poured onto a funnel with an ashless paper filter, together with distilled water. The funnel with the filter and the test sample was calcined in an oven at a temperature of 800±25 °C, cooled in a desiccator above $CaCl_2$ and weighed.

The formula for determining chemical stability (X , %) is as follows:

$$X = \frac{m - m_1}{m} \cdot 100 , \quad (5)$$

where m is the sample mass before the test, g;

m_1 is the sample mass after testing, g.

The final result was adopted as the average value of the test results for three samples of each composition.

3. Results and Discussion

3.1. Physical and mechanical properties

The results of studying the impact of chemical and mineralogical composition (siliceous rock + thermonatrite) of the charge on the bulk density and compressive strength of porous glass-ceramic samples are presented in Fig. 1. During the experiment, 17 compositions of five samples each were tested.

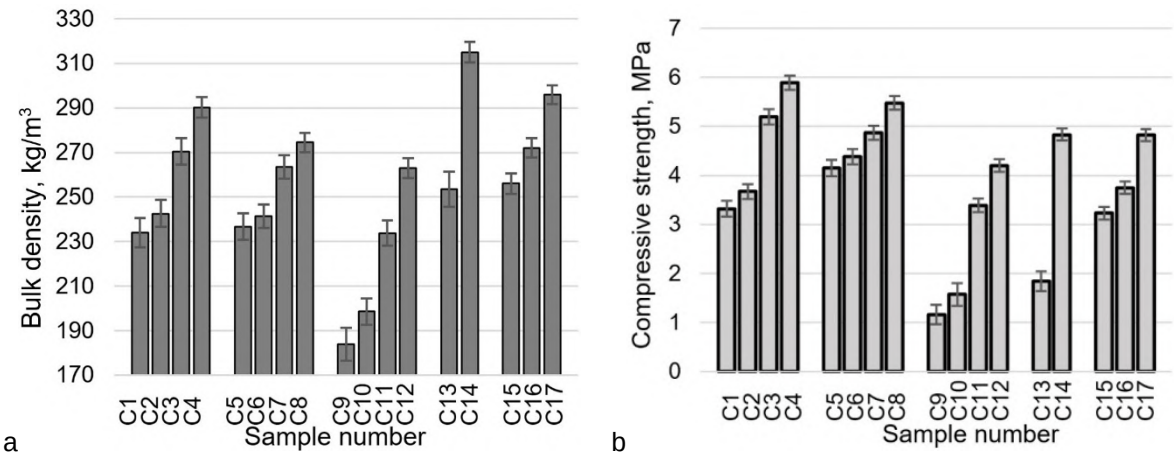

Figure 1. Bulk density (a) and compressive strength (b) of samples.

According to the obtained data (Fig. 1, *a*), an increase in the diatomite amount (rock R6) in the charge composition causes the bulk density of porous glass ceramic samples to increase linearly. For example, the density of samples increases by almost 25 % when 15 % of tripoli (rock R1) is replaced with diatomite (compositions C1 and C4, respectively) in the charge composition. This is probably due to the fact that the decrease in the bulk sample density (when replacing part of tripoli with diatomite) is a consequence of a heulandite (a mineral from the zeolite group) content decrease in the charge composition. As per researches [15, 26], the zeolite group minerals are ones of main sources for pore formation in the production of glass ceramic materials based on siliceous rocks (for one charge heating). According to studies carried out, samples C1, C5 and C11 have the lowest bulk density (≈ 230 kg/m^3). The heulandite content in the rock, from which the samples are made, is 17–19 %. The results obtained when testing samples of compositions C9 and C10 were not taken into account, since they had an uneven porous structure. The samples of C14 composition have the highest density (≈ 315 kg/m^3). In this case, the heulandite amount in the rock is the smallest (8.5 %).

Despite the deterioration of some indicators, such as density increase, the introduction of diatomite into the charge is necessary in some cases. For example, tripoli R4 and R5 contain a large amount of calcite (>

20 %). Without adding diatomite to the charge, it was not possible to obtain foamed glass ceramic materials based on these rocks. Samples based on tripoli R5 (21.5 % $CaCO_3$) have a uniform porous structure when at least 45 % of tripoli is replaced by diatomite in the charge. Based on the composition with tripoli R4 (22.4 % $CaCO_3$), it was possible to obtain porous glass ceramic materials with not less than 50 % of diatomite content from the total mass of siliceous rocks in the charge. According to the data in Table 2, the diatomite used in the study consists of an amorphous phase for 75 %, which is characterized by high reactivity. When diatomite is introduced into the charge, the fluxing agent amount increases at a lower temperature, the material has a uniform structure [14, 18]. In addition, the amount of calcite decreases with replacing the part of tripoli by diatomite in the charge composition. As is known [33], calcite contributes to the production of melt in the charge at high temperatures.

The pore structure of glass ceramic materials based on tripoli R3 becomes uniform, when at least 10 % of tripoli is replaced by diatomite in the charge. The main difference between the mineralogical composition of tripoli R3 from R1 is an increased muscovite content (by 1.8 %), as well as a lower amount of cristobalite (by 3.6 %). However, foam glass ceramic samples based on tripoli R1 have uniform porosity even without the diatomite inclusion. Therefore, in order to obtain a uniform porous structure of glass ceramic materials based on the presented siliceous rocks, the total amount of cristobalite and the amorphous phase has to be more than 44.5 %. The amount of quartz, calcite and muscovite should not exceed 12 %.

According to the studies (Fig. 1, b), it was found that the compressive strength of porous glass ceramic samples (C1–C12) is linearly dependent on their bulk density. These samples were obtained using tripoli R1–R3, which differ slightly in chemical and mineralogical composition. The samples of C4 composition have the highest compressive strength (≈ 6 MPa) for. The bulk density of the samples is 290 kg/m^3. The compressive strength of the developed porous glass ceramic materials with an equal bulk density is greater than that of foam glass from glass waste and coal fly ash (fly ash) [1, 4, 5, 10, 30].

Samples of foamed glass ceramic materials based on tripoli R4 and R5 have lower compressive strength compared to samples based on rocks R1–R3 (with equal bulk density). For example, at almost the same density (≈ 290 kg/m^3), the compressive strength of C17 samples is almost 20 % lower than the strength of C4 samples. According to the data in Table 1, this is most likely due to a decrease in Al_2O_3 amount in the material composition. A decrease in the strength characteristics of glass ceramic materials due to a decrease of aluminum oxide in their composition was represented in various researches [27–29].

3.2. Hydrophysical properties

The results of studying the water absorption for foamed glass ceramic samples based on siliceous rocks are presented in Fig. 2.

According to the scientific literature [16, 17], it is known that the water absorption of porous glass ceramic materials depends on the source of pore formation, the rate of temperature rise and burning, etc. Analyzing the data obtained (Fig. 2) showed that the water absorption of samples of the developed materials depends primarily on their bulk density. Samples of C9 composition have the greatest water absorption by volume (≈ 32 %). The bulk density of the samples is 180 kg/m^3. And the least water absorption (≈ 2.5 % by volume) is in samples of compositions C14 and C17. The density of these samples is 315 kg/m^3 and 295 kg/m^3, respectively.

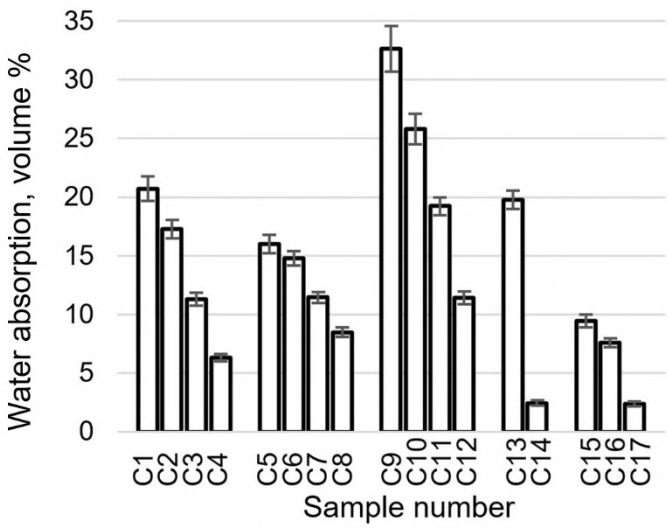

Figure 2. Water absorption of samples.

It should be noted that the amount of water adsorbed by the samples decreases with an increase of diatomite content in the initial charge composition. For example, the water absorption of C3 composition samples (7.9 % of diatomite) is almost 50 % higher than the composition of C16 (37 % of diatomite) at an almost equal value of the bulk density (≈ 270 kg/m³). As noted earlier, this is due to the prevalence of closed pores in the material structure due to an increase in the amount of fluxing agent at a lower temperature.

According to the results of experimental studies regarding determining the sorption humidity of samples of developed foam glass ceramic materials, the following was determined. After 30 days of holding the samples at a temperature of 20±2 °C and a relative humidity of 40, 80 and 97 %, the sorption humidity of the material does not exceed 0.07, 0.10, 0.14 %, respectively. The mass of samples continues to increase. The impact of chemical and mineralogical composition of siliceous rocks (used for the research) on the equilibrium moisture content of samples from developed materials is not exposed at this stage. According to researches [16, 17], the sorption humidity index for samples of foam glass and foamed glass ceramic is stabilized for some compositions only after 1 year of testing. Our results after 30 days of testing correlate with data obtained by other authors [16, 17].

3.3. Thermophysical properties

The results of the thermal conductivity test for porous glass ceramic samples, which are based on siliceous rocks with various bulk densities, are presented in Fig. 3. During the experiment, three samples for each of 17 compositions were tested.

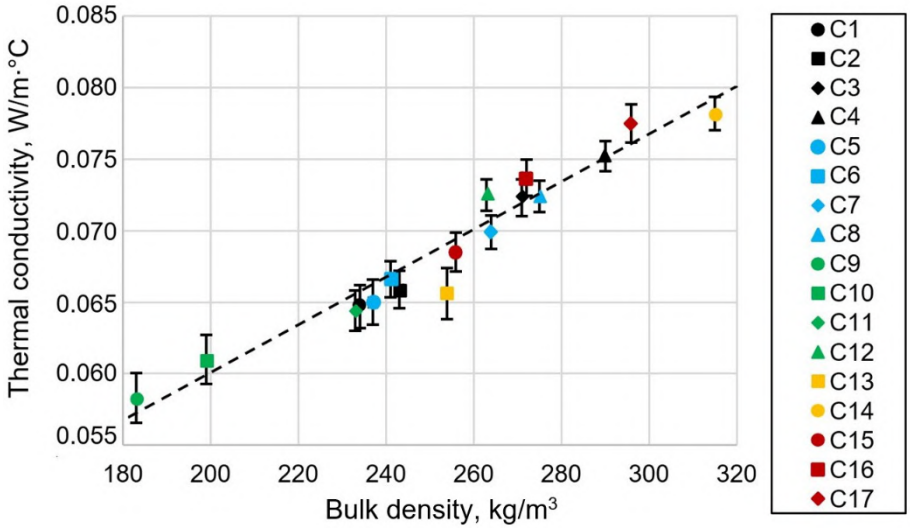

Figure 3. Thermal conductivity of samples.

According to the data presented in Fig. 3, the thermal conductivity of dry samples increases linearly from 0.0583 to 0.0782 W/m·°C with an increase in the material density from 180 to 320 kg/m³. The dependence of thermal conductivity (λ , W/m·°C) on the density of studied materials is represented by the following formula:

$$\lambda = \frac{0.02\rho + 3.2}{120}, \tag{6}$$

where ρ is the bulk density of the material in the dry state, kg/m³.

The approximation certainty factor is R^2 = 0.9405.

As a result of conducted research, it was found that the density of dry porous glass ceramic materials from siliceous rocks with a thermal conductivity of not higher than 0.060 W/m·°C should be less than 200 kg/m³. For thermal conductivity of not more than 0.070 W/m·°C the density has to be less than 260 kg/m³. No significant impact of the chemical and mineralogical composition of siliceous rocks (used in the study) on the thermal conductivity of developed material samples was detected. The results obtained correlate with the data of many researchers [11, 14, 20, 28].

According to various studies [1, 27, 28], the building materials used for the thermal insulation of industrial equipment must have high thermal stability (not to collapse under abrupt temperature changes). The results of testing the thermal stability of porous glass ceramic samples from siliceous rocks are represented in Fig. 4.

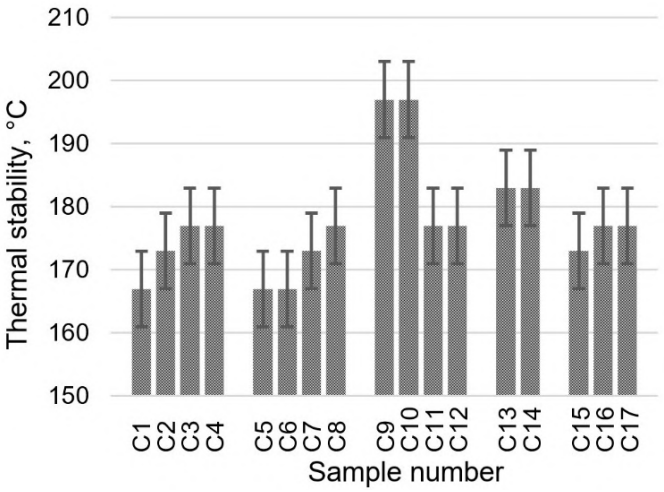

Figure 4. Thermal stability of samples.

Analyzing the data presented in Fig. 4, it can be concluded that the thermal stability of developed material samples is within the 167–183 °C range. Insufficiently values of the indicator are apparently associated with the presence of both amorphous phase and crystalline minerals in the material. They have different thermal expansion coefficients. As a result, with an abrupt temperature drop of more specific intervals, the material is destroyed by internal stresses. As was determined earlier [26], the ratio of crystalline to amorphous phase is approximately 40:60 for the foamed glass ceramic materials based on siliceous rocks. Samples of compositions C9 and C10 withstood temperature gradient of almost 200 °C. Such effect is likely associated with the open porosity of the material, as evidenced by the high rate of water absorption of the samples (Fig. 2). According to the test method, heated samples were immersed in water. Penetrating into the material, it contributed to a more uniform cooling. Consequently, the thermal stability of the samples increased.

It should be noted that the thermal stability of foamed glass ceramic samples increases with an increase in the diatomite content in charge composition. Disregarding the test results of C9 and C10 composition samples, the compositions with a diatomite content in the charge of more than 39.5 % (C13 and C14) have highest thermal stability (183 °C). The lowest value of the indicator is for samples (compositions C1, C5, C6), for which the diatomite content in the charge does not exceed 3.95 %.

In terms of thermal stability, porous glass ceramic materials from siliceous rocks are comparable to foamed glass ceramic from industrial wastes, but slightly inferior to foamed glass [27, 28].

The results of studies on determining the application limit temperature of the developed materials (residual changes in the size of the samples after holding for 2 hours at a given temperature) are presented in Table 4.

Table 4. Residual changes in the size of samples after holding for 2 hours at a given temperature.

Comp. number	Residual changes in the size of samples after holding for 2 hours at a given temperature, %*		
	750 °C	800 °C	850 °C
C1	0.00	–0.10	–0.21
C2	0.00	–0.10	–0.29
C3	0.00	–0.12	–0.49
C4	–0.12	–0.43	–1.17
C5	0.00	–0.13	–0.39
C6	0.00	–0.29	–0.75
C7	0.00	–0.31	–0.97
C8	–0.17	–0.34	–2.32
C9	0.00	0.00	–0.15
C10	0.00	–0.11	–0.27
C11	0.00	–0.18	–0.43
C12	0.00	–0.30	–0.88
C13	–0.06	–0.18	–1.04
C14	–0.76	–0.82	–3.04
C15	–0.11	–0.68	–5.36
C16	–0.13	–0.76	–4.71
C17	–0.22	–0.78	–5.48

* − The standard deviation (σ) of the results does not exceed 0.02 % (from 0 to – 1 % for the results).

Analyzing the data in Table 4 shows that individual compositions of the developed materials (C1–C3, C5–C7, C9–C12) can be operated at a temperature of ≤ 850 °C. After holding for 2 hours at a temperature of 870 °C, the sizes of samples of all compositions decreased by more than 1 %. With an increase of the charge diatomite content to more than 11.85 % in the composition, the application limit temperature of the samples decreases to 800 °C. After holding the samples for 2 hours at a temperature of 850 °C, their sizes decreased by only 0.15 % (C9 composition), and decreased by more than 5 % for C17 composition. According to the data in Tables 1 and 3, a C9 composition sample was obtained from siliceous rock (R3) with an Al_2O_3 content of ≈ 7.6 % (the amount of diatomite is 0). The total amount of aluminum oxide in the C17 charge does not exceed 6 %. According to the researches [27–29, 32], the stability of ceramic materials to prolonged exposure to high temperatures increases with an increase in the amount of Al_2O_3 and decreases with an increase in Fe_2O_3. It is likely that the increased content of Fe_2O_3 (2.7 %) in the composition of siliceous rock (R4) contributed to a decrease in the application limit temperature of samples based on it (C13, C14) up to 800 °C. It is important to note that the amount of alumina in the charge, from which samples C13 and C14 are made, is approximately 7 %.

Regarding the application limit temperature, the developed materials are comparable to foamed glass ceramic from industrial waste, and significantly exceled foamed glass [28]. The application limit temperature of the latter rarely exceeds 600 °C [1]. Porous glass ceramic materials based on siliceous rocks (presented in the research) can be used as thermal insulation of industrial equipment, such as melting furnaces, boiler equipment, etc.

3.4. Chemical stability

Table 5 presents data on the weight loss of foamed glass ceramic samples (crushed to a fraction of 0.315–0.630 mm) after 3 hours of boiling in various chemical media.

According to the experimental data, with an increase in the diatomite content in the charge composition, the dissolution of powdery glass ceramic samples decreases upon boiling for 3 hours in water, an aqueous HCl solution, and also in alkaline solution. The pattern is typical for samples obtained from a charge based on siliceous rocks R1–R3 (compositions C1–C12). Thus, the mass of developed material samples based on R1 composition tripoli (sample C1) decreased on average by 0.9 % after 3 hours of boiling in water. In an alkaline solution it decreased by 7.51 %, and by 3.62 % in an acid solution. When replacing 15 % of tripoli with diatomite, the weight loss of samples (C4) after 3 hours of boiling in water is on average 0.36 %. For an alkaline solution this value is 7.16 %, and for acid solution – 1.78 %.

Table 5. The change in mass of samples after boiling in various chemical media for 3 hours.

Comp. number	The change in mass of samples after boiling in various chemical media for 3 hours, %					
	Average value			Standard deviation (σ)		
	H_2O	6N HCl solution	1N Na_2CO_3 solution + 1N NaOH solution (1:1)	H_2O	6N HCl solution	1N Na_2CO_3 solution + 1N NaOH solution (1:1)
C1	0.90	7.51	3.62	0.08	0.45	0.25
C2	0.75	7.44	2.37	0.06	0.52	0.17
C3	0.57	7.33	1.94	0.05	0.44	0.10
C4	0.36	7.16	1.78	0.03	0.36	0.11
C5	0.74	7.43	3.6	0.05	0.45	0.22
C6	0.58	7.38	2.48	0.05	0.44	0.12
C7	0.49	7.24	2.03	0.04	0.51	0.14
C8	0.42	7.13	1.94	0.03	0.50	0.12
C9	0.61	6.99	3.41	0.05	0.35	0.24
C10	0.54	6.71	2.97	0.04	0.40	0.15
C11	0.48	6.35	2.74	0.04	0.44	0.14
C12	0.32	6.13	2.51	0.03	0.31	0.18
C13	0.86	6.45	2.08	0.06	0.38	0.17
C14	0.99	6.38	1.91	0.09	0.43	0.10
C15	0.08	6.51	1.97	0.01	0.46	0.12
C16	0.33	6.43	1.89	0.02	0.32	0.13
C17	0.89	6.42	1.87	0.08	0.39	0.13

The dissolution of samples from a charge based on siliceous rocks R4 and R5 (compositions C13–C17) is greater with an increase of diatomite content in the mixture. After 3 hours of boiling in water, samples of composition C15 lost only 0.08 % by weight. At the same time, samples of composition C17 lost 0.89 %. Both variants of samples were obtained on the basis of tripoli with the R5 composition. There is by 4.9 % more

diatomite in the C17 charge composition than in C15. The chemical stability of these samples in HCl and alkaline solutions varies slightly. Samples lost on average 1.91 % after 3 hours of boiling in a HCl solution, and 6.46 % after boiling in an alkaline solution.

According to the researches [34, 35], the chemical stability of glass-ceramic materials depends on many factors. The main influence is provided by their chemical and mineralogical composition. Pisciella P. in the study [31] came to the conclusion that the chemical stability of glass ceramics primarily depends on the material's structure formation. As mentioned above, the amount of fluxing agent increases at a lower temperature with the introduction of diatomite in the charge composition. This possibly contributes to the material's structure formation, characterized by greater chemical stability. It was determined that the chemical stability of glass ceramic materials is directly affected by the content of CaO in the composition [32]. The chemical stability increases with a decrease in calcium oxide in the material composition. According to the data in Table 1, the CaO content in the diatomite used (R6) is several times lower compared to tripoli (R1–R5). When replacing part of tripoli in the mixture with diatomite, the amount of calcium oxide in the calcined material decreases. Apparently, this also contributes to an increase in the chemical stability of the samples.

The experimental tests of foamed glass materials showed their high chemical stability in water, in an aqueous HCl solution, as well as in an alkaline solution. Regarding this indicator, the developed materials excelled foamed glass [11, 34, 35]. The above mentioned allows recommending porous glass ceramic materials to be used as insulation of pipelines, industrial plants, etc.

4. Conclusions

The impact of chemical and mineralogical composition of siliceous rocks on the properties of porous glass ceramic samples is studied. The samples were obtained by burning a mechanochemically activated charge. Siliceous rocks from six deposits were ground together with thermonatrite ($Na_2CO_3 \cdot H_2O$). The resulting mixture was burned at a temperature of 850 °C. The following properties were experimentally determined: bulk density, compressive strength, water absorption, sorption humidity, thermal conductivity, application limit temperature, thermal and chemical stability of samples. The major findings of the research are as follows:

1. The bulk density of the samples depends more on the mineralogical composition of the siliceous rocks, from which they were made. In order to obtain glass ceramic materials with a uniform porous structure, the total amount of cristobalite and the amorphous phase in the rock composition has to be more than 44.5 %. The amount of quartz, calcite and muscovite in the charge composition should be less than 12 %. The bulk density of the samples decreases with an increase in the heulandite content in the charge composition.

2. The compressive strength of the developed materials is linearly dependent on their bulk density. Moreover, this indicator decreases with a decrease in the amount of Al_2O_3 in the charge composition. The greatest compressive strength (≈ 6 MPa) was found in samples with a bulk density of 290 kg/m^3. The compressive strength of the developed porous glass ceramic materials with an equal bulk density is several times higher than that of foamed glass from waste glass and coal fly ash.

3. Water absorption of samples of developed materials decreases with a diatomite content increase in the charge composition. The greatest water absorption by volume (≈ 32 %) is in samples based on a charge without diatomite. The least absorption (≈ 2.5 %) is in samples obtained from a charge with a diatomite content of at least 39.5 %. The decrease in water absorption as a result of replacing part of tripoli with diatomite is apparently due to the prevalence of closed pores in the material structure. This is due to an increase in the amount of fluxing agent at a lower temperature.

4. The thermal conductivity of dry foamed glass ceramic samples from siliceous rocks increases almost linearly from 0.0583 to 0.0782 W/m·°C with an increase in the material density from 180 to 320 kg/m^3. No significant effect of the chemical and mineralogical composition of siliceous rocks (used in the study) on the thermal conductivity of the samples was revealed.

5. The thermal stability of the foam glass ceramic samples increases from 167 to 183 °C with diatomite content increase in the charge composition from 0 to 39.5 %. Insufficiently values of the indicator are apparently associated with the presence of both amorphous phase and crystalline minerals in the material. They have different thermal expansion coefficients.

6. The application limit temperature of porous glass ceramic materials reaches 850 °C. This indicator for samples decreases to 800 °C with an increase of diatomite in the charge composition of more than 11.85 %. It was determined that the application limit temperature decreases with a decrease in the amount of Al_2O_3 in the charge composition, as well as with an increase in Fe_2O_3.

7. The developed materials showed high chemical stability after boiling in water, in an aqueous HCl solution and in alkaline solution. It was determined that the dissolution of powdery glass ceramic samples

upon boiling for 3 hours in chemical media decreases with diatomite content increase in the charge composition.

8. Considering the number of indicators, porous glass ceramic materials based on siliceous rocks excel foamed glass and can be used as insulation for pipelines, industrial plants (melting furnaces, boiler equipment), etc.

5. Acknowledgement

The study was conducted using research grant from the Russian Science Foundation (project No. 18-73-00213).

References

1. Fernandes, H.R., Tulyaganov, D.U., Ferreira, J.M.F. Preparation and characterization of foams from sheet glass and fly ash using carbonates as foaming agents. Ceramics International. 2009. 35(1). Pp. 229–235. DOI: 10.1016/j.ceramint.20-07.10.019
2. Vatin, N.I., Nemova, D.V., Kazimirova, A.S., Gureev, K.N. Increase of energy efficiency of the building of kindergarten. Advanced Materials Research. 2014. No. 953–954. Pp. 1537–1544. DOI: 10.4028/www.scientific.net/AMR.953-954.1537
3. Vatin, N.I., Nemova, D.V., Tarasova, D.S., Staritcyna, A.A. Increase of energy efficiency for educational institution building. Advanced Materials Research. 2014. No. 953–954. Pp. 854–870. DOI: 10.4028/www.scientific.net/AMR.953-954.854
4. Bai, J., Yang, X., Xu, S., Jing, W., Yang, J. Preparation of foam glass from waste glass and fly ash. Materials Letters. 2014. No. 136. Pp. 52–54. DOI: 10.1016/j.matlet.2014.07.028
5. Zhu, M., Ji, R., Li, Z., Wang, H., Liu, L., Zhang, Z. Preparation of glass ceramic foams for thermal insulation applications from coal fly ash and waste glass. Construction and Building Materials. 2016. No. 112. Pp. 398–405. DOI: 10.1016/j.conbuildmat.2016.02.183
6. König, J., Petersen, R.R., Yue, Y. Fabrication of highly insulating foam glass made from CRT panel glass. Ceramics International. 2015. 41(8). Pp. 9793–9800. DOI: 10.1016/j.ceramint.2015.04.051
7. Cao, J., Lu, J., Jiang, L., Wang, Z. Sinterability, microstructure and compressive strength of porous glass-ceramics from metallurgical silicon slag and waste glass. Ceramics International. 2016. 42(8). Pp. 10079–10084. DOI: 10.1016/j.ceramint.2016.03.113
8. Khater, G.A. Glass-ceramics in the $CaO–MgO–Al_2O_3–SiO_2$ system based on industrial waste materials. Journal of Non-Crystalline Solids. 2010. 356(52–54). Pp. 3066–3070. DOI: 10.1016/j.jnoncrysol.2010.02.030
9. Yatsenko, E.A., Gol'tsman, B.M., Kosarev, A.S., Karandashova, N.S., Smolii, V.A., Yatsenko, L.A. Synthesis of Foamed Glass Based on Slag and a Glycerol Pore-Forming Mixture. Glass Physics and Chemistry. 2018. 44(2). Pp. 152–155. DOI: 10.1134/S1087659618020177
10. Chen, X., Lu, A., Qu, G. Preparation and characterization of foam ceramics from red mud and fly ash using sodium silicate as foaming agent. Ceramics International. 2013. 39(2). Pp. 1923–1929. DOI: 10.1016/j.ceramint.2012.08.042
11. Liu, T., Li, X., Guan, L., Liu, P., Wu, T., Li, Z., Lu, A. Low-cost and environment-friendly ceramic foams made from lead-zinc mine tailings and red mud: Foaming mechanism, physical, mechanical and chemical properties. Ceramics International. 2016. 42(1). Pp. 1733–1739. DOI: 10.1016/j.ceramint.2015.09.131
12. Erofeev, V., Korotaev, S., Bulgakov, A., Tretiakov, I., Rodin, A. Getting Fired Material with Vitreous Binder Using Frame Technology. Procedia Engineering. 2016. No. 164. Pp. 166–171. DOI: 10.1016/j.proeng.2016.11.606
13. Ivanov, K.S. Granulated foam-glass ceramics for ground protection against freezing. Magazine of Civil Engineering. 2018. 3(79). Pp. 95–102. DOI: 10.18720/MCE.79.10
14. Ivanov, K.S. Optimization of the structure and properties of foam-glass ceramics. Magazine of Civil Engineering. 2019. 89(5). Pp. 52–60. DOI: 10.18720/MCE.89.5
15. Kazantseva, L.K., Rashchenko, S.V. Optimization of porous heat-insulating ceramics manufacturing from zeolitic rocks. Ceramics International. 2016. 42(16). Pp. 19250–19256. DOI: 10.1016/j.ceramint.2016.09.091
16. Sokolova, S.N., Vereshagin, V.I. Lightweight granular material from zeolite rocks with different additives. Construction and Building Materials. 2010. 24(4). Pp. 625–629. DOI: 10.1016/j.conbuildmat.2009.10.010
17. Volland, S., Kazmina, O., Vereshchagin, V., Dushkina, M. Recycling of sand sludge as a resource for lightweight aggregates. Construction and Building Materials. 2014. No. 52. Pp. 361–365. DOI: 10.1016/j.conbuildmat.2013.10.088
18. Yatsenko, E.A., Smolii, V.A., Gol'tsman, B.M., Ryabova, A.V., Klimova, L.V., Gol'tsman, N.S. Optimal Fractional Composition of Batch for Synthesis of Foam-Glass Materials Based on Diatomite from the Chernoyarskoe Deposit. Glass and Ceramics (English translation of Steklo i Keramika). 2019. 75(9–10). Pp. 391–393. DOI: 10.1007/s10717-019-00092-8
19. Zhimalov, A.A., Bondareva, L.N., Igitkhanyan, Y.G., Ivashchenko, Y.G. Use of Amorphous Siliceous Rocks – Opokas to Obtain Foam Glass with Low Foaming Temperature. Glass and Ceramics (English translation of Steklo i Keramika). 2017. 74(1–2). Pp. 13–15. DOI: 10.1007/s10717-017-9916-1
20. Chen, W.-Q., Gao, S.-Y., Liu, J., Dong, Y.-Q. Preparation and properties of glass-ceramics from gold tailings by melting method. Rengong Jingti Xuebao/Journal of Synthetic Crystals. 2014. 43(1). Pp. 217–221.
21. Zhang, K., Liu, J., Liu, W., Yang, J. Preparation of glass-ceramics from molten steel slag using liquid-liquid mixing method. Chemosphere. 2011. 85(4). Pp. 689–692. DOI: 10.1016/j.chemosphere.2011.07.005
22. Huo, W., Yan, S., Wu, J.-M., Liu, J., Chen, Y., Qu, Y., Tang, X., Yang, J. A novel fabrication method for glass foams with small pore size and controllable pore structure. Journal of the American Ceramic Society. 2017. 100(12). Pp. 5502–5511. DOI: 10.1111/jace.15089
23. Mueller, A., Sokolova, S.N., Vereshagin, V.I. Characteristics of lightweight aggregates from primary and recycled raw materials. Construction and Building Materials. 2008. 22(4). Pp. 703–712. DOI: 10.1016/j.conbuildmat.2007.06.009
24. Boldyrev, V.V. Mechanochemistry and mechanical activation of solids. Russian Chemical Reviews. 2006. 75(3). Pp. 177–189. DOI: 10.1070/RC2006v075n03ABEH001205
25. Takacs, L. The historical development of mechanochemistry. Chemical Society Reviews. 2013. 42(18). Pp. 7649–7659. DOI: 10.1039/c2cs35442j
26. Erofeev, V.T., Rodin, A.I., Kravchuk, A.S., Kaznacheev, S.V., Zaharova, E.A. Biostable silicic rock-based glass ceramic foams. Magazine of Civil Engineering. 2018. 84(8). Pp. 48–56. DOI: 10.18720/MCE.84.5

27. Keyvani, N., Marghussian, V.K., Rezaie, H.R., Kord, M. Effect of Al_2O_3 content on crystallization behavior, microstructure, and mechanical properties of SiO_2–Al_2O_3–CaO–MgO glass-ceramics. International Journal of Applied Ceramic Technology. 2011. 8(1). Pp. 203–213. DOI: 10.1111/j.1744-7402.2009.02428.x
28. Kim, E.S., Yeo, W.J. Thermal properties of $CaMgSi_2O_6$ glass-ceramics with Al_2O_3. Ceramics International. 2012. 38(1). Pp. S547–S550. DOI: 10.1016/j.ceramint.2011.05.074
29. Kang, M., Kang, S. Influence of Al_2O_3 additions on the crystallization mechanism and properties of diopside/anorthite hybrid glass-ceramics for LED packaging materials. Journal of Crystal Growth. 2011. 326(1). Pp. 124–127. DOI: 10.1016/j.jcrysgro.2011.01.081
30. Zhou, M., Ge, X., Wang, H., Chen, L., Chen, X. Effect of the CaO content and decomposition of calcium-containing minerals on properties and microstructure of ceramic foams from fly ash. Ceramics International. 2017. 43(12). Pp. 9451–9457. DOI: 10.1016/j.ceramint.2017.04.122
31. Yang, Z., Lin, Q., Lu, S., He, Y., Liao, G., Ke, Y. Effect of CaO/SiO_2 ratio on the preparation and crystallization of glass-ceramics from copper slag. Ceramics International. 2014. 40(5). Pp. 7297–7305. DOI: 10.1016/j.ceramint.2013.12.071
32. Ren, X.-Z., Zhang, W., Zhang, Y., Zhang, P.-X., Liu, J.-H. Effects of Fe_2O_3 content on microstructure and mechanical properties of CaO–Al_2O_3–SiO_2 system. Transactions of Nonferrous Metals Society of China (English Edition). 2015. 25(1). Pp. 137–145. DOI: 10.1016/S1003-6326(15)63588-9
33. Kazantseva, L.K., Lygina, T.Z., Rashchenko, S.V., Tsyplakov, D.S. Preparation of Sound-Insulating Lightweight Ceramics from Aluminosilicate Rocks with High $CaCO_3$ Content. Journal of the American Ceramic Society. 2015. 98(7). Pp. 2047–2051. DOI: 10.1111/jace.13581
34. Pisciella, P., Crisucci, S., Karamanov, A., Pelino, M. Chemical durability of glasses obtained by vitrification of industrial wastes. Waste Management. 2001. 21(1). Pp. 1–9. DOI: 10.1016/S0956-053X(00)00077-5
35. Abdel-Hameed, S.A.M., El-kheshen, A.A. Thermal and chemical properties of diopside-wollastonite glass-ceramics in the SiO_2–CaO–MgO system from raw materials. Ceramics International. 2013. 29(3). Pp. 265–269. DOI: 10.1016/S0272-8842(02)00114-1

Contacts:

Vladimir Erofeev, yerofeevvt@mail.ru

Alexander Rodin, al_rodin@mail.ru

Viktor Bochkin, sovelitnew@mail.ru

Anatolij Ermakov, anatoly.ermakov97@mail.ru

© Erofeev, V.T., Rodin, A.I., Bochkin, V.S., Ermakov, A.A., 2021

Magazine of Civil Engineering

ISSN 2712-8172

journal homepage: http://engstroy.spbstu.ru/

DOI: 10.34910/MCE.102.3

Flammability of polymeric materials used in construction

N.I. Konstantinova[a]*, N.V. Smirnov[a], A.Y. Shebeko[a], L.T. Tanklevsky[b]
[a] FGBU VNIIPO of EMERCOM of Russia, VNIIPO district, Balashiha, Russia
[b] Peter the Great St. Petersburg Polytechnic University, St. Petersburg, Russia
** E-mail: konstantinova_n@inbox.ru*

Keywords: fires, fire protection, buildings, flame retardants, fire resistance, flammability, smoke

Abstract. This article is devoted to the results of fire risk studies of polymer construction materials (PCMs), in particular decorative and finishing materials. The article summarizes the results of longstanding research carried out at VNIIPO EMERCOM in Russia and covers the main areas such as a review of existing regulatory and technical bases, experimental study of fire hazard (mainly the ability to ignite) for decorative and finishing facing materials, estimation of the flammability of paint and varnish coverings (P&VC), development of a method to determine fields of application for decorative and finishing materials, based on the condition of non-flammability in the case of fire, development of permissible usage conditions for decorative and finishing materials in premises (especially along evacuation routes) and determining methods for establishing permissible finish height. Research conducted in the specified areas allows to formulate the conditions for fire-safe P&VC application, taking into account the established maximum values of heat flux density, as well as to propose methods for determining the ignition time, the critical density of the heat flux ignition and the amount of heat necessary to ignite a unit of the coating surface for further practical use. Fire-safe P&VC application means no fire hazard from such coatings under the conditions of their particular use. Experimental studies of the influence of P&VC thickness (number of layers) and base (substrate) type on the flammability indexes made it possible to establish a number of corresponding dependencies.

1. Introduction

The primary objective of this work are polymer finishing materials for walls and floors, which can contribute into fire spreading and occurring of other hazardous factors (such as flame, smoke, etc.). The subject of this research is flammability of polymer building materials under the influence of heat flux of different densities and the assessment of their parameters which can impact their possible application. Authors have not found any published researches concerning described materials and methods which can be used for their investigating.

Some types of epoxy and alkyd enamels, water dispersion paints, samples of painted metal panels and decorative and protective plaster used for finishing the exterior and interior walls of buildings were selected for the studies.

The flammability of polymer materials is a large problem of fire safety. Works in the area of fire safety are mostly concentrated on prevention [1−4]. There are many works devoted to the flammability of polymer building materials. [5−11], however most of the researches were focused on comparative tests and experimental data analysis, which is not connected with different fire modes and possible heat fluxes in specific conditions. If we talk about the application of different polymer coatings in fire conditions, we can mention works [12−14] which are concentrated on flammability of intumescent fire-protective coatings. Some other researches concerning the low flammable building materials are represented in [15, 16].

The relevance of a work to assess the fire hazard of polymeric building materials and the development of a fire prevention measures for their use especially on the evacuation routes is due to the need to ensure

Konstantinova, N.I., Smirnov, N.V., Shebeko, A.Y., Tanklevsky, L.T. Flammability of polymeric materials used in construction. Magazine of Civil Engineering. 2021. 102(2). Article No. 10203. DOI: 10.34910/MCE.102.3

This work is licensed under a CC BY-NC 4.0

the safety of people during fire and also to limit the spread of a fire in a building to minimize material and environmental damage.

The aim of the current research is to estimate flammability of polymer building materials in conditions which are close to real fire scenario. The following tasks were formulated:

- To choose and justify the parameters of forecasting and assessment of polymer building materials fire hazard;
- To choose and justify the type of materials which will be used during research;
- To investigate flammability of samples and find out correlations;
- To show the possibility of determination of the area of safe application of polymer building materials considering obtained experimental data of their flammability.

From a fire occurrence perspective, in preventing the possible spread of fire through the building (or room) the flammability of combustible of PCM is the most important fire hazard property. Having achieved non-flammability of PCMs in the case of fire (along evacuation routes in particular), it is possible to limit the spread of fire, providing a safe means of evacuation and considerably reducing material and ecological damage.

The parameters, most often used for estimating the flammability of PCMs, are flammability temperature (°C), the critical density of the heat flux rate (q^{flm}_{cr}, kW/m^2) and flammability time under the predetermined density of the heat flux rate ($\tau_{flm,cr}$) [17]. Another important and informative parameter that can be used in the assessment of PCM flammability is the quantity of supplied heat needed for flammability of a material surface unit ($Q_{flm,}$ kJ/m^2), calculated from Eq. (1):

$$Q_{flm} = \int_0^{\tau\, flm} q(\tau) d\tau\,, \tag{1}$$

where $q(\tau)$ is the heat flux density influencing the material at a point in time τ and τ is the current time (s).

Under $q(\tau)$ = constant rate,

$$Q_{flm} = q\mathrm{eqv} \ \ {}^{*}\tau_{flm}\,, \tag{2}$$

To obtain a more objective assessment of flammability, all the parameters need to be considered as a result of the influence of heat flux and it is necessary to implement experimental conditions maximally close to the real ones, including the correspondence of the heat flux mode to the real heat flux.

Experimental data from [14] shows the change in heat flux density influencing the most dangerous section (from the point of flammability) during a fire. The data was obtained from results of field experiments at a polygonal installation, “High-rise building fragment”, with a fire load of 30 kg/m^2 (fire centre) in a room of 20 m^2, which corresponds to the majority of corridor-type buildings [18, 19]. In [14] it is shown how rates Q_{flm} and q^{flm}_{cr} are calculated in a diagram. With a known value of q^{flm}_{cr}, it is possible to determine the permissible height of corridor finish [17]. In the example presented, the case of determining the maximum allowable flame propagation in a fire is not considered.

Research on the flammability of different PCMs under conditions of variable and constant heat flux density over a period of time made it possible to introduce the concept of “equivalent heat flux density over time”, q_{eqv}. q_{eqv} is a constant heat flux density over a period of time, which influences the material and provides flammability results identical to those obtained for a variable heat flux density over a period of time.

The results in [17] Fig. 2 were obtained experimentally in large-scale tests. In other specific cases, this dependence may have a different look and be different from linear. The research undertaken here can be used in future to maintain conditions for the fire-safe application of polymeric materials in a construction area, depending on the purpose of the materials and the purpose of the buildings.

The most potentially dangerous materials in terms of possible fire spread in a building are decorative and finishing facing materials used along evacuation routes and in rooms.

Any protective and decorative polymer coating applied to a non-flammable substrate (sand-cement mortar, concrete, brick, metal, mineral fibre plates, etc.) does not allow the material to be classified as non-combustible. This is because the combustibility test method (in Russia) for classifying construction materials as non-combustible or combustible only applies to homogeneous building materials. For laminates, it can only be used as an evaluation and tests are carried out for each layer of material separately. Thus, in the case of a composite of a non-flammable finishing material and a combustible polymer coating applied thereon, the composition cannot be classified as non-combustible due to the presence of a layer of combustible material

in its composition. In the course of research within the present framework, an analytical evaluation was carried out of the thermal impact on the facade system structure during fire spread on the outer surface of exterior wall in tests according to [21]. For this purpose, tests were conducted at FGBU VNIIPO EMERCOM, Russia, assessing the fire hazard of facade insulating composite system samples with external plaster layers. The samples were assigned to fireproof class.

The temperature regime regulated by [21], it corresponds closely to real fire conditions and the maximum temperature values on the tested facade system surface are reached on the system surface at the flame exit point from the open aperture of the fire chamber at approximately 0.2–0.4 m from the upper boundary (upper slope). The maximum temperature values, recorded in the gas column (at 150 mm from the facade system sample surface) at the indicated location when testing various facade thermal insulation composite system (FTICS) samples were 600–650°C and on the facade system sample surface were 550–600°C, which corresponds to the average density value of incident heat flux on a facade system surface of approximately 50 kW/m^2. P&VC applied to the outer surface of the facade system finishing or facing surface almost completely burned out in the zone of direct exposure to the flame. This is confirmed by the test results for P&VC samples considered in the framework of the present work, according to standard [21]. Outside the zone of direct flame action (for example, at a distance of 1.8 m from the upper boundary of the fire chamber aperture) the maximum values of fixed temperatures in the gas column are in the range 300–350°C and on the facade system sample surface are 250–300°C, which corresponds to an average value of incident heat flux density on the facade system surface of approximately 15 kW/m^2.

2. Materials and Methods

To establish the extent to which the protective and decorative layer of the material can affect fire hazard, comprehensive experimental studies were conducted to determine the flammability, flame propagation over the surface, smoke-generating capacity and toxicity of the combustion products of certain facing materials, using different non-flammable bases (in particular, metal and cement) and different chemical compositions and thickness of P&VC paint coatings. To carry out the experiments assessing the fire hazard of such materials, standard test methods (Russian) were used.

An experimental evaluation of flame propagation was the simultaneous action of a 32 kW/m^2 radiation source and a pilot burner flame, and the measurement result was a dimensionless value of the flame propagation index taking into account the linear motion of the flame front and the temperature of the flue gases generated during combustion.

The method of determining the toxicity index (Toxicity index of combustion products) is biological and consisted of burning the test material in the combustion chamber at a known heat flux density and identifying the dependence of the lethal effect of gaseous combustion products on the mass of material, referred to the unit volume of the exposure chamber. There are four hazard classes of materials (T1-T4) according to the value of the toxicity indicator, of which class T1 is considered to be low hazardous.

The essence of the method for determining the smoke generation coefficient (D_m, m^2/kg) was to determine the optical density of the smoke generated during combustion or decay of an amount of material distributed in some volume. Three groups of materials are distinguished with low (S1), moderate (S2) and high (S3) smoke-generating ability.

To obtain the dependences of the critical falling heat flux density (CFHFD) and the linear velocity of flame propagation over the surface from the thickness of the P&VC, various types of epoxy and alkyd enamels and water-dispersion paints were used for finishing the exterior and interior walls of buildings. In addition, comprehensive study of fire hazard indicators was carried out for samples of finished painted metal panels and finishing compositions for the external surfaces of exterior walls of buildings and structures (facade compositions).

It is important to note that the P&VC layers were applied to a non-flammable substrate (or composition) in accordance with the normative and technical documentation development, with a consequent increase in the thickness of the upper layer (samples 1, 3, 4 and 5). Since in most cases of decorative property loss, P&VC layers are not removed, but are applied over the existing ("old") P&VC layer (repainting), the thickness of the upper layer of the coating increases. Samples 6–8 comprised the external coating of building materials and structures (in this work, metal facing panels and facade composition).

The total thickness of outer decorative and protective plaster (base and finishing layers) in the facade compositions was not less than 7.0 mm, with a thickness of the base plaster layer not less than 5.0 mm. The thickness of increased strength, weatherproof, vapour permeable P&VC, used for thin-layer colouring (levelling) on the outer surface of the finishing/finishing layer of decorative protective plaster, was not more than 180–200 μm.

According to the results of the experimental studies conducted according to the [22], it was established that none of the samples of materials (compositions) investigated are in the group of non-combustible (NC) materials, with only one parameter considered – combustion duration (more than 10 s).

To answer the question of the extent to which the protective and decorative coating applied to different base types can affect composition flammability as a whole, experimental studies of various chemical compositions and thicknesses of P&VC were carried out. For this purpose, the chosen P&VC types were those used for finishing and repairing building premises and structures (walls, ceilings), in particular, water-dispersion acrylic enamel (WD) and pentaphthalic (PP) and oil (O) enamels. The bases were chrysotile cement sheets (CCS), gypsum plasterboard sheets (GPS) and GPS with glued fibreglass wallpaper. The bases for P&VC were chosen taking into account the most common surfaces for painting in buildings and structures. The main characteristics of the bases for coating are shown in Table 1. The term consumption (g/m^2) refers to the amount of paint applied to the surface to be protected to achieve the required coating thickness.

Table 1. Main characteristics of bases for coating.

Base	Thickness (mm)	Consumption (g/m^2)	Density
Chrysotile cement sheets	10	–	1600 kg/m^3
Plasterboard sheets	9.5	–	800 kg/m^3
Fibreglass wallpaper	0.3–0.5	–	120–140 g/m^2
PVA glue “Builder” universal	–	140–160	–

The choice of the number of P&VC layers was based on the possibility of repeated coatings of paint being applied in the case of repair work, mainly because of the need to allow for the required decorative and operational properties of the structure surface.

To establish the most probable numerical values of heat flux density during the development of fire in a room (or along evacuation routes), the following circumstances were taken into account. In large-scale studies of the behaviour of corridor wall finishing in conjunction with fire development in an adjacent room, it has been established that thermal impact intensity varies with the height from the floor level. The corridor wall section at a height of 2.0–2.5 m is exposed to the greatest thermal impact, with a heat flux density in the range of 25–30 kW/m^2 [23]. In this regard, when studying the flammability of P&VC used for finishing walls and ceilings, a maximum value of 30 kW/m^2, as the most dangerous, was taken as the value of the incident heat flux density.

For an intermediate number of layers (from 3 to 5), the P&VC values are determined to a great extent by the thermophysical properties of the base, namely its thermal diffusivity, i.e. the value characterizing the change rate in the temperature field of material when exposed to an external heat source. The density data and thermophysical properties of the bases considered in this work, as well as the results of calculating the thermal diffusivity coefficient based on these, are presented in Table 2. From these data, it is evident that gypsum board thermal diffusivity is more than 1.7 times higher than the corresponding coefficient for asbestos-cement, which qualitatively explains the regularities obtained in experiments for the case in which the P&VC is thermally thin and the dynamics of heating to a significant degree depend on the thermophysical properties of the substrate to which it is applied.

Table 2. Thermophysical properties of bases.

Base	Density (kg/m^3)	Coefficient of thermal conductivity (W/m·K)	Specific heat (J/kg ·K)	Thermal conductivity (10^7·m^2/s)
Chrysotile cement sheet	1600	0.35	1500	1.5–1.6
Plasterboard sheet	800	0.2	950	2.6

3. Results and Discussion

The characteristics of samples and finishing compositions and the results of the experimental studies are presented in Table 3. CFHFD reflects the value of the heat flow delivered to the exposed surface at which steady flame burning was observed when approaching the specified surface of the pilot flame. Repeatability of the results obtained was less than 15 %, and the error of the determined parameters did not exceed 10 %.

Experimental studies determining the critical surface heat flux density for paint materials considered within the framework of this work were carried out using the test method and measuring instruments in accordance with the requirements of [24]. Experimental data characterizing the CFHFD changes for P&VC samples, depending on the chemical composition, thickness and type of the base, are shown in Fig. 1, 2 and 3.

With a CFHFD of 30 kW/m^2, P&VC samples based on WD enamel do not ignite when 2–5 layers are applied to CCS, GPS and GPS with glued fibreglass wallpaper glued, which indicates the potential for fire-safe application in corridors of buildings. In this case, taking into account the maximum heat flux density, q_{max} (30 kW/m^2), which affects the most heated section of the wall, the condition of CFHFD q_{max} will be fulfilled, thus ensuring non-flammability and hence system fire safety.

From the dependences presented in Fig. 1, 2, and 3, it also follows that differences in the chemical composition of P&VC and different types of bases have different coating critical thickness values at CFHFD = 30 kW/m^2. This conclusion is of practical interest because it is possible to regulate the fire-safe (permissible) number of deposited layers or the thickness of P&VC along evacuation routes and in indoor spaces.

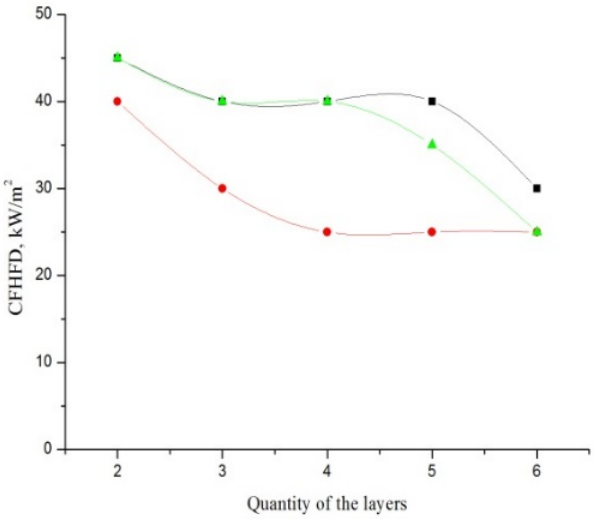

Figure 1. Dependence of CFHFD based on the number of layers:
■ water-dispersive enamel (base – chrysotile cement sheet);
● water-dispersive enamel (base – gypsum plasterboard sheet);
▲water-dispersive enamel (base – plasterboard sheet with glued fibreglass wallpaper).

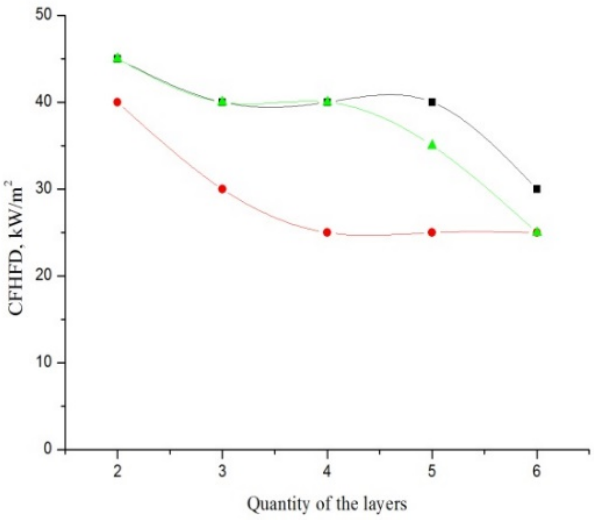

Figure 2. Dependence of CFHFD based on the number of layers:
■ water-dispersive enamel (base – chrysotile cement sheet);
● water-dispersive enamel (base – gypsum plasterboard sheet);
▲water-dispersive enamel (base – plasterboard sheet with glued fibreglass wallpaper).

Table 3. Characteristics and test results of paint and varnish coatings.

No.	Name (characteristic) of the paint and varnish coating (enamel)	Thickness of a layer of the material, μm	Combustibility group T °C/ S_L,%	Flammability group CFHFD (kW/m^2) (flammability time, s)	Coefficient of smoke formation (D_m, m^2/kg) smoke-forming capacity	Toxicity index of combustion products combustion product toxicity group	Flame spreading index
1.	Complex coating (waterborne acrylic facade primer, waterborne acrylic facade paint)	180–200 (primer:10–15 μm, paint:170–185 μm)	106/11	F1/40 (304)	174/S2	> 120/T1	0.7
		280–300 (primer: 10–15 μm, paint: 270–285 μm)	108/12	F1/40 (196)	174/S2	> 120/T1	1.2
		370–400 (primer : 10–15 μm, paint; 360–385 μm)	114/17	F2/30 (676)	174/S2	> 120/T1	2.3
2.	Complex coating (facade primer based on an aqueous silane/siloxane emulsion, water-based facade paint based on emulsion of silicone resin)	280–300 (primer: 10–15 μm, paint: 270–285 μm)	108/13	F1/40 (46)	192/S2	> 120/T1	2,8
3.	Complex coating (waterborne acrylic primer, waterborne acrylic paint)	200–240 (primer: 15–20 μm, paint:185–220 μm)	106/11	F1/40 (138)	165/S2	> 120/T1	0.5
		280–300 (primer: 15–20 μm, paint: 265–280 μm)	109/13	F1/40 (21)	165/S2	> 120/T1	1.1
		370–400 (primer: 15–20 μm, paint: 355–380 μm)	115/16	F2/30 (324)	165/S2	> 120/T1	1.8
4.	Complex coating (latex putty, alkyd enamel)	280–310 (putty: 240–260 μm, paint: 40–50 μm)	110/13	F1/35 (214)	292/S2	> 120/T1	23.4
		320–350 (putty: 240–260 μm, paint: 80–90 μm)	112/16	F2/25 (302)	292/S2	> 120/T1	>20
		360–410 (putty: 240–260 μm, paint: 120–150 μm)	123/24	F2/25 (118)	292/S2	> 120/T1	>20

No.	Name (characteristic) of the paint and varnish coating (enamel)	Thickness of a layer of the material, μm	Combustibility group T °C/ S_L,%	Flammability group CFHFD (kW/m^2) (flammability time, s)	Coefficient of smoke formation (D_m, m^2/kg) smoke-forming capacity	Toxicity index of combustion products combustion product toxicity group	Flame spreading index
5.	Complex coating (two-component epoxy putty, three-component epoxy enamel)	190–230 (putty: 120–140 μm, paint: 70–90 μm)	108/15	F2/20 (742)	802/S3	42/T2	2.72
		260–320 (putty: 120–140 μm, paint: 140–180 μm)	112/15	F2/20(608)	802/S3	42/T2	7.43
		380–420 (putty: 120–140 μm, paint: 260–280 μm)	113/16	F2/20 (496)	802/S3	42/T2	>20
6.	Polyether powder paint	80	107/11	F1/50	43/S1	> 120/T1	0
7.	Coating based on polyvinylidene fluoride (PVDF)	30	107/11	F1/50	32/S1	> 120/T1	0
8.	Organic-soluble acrylic paint on cement plaster with a layer of 2 cm	200 (paint)	105/9	F1/50	40/S1	> 120/T1	1.3

Note: For samples 1–5, paint and varnish coatings were applied to 10 mm thick chrysotile cement sheets; for samples 6–7, paint coatings formed a protective layer for metal panels with a thickness of 3 mm); sample 8 was a composition of a facade mineral plaster on a non-combustible mineral wool board.

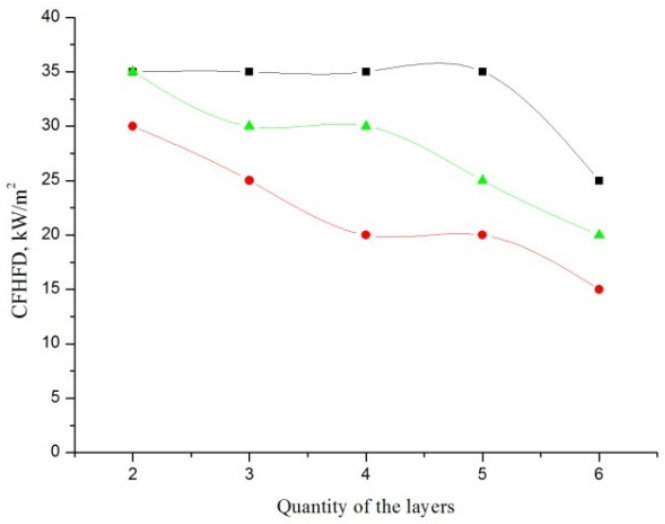

Figure 3. Dependence of CFHFD based on the number of layers:
■ pentaphthalic enamel (base – chrysotile cement sheet);
● enamel pentaphthalic (base – plasterboard sheet);
▲ pentaphthalic enamel (base – gypsum plasterboard with glued fibreglass wallpaper).

Analysing the dependences obtained (Fig. 1), one more important conclusion can be drawn. Given the absence of any control over the number of coatings applied along evacuation routes in buildings, the use of P&VC with synthetic varnishes should be allowed on any base because the condition of CFHFD q_{max} cannot be met.

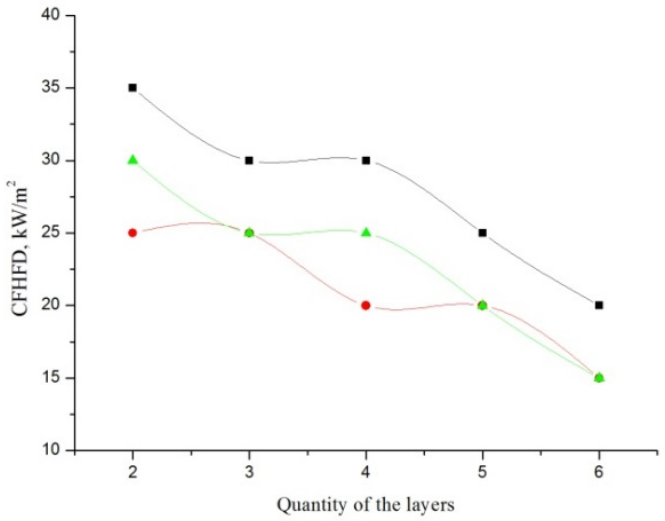

Figure 4. Dependence of CFHFD based on the number of layers:
■ enamel oil (base – chrysotile cement sheet);
● enamel oil (base – plasterboard sheet);
▲ enamel oil (base – plasterboard sheet with glued fibreglass wallpaper).

The results of the analysis of the influence of base type, namely the thermophysical properties, on the CFHFD values of the P&VC studied in the framework of this work are important. For example, for WD enamel in the case of four layers deposited on a non-flammable substrate, the indication for the number of layers deposited corresponds to the maximum possible in accordance with the requirements of [21], with the CFHFD value ranging from 25 to 40 kW/m^2, i.e. 60 % with respect to the minimum value for the various types of bases investigated in the present work. This requires an explanation, both from the point of view of an objective assessment of the CFHFD for P&VC applied on various bases and from the analytical point of view due to deficiencies in the regulatory requirements for the test procedure determining the CFHFD.

It should be noted that the smallest differences in the CFHFD values, depending on the type of the non-combustible base, are observed for the minimum number of layers (2) and for the maximum number of layers (6). In the case of the minimum number of layers, the CFHFD values are in the range 40–50 kW/m^2 and 30–35 kW/m^2 for WD and PP enamels, respectively. In terms of the values for incident heat flux derived using the standard test procedure according to [24], the impact on the sample under investigation is a result of thermal shock and the ignition of the P&VC sample occurs in a considerably shorter time than the corresponding time for P&VC samples with a deposit of 3–5 layers on a non-flammable substrate, which indicates that there is no effect of dissipation (removal) of heat from the source of thermal radiation through a non-flammable base. In the case of the maximum number of layers, the coating applied to the substrate ceases to be thermally thin, that is, the thermophysical properties of the coating itself have a significant influence on the heating of the composition of the P&VC base.

As the standard procedure for determining CFHFD according to [24] allows only one type of non-flammable substrate (asbestos-cement [chrysotile cement] sheets with a thickness of 10 or 12 mm), the results will be a characteristic not only of the coating, but also its composite combination with the chrysotile cement sheet. This can be disputed on the grounds that the CFHFD value is a classification characteristic defined under standard conditions and is intended only for assigning the material to a particular flammability group F1-F3 in accordance with Russian classification of building materials. The conditions of standard tests should, as far as possible, approximate the conditions of thermal impact on the material under investigation, which is realized in real fires. The main problems arising and their solutions are as follows.

First, the definition of the CFHFD as exclusively a characteristic of the material under investigation implies the absence of influence of the non-combustible base type (its thermophysical properties). For this, non-combustible bases with thermal diffusivity values that are significantly smaller than the corresponding values for the types of bases studied herein can be used. P&VC thickness should be such that the effect of the incombustible base on its heating is negligible. This can be achieved, for example, by increasing the minimum number of P&VC layers required for a standard test. Such an approach may not meet the conditions for the application of P&VC in practice (in terms of the number of layers deposited on the base), but will give a certain margin of safety with regard to determining the CFHFD.

Second, there is the problem of determining the CFHFD as a characteristic of the composite combination of P&VC and a specific non-flammable base (or other non-flammable base with similar thermophysical characteristics). The approach herein allows us to determine the CFHFD for P&VC not only in combination with a non-flammable base, but also with a combustible base. In this case, an objective assessment of the CFHFD will be obtained to predict the behaviour of the PP under the conditions of the development of a real fire.

As already noted above, the practical purpose of the studies presented is to ensure the fire safety of PCMs used in construction and their non-flammability, in particular focusing on P&VC. In this regard, we focus on ensuring non-flammability in a fire, for which it is necessary to have a distribution of the heat fluxes affecting the building structures under real conditions. As an example, let us consider the distribution of heat fluxes along the height of the corridor during a fire in a room. At a known value of q^{flm}_{cr} (established under the influence of time-varying heat flux), it is possible to determine the permissible height of the corridor wall finish. Taking into account the experimental data obtained, the conditions $q^{flm}_{cr} > q_{max}$ and CFHFD > q_{max} are satisfied only for WD enamel applied to non-flammable substrate (q^{flm}_{cr} and CFHFD for WD enamel of more than 40 kW/m^2).

The presented experimental data on the dependence of the values of heat fluxes (CFHFD (kW / m^2)) on the thickness of the applied coating and the type of basis sufficiently correspond to similar research results obtained by S.V. Stebunov in his PhD thesis «Investigation of the fire hazard properties of paint coatings» with regard to complex coating (waterborne acrylic facade primer, waterborne acrylic facade paint).

Also it is important to note that due to information we possess no researches on the similar coatings were performed before us.

4. Conclusion

1. In this article, the results of longstanding research assessing the ignitability of PCMs (including P&VC) are presented, according to the standards and especially the methods developed by the FGBU VNIIPO EMERCOM, Russia, which are designed to solve various problems in ensuring the fire safety of buildings (assessment of ignition in classification, development of formulations, confirmation of compliance, determining the area of acceptable use, etc.).

2. This article describes approaches to forecasting of flammability of decorative, finishing, facing materials and paint coatings. These approaches are based on particular experimental data and findings

about a possible fireproof application of those materials, for example, on the evacuation routes of public buildings. This research is of practical and scientific interest for a wide range of specialists, approaches and methods represented in it can be applied by specialists both in Russia and abroad for assessment of the possibility of using building materials in rooms of various functional purposes. The presented approaches are illustrated by specific examples.

3. Studies of the fire hazard of various P&VC have been conducted, taking into account the type of material, base thickness (number of layers) and coating. Appropriate dependences have been obtained, which make it possible to resolve practical issues of the application of P&VC in construction, ensuring the non-proliferation of fire in a building (premises) and the safety of people. New methods have been developed with the aim of determining more complete and objective indicators for PCMs.

4. A complex of experimental data on fire hazard of finishing materials was obtained. This data (mostly on the critical heat flux densities which cause burning of polymer building materials) contributes into previous results obtained by other researchers.

References

1. Gravit, M.V., Golub, E.V., Grigoriev, D.M., Ivanov, I.O. Fireproof suspended ceilings with high fire resistance limits. Magazine of Civil Engineering. 2018. 84(8). Pp. 75–85. DOI: 10.18720/MCE.84.8
2. Ustinov, A., Zybina, O., Tanklevsky, L., Lebedev, V., Andreev, A. Intumescent coatings with improved properties for high-rise construction E3S Web of Conferences. 2018. 33.
3. Ustinov, A., Zybina, O., Andreev, A.: On the impact caused by titanium dioxide of different trademarks on the properties of Intumescent fire-protective coatings. International Scientific Conference on FarEastCon, ISCFEC. Vladivostok, 2018. 945. Pp. 212−217.
4. Gravit, M.V., Serdjuks, D., Bardin, A.V., Prusakov, V., Buka-Vaivade, K. Fire Design Methods for Structures with Timber Framework. Magazine of Civil Engineering. 2019. 85(1). Pp. 92–106. DOI: 10.18720/MCE.85.8
5. Hirschler, M. Polyvinyl chloride and its fire properties. Fire and Materials. 2017. 41 (8). DOI: https://doi.org/10.10-02/fam.2431
6. Vahabi, H., Kandola, B.K., Reza Saeb, M. Flame Retardancy Index for Thermoplastic Composites. Polymers. 2019. 11 (3): 407. DOI: 10.3390/polym11030407
7. Drysdale, D. An introduction to fire dynamics. Wiley – Intersceince. London, 1992. 574 p.
8. Barnett, B. A new approach to testing the flammability characteristics of surface coatings. Fire and Materials. 1976. 1 (1). Pp. 14−18.
9. Wang, X., Song, L., Xing, W., et al. Flame retardancy and thermal properties of novel UV-curing epoxy acrylate coatings modified by phosphorus-containing hyperbranched macromonomer. Journal of Polymer Research. 2013. 20 (7).
10. McGraw, J.R., Mowrer, F.W. Flammability of Painted Gypsum Wallboard Subjected to Fire Heat Fluxes. Proceedings of 8-th International Conference on Fire Science and Engineering, Interflame'99. Edinburgh, 1999. Pp. 1325−1330.
11. Mikkola, E., Wichman, I.S. On the thermal ignition of combustible materials. Fire and Materials. 1987. 14. Pp. 87−96.
12. Lucherini, A., Maluk, C. Assessing the onset of swelling for thin intumescent coatings under a range of heating conditions. Fire Safety Journal. 2019. 106. Pp. 1-
13. De Silva, D., Bilotta, A. Experimental investigation on steel elements protected with intumescent coating. Construction and Building Materials. 2019. 205. Pp. 232−244.
14. Inerhunwa, I., Chang Wang, Y., Su, M. Reliability analysis of intumescent coating protected steel members under the standard fire condition. Fire Safety Journal. 2019. 104. Pp. 43−56.
15. Loganina, V., Petukhova, N., Fediuk, R., Timokhin, R. Polystyrene paint with reduced contents of volatile compounds. Magazine of Civil Engineering. 2019. 4 (88). Pp. 25−41.
16. Vedishcheva, I., Ananin, M., Al Ali, M., Vatin, N. Influence of heat conducting inclusions on reliability of the system “sandwich panel – metal frame”. Magazine of Civil Engineering. 2018. 2 (78). Pp. 116−127.
17. Smirnov, N.V., 2002. Forecasting of fire danger of materials. Dr. Tech. Sci. diss., Moscow, pp. 202–273.
18. Smirnov, N.V., Kaziev, M.M., Titov, G.E. 1988. The conditions for a comprehensive study of the fire hazard of polymeric facing, finishes and coatings of building structures. Provision of fire safety of buildings and structures. Moscow. VNIIPO. Pp. 5–7.
19. Smirnov, N.V, Moldchadsky, I.S., Korolchenko, A.Y., Serkov, B.B. 1989. Flammability of polymer finishes of building structures. Fire resistance of building designs and maintenance of fire safety of people and material assets. 1989. Moscow. VNIIPO. Pp. 81−89.
20. BS EN ISO 1182:2010 Reaction to fire tests for products – Noncombustibility test.
21. DIN 4102 Part 15 Fire behavior of building materials and elements 'Brandschacht'.
22. ISO 5657:1997(E) Reaction to fire tests. Ignitability of building products using a radiant heat source.
23. ISO 13785-2:2002 Reaction-to-fire tests for façades – Part 2: Large-scale test.
24. FGU VNIIPO EMERCOM, 2009. Set of rules. SR 2.13130.2012. Systems of fire protection. Fire-resistance security of protecting units.

Contacts:

Nataliya Konstantinova, konstantinova_n@inbox.ru
Nikolay Smirnov, firelab_vniipo@mail.ru
Aleksey Shebeko, ay_shebeko@mail.ru
Leonid Tanklevskiy, tanklevskij_lt@spbstu.ru

© Konstantinova, N.I., Smirnov, N.V., Shebeko, A.Y., Tanklevskiy, L.T., 2021

Magazine of Civil Engineering

ISSN 2712-8172

journal homepage: http://engstroy.spbstu.ru/

DOI: 10.34910/MCE.102.4

Performance of two-way hinges in reinforced concrete structures

S. Chahal[a]*, O. Baalbaki[b], Y. Temsah[b], H. Ghanem[b], Z. Abu Saleh[c]

[a] *Order of Engineers and Architects, Tripoli, Lebanon*

[b] *Beirut Arab University, Beirut, Lebanon*

[c] *Rafic Hariri University, Beirut, Lebanon*

**E-mail: safwanchahal79@gmail.com*

Keywords: two-way hinge, reinforced concrete, finite element method, load-displacement curve, amplification factor, shear friction

Abstract. Two-way hinges are frequently practiced in bridge columns aiming to avoid the transfer of bending moment to the foundation. The reduction of the concrete column section over a very small height portion is mainly sufficient to create a hinge like behavior. Currently, ACI Code proposes an amplification factor, limited to two, to account for the increasing of the hinge axial capacity due to the column confinement effect. The shear capacity of two-way hinges is defined as well by the shear friction theory imposed by the code. This paper presents a finite element analysis of two-way hinges to evaluate their behaviors. The experimental data were taken from a recent experimental investigation of two way hinges specimens subjected to axial load only. A numerical analysis was done using ABAQUS software. Based on the good convergence between the numerical and experimental results, a further analysis was conducted to investigate the hinge behavior under the simultaneous effect of axial and lateral loads. It was observed that the tri-axial stresses and confinement provided by the larger area strengthen the throat region, and the axial capacity of the hinge is amplified by a confinement factor equal to three. Furthermore, the confining stress produced by the column on the throat increased the hinge shear capacity more than what the code indicates.

1. Introduction

Concrete hinges have been perfectly used in civil engineering structures for nearly 120 years. They are used to either reduce bending moment transferred to the foundations or redistribute the forces and stresses applied. A recent literature in bridge construction mentioned that Freyssinet and Mesnager concrete hinges are the most developed hinges in the different types of bridge applications since the early last century [1].

Hinges are produced by different means. The reduction of the concrete column cross section over a very small height portion is enough to create a hinge like behavior. The dowel bars are extended from the footing into the column [2]. The stress induced by the bending moment in the smaller section leads the structure to attain the maximum capacity quickly. Consequently, the cracks appear and the section is not capable of sustaining further moment [3].

Two types of hinges are commonly used in bridge construction: one-way and two-way hinges. One-way hinge transmits moment in the strong direction, whereas the moment transferred in the other direction is practically neglected [4–6]. However, two-way hinge restricts the moment transfer in both directions, and thereby reduce the size and cost of the foundation [7–9]. Whereas, previous studies concluded that although the moment at the hinge was not totally neglected, it was substantially lower than the moment capacity of the full section. Thereby, the hinge moment is required to account for in design [2].

Another advantage of using a two-way hinge is the low cost of repairing a damaged two-way hinge compared to that of a damaged full moment connection [10].

Recent researches emphasized that hinges performed a moment-free connections while transferring shear and axial loads, and exhibited large rotations without afflicting their performance [11–12]. Likewise, pipe pins hinge showed well performance in transferring the shear forces to the footing through the pipes interaction and friction [4–5, 13–14]. The well confinement of the two-way hinge by the upper column and the lateral

Chahal, S., Baalbaki, O., Temsah, Y., Ghanem, H., Abu Saleh, Z. Performance of two-way hinges in reinforced concrete structures. Magazine of Civil Engineering. 2021. 102(2). Article No. 10204. DOI: 10.34910/MCE.102.4

This work is licensed under a CC BY-NC 4.0

reinforcement allows the throat region to maintain large strains [15–16]. Besides, a past study demonstrated that the compressive strength of one-way hinge was largely increased by the confinement provided by the upper column and the lower footing surfaces [2].

However, the effect of tri-axial confinement on the two-way hinge capacity is not extensively discussed in current codes and literature. Therefore, this paper comes to present a numerical investigation of two-way hinges in reinforced concrete members. The experimental data were taken from a recent experimental investigation of two-way hinges specimens subjected to axial load only [17]. A numerical analysis was done using ABAQUS software. Following the good convergence between the numerical and experimental results, a further analysis was conducted to investigate the hinge behavior under the combined effect of axial and lateral loads.

The objectives of this research is to investigate the behavior and the failure modes of two-way hinges subjected simultaneously to axial and lateral loads, as well as to understand the confinement effect imposed by the larger concrete column area on the smaller hinge region, and ultimately to introduce a codified guideline design method of two-way hinges in reinforced concrete structures.

2. Method

2.1. Introduction

The input data used in the numerical analysis are the experimental results performed by Chahal et al. (2019), at Beirut Arab University, Lebanon [17]. The experimental program was composed of eighteen 1/3-scale specimens of two-way reinforced concrete hinges divided into three major series, each consisted of six specimens as provided in Table 1. A 300 mm × 300 mm square footing was used in all cases, with 300 mm height, reinforced by a mesh of 4ϕ14 in the both directions. A 70 mm × 70 mm square hinge area (A_h), with 30 mm thick, and reinforced by 4ϕ10 is used in all models as well. The area of the column (A_c) was accordingly changed to evaluate to effect of different confinement levels. Thus, the ratio $\sqrt{A_c / A_h}$ ranged between 2 and 4 throughout the case. The sizes of specimens are detailed in Fig. 1. The specimens are subjected to an increasing axial load only.

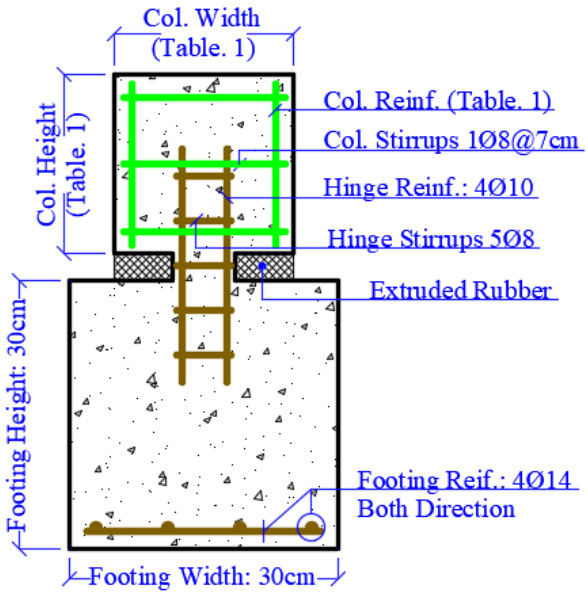

Figure 1. Specimen detail.

Table 1. Characteristics of specimens.

Specimen			Square Column		$\sqrt{A_c / A_h}$
Concrete Compressive Strength, f'c (MPa)					
22	32	40	Width ; Height (mm)	Reinforcement (mm²)	
CS14-22	CS14-32	CS14-40	140	4ϕ12	2.00
CS20-22	CS20-32	CS20-40	200	4ϕ14	2.86
CS21-22	CS21-32	CS21-40	210	8ϕ12	3.00
CS23-22	CS23-32	CS23-40	230	8ϕ12	3.29
CS25-22	CS25-32	CS25-40	250	8ϕ12	3.57
CS28-22	CS28-32	CS28-40	280	8ϕ14	4.00

2.2. Modeling methodology

As indicated earlier, the advanced finite element software ABAQUS was used in the analysis. The standard linear volumetric element type C3D8R with a hexahedral shape was used to model the concrete members as illustrated in Fig. 2. This is an 8 nodded element type with a reduced integral and hourglass control, which is the optimal mesh type to simulate the concrete members and to give the most accurate results with the least run time [18–19]. Steel was assigned as plastic material with a strain hardening curve. As shown in Fig. 3, the standard linear wire truss element type T3D2 was used to model the reinforcement and to prevent any unwanted bending moments. This element type takes axial forces only.

A rigid body constrain between the top of the column and a reference point was assigned. This is to avoid any stress concentration or singularities upon loading. A displacement controlled analysis was proposed to determine the behavior of the cases considered. The models were analyzed using Static/Risk analysis in ABAQUS. A uniformly increasing imposed axial displacement of 20 mm was applied. This is much greater than the failure displacement of all cases. The corresponding reactions were then recorded and plotted.

The bottom of the footing was assigned a fixed boundary condition. It was restrained against translation in all directions. This is to forbid the formation of bending moment which may causes tilting of the footing. Hinged columns usually are stable in structures as they are braced by each other. To avoid such instabilities, and to prevent the formation of bending moments on the column, the top of the column was assigned a restrain against lateral movement.

An embedment constrain was assigned to the steel reinforced in the concrete. This constrain ensures full bond and strain compatibility between the concrete and steel. No direct steel slippage properties were assigned to the reinforcement or to the interface between the concrete and steel reinforcement.

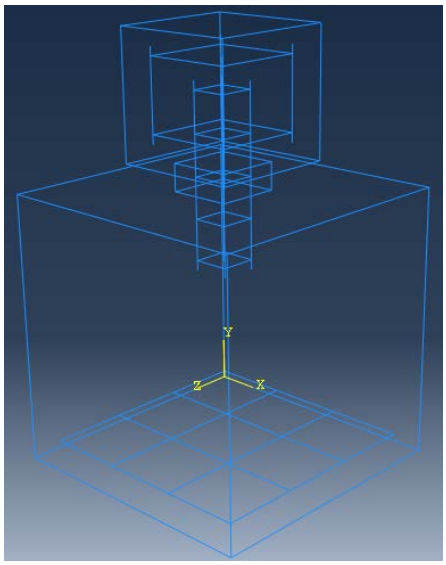

Figure 2. Concrete meshing.

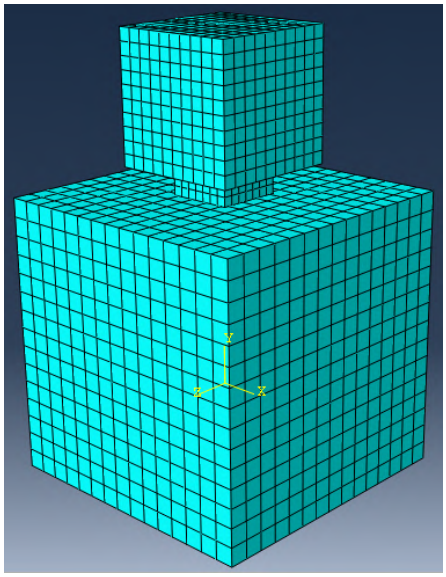

Figure 3. Steel reinforcement meshing.

2.3. Concrete damage plasticity

Concrete damaged plasticity method (CDP) was used to model the concrete behavior. The method was introduced on 1989 by Lubliner, and developed later on 1998 by Lee and Fenves [20–22]. Different parameters are used in the CDP to describe the nonlinear behavior of concrete, such as the cracking and inelastic strains, as well as stiffness degradation and other parameters. CDP method comprises majorly two independent behaviors in tension and compression as defined by stress strain graphs separately, Fig. 4. The concrete inelastic strain in compression "ε^{in}", and the cracking strain in tension "ε^{ck}" are:

$$\varepsilon^{in} = \varepsilon_c - \frac{\sigma_c}{E_0} \tag{1}$$

$$\varepsilon^{ck} = \varepsilon_t - \frac{\sigma_t}{E_0} \tag{2}$$

Where "σ_c" and "σ_t" are respectively the compressive and tensile stresses in concrete, and "E_0" is the initial modulus of elasticity.

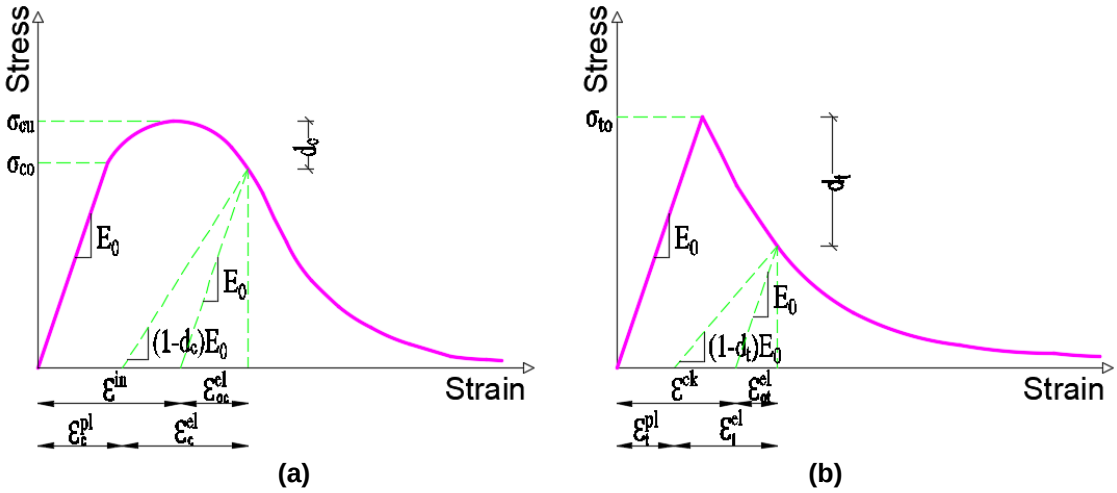

Figure 4. Uniaxial behavior of concrete: (a) under compression, (b) under tension.

Further, two isotropic damage parameters "d_c" and "d_t" are used accordingly to describe the stiffness degradation of concrete in compression and in tension respectively. The parameters are assigned as the concrete is strained beyond its elastic limit. The damage parameters have a maximum value of 1, where the material have reached full damage [23–26]. Equations 3 and 4 represents the damage parameters for compression and tension respectively.

$$d_c = 1 - \frac{\sigma_c}{E_0\left(\varepsilon_c - \varepsilon_c^{pl}\right)} \tag{3}$$

$$d_t = 1 - \frac{\sigma_t}{E_0\left(\varepsilon_t - \varepsilon_t^{pl}\right)} \tag{4}$$

Using the damage parameters, the inelastic and crack strains are then transferred into plastic strains at compression " ε_c^{pl} "and tension " ε_t^{pl} " as follows:

$$\varepsilon_c^{pl} = \varepsilon^{in} - \left(\frac{d_c}{1-d_c}\right)\left(\frac{\sigma_c}{E_0}\right) \tag{5}$$

$$\varepsilon_t^{pl} = \varepsilon^{ck} - \left(\frac{d_t}{1-d_t}\right)\left(\frac{\sigma_t}{E_0}\right) \tag{6}$$

The parameters provided were accomplished by following up a reliable approach in the triad "composition, structure, and properties" [27–29]. The concrete mechanical properties used in CDP are summarized in Table 2. The steel reinforcement was modeled using the elastoplastic behavior, and the mechanical properties of steel rebars are stated in Table 3.

Table 2. Mechanical properties of concrete.

Parameter	Unit	Symbol	Value		
Compressive strength	MPa	f'_c	22	32	40
Tensile strength	MPa	f_t	2.91	3.51	3.92
Elastic modulus	MPa	E_c	22,045	26,587	29,725
Poisson's ratio		ν	0.2		
Density	KN/m^3	ρ	2400		
Dilation angle	°	ψ	30		
Eccentricity		ε	0.1		
Bi-axial to uni-axial strength ratio		f_{b0}/f_{t0}	1.16		
Second stress invariant ratio		K	0.667		
Viscosity parameter		μ	0.00001		

Table 3. Mechanical properties of steel reinforcement.

Parameter	Unit	Symbol	Value
Yield strength	MPa	f_y	520
Ultimate strength	MPa	f_u	624
Elastic modulus	MPa	E_s	200,000
Poisson's ratio		ν	0.3
Density	KN/m^3	ρ	78.5

3. Results and Discussion

3.1. Model calibration

As mentioned earlier, the eighteen models were analyzed using ABAQUS software. An imposed displacement of 20 mm was applied only on the top center of the column's specimen of each model. As indicated earlier, ACI 318-14 limits the increase in strength due to confinement up to $\sqrt{A_c / A_h}$ = 2 [30]. The column sizes were increased as much as 16 times the hinge area in order to reach double the code limitation.

Several failure modes were experienced in the hinge area. Two-way hinges with low area ratios $\sqrt{A_c / A_h}$ = 2, mainly failed by hinge crushing as for models CS14-22, CS14-32 and CS14-40. The red volumes seen in Fig. 5 indicates the crushed concrete elements. The crushing starts from a distance up through the column. The stress concentrated in the failed zone and are transferred through the hinge. Fig. 6 describes the axial stress distribution throughout the model. The hinge axial capacity is amplified due to the confinement effect produced by the column on the throat area, even though it was not enough to withstand the vertical stress induced.

ABAQUS references the x, y and z axis as 1, 2 and 3 respectively. In the pure stresses states, tensile forces and stresses are positive while compressive forces and stresses are negative.

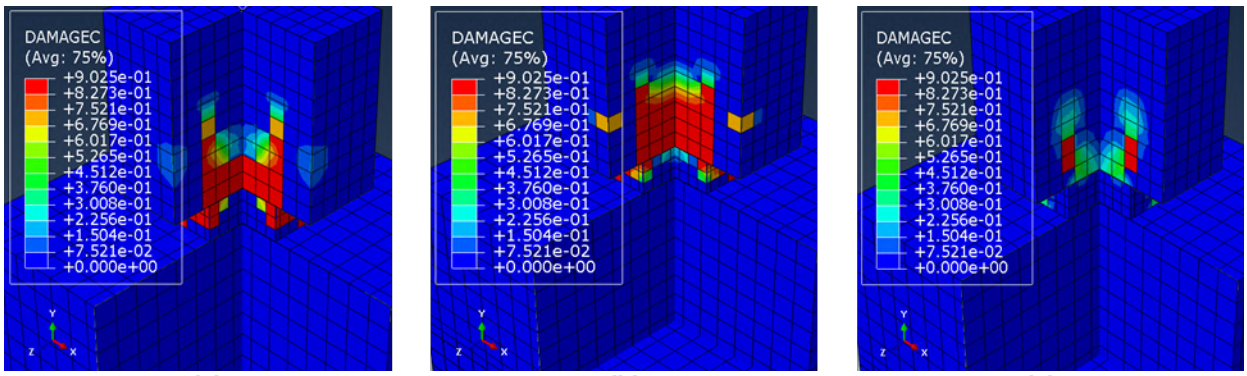

(a) **(b)** **(c)**

Figure 5. Hinge failure of two-way hinges with low area ratios: (a) SC14-22, (b) SC14-32, (c) SC14-40.

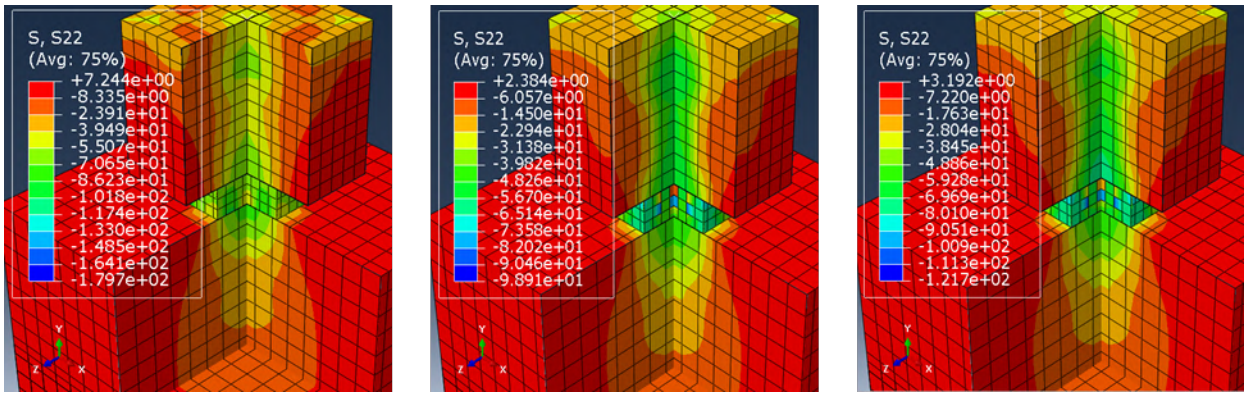

(a) **(b)** **(c)**

Figure 6. Vertical stress of two-way hinges with low area ratios: (a) SC14-22, (b) SC14-32, (c) SC14-40.

On the other hand, the next fifteen models with high area ratios $\sqrt{A_c / A_h} > 2$, failed by splitting failure above throat area. The red plan seen in Fig. 7 presents the shear failure plane, and the splitting failure above the hinge area is provided as well. Fig. 8 clarifies the spreading of stress S22 throughout the hinge. It was observed that the confining stress produced by the column on the throat area increased the hinge axial capacity to become greater than what the column can withstand.

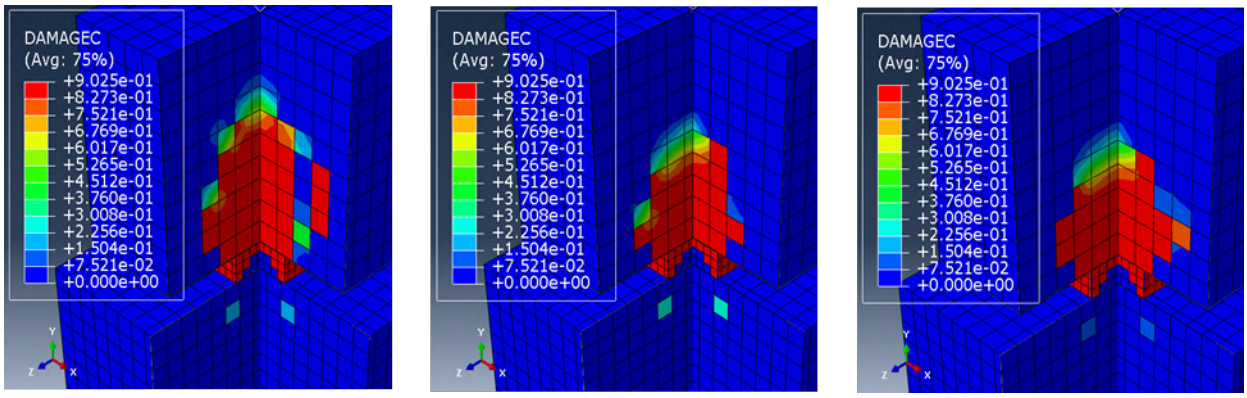

(a) **(b)** **(c)**

Figure 7. Splitting failure of two-way hinges with high area ratios: (a) SC23-22, (b) SC23-32, (c) SC23-40.

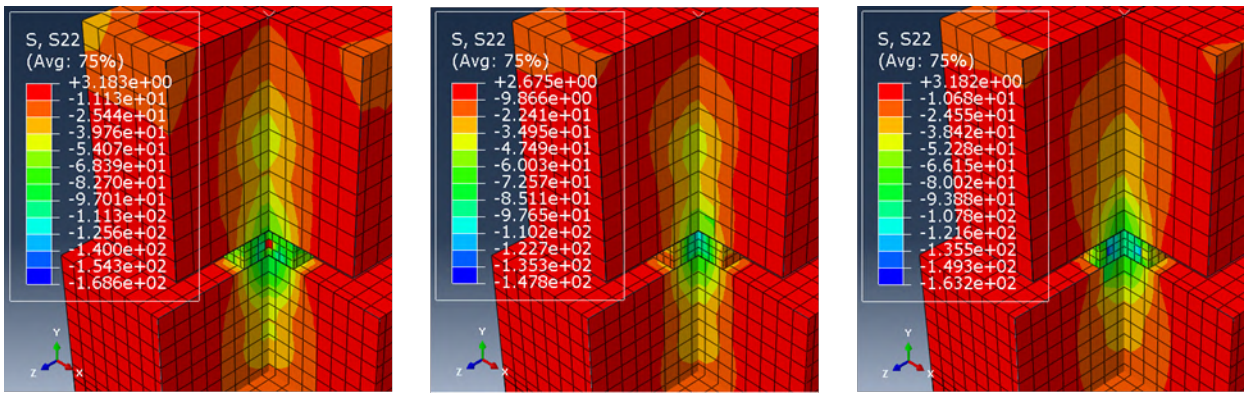

(a) **(b)** **(c)**

Figure 8. Vertical stress S22 of two-way hinges with high area ratios: (a) SC23-22, (b) SC23-32, (c) SC23-40.

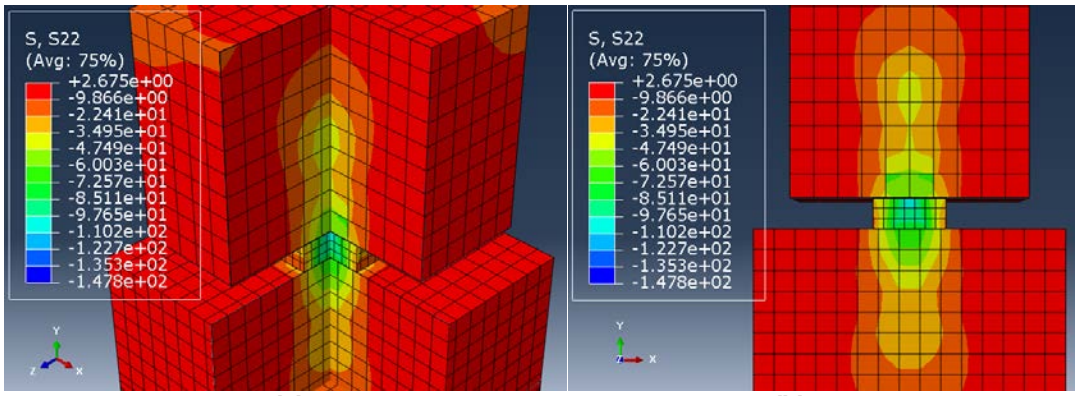

(a) **(b)**

Figure 9. CS23-32 vertical stress S22: (a) 3-D section, (b) Planner section.

The model CS23-32, $\sqrt{Ac / Ah}$ = 3.29, was selected to illustrate the transfer of stress through the hinge. ABAQUS references the x, y and z axis as 1, 2 and 3 respectively. In the pure stress states, the tensile stress is positive however the compressive stress is negative. Fig. 9 describes the vertical stress S22 distribution through the model CS23-32. The hinge reached the ultimate axial strength at a value of 115 MPa, which is way larger than the concrete compressive strength (32 MPa). The hinge axial capacity is amplified up due to the confining stresses S11 and S33 imposed by the larger area surrounding the throat region. The vertical Stress S22 in the column upper portion, where there is less confining effects is about 32 MPa. This demonstrates the abrupt increase in the stress as it passes through the smaller throat area. The stress concentrated at a distance approximately equal to half the width of the column.

Fig. 10 shows the lateral confining stresses S11 and S33 of CS23-32. It is obvious that the stresses are mainly provided at the hinge area. The maximum confining stress developed is in the range of 34 MPa, which highly amplifies the hinge bearing capacity.

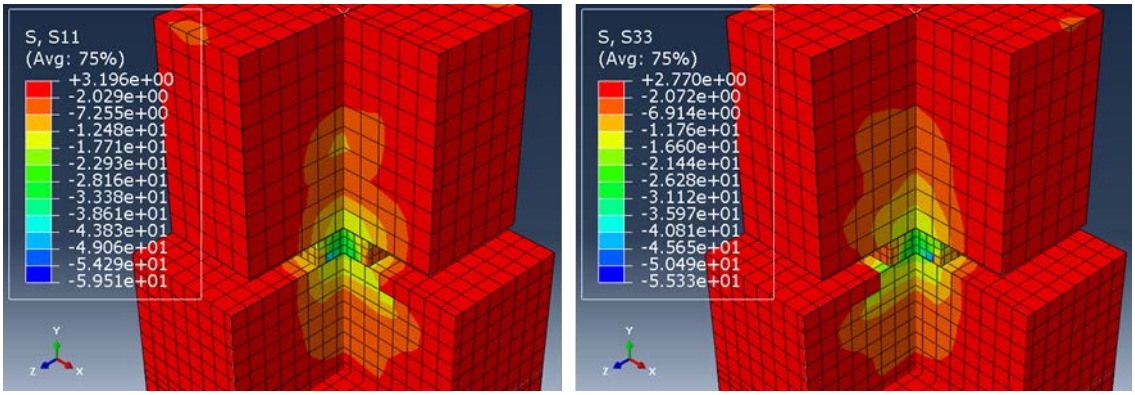

(a) **(b)**

Figure 10. CS23-32 lateral stresses: (a) stress S11, (b) stress S33.

On the other hand, consider the model CS14-32 which is a two-way hinge with a small area ratio, $\sqrt{Ac / Ah}$ = 2. Fig. 11 shows the distribution of vertical stress S22 through the hinge. The model reached the ultimate axial strength at a value of 85 MPa.

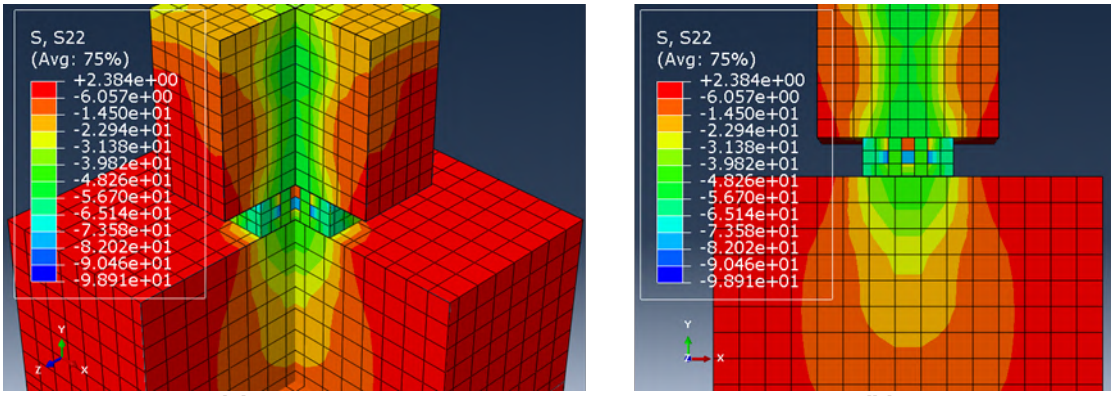

(a) **(b)**

Figure 11. CS14-32 vertical stress S22: (a) 3-D section, (b) Planner section.

The lateral confining stresses S11 and S33 of model CS14-32 are illustrated in Fig. 12. The model do not have enough distance to reach the optimum confining levels. The stresses S11 and S33 in the throat zone are both about to 14 MPa, which is much smaller than the corresponding lateral stress of CS23-32 (34 MPa).

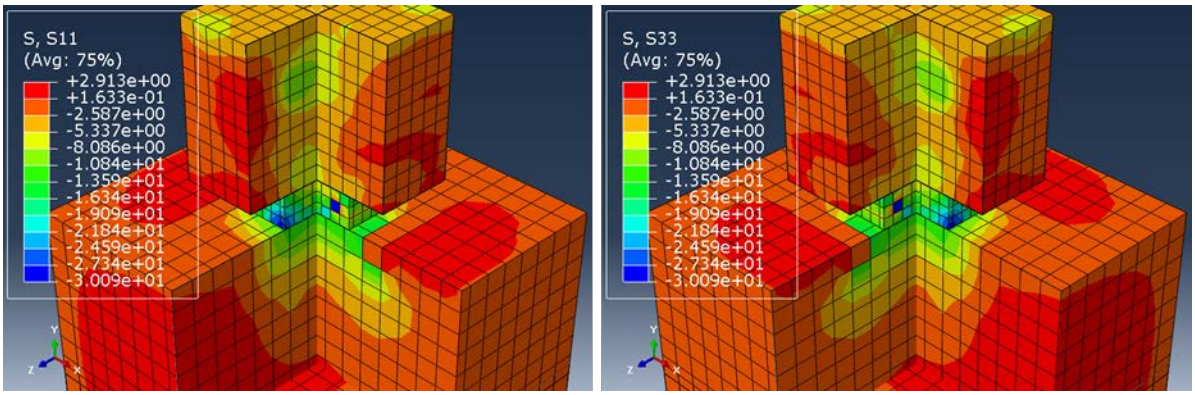

(a) **(b)**

Figure 12. CS14-32 lateral stresses: (a) stress S11, (b) stress S33.

Fig. 13 shows a comparison between the finite element analysis and experimental results of load displacement curves for CS14 and CS23 with the different concrete compressive strengths.

The load displacement curves due to the FEA for all cases are plotted in Fig. 14. The ABAQUS outcomes are in a very good agreement compared with the experimental results. Although all the models failed way before 20 mm displacement, the hinges with high area ratios exhibited ductile failure modes.

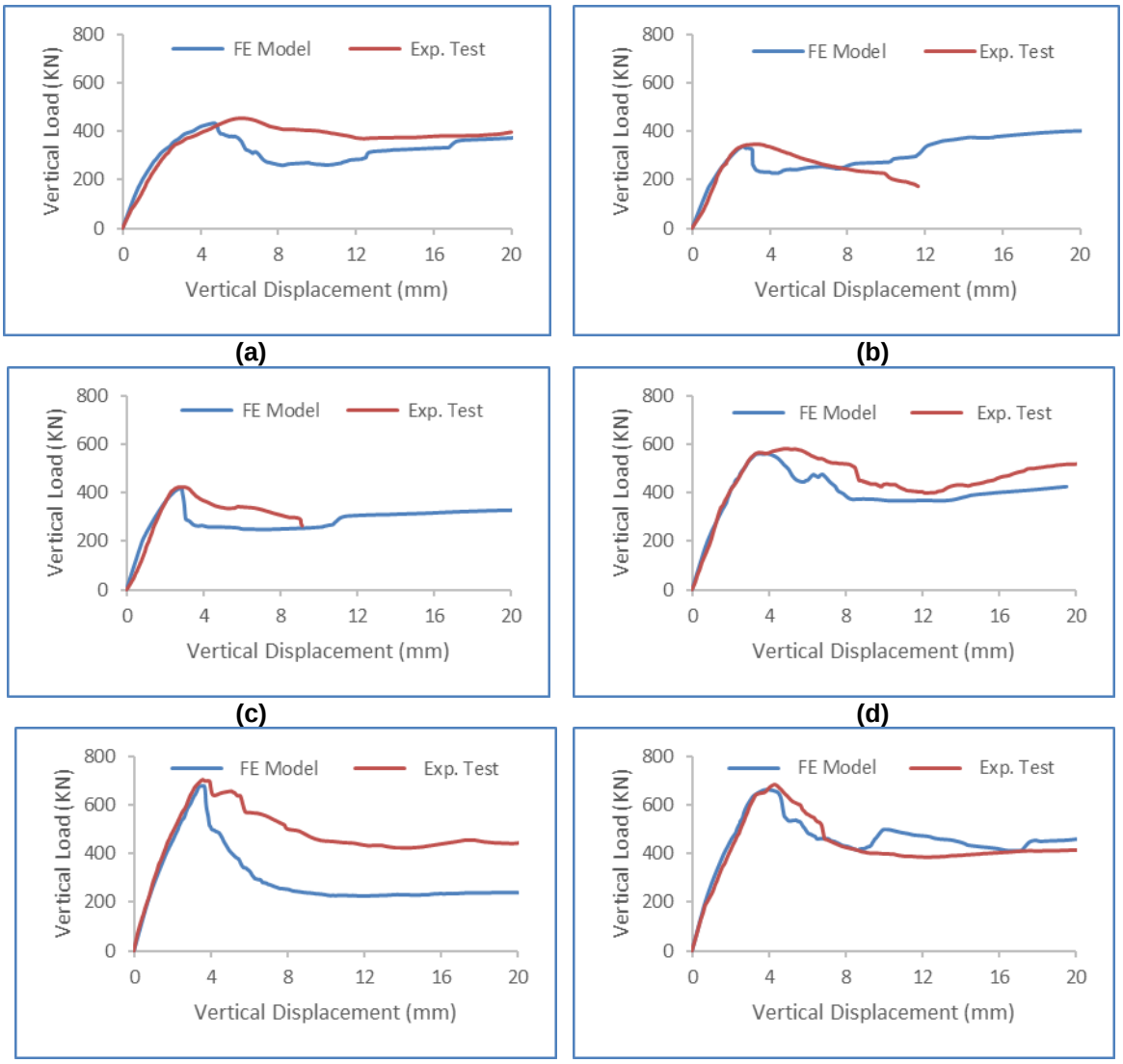

(a) **(b)**

(c) **(d)**

(e) **(f)**

Figure 13. FE model and experimental test of load displacement curves for CS14 and CS23: (a) CS14-22, (b) CS23-22, (c) CS14-32, (d) CS23-32, (e) CS14-40, (f) CS23-40.

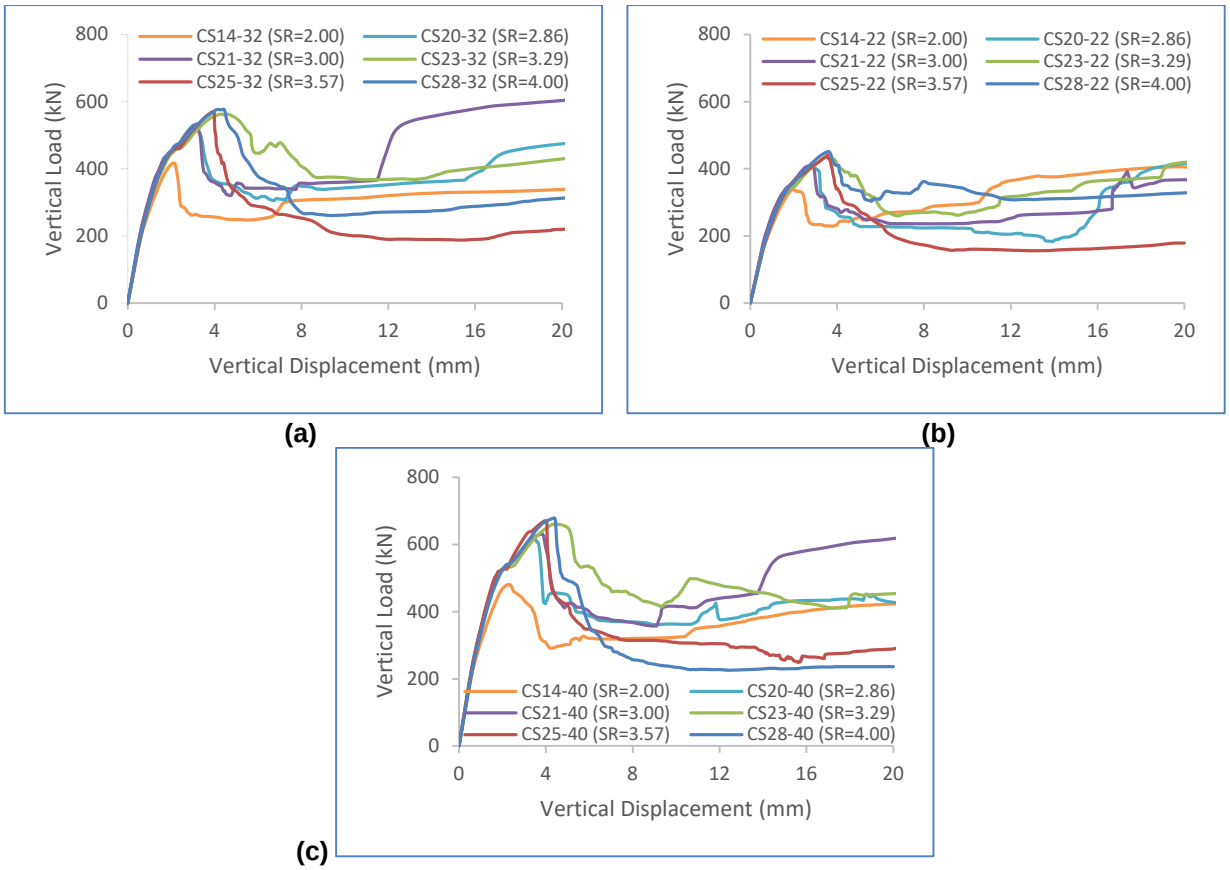

Figure 14. Axial load-displacement curves: (a) CS-22, (b) CS-32, (c) CS-40.

Fig. 15 displays the hinge axial capacity versus the square ratio of column to hinge area $\sqrt{A_c / A_h}$.

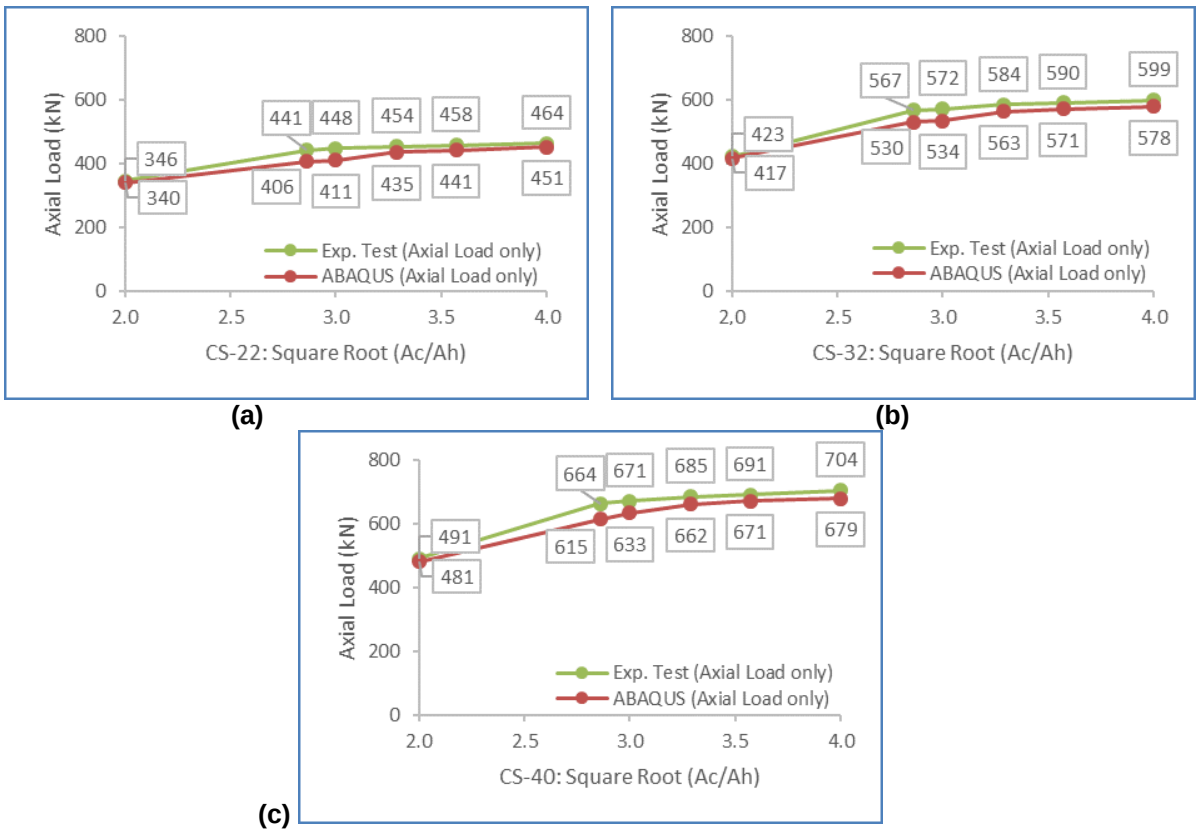

Figure 15. Square root of area ratio vs hinge capacity: (a) CS-22, (b) CS-32, (c) CS-40.

According to ACI Code, the hinge ultimate capacity P_{ulh} is:

$$P_{ulh} = 0.85 f'c(A_h - A_{st})\sqrt{A_c / A_h} + f_y A_{st} \tag{7}$$

where A_h is the gross sectional area of the concrete hinge and A_{st} is the area of hinge reinforcement.

ACI code stipulates that the amplification factor "$\sqrt{A_c / A_h}$" is limited to two. Beyond that, the confinement effect produced by the larger area on the throat would not effectively amplify the hinge capacity even if the column area is increased. Following the ABAQUS results, two-way hinge capacity did not have the same limit as the code stipulates. Obviously, the hinge capacity was amplified up by a confinement factor "CF" equal to three (Eq. 8). Indeed, the confinement factors reached an asymptotic value equal to 3.5 as indicated in Table 4. Despite the code recommends using the amplification factor in case the hinge is confined from both directions, many design methods consider using the factor for one-way hinge as well.

$$CF = \frac{P_{ulh} - f_y A_{st}}{0.85 f'c(A_h - A_{st})} \tag{8}$$

Table 4. Hinge confinement factor (CF).

Model	$\sqrt{A_c / A_h}$	Hinge Axial Load (KN)		Confinement Factor "CF"
		Exp.	ABAQUS	
CS14-22	2.00	346	340	2.06
CS20-22	2.86	441	406	2.83
CS21-22	3.00	448	411	2.89
CS23-22	3.29	454	435	3.17
CS25-22	3.57	458	441	3.24
CS28-22	4.00	464	451	3.36
CS14-32	2.00	423	417	2.03
CS20-32	2.86	567	530	2.94
CS21-32	3.00	572	534	2.97
CS23-32	3.29	584	563	3.20
CS25-32	3.57	590	571	3.27
CS28-32	4.00	599	578	3.32
CS14-32	2.00	491	481	2.10
CS20-32	2.86	664	615	3.21
CS21-32	3.00	671	633	3.26
CS23-32	3.29	685	662	3.35
CS25-32	3.57	691	671	3.38
CS28-32	4.00	704	679	3.47

3.2. Model analysis due to the dual effect of axial and lateral loads

The finite element calibrated and verified the experimental work. The models were further analyzed, using ABAQUS, to investigate their behaviors under the dual effect of axial and lateral loads. Simultaneously, an imposed vertical displacement of 10 mm was applied at the top center of the column of each model, and a lateral displacement of 10 mm imposed at the center of the hinge thickness as well.

Several failure modes were observed. The models CS14-22, CS14-32 and CS14-40, with low area ratios $\sqrt{A_c / A_h}$ = 2, exhibited bearing failure at the throat region. As shown in Fig. 16, the red volumes presents the crushed concrete elements. The crushing starts from a distance up through the column. The deformation increased and the stiffness degraded through the test. The hinge reached the ultimate axial capacity before the shear slippage takes place. This implies that the confining stress produced by the column on the hinge was not enough to withstand the vertical stress induced. Fig. 17 describes the axial stress distribution of the cases mentioned. The stress concentrated but did not amplify the throat capacity. This is probably due to the presence of the shear stress which contributes in decreasing the hinge axial capacity by about 30~35 % as indicated next.

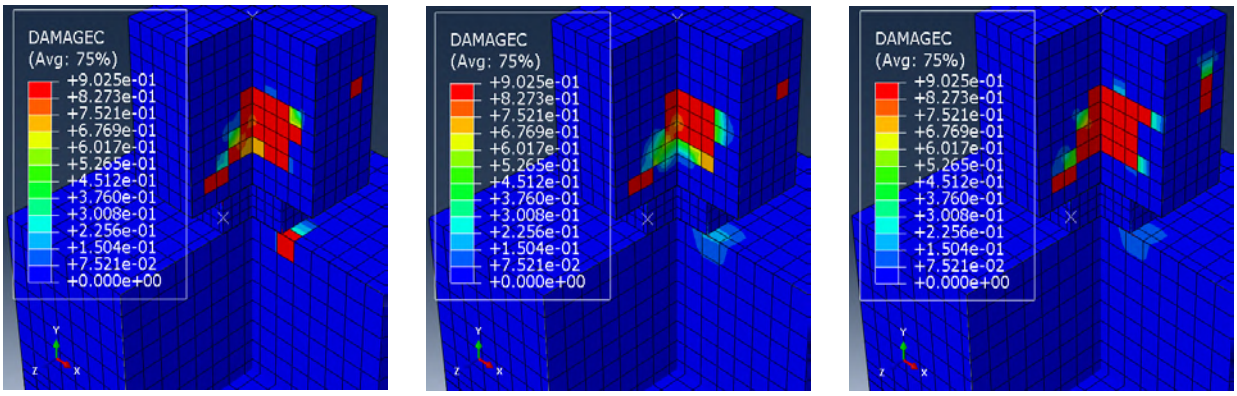

(a) (b) (c)

Figure 16. Hinge failure of two-way hinges with low area ratios: (a) SC14-22, (b) SC14-32, (c) SC14-40.

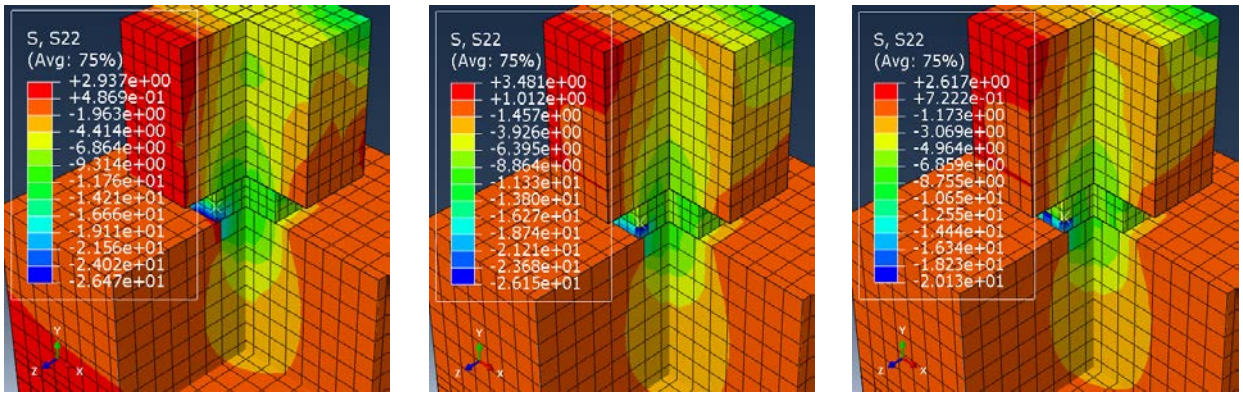

(a) (b) (c)

Figure 17. Vertical stress of two-way hinges with low area ratios: (a) SC14-22, (b) SC14-32, (c) SC14-40.

The models with high area ratios $\sqrt{Ac / Ah}$ > 2, failed by hinge-footing slippage interface as seen in Fig. 18. This indicates that the shear stress is greater than the confining stress produced by the column on the throat area. The red volume presents the concrete damage imposed by the shear slippage failure. It was observed that the deterioration was quite substantial right after the model reached the peak shear strength. Fig. 19 shows the stress distribution throughout the hinge. The stress concentrated and slightly amplified the throat axial capacity. Similarly to the above mentioned, the presence of the shear stress dropped the hinge axial capacity by about 30~35 %.

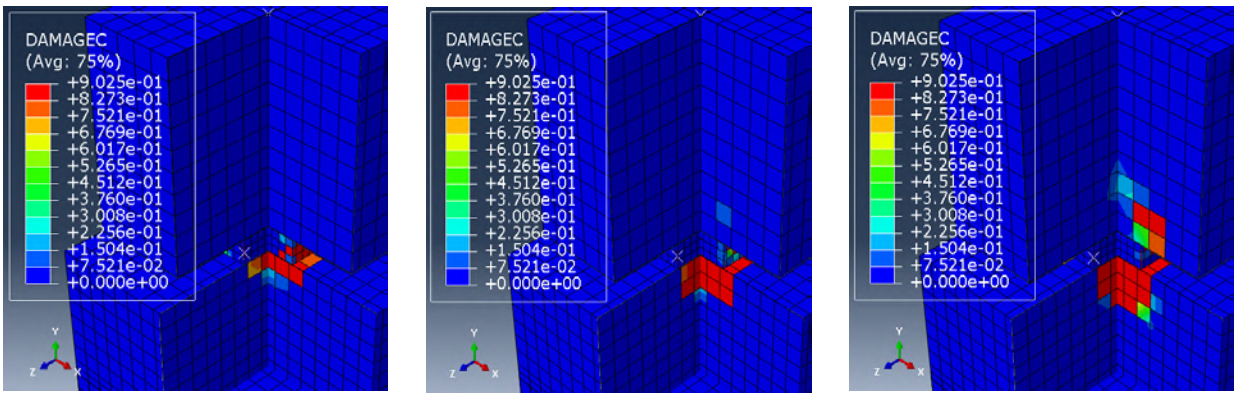

(a) (b) (c)

Figure 18. Shear slippage failure of two-way hinges with high area ratios: (a) SC23-22, (b) SC23-32, (c) SC23-40.

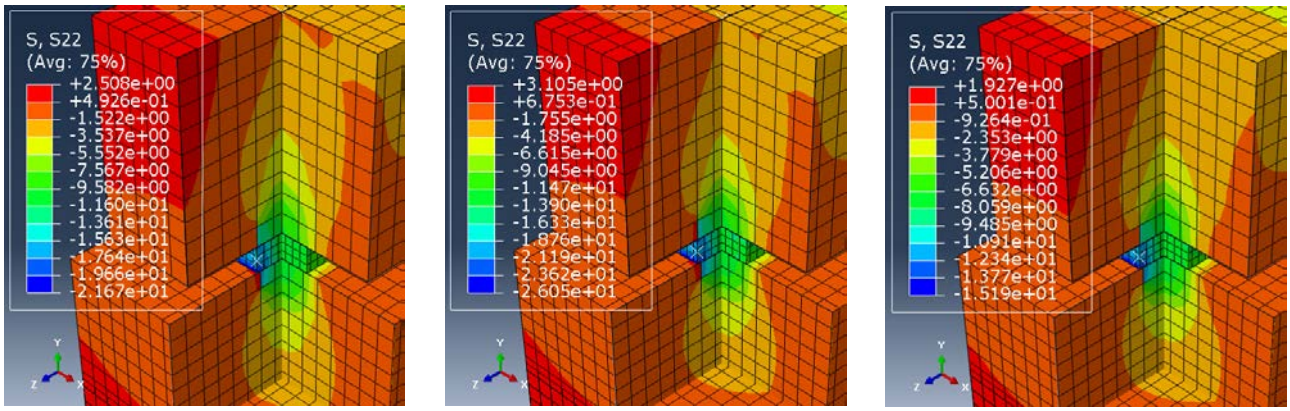

(a) **(b)** **(c)**

Figure 19. Vertical stress of two-way hinges with high area ratios: (a) SC23-22, (b) SC23-32, (c) SC23-40.

The drop of the hinge axial capacity is primarily due to the presence of the lateral shear stress which contributes in degrading the throat stiffness. As summarized in Table 5, the confinement factor "CF" is decreased to 1 for the hinges with low area ratios and to 1.5 for those with the high ones. Therefore, "CF" is not practically valuable. Fig. 20 presents the axial load displacement curves performed by ABAQUS for the different cases considered. Fig. 21 displays the hinge axial capacity versus the square root ratio of column to hinge area $\sqrt{A_c / A_h}$.

Table 5. Hinge axial capacity.

Model	$\sqrt{A_c / A_h}$	ABAQUS (Axial Load only) KN	ABAQUS (Axial & Lateral Loads) KN	Capacity Drop %	Confinement Factor (CF)
CS14-22	2.00	340	235	31%	0.84
CS20-22	2.86	406	281	31%	1.37
CS21-22	3.00	411	284	31%	1.41
CS23-22	3.29	435	287	34%	1.44
CS25-22	3.57	441	291	34%	1.49
CS28-22	4.00	451	302	33%	1.62
CS14-32	2.00	417	278	33%	0.92
CS20-32	2.86	530	341	36%	1.42
CS21-32	3.00	534	346	35%	1.46
CS23-32	3.29	563	363	36%	1.60
CS25-32	3.57	571	370	35%	1.66
CS28-32	4.00	578	376	35%	1.71
CS14-40	2.00	481	314	35%	0.97
CS20-40	2.86	615	413	33%	1.60
CS21-40	3.00	633	420	34%	1.65
CS23-40	3.29	662	425	36%	1.68
CS25-40	3.57	671	431	36%	1.72
CS28-40	4.00	679	438	35%	1.76

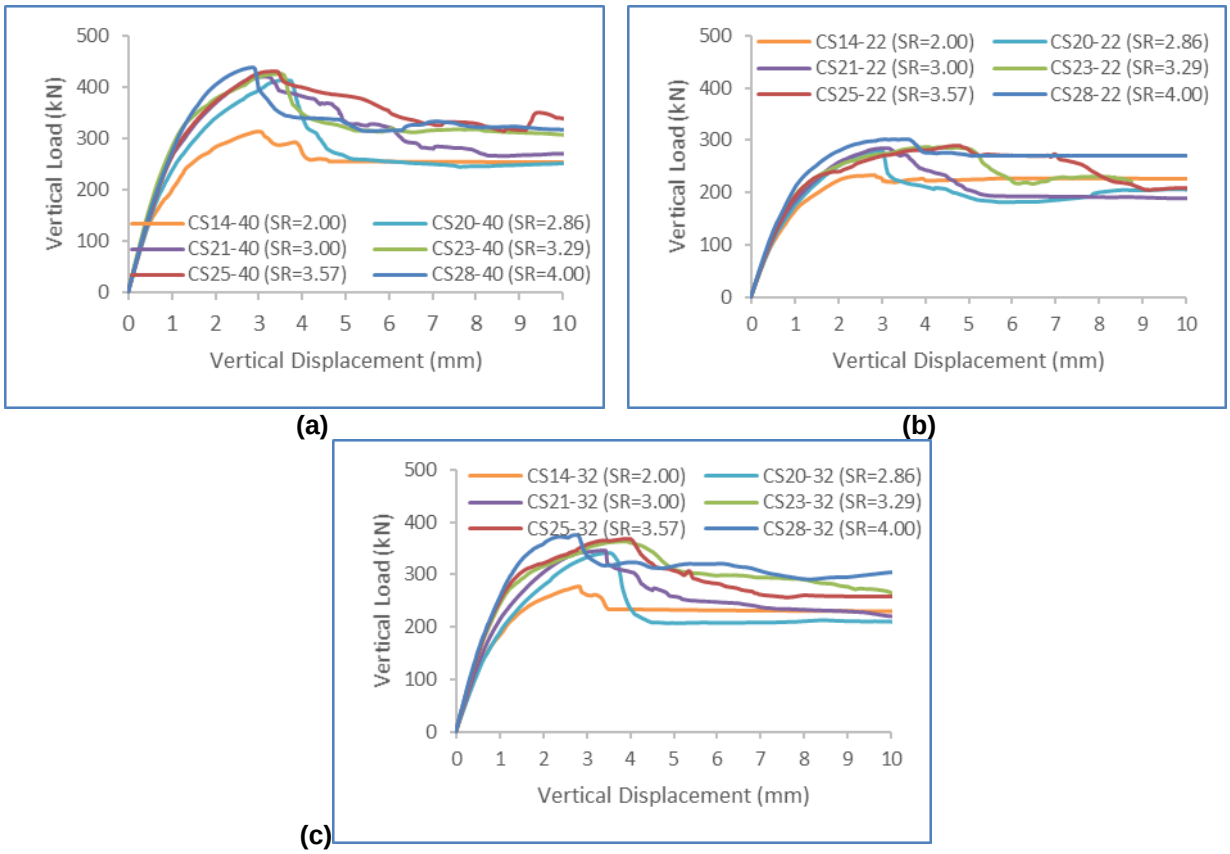

Figure 20. Axial load-displacement curves: (a) CS-22, (b) CS-32, (c) CS-40.

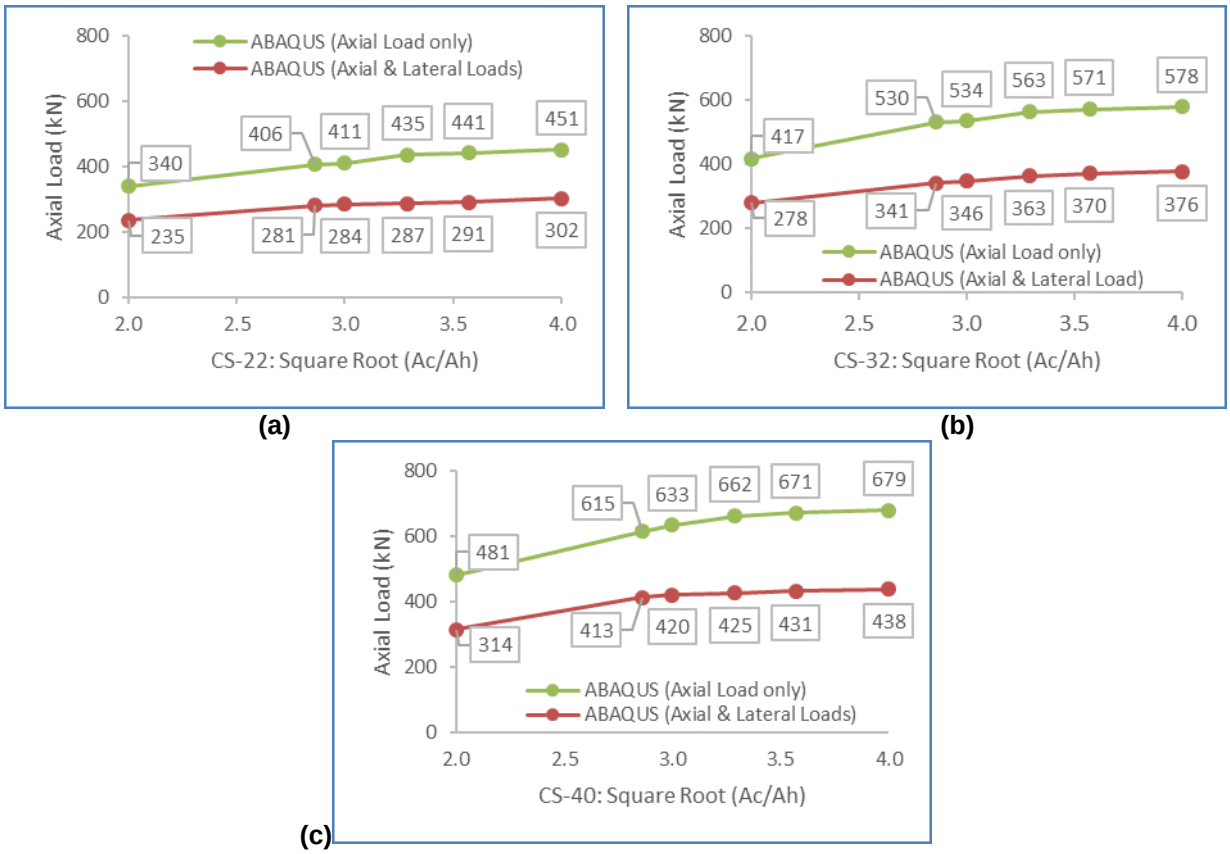

Figure 21. Square root of area ratio vs hinge capacity: (a) CS-22, (b) CS-32, (c) CS-40.

According to ACI code, the hinge nominal shear V_{hn} is [30–32]:

$$V_{hn} = \min\{0.2 f_c^{'} A_c; (3.3 + 0.08 f_c^{'}) A_c; 11 A_c\} \tag{9}$$

The confining stress produced by the column on the throat area, has a great influence on the hinge shear strength. Regardless of the level of the column/hinge area ratio, the shear capacity of two-way hinges was five times higher than the code states, as indicated on Table 6. Fig. 22 presents the lateral load displacement curves performed by ABAQUS for the different cases considered.

Table 6. Hinge shear strength.

Model	$\sqrt{Ac / Ah}$	Hinge Shear Strength (KN)		Increasing Rate
		ACI Code	ABAQUS	
CS14-22	2.00	22	105	4.77
CS20-22	2.86	22	117	5.32
CS21-22	3.00	22	114	5.18
CS23-22	3.29	22	116	5.27
CS25-22	3.57	22	117	5.32
CS28-22	4.00	22	117	5.32
CS14-32	2.00	29	126	4.34
CS20-32	2.86	29	137	4.72
CS21-32	3.00	29	139	4.79
CS23-32	3.29	29	138	4.76
CS25-32	3.57	29	139	4.79
CS28-32	4.00	29	140	4.83
CS14-40	2.00	32	143	4.47
CS20-40	2.86	32	163	5.09
CS21-40	3.00	32	161	5.03
CS23-40	3.29	32	162	5.06
CS25-40	3.57	32	162	5.06
CS28-40	4.00	32	163	5.09

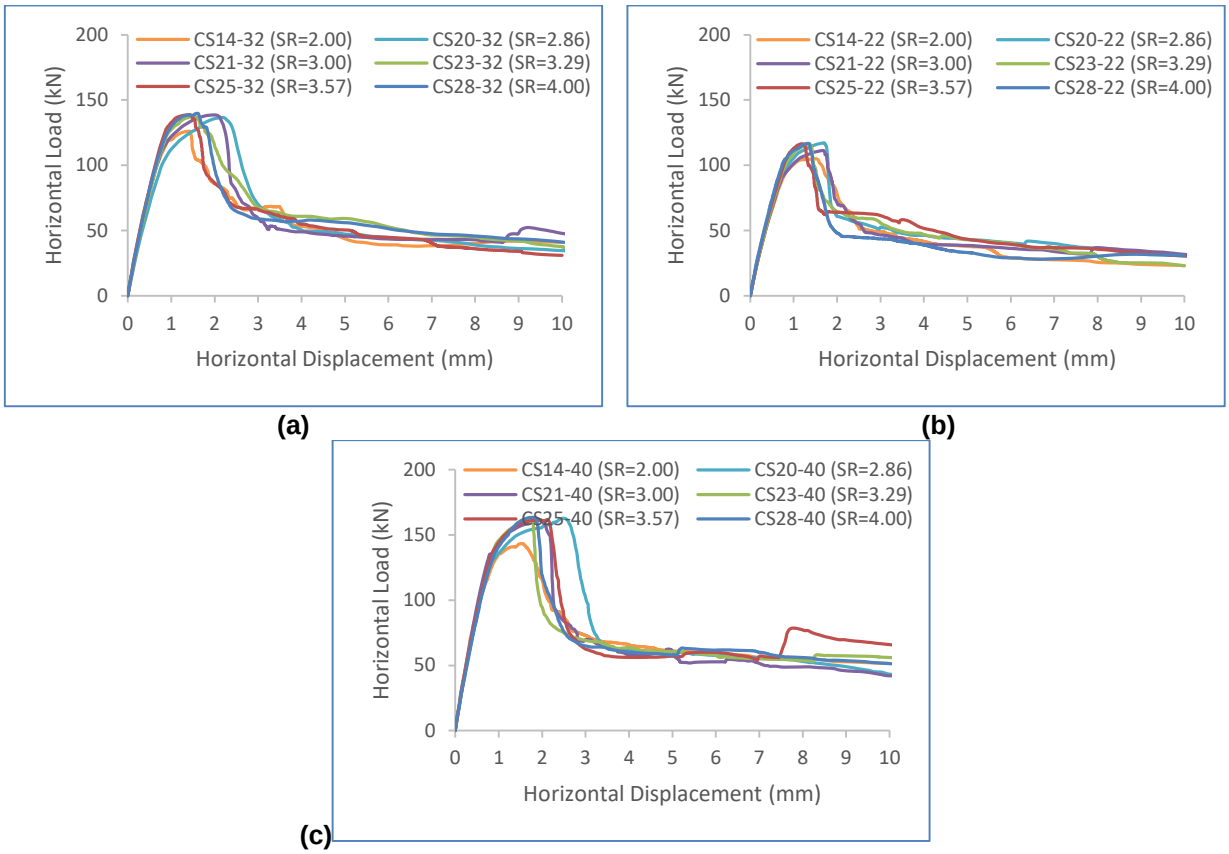

Figure 22. Lateral load-displacement curves:
(a) CS-22, (b) CS-32, (c) CS-40.

4. Conclusions

This paper investigates the behavior of two-way hinges in reinforced concrete structures using the finite element method. The main conclusions are as follows:

1. The hinges with low area ratios $\sqrt{A_c / A_h}$ = 2, mainly failed by hinge crushing. This implies that the confining stress produced by the column on the hinge was not enough to bear the vertical stress induced. On the other side, the hinges with high area ratios $\sqrt{A_c / A_h}$ > 2, failed by splitting failure above throat area. This means that the confining stress produced by the column on the hinge was greater than what the column can withstand.

2. The hinges with high area ratios $\sqrt{A_c / A_h}$ > 2, exhibited ductile failure modes, noting that a large displacement was imposed by ABAQUS prior to complete failure. The transfer of stress through the hinge indicates that the hinges with high area ratios showed better confinement than those with low ratios.

3. Two-way hinge axial capacity did not have the same limit as the code stipulates. The capacity was noticeably amplified up by a confinement factor “CF” equal to three.

4. Subjected to the dual effect of lateral and axial loads, two-way hinges with low area ratios $\sqrt{A_c / A_h}$ = 2, exhibited bearing failure at the hinge region. This entails that the confining stress produced by the column on the hinge was not enough to withstand the vertical stress induced. However, the hinges with high area ratios $\sqrt{A_c / A_h}$ > 2, failed by hinge-footing slippage interface. This indicates that the confining stress increased the hinge bearing capacity and thereby, the hinge failed once the shear stress exceeded the shear capacity.

5. The confining stress produced by the column on the throat area has a great influence on the hinge shear strength. Regardless of the level of the column/hinge area ratio, the shear capacity of two-way hinges was five times higher than what the code states.

6. The presence of the shear stress decreased the axial capacity of the hinge by about 30~35 %, and the amplification factor due to the confinement effect was decreased to nearly 1 for the models with low area ratios and to 1.5 for those with the high ones.

References

1. Marx, S., Schacht, G. Concrete hinges in bridge engineering. Proceedings of the Institution of Civil Engineers, Engineering History and Heritage. 2015. 168(2). Pp. 64–74. DOI: 10.1680/ehah.14.00020
2. Griezic, A., Zeyl, P.E., Cook, W.D., Mitchell, D. Experimental studies of hinges in existing bridge columns. 7th Canadian Conference on Earthquake Engineering, Montreal. 1995.
3. Hillis, D., Saiidi, M.S. Construction and nonlinear dynamic analysis of three bridge bents used in a bridge system test. Center for Civil Engineering Earthquake Research, Department of Civil and Environmental Engineering, University of Nevada. 2009. Report No. CCEER-09-03. [Online]. https://scholarworks.unr.edu/handle/11714/7166. (Accessed: 05.04.2020).
4. Zaghi, A.E., Saiidi, M.S. Seismic performance of pipe-pin two-way hinges in concrete bridge columns. Journal of Earthquake Engineering. 2010. 14(8). Pp. 1253–1302. DOI: 10.1080/13632469.2010.490321
5. Zaghi, A.E., Saiidi, M.S. Bearing and shear failure of pipe-pin hinges subjected to earthquakes. ASCE Journal of Bridge Engineering. 2011. 16(3). Pp. 340–350. DOI: 10.1061/(ASCE)BE.1943-5592.0000160
6. Jiang, Y., Saiidi, M.S. Response and design of R/C one-way pier hinges in strong direction. ASCE Journal of Structural Engineering. 1995. 121(8). Pp. 1236–1244. DOI: 10.1061/(ASCE)0733-9445(1995)121:8(1236)
7. Saiidi, M.S., Cheng, Z.-Y, Sanders, D.L. An experimental study of two-way reinforced concrete column hinges under seismic load. ACI Structural Journal. 2009. 106(3). Pp. 340–348. DOI: 10.14359/56498
8. Saiidi, M.S., Orie, J., Douglas, B. Lateral load response of R/C bridge columns with a one-way pinned end. ACI Structural Journal. 1988. 85(6). Pp. 609–616. [Online]. https://www.researchgate.net/publication/296225889_Lateral_load_response_of_reinforced_concrete_bridge_columns_with_a_one-way_pinned_end. (Accessed: 05.04.2020).
9. McLean, D.I., Lim, K.Y. Moment-reducing hinge details for the bases of bridge columns. Washington State Department of Transportation. 1990. Report No. WA-RD 220.1. [Online]. https://www.wsdot.wa.gov/research/reports/fullreports/220.1.pdf. (Accessed: 05.04.2020).
10. Yuan, F., Wu, Y.F. Effect of load cycling on plastic hinge length in RC columns. Engineering Structures. 2017. 147. Pp. 90–102. DOI: 10.1016/j.engstruct.2017.05.046
11. Doyle, K.A., Saiidi, M.S. Seismic response of telescopic pipe pin connections. Center for Civil Engineering Earthquake Research, Department of Civil Engineering, University of Nevada. 2008. Report No. CCEER-08-01. [Online]. https://wolfweb.unr.edu/homepage/saiidi/caltrans/Pipe-Pins/PDFs/CCEER%2008_1.pdf. (Accessed: 05.04.2020).
12. Roberts, J.E. Caltrans structural control for bridges in high-seismic zones. Earthquake Engineering & Structural Dynamics. 2005. 34(4–5). Pp. 449–470. DOI: 10.1002/eqe.439
13. Mehrsoroush, A., Saiidi, M.S. Earthquake-resistant telescopic pipe pin column base connections for accelerated bridge construction. 10th U.S. National Conference on Earthquake Engineering, Frontiers of Earthquake Engineering. 2014. Alaska. DOI: 10.4231/D37S7HT0V
14. Mehrsoroush, A., Saiidi, M.S. Cyclic Response of Precast Bridge Piers with Novel Column-Base Pipe Pins and Pocket Cap Beam Connections. ASCE Journal of Bridge Engineering. 2016. 21(4): 04015080. DOI: 10.1061/(ASCE)BE.1943-5592.00-00833

15. Cheng, Z., Saiidi, M.S., Sanders, D. Development of a seismic design method for reinforced concrete two-way bridge column hinges. Center for Civil Engineering Earthquake Research, Department of Civil Engineering, University of Nevada. 2006. Report No. CCEER-06-01. [Online]. https://www.nevadadot.com/home/showdocument?id=3858. (Accessed: 05.04.2020).
16. Saiidi, M.S., Straw, D. Monotonic and cyclic response of one-way R/C Bridge pier hinges in the strong direction. ACI Structural Journal. 1993. 90(5). Pp. 568–573. [Online]. https://trid.trb.org/view/382330. (Accessed: 05.04.2020).
17. Chahal, S., Baalbaki, O., Timsah, Y., Ghanem, H., Abu Saleh, Z. Experimental Investigation of Two-Way Hinges in Reinforced Concrete Members. Proceedings of the 3rd GeoMEast International Congress and Exhibition. 2019. Pp. 128–146. DOI: 10.1007/978-3-030-34216-6_9
18. Chaudhari, S., Chakrabarti, M. Modeling of concrete for nonlinear analysis Using Finite Element Code ABAQUS. International Journal of Computer Applications. 2012. 44(7). Pp. 14–18. DOI: 10.5120/6274-8437
19. Wahalathantri, B.l., Thambiratnam, D.p., Chan, T.H.T., Fawzia, S. A material model for flexural crack simulation in reinforced concrete elements using Abaqus. Proceedings of the First International Conference on Engineering, Designing and Developing the Built Environment for Sustainable Wellbeing, Queensland University of Technology, Brisbane, Qld. 2011. Pp. 260–264. [Online]. https://eprints.qut.edu.au/41712/. (Accessed: 05.04.2020).
20. Kmiecik, P., Kaminski, M. Modelling of reinforced concrete structures and composite structures with concrete strength degradation taken into consideration. Archives of civil and mechanical engineering. 2011. 11(3). Pp. 623–636. DOI: 10.1016/S1644-9665(12)60105-8
21. Lubliner. J., Oliver. J., Oller. S., Onate. E. A plastic-damage model for concrete. International Journal of Solids and Structures. 1989. 25(3). Pp. 299–326. DOI: 10.1016/0020-7683(89)90050-4
22. Szczecina, M.S., Andrzej, W. Calibration of the CDP model parameters in Abaqus. The 2015 World Congress on Advances in Structural Engineering and Mechanics (ASEM15), Korea. 2015. [Online]. https://www.academia.edu/32626413/Calibration_of_the_CDP_model_parameters_in_Abaqus. (Accessed: 05.04.2020).
23. Lee, J., Fenves, G.L. Plastic-damage model for cyclic loading of concrete structures. Journal of Engineering Mechanics. 1998. 124(8). Pp. 892–900. DOI: 10.1061/(ASCE)0733-9399(1998)124:8(892)
24. Jankowiak, T., Lodygowski, T. Identification of parameters of concrete damage plasticity constitutive model. Foundations of Civil and Environmental Engineering, Poznan University of Technology. 2005. No. 6. Pp. 53–69. ISSN 1642–9303. [Online]. https://www.academia.edu/9635025/F_IDENTIFICATION_OF_PARAMETERS_OF_CONCRETE_DAMAGE_PLASTICITY_CONSTITUTIVE_MODEL. (Accessed: 05.04.2020).
25. Genikomsou, A.S., Polak, M.A. Finite element analysis of punching shear of concrete slabs using damage plasticity model in ABAQUS. Engineering Structures. 2015. 98. Pp. 38–48. DOI: 10.1016/j.engstruct.2015.04.016
26. Jahami, A., Temsah, Y., Khatib, J. The efficiency of using CFRP as a strengthening technique for reinforced concrete beams subjected to blast loading. International Journal of Advanced Structural Engineering. 2019. 11(4). Pp. 411–420. DOI: 10.1007/s40091-019-00242-w
27. Fediuk, R.S., Lesovik, V.S., Liseitsev, Y.L., Timokhin, R.A., Bituyev, A.V., Zaiakhanov, M.Y., Mochalov, A.V. Composite binders for concretes with improved shock resistance. Magazine of Civil Engineering. 2019. 85(1). Pp. 28–38. DOI: 10.18720/MCE.85.3
28. Fediuk, R.S., Lesovik, V.S., Mochalov, A.V., Otsokov, K.A., Lashina, I.V., Timokhin, R.A. Composite binders for concrete of protective structures. Magazine of Civil Engineering. 2018. 82(6). Pp. 208–218. DOI: 10.18720/MCE.82.19
29. Fediuk, R., Smoliakov, A., Muraviov, A. Mechanical properties of fiber-reinforced concrete using composite binders. Advances in Materials Science and Engineering. 2017. Article ID 2316347. Pp. 1–14. DOI: 10.1155/2017/2316347
30. Building code requirements for structural concrete (ACI 318-19). American Concrete Institute. 428 p, 433 p. DOI: 10.143-59/51716937
31. MacGregor, J., Wight, J. Reinforced Concrete Mechanics and Design. 6th edition. Pearson Education. New Jersey, 2012. 858 p.
32. Hassoun, M., Al-Manaseer, A. Structural Concrete Theory and Design. 6th edition. John Wiley & Sons. New Jersey, 2015. 456 p.

Contacts:

Safwan Chahal, safwanchahal79@gmail.com

Oussama Baalbaki, obaalbaki@bau.edu.lb

Yehia Temsah, ytemsah@bau.edu.lb

Hassan Ghanem, h.ghanem@bau.edu.lb

Zaher Abu Saleh, abousalehza@rhu.edu.lb

© Chahal, S., Baalbaki, O., Temsah, Y., Ghanem, H., Abu Saleh, Z., 2021

Magazine of Civil Engineering

ISSN 2712-8172

journal homepage: http://engstroy.spbstu.ru/

DOI: 10.34910/MCE.102.5

Methodology for calculation and design of earthquake-resistant vibroisolated turbine foundations

V. Tarasov*, V.V. Lalin, A.E. Radaev, A. Mentishinov

Peter the Great St. Petersburg Polytechnic University, St. Petersburg, Russia

**E-mail: vtarasov1000@yandex.ru*

Keywords: structural dynamics, civil engineering, structure seismic stability, earthquake protection, seismic resistance, vibration insulation, turbogenerator set foundation, response spectra

Abstract. The object of research in the article is the vibroisolated foundation of a high-power turbine unit (1000 MW). World energy is developing rapidly today and there is a need to build energy facilities in areas of high seismicity. The acute question is the lack of a comprehensive methodology for calculating and designing earthquake-resistant foundations of turbine units. The article proposes a general procedure of actions aimed at increasing the seismic resistance of the foundations of turbine units. Implementation of the proposed methodology was carried out on a specific example of a vibroisolated foundation: the dependences of seismic accelerations and displacements were obtained for different variants of seismic isolation. Application of the above technique allows to reduce seismic acceleration on capacitors by more than 2 times, seismic movements of capacitors by more than 3 times.

1. Introduction

In the current conditions of the development of world industry and nuclear energy, the construction of industrial and energy facilities in areas with high seismic activity as part of the development of the corresponding capacities of individual regions and states is of particular importance. This circumstance is due to the need to ensure high reliability of the operation of the relevant construction projects, including through the implementation of measures to reduce the negative physical effects on the structural elements of construction projects, due to both internal and external factors. Moreover, among external factors, a special form of natural influences – seismic – is of particular importance. This circumstance is associated primarily with the nature of the impact of these loads on the structural elements of construction objects, as well as the difficulty in predicting the scale and time intervals for the manifestation of the corresponding natural phenomena, as well as the severity of the possible consequences. The complexity of developing appropriate structural, organizational and technological solutions is determined not only by the need to ensure rigidity and strength of the corresponding structural elements of construction objects, but also by the importance of taking into account the characteristics of soils located in the construction location. Based on the above-mentioned, a conclusion was drawn on the feasibility of conducting a study, the purpose of which is to develop a procedure for substantiating the characteristics of structural solutions in the field of protecting structural elements of industrial and energy construction from seismic loads. To achieve this goal, the following research objectives were formulated:

1. Review and analysis of scientific work on the research topic.
2. Development of a procedure for substantiating structural solutions in the field of protecting structural elements of industrial and energy construction from seismic loads.
3. Implementation of the developed procedure on a practical example.

At the initial stage of the study, a review and analysis of literary sources related to the research topic was carried out. Despite the large number of scientific works in the field of designing structural elements as

Tarasov, V., Lalin V.V., Radaev, A.E., Mentishinov, A. Methodology for calculation and design of earthquake-resistant vibroisolated turbine foundations. Magazine of Civil Engineering. 2021. 102(2). Article No. 10205. DOI: 10.34910/MCE.102.5

This work is licensed under a CC BY-NC 4.0

part of industrial and energy construction, the number of methodological developments and tools directly related to solving the problems of substantiating the characteristics of the above elements from the point of view of protection against seismic loads is relatively small. This circumstance is mainly due to the need to take into account the dynamic factor in the formulation and solution of the corresponding design problems, which, in turn, determines the high complexity of the calculations, the effectiveness of which is directly determined by the level of development of information and computer technologies. That is why the first applied research in the field of protection of structural elements from seismic loads began only in the second half of the XX century. In particular, in the Soviet Union, the first research in the field of seismic protection of building structure elements was carried out at the Central Scientific and Research Institute of Civil Engineering under the direction of Ya.M. Eisenberg [1–2]. The results of these studies were the basis for scientific and methodological developments and tools in the corresponding field of research. In the late 70^{s} of the 20th century, the first mass construction of buildings and structures with seismic isolation systems in the form of turn-on and turn-off connections during the construction of the Baikal–Amur Mainline route began.

The city of railroad workers (82 buildings) was built up with seismically insulated buildings based on large-panel series 122. This was the first experience in the world in applying such a seismic protection system in residential buildings [1]. These circumstances, in particular, determined Russia's advancement to the leading places in the world in the number of built structures with various seismic isolation systems (more than 600 objects).

The appearance of new and improvement of already created scientific developments in the field of seismic isolation of building structures is inextricably linked with the development of dynamic calculations (in particular, seismic), the development of various methods of mathematical modeling in the calculation of structures, the improvement of construction-base interaction theories, soil calculation methods, and much more.

Among domestic and world scientists in the direction of seismic design calculations, it should be noted such scientists as Y.M. Eisenberg, A.N. Birbraer, I.I. Goldenblat, M.F. Barshtein, B.G. Koronev, I.M. Rabinovich, I.A. Konstantinov, N. Newmark, E. Rosenblatt, S.L. Timoshenko, S.T. Shulman.

General issues of designing structural elements as part of industrial and energy construction in areas with high seismic activity are covered in works of Hiraki (2014), Chen (2014), Kumar, Whittaker and Constantinou (2015) [3–7].

A detailed description of the relevant design solutions in the field of protecting elements of building structures as part of industrial and energy construction is presented in works of Medel-Vera (2015), Sayed (2015), Firoozabad (2015), Zhou, Wong and Mahin (2016), Kostarev, Petrenko and Vasilyev (2007) Sargsyan (2013), Birbraer (2017) Turilov (2017), Tyapin (2019) [8–24]. These decisions include the following:

- the use of seismic isolation systems to reduce the lower natural frequencies of structural elements of buildings and structures, as well as related technological equipment;
- the use of damping devices to increase the dissipation of kinetic energy that appears in the structural elements of the building under seismic impact;
- use of a non-standard approach in the field of Soil Structure Interaction.

It is important to note that the implementation of the above design solutions in the general case is characterized by rather high labor and money costs, but it does not always provide a high level of reliability of the operation of the construction site in conditions of increased seismic activity for the following main reasons:

- the difficulty of conducting full-scale tests of fully seismically insulated heavy buildings, and, as a result, the difficulty of verifying design methods;
- the difficulty of correct accounting in dynamic design models of construction objects for the stiffness and attenuation of individual elements of building structures, as well as large-sized technological equipment.
- unreasonable increase in damping characteristics in the ground.

To increase the efficiency of constructive solutions and reduce the complexity of the process of their development in the works of Belash (2019), Muravyeva and Vatin (2014), Egarmin (2015), Dražić and Vatin (2016) Rutman and Ostrovskaya (2018) [25–30] offers various options for dynamic calculation methods, including taking into account damping.

However, the relevant works describe only the general principles of accounting for seismic effects without taking into account the features of structural elements in industrial and energy construction facilities (these features are determined, in particular, by the purpose of the facility, the appropriate space-planning solution, the applied technological equipment, etc.). At the same time, the specified works do not provide specific methods for substantiating the characteristics of structural solutions in the field of protecting structural elements in construction objects from seismic influences.

Thus, according to the results of the review and comparative analysis of literary sources on the research topic, the following conclusions were made:

- a relatively small proportion of the number of works devoted to the development and analysis of design solutions in the field of protecting industrial and energy construction objects from seismic loads in the total number of works related to the design of industrial and energy construction objects;
- lack of tools providing substantiation of the characteristics of structural solutions in the field of protection of structural elements in industrial and energy construction objects from seismic effects.

The above conclusions once again confirmed the relevance of the study and were the basis for the implementation of its subsequent stages – the development of a procedure for substantiating the characteristics of structural solutions, a more detailed description of which is presented in the following sections of the work.

The object of research is the vibroisolated foundations of high-power turbine units (1000 MW). The aim of the study is to determine and formulate a comprehensive methodology for calculating and designing earthquake-resistant vibroisolated foundations of turbine units. During the study, the following main tasks were posed and solved:

1. Formulation of methods for calculating and designing earthquake-resistant vibroisolated foundations of turbine units;

2. Implementation of the proposed methodology on a specific example, by conducting computational experiments;

3. Analysis of increasing the seismic resistance of the vibroisolated foundation of the turbine unit when applying the proposed methodology.

2. Methods

As part of the next phase of the study, a procedure was proposed for substantiating the characteristics of structural solutions for protecting structural elements in industrial and energy construction from seismic effects. The structure of the developed procedure is presented in the form of a flowchart in Fig. 1 and has the following main features:

1. The general process of solving the problem of substantiating the characteristics of structural solutions to protect the structural elements of building objects from seismic influences includes the following key steps:

- construction of a comprehensive model containing adjustable and unregulated parameters of the studied structural elements, as well as design characteristics for evaluating alternative constructive solutions;
- description of alternative constructive solutions by forming appropriate combinations of adjustable parameter values;
- creation of a calculation model (in a pre-selected software environment) based on the above calculation;
- implementation of computational experiments on the developed computational model in accordance with pre-formed alternative design options;
- the choice of the most preferred design solution based on the results obtained from the implementation of computational experiments.

2. The basic principles for constructing a comprehensive model are the following:

- as unregulated are assigned parameters that describe the construction object and its structural elements, which, when perceived by seismic loads, do not cause a decrease in the reliability indicators of the facility;
- as adjustable parameters are assigned that describe the structural elements of the construction object or appropriate technological equipment, the perception of which seismic loads significantly affects the reliability indicators of the facility;
- as design characteristics for evaluating the effectiveness (preference) of structural solutions for protecting structural elements of an object from seismic influences, particular indicators are assigned that are determined by analyzing the dependences of seismic accelerations and displacements in the corresponding supporting components of structural elements on the time factor or frequency characteristics of external influence (for example, peak seismic acceleration, zero period acceleration (ZPA) and deformation of support components).

3. General requirements for software in the field of modeling of computational models, which can be used to solve the problem, are the following:

- the possibility of implementing the finite element method of the spatial configuration;
- the ability to implement dynamic calculations by directly integrating the equations of motion;
- the ability to account for concentrated dampers in the design scheme;
- the ability to numerically and graphically display selected design characteristics.

4. The construction of the calculation model is based on the corresponding complex model according to the following basic principles:

- unregulated and adjustable input parameters of the model are formed in accordance with unregulated and adjustable (according to the design options) parameters of the structural elements of the object in question, taking into account the structural features of the models within the selected software environment;
- model output parameters are formed on the basis of design characteristics for evaluating the effectiveness (preference) of structural solutions and, in the general case, describe the dependence of the seismic resistance characteristics of the considered structural elements or technological equipment on the time factor or on the frequency characteristics of external influence.

5. The choice of the most preferable constructive solution based on the results of the implementation of computational experiments in the selected software environment is advisable to carry out by the method of linear convolution. The corresponding mathematical expressions have the form:

$$i^*: \; Q_{i^*} = \max_i \{Q_i\}, \tag{1}$$

$$Q_i = \sum_{j=1}^{n} \alpha_j \cdot \frac{q_{ij} - q_j^{\text{worst}}}{q_j^{\text{best}} - q_j^{\text{worst}}}; \tag{2}$$

where i^* is index of the most preferred design solution in the field of protecting structural elements of an object from seismic effects;

Q_i is the value of a generalized indicator of the effectiveness i ($i = 1, 2, ..., m$, where m is total number of options) of a design solution option;

n is total number of design characteristics for evaluating the effectiveness (preference) of constructive solutions;

α_j is coefficient of significance of accounting for the calculated characteristic j ($j = 1, 2, ..., n$) to evaluate the effectiveness (preference) of constructive solutions; coefficients $\{\alpha_j\}$ must satisfy the conditions:

$$\begin{cases} \alpha_j \geq 0, \; j = 1, 2, ..., n; \\ \sum_{j=1}^{n} \alpha_j = 1. \end{cases} \tag{3}$$

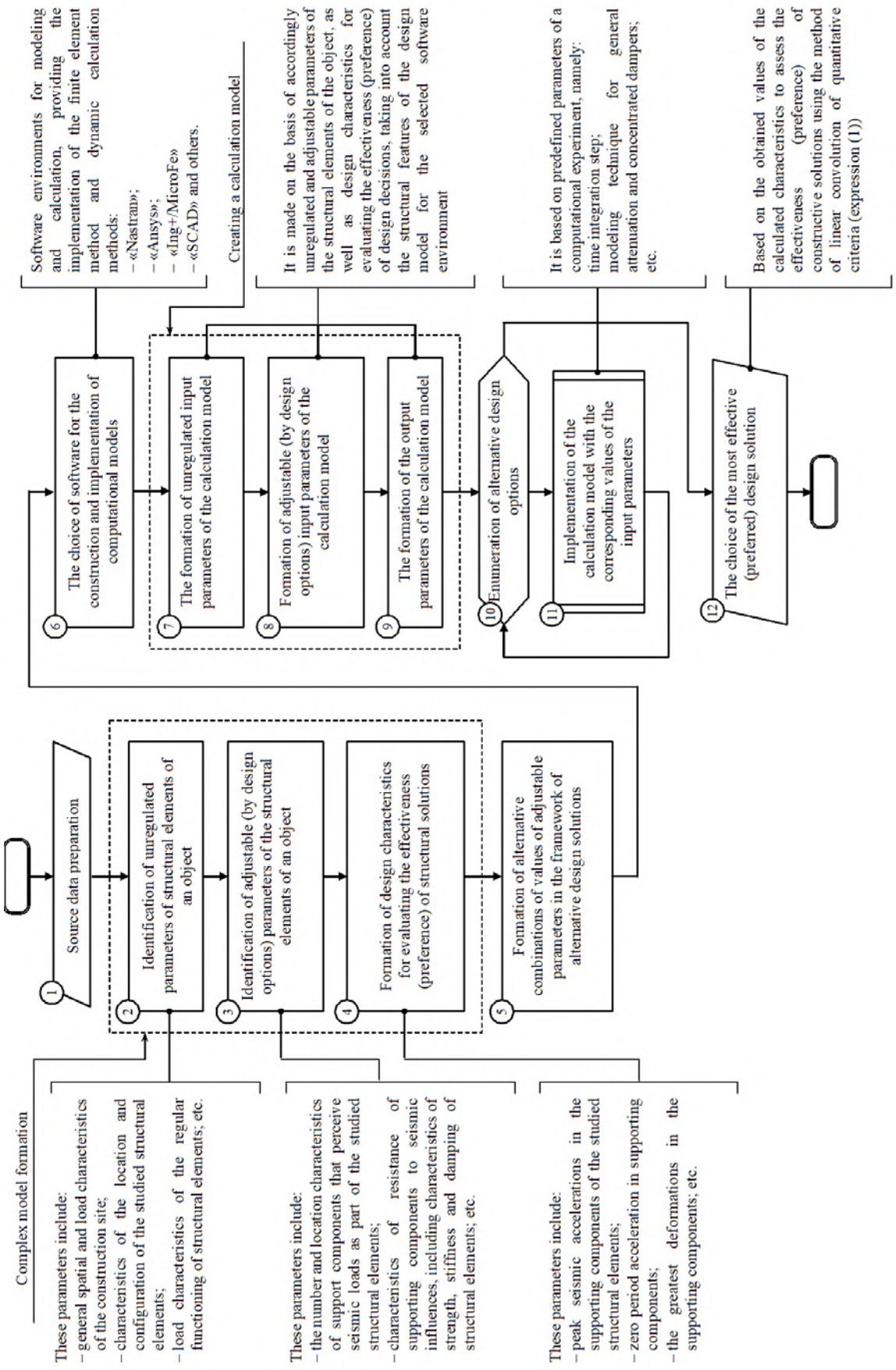

Figure 1. A flowchart describing the structure of the proposed procedure.

q_{ij} is value of design characteristic j ($j = 1, 2, ..., n$) to evaluate the effectiveness (preference) in relation i ($i = 1, 2, ..., m$) to the design solution;

q_j^{best}, q_j^{worst} are respectively, the most and least preferred value of the design characteristic j ($j = 1, 2, ..., n$) to evaluate the effectiveness (preference) of constructive solutions;

$$q_j^{\text{best}} = \begin{cases} \max\limits_i \{q_{ij}\}, & \text{if the growth of the characteristic determines increased preference;} \\ \min\limits_i \{q_{ij}\}, & \text{otherwise;} \end{cases} \quad (4)$$

$$q_j^{\text{worst}} = \begin{cases} \min\limits_i \{q_{ij}\}, & \text{if the growth of the characteristic determines increased preference;} \\ \max\limits_i \{q_{ij}\}, & \text{otherwise.} \end{cases} \quad (5)$$

A detailed description of the implementation process of the proposed procedures on a practical example of use in the next section of the work.

3. Results and Discussion

At the next stage of the study, the proposed procedure was implemented using a practical example – substantiating the characteristics of a structural solution for technological equipment – a high-speed turbine unit – as a structural element of an energy facility – a turbine building with a monolithic reinforced concrete frame – as part of a power plant. At the initial stage of solving the problem, the initial data were collected and systematized (block 1 of the scheme in Fig. 1). The generated schematic description of the structural

At further stages of solving the problem, an integrated model for solving the problem was created. A description of the main adjustable and unregulated parameters of the complex model (blocks 2–4 of the circuit shown in Fig. 2) is presented in Table 1.

Table 1. Structural elements of the developed calculation model.

№ in order.	Name	UoM.	Value / Category
1	**Unregulated parameters**		
1.1	Turbine building length	m	100
1.2	Turbine building width	m	60
1.3	Turbine building height	m	35
1.4	The altitude mark of the placement of the foundation of the turbine unit	m	15
1.5	Frame material	-	concrete B25
1.6	The mass of the turbine building with equipment, more	t	115000
1.7	Mass of the isolated foundation of the turbine unit, more	t	9000
1.8	Seismic impact area	-	base plate bottom surface *
1.9	Locations of points (at the installation marks of the turbine unit and condensers) for calculating the design characteristics	-	see Fig. 2, b and 2, c
1.10	Number of marks for calculating design characteristics:		
1.10.1	at the installation mark of the turbine unit	un.	12
1.10.2	at the installation mark of capacitors	un.	8
1.11	Total attenuation (damping)	%	4
1.12	Peak acceleration on the free surface of the soil in the horizontal direction	m/s^2	1.7

№ in order.	Name	UoM.	Value / Category
2	**Adjustable parameters (by design options)**		
2.1	The number of insulating elements at the installation marks of the turbine unit and condensers	un.	value
2.2	Type of insulating elements at the installation marks of the turbine unit and condensers	-	value
3	**Design characteristics for evaluating the effectiveness of structural solutions**		
3.1	Averaged spectrum of the response of seismic accelerations at the installation marks of the turbine unit and condensers for axial, transverse and vertical directions	m/s^2 from *f* (Hz)	dependence
3.2	Peak seismic acceleration at the installation marks of the turbine unit and condensers for axial, transverse and vertical directions	m/s^2	value
3.3	Acceleration of the zero period at the installation marks of the turbine unit and condensers for axial, transverse and vertical directions	m/s^2	value
3.4	Normalized greatest strains in insulators at the installation marks of the turbine unit and condensers for axial, transverse and vertical directions	Mm	value

Note: * it was assumed that the lower foundation slab is absolutely rigid, therefore, the influence of soil properties in the calculation was not taken into account.

As adjustable (by design options) parameters, the characteristics of vibration-insulating systems were considered in terms of the number and type of insulating elements in two groups placed in the support components of the turbine unit (Levels 1-2 in Fig. 2, a) and the condenser (Levels 3-4 on Fig. 2, a), respectively.

At the next stage of solving the problem, alternative constructive solutions were developed for vibration isolation of the technological equipment under consideration (block 5 of the diagram in Fig. 1). In total, five different constructive solutions were developed; their detailed description is presented in Table 2.

As part of the next stage of the study, the choice was made of software for creating a calculation model based on a previously developed integrated model (block 6 of the scheme in Fig. 1). As the specified software, the Nastran program was chosen for performing dynamic calculations, as it provides the optimal ratio of the complexity of creating and implementing the calculation model and the adequacy of the results obtained in the implementation of the corresponding computational experiments.

Further, using the selected program, a calculation model of the object of study was created. The basis of this development was the finite element model, a graphical description of which is presented in Fig. 3.

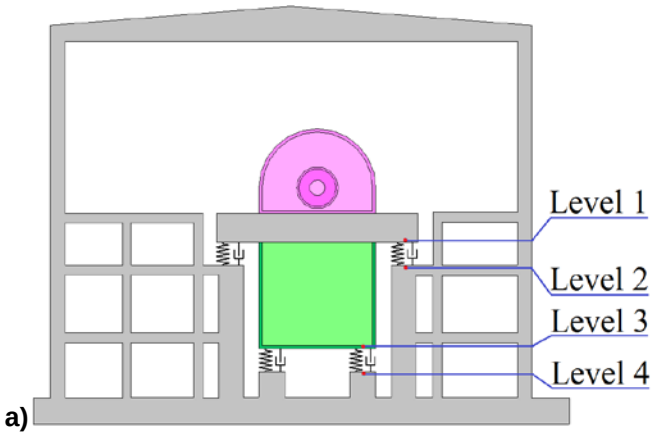

a)

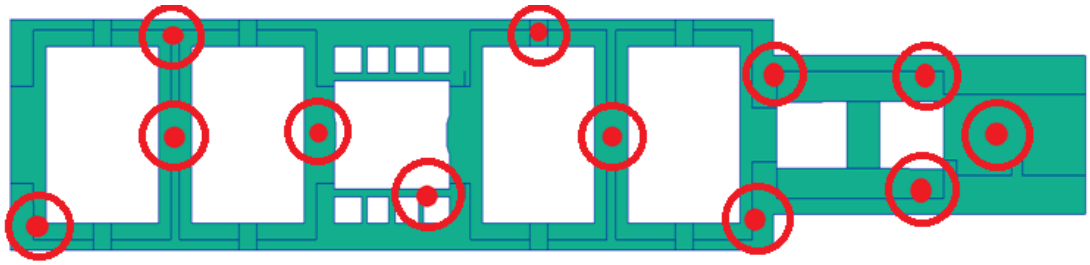

b)

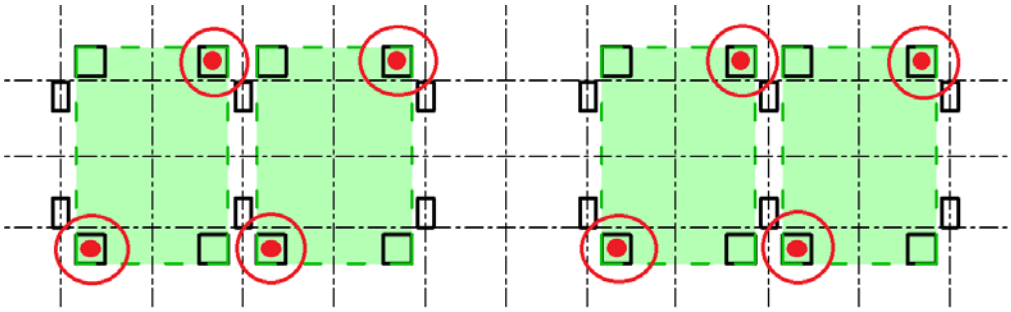

c)

Figure 2. Description of the structural element under consideration – the foundation of the turbine unit – as part of the construction project: a) – generalized scheme (cross section); b) –points for calculating the output characteristics of the calculation model at the turbine unit mark (levels 1-2); c) – points for calculating the output characteristics of the calculation model on capacitors (levels 3-4).

The structural elements of this model in terms of adjustable and unregulated input parameters, as well as output parameters (blocks 7–9 of the circuit in Fig. 1) correspond to the corresponding elements of the complex model. The main principles of creating a calculation model were the following:

- characteristics of the finite element mesh – the number of nodes and the configuration of their interconnections is determined by the spatial characteristics of the investigated construction object and its structural elements;
- environmental impact characteristics – seismic effects – are determined by quantitative characteristics – peak acceleration on the free surface of the soil, frequency composition of the synthesized accelerogram;
- the averaged response spectra of seismic accelerations at the installation marks of the turbine unit and condensers for axial, transverse and vertical directions (paragraph 3.1 of Table 1) were obtained as the average of all spectra at this mark, with peak expansion by 15 %. No additional peak reduction was performed.

At the next stage of solving the problem, computational experiments were performed, each of which corresponded to a separate version of the design solution for protecting technological equipment (as a structural element in the construction site) from seismic loads (blocks 10, 11 of the circuit in Fig. 1). The general parameters for the implementation of computational experiments on the model developed by Nastran are presented in Table 3. A graphic description of the output parameters of the model calculated as part of the above experiments is presented in Fig. 4.

Table 2. Description of design options for protecting process equipment from seismic loads.

Design option number	Design element name	Designation in Fig. 2 a	The number of insulating elements *			
			Spring insulators	Rigid spring insulators **	Spring damper insulators	Dampers
1	Capacitor supports	levels 1-2	4×4			
	Turbine unit foundation supports	levels 3-4	94			
2***	Capacitor supports	levels 1-2	4×4			
	Turbine unit foundation supports	levels 3-4	62		32	
3	Capacitor supports	levels 1-2	4×4			4×4
	Turbine unit foundation supports	levels 3-4	62		32	
4	Capacitor supports	levels 1-2		4×4		4×4
	Turbine unit foundation supports	levels 3-4	62		32	
5	Capacitor supports	levels 1-2		4×4		
	Turbine unit foundation supports	levels 3-4	62		32	

Note: * the maximum possible number of insulating elements is limited by a fixed size of the supporting surface area, layout, as well as maintenance requirements;
** horizontal stiffness of spring insulators doubled compared to standard;
*** this option is a standard version of the vibration-insulated foundation of a turbine unit, which differs from that used in areas with low seismic activity only by an increased number of damping elements.

Table 3. General parameters for the implementation of computational experiments on a model developed in the "Nastran" program.

№ in order.	Name	UoM.	Value
1	Dynamic calculation method	-	direct integration method of equations of motion
2	Integration step in the calculation of spectra	s	0.002
3	Integration step for calculating displacements	s	0.005
4	General attenuation modeling technique	-	Rayleigh technique

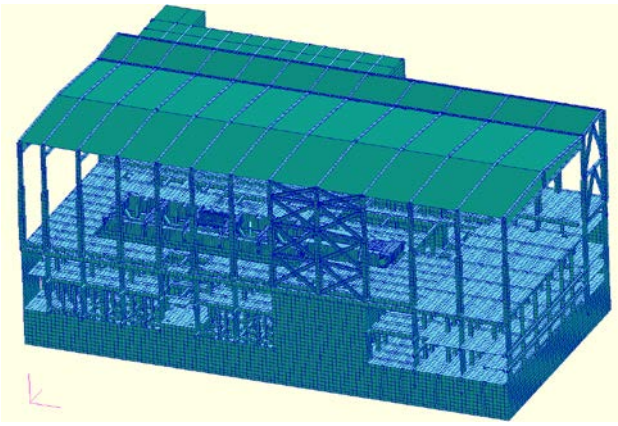

Figure 3. Graphic description of the finite element model of a turbine building developed in the "Nastran" program

At the final stage of solving the problem, the most effective (preferred) version of the constructive solution was selected to protect the technological equipment as part of the construction object from seismic loads (block 12 of the diagram in Fig. 1) by the highest value of the generalized efficiency indicator (expressions (1) and (2)) calculated according to the following basic principles:

- minimization of peak seismic accelerations at the installation marks of the turbine unit and condensers for axial, transverse and vertical directions;
- minimization of zero-period accelerations at the installation marks of the turbine unit and condensers for axial, transverse and vertical directions;
- minimization of the greatest seismic deformations in insulating elements for axial, transverse and vertical directions.

When performing the appropriate calculations, it was assumed that the above calculated characteristics were equivalent in evaluating the effectiveness of structural solutions, determined by identical values of the corresponding coefficients $\{\alpha_j\}$. In the case of additional critical requirements for seismic accelerations or displacements received from the equipment manufacturer or from technologists, it is possible to vary the coefficients $\{\alpha_j\}$. The results of calculating the values of the generalized performance indicator for alternative options for constructive solutions are presented in Table 4.

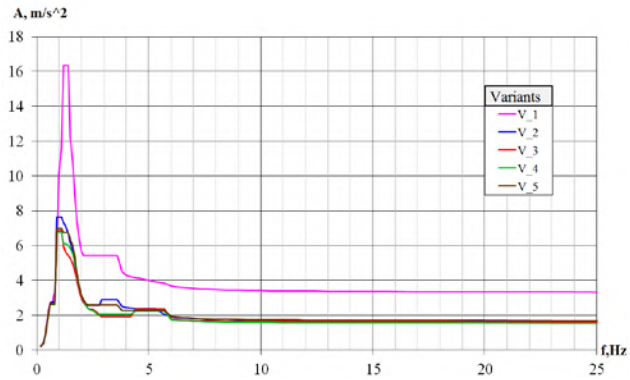

a)

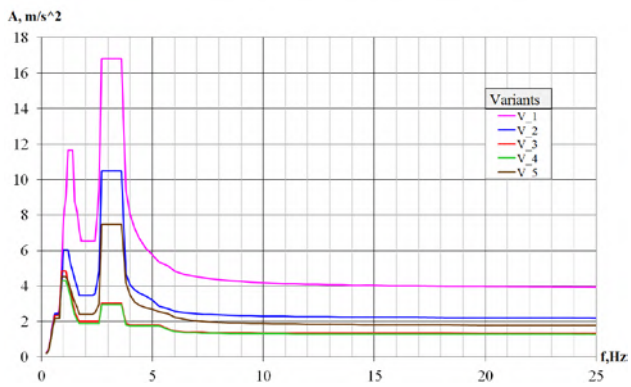

d)

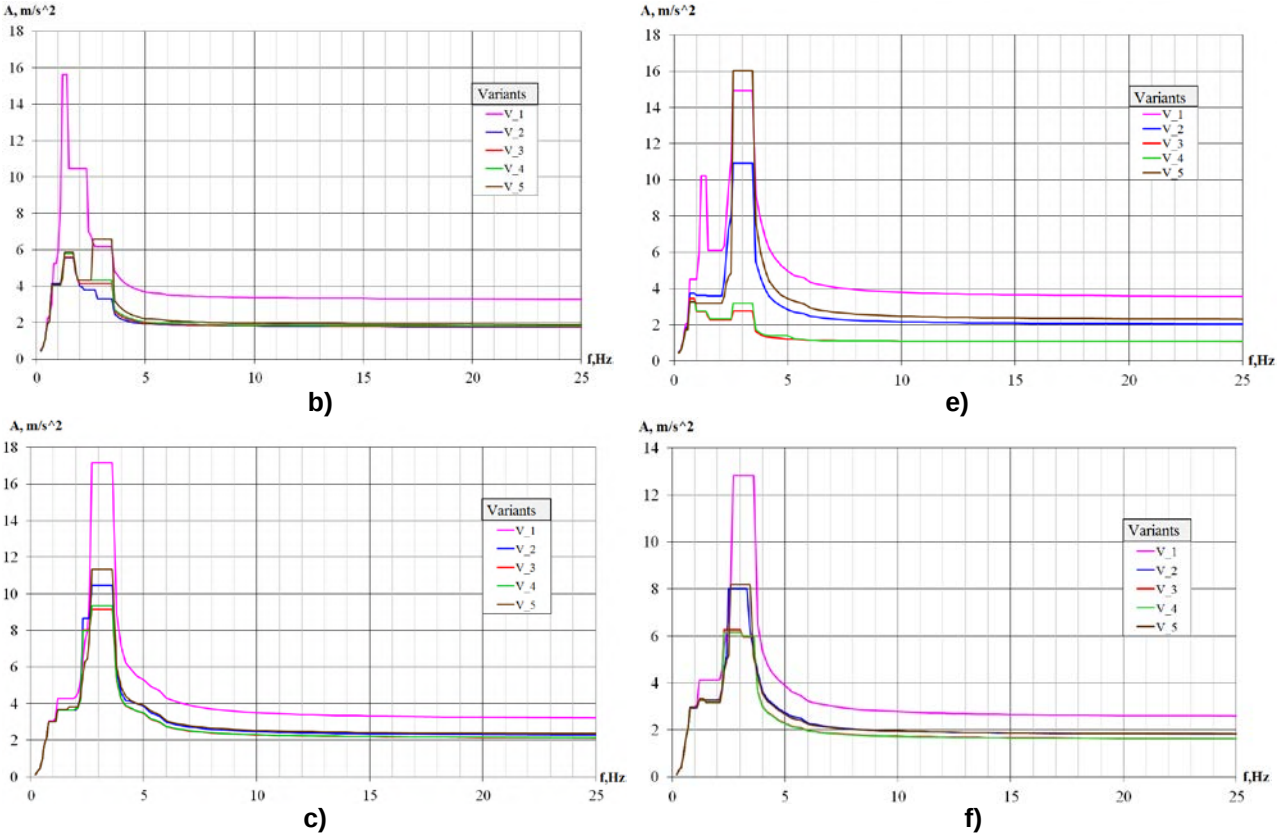

Figure 4. Graphic description of the results of the implementation of simulation experiments in terms of the averaged spectrum of the response of seismic accelerations:
a) at the installation marks of the turbine unit, axial direction;
b) at the installation marks of the turbine unit, transverse direction;
c) at the installation marks of the turbine unit, vertical direction;
d) at the installation marks of the capacitors, axial direction;
e) at the installation marks of the capacitors, transverse direction;
f) at the installation marks of the capacitors, vertical direction.

Based on the results presented in Table 4, it was concluded that option 4 of the design solution for protecting process equipment from seismic effects is most preferred, since the highest value of the generalized efficiency indicator corresponds to this option. The next preferred option is option 3, since the corresponding value of the generalized performance indicator is slightly less than the value of the same indicator for option 4. Moreover, from the point of view of a direct analysis of the results of computational experiments, these options provide a decrease at the installation marks of the capacitors of both peak seismic accelerations and zero period acceleration by more than 2 times, and the extreme values of deformations – by 2-4 times in comparison with the basic version 1 of the design solution. At the same time, at the installation marks of the turbine unit for the indicated design options, the peak seismic accelerations decrease by 4–5 times, the zero period acceleration – by about 3 times, and the largest deformations – by more than 5 times in comparison with the basic version 1.

It is important to note that the results obtained in the framework of the implementation of the proposed procedure on a practical example, in general, correspond to real data for the designs of vibration-insulated foundations of turbine units of power plants with a rigid connection of capacitors to the turbine unit (from the bottom, the capacitors are mounted on spring insulators to compensate for temperature deformations) – relevant examples are high-speed turbine units of the K-1000 and K-1200 models manufactured at the Leningrad Metal Plant (LMP). This circumstance allowed us to conclude that the proposed tool is highly practical.

Based on the comprehensive literature review presented in introduction, we see that there are no publications with methodological recommendations for calculating and designing earthquake-resistant vibroisolated foundations of turbine units.

There are also no articles with numerical results for calculating the vibration-isolated foundations of turbine units.

General conclusions based on the results of seismic calculations are in good agreement with the conclusions obtained in studies on the seismic isolation of buildings and structures of nuclear power plants [3–21].

Table 4. The results of the calculation of the values of the generalized performance indicator for alternatives of constructive solutions.

№ in order	Name of design characteristic			Value for design option (i)					Significance factor
				1	2	3	4	5	
j	-			$q_{i=1,j}$	$q_{i=2,j}$	$q_{i=3,j}$	$q_{i=4,j}$	$q_{i=5,j}$	α_j
1	Normalized peak acceleration at the turbine unit installation marks, axial direction			1	0,47	0,42	0,41	0,43	0,056
2	Normalized peak acceleration at the turbine unit installation marks, transverse direction			1	0,36	0,36	0,37	0,38	0,056
3	Normalized peak acceleration at the turbine unit installation marks, vertical direction			1	0,61	0,53	0,54	0,66	0,056
4	Normalized zero period acceleration at turbine unit installation marks, axial direction			1	0,51	0,49	0,47	0,51	0,056
5	Normalized zero period acceleration at turbine unit installation marks, transverse direction			1	0,54	0,54	0,56	0,58	0,056
6	Normalized zero period acceleration at turbine unit installation marks, vertical direction			1	0,71	0,66	0,66	0,73	0,056
7	Normalized largest value of deformation at the turbine unit installation marks, axial direction			1	0,49	0,3	0,19	0,22	0,056
8	Normalized largest value of deformation at the turbine unit installation marks, transverse direction			1	0,31	0,19	0,12	0,22	0,056
9	Normalized largest value of deformation at the turbine unit installation marks, vertical direction			1	0,33	0,29	0,31	0,39	0,056
10	Normalized peak acceleration at capacitor installation marks, axial direction			1	0,62	0,18	0,18	0,44	0,056
11	Normalized peak acceleration at capacitor installation marks, transverse direction			1	0,35	0,26	0,27	0,31	0,056
12	Normalized peak acceleration at capacitor installation marks, vertical direction			1	0,62	0,49	0,48	0,64	0,056
13	Normalized zero period acceleration at capacitor installation marks, axial direction			1	0,56	0,34	0,33	0,45	0,056
14	Normalized zero period acceleration at capacitor installation marks, transverse direction			1	0,57	0,3	0,3	0,64	0,056
15	Normalized zero period acceleration at capacitor installation marks, vertical direction			1	0,7	0,63	0,63	0,71	0,056
16	Normalized largest strain value at capacitor installation marks, axial direction			1	0,48	0,41	0,39	0,4	0,056
17	Normalized largest strain value at capacitor installation marks, transverse direction			1	0,26	0,23	0,22	0,24	0,056
18	Normalized largest strain value at capacitor installation marks, vertical direction			1	0,32	0,36	0,35	0,43	0,056
	Generalized indicator of the effectiveness of a constructive solution	Q_i	-	0	0,823	0,977	**0,991**	0,846	

4. Conclusion

As part of the study, the following main results were obtained:

1. The procedure for substantiating the characteristics of structural solutions in the field of protecting vibroisolated foundations of turbine units from seismic influences is proposed;

2. The specified procedure was implemented to solve a practical problem – substantiating the characteristics of the constructive solution of the vibroisolated foundation of the turbine unit. Alternative options are considered, the most preferred option is selected. This option involves the installation of spring insulators of increased stiffness and dampers in the capacitor supports, as well as the installation of spring and spring-damper insulators in the foundation supports of the turbine unit;

3. The certain preferred embodiment of the vibroisolated foundation of the turbine unit allows to reduce seismic acceleration on capacitors by more than 2 times and reduce horizontal seismic movements of capacitors by more than 3 times, compared with existing options.

At further stages of the study, it is planned to improve the developed procedure for calculating and designing earthquake-resistant vibroisolated foundations of turbine units in terms of classifying the corresponding tasks and a more detailed description of the structural features of complex and computational models.

5. Acknowledgments

We express our special gratitude for the assistance in carrying out this study to the chief specialist on the dynamics of the structures of the Construction Department of JSC ATOMPROEKT Babskiy Alexander.

References

1. Smirnov, V.I. Seysmoizolyatsiya -innovatsionnaya tekhnologiya zashchity vysotnykh zdaniy ot zemletryaseniy v Rossii i za rubezhom [Seismic isolation – an innovative technology for protecting high-rise buildings from earthquakes in Russia and abroad]. Sb.80 let TsNIISK im. V.A.Kucherenko. 2007. Pp. 24–32. (rus)
2. Smirnov, V.I. Sovremennaya zashchita ot zemletryaseniy[Modern protection against earthquakes]. High rise buildings. 2008. No. 4. Pp. 110–115. (rus)
3. Hiraki, T., Nagata, S., Kanazawa, K., Imaoka, T., Nakayama, T., Umeki, Y., Jimbo, M., Shimizu, H. Development of an evaluation method for seismic isolation systems of nuclear power facilities (Part 9), ultimate properties of full-scale lead rubber bearings based on breaking test. American Society of Mechanical Engineers, Pressure Vessels and Piping Division (Publication) PVP. 2014. DOI: 10.1115/PVP2014-29001
4. Chen, J., Zhao, C., Xu, Q., Yuan, C. Seismic analysis and evaluation of the base isolation system in AP1000 NI under SSE loading. Nuclear Engineering and Design. 2014. No. 278. Pp. 117–133. DOI: 10.1016/j.nucengdes.2014.07.030
5. Kumar, M., Whittaker, A.S., Constantinou, M.C. An advanced numerical model of elastomeric seismic isolation bearings. Earthquake Engineering and Structural Dynamics. 2014. No. 43(13). Pp. 1955–1974. DOI: 10.1002/eqe.2431
6. Kumar, M., Whittaker, A.S., Constantinou, M.C. Extreme earthquake response of nuclear power plants isolated using sliding bearings. Nuclear Engineering and Design. 2017. No. 316. Pp. 9–25. DOI: 10.1016/j.nucengdes.2017.02.030
7. Kumar, M., Whittaker, A.S., Constantinou, M.C. Seismic isolation of nuclear power plants using elastomeric bearings. Technical Report MCEER-15-0006. 2015.
8. Medel-Vera, C., Ji, T. Seismic protection technology for nuclear power plants: A systematic review. Journal of Nuclear Science and Technology. 2015. DOI: 10.1080/00223131.2014.980347
9. Politopoulos, I., Sergis, I., Wang, F. Floor response spectra of a partially embedded seismically isolated nuclear plant. Soil Dynamics and Earthquake Engineering. 2015. No. 78. Pp. 213–217. DOI: 10.1016/j.soildyn.2015.06.017
10. Sayed, M.A., Go, S., Cho, S.G., Kim, D. Seismic responses of base-isolated nuclear power plant structures considering spatially varying ground motions. Structural Engineering and Mechanics. 2015. No. 54(1). Pp. 169–188. DOI: 10.129-89/sem.2015.54.1.169
11. Salimi Firoozabad, E., Jeon, B.G., Choi, H.S., Kim, N.S. Seismic fragility analysis of seismically isolated nuclear power plants piping system. Nuclear Engineering and Design. 2015. No. 284. Pp. 264–279. DOI: 10.1016/j.nucengdes.2014.12.012
12. Zhou, Z., Wong, J., Mahin, S. Potentiality of Using Vertical and Three-Dimensional Isolation Systems in Nuclear Structures. Nuclear Engineering and Technology. 2016. No. 48(5). Pp. 1237–1251. DOI: 10.1016/j.net.2016.03.005
13. Kostarev, V.V., Petrenko, A.V., Vasilyev, P.S. An advanced seismic analysis of an NPP powerful turbogenerator on an isolation pedestal. Nuclear Engineering and Design. 2007. No. 237(12). Pp. 1315–1324. DOI: 10.1016/j.nucengdes.2006.10.004
14. Chasalevris, A. Stability and Hopf bifurcations in rotor-bearing-foundation systems of turbines and generators. Tribology International. 2020. DOI: 10.1016/j.triboint.2019.106154
15. Yang, Y., Bashir, M., Li, C., Wang, J. Analysis of seismic behaviour of an offshore wind turbine with a flexible foundation. Ocean Engineering. 2019. DOI: 10.1016/j.oceaneng.2019.02.077
16. Wang, P., Zhao, M., Du, X., Liu, J., Xu, C. Wind, wave and earthquake responses of offshore wind turbine on monopile foundation in clay. Soil Dynamics and Earthquake Engineering. 2018. DOI: 10.1016/j.soildyn.2018.04.028
17. Anand, V., Satish Kumar, S.R. Seismic Soil-structure Interaction: A State-of-the-Art Review. Structures. 2018. DOI: 10.1016/j.istruc.2018.10.009
18. Najafijozani, M., Becker, T.C., Konstantinidis, D. Evaluating adaptive vertical seismic isolation for equipment in nuclear power plants. Nuclear Engineering and Design. 2020. DOI: 10.1016/j.nucengdes.2019.110399
19. Yu, C.C., Bolisetti, C., Coleman, J.L., Kosbab, B., Whittaker, A.S. Using seismic isolation to reduce risk and capital cost of safety-related nuclear structures. Nuclear Engineering and Design. 2018. DOI: 10.1016/j.nucengdes.2017.11.016

20. Jeong, Y.S., Baek, E.R., Jeon, B.G., Chang, S.J., Park, D.U. Seismic performance of emergency diesel generator for high frequency motions. Nuclear Engineering and Technology. 2019. DOI: 10.1016/j.net.2019.03.012
21. Sargsyan, A.Ye. Dinamika i seysmostoykost sooruzheniy atomnykh stantsiy [Dynamics and seismic resistance of nuclear power plants]. Sarov: Izd-vo FGUP «RFYaTs VNIIEF», 2013. 550 p. (rus)
22. Chernukha, N.A., Lalin, V.V., Birbrayer, A.N. Veroyatnostnoye obosnovaniye dinamicheskikh nagruzok na oborudovaniye AES pri udare samoleta [Probabilistic justification of dynamic loads on npp equipment caused by aircraft impact]. St. Petersburg Polytechnic University Journal of Engineering Science and Technology. 2017. T. 23. No. 4. Pp. 159–171. DOI: 10.18721/jest.230416. (rus)
23. Turilov, V.V., Utkin, I.A. Primeneniye metoda modalnoy superpozitsii v neklassicheskoy forme dlya resheniya zadach vzaimodeystviya zdaniy i sooruzheniy AES s gruntovym osnovaniyem pri seysmicheskikh vozdeystviyakh [The use of the method of modal superposition in non-classical form to solve the problems of the interaction of buildings and structures of a nuclear power plant with a soil base under seismic effects]. Earthquake-resistant construction. Safety of structures. 2017. No. 2. Pp. 30–35. (rus)
24. Tyapin, A.G., Naumkin, A.V. Proyektnoye i maksimalnoye raschetnyye seysmicheskiye vozdeystviya: normalnoye i anomalnoye sootnosheniya [Design and maximum design seismic effects: normal and abnormal relationships]. Earthquake-resistant construction. Safety of structures. 2019. No. 2. Pp. 9–15. (rus)
25. Belash, T.A., Astafyeva, A.V. Ispolzovaniye seysmoizolyatsii pod kompleksami ryadom stoyashchikh zdaniy [Use of seismic isolation under complexes of adjacent buildings]. Earthquake-resistant construction. Safety of structures. 2019. No. 3. Pp. 17–21. (rus)
26. Muravyeva, L., Vatin, N. Risk assessment for a main pipeline under severe soil conditions on exposure to seismic forces. Applied Mechanics and Materials. 2014. No. 635. Pp. 468–471. DOI: 10.4028/www.scientific.net/AMM.635-637.468
27. Tarasov, V.A., Baranovskiy, M.Yu., Redkin, A.V., Sokolov, Ye.A., Stepanov, A.S. Sistemy seysmoizolyatsii [Seismic isolation systems]. Construction of Unique Buildings and Structures. 2016. No. 43(4). Pp. 117–140. (rus)
28. Tarasov, V.A., Baranovskiy, M.Yu., Pavlushkina, Yu.Ye., Meleshchenkov, L.S., Shakirov, R.M., Imeskenov, T.L., Zagidullina, E.G. Sravneniye rezultatov seysmicheskogo rascheta po SNiP II-7-81* 1995 goda i po SP 14.13330.2014 [Comparison of the results of seismic calculation according to SNiP II-7-81* 1995 and SP 14.13330.2014]. Construction of Unique Buildings and Structures. 2015. No. 28(1). Pp. 52–73. (rus)
29. Dražić, J., Vatin, N. The Influence of Configuration on to the Seismic Resistance of a Building. Procedia Engineering. 2016. No. 165. Pp. 883–890. DOI: 10.1016/j.proeng.2016.11.788
30. Vatin, N.I., Ivanov, A.Y., Rutman, Y.L., Chernogorskiy, S.A., Shvetsov, K.V. Earthquake engineering optimization of structures by economic criterion. Magazine of Civil Engineering. 2017. 76(8). Pp. 67–83. DOI: 10.18720/MCE.76.7

Contacts:

Vladimir Tarasov, vtarasov1000@yandex.ru

Vladimir Lalin, vllalin@yandex.ru

Anton Radaev, TW-inc@yandex.ru

Alexey Mentishinov, Mentishinov@yandex.ru

© Tarasov, V., Lalin, V.V., Radaev, A.E., Mentishinov, A., 2021

Magazine of Civil Engineering

ISSN 2712-8172

journal homepage: http://engstroy.spbstu.ru/

DOI: 10.34910/MCE.102.6

Structure and properties of mortar printed on a 3D printer

R.Kh. Mukhametrakhimov*, L.V. Lukmanova
Kazan State University of Architecture and Engineering, Kazan, Russia
**E-mail: muhametrahimov@mail.ru*

Keywords: concretes, cements, mortar, 3D printing, extrusion, additive manufacturing, 3DCP

Abstract. The influence of the molding process of sand-cement mortar printed on a 3D printer on its structure and properties is investigated. The mortar mix was characterized by a mobility P_k = 2, which corresponds to an immersion depth of the etalon cone of 5 cm. Determination of compressive strength was carried out on standard samples of beams with dimensions of 40×40×160 mm by loading them on a press in pure compression mode. Water absorption was defined as the ratio of the difference between the mass of a water-saturated sample and the mass of a dried sample to the mass of a dried sample. The porosity of the hardened mortar samples was determined by the results of determining their density, water absorption and sorption moisture. Defects of the sand-cement mortar mix and hardened composites, formed by the extrusion (3D printing), were determined by the visual and instrumental methods using a measuring metal rule. It is shown that the raw mixes currently used (similar to accepted in experimental studies) are not adapted for their extrusion (3D printing), as reflected in the appearance of various defects – different layer thicknesses, crushing of the underlying layers, cracks, skew of the mixture, inhomogeneous structure of the hardened composite, mix spreadability, high porosity. It was found that the molding of the studied sand-cement mortar by the extrusion (3D printing) leads to increased total pore volume by 10 %, open capillary pore volume by 22 %, conditionally closed pore volume by 9 %, microporosity by 8 %, reduction in open non-capillary volume by 65 % compared to the traditional injection molding samples of a similar composition with further compaction. This leads to a decrease in compressive strength by half compared with the injection molding method with further compaction, and an increase in water absorption by 22 %. Based on the results, the directions of improving the raw mixes for 3D printing are determined.

1. Introduction

There is a quick growth of additive manufacturing market in different areas of human activities at the present time. In 2018 market volume exceeded $5 billion, in 2025 projected market volume will be more $21 billion (Fig. 1). It should be noted that more than 50 % of the global additive manufacturing market is controlled by such countries as the USA, Germany, Great Britain, Japan, etc. In the long-term perspective it defines them as leaders in the development of this technology. While addressing manufacturers of equipment for additive manufacturing, the following leading companies should be highlighted: 3D Systems (USA), EOS Gmbh (Germany), SLM Solutions (Germany), Stratasys (USA), ObjectGeometries (USA-Israel), Envisiontec (USA-Germany (DLP), ExOne (USA), Voxeljet (Germany), Arcam AB (Sweden).

Considering the market of 3D construction printing, it should be noted that the largest market share in terms of cost and volume is 3D printing by the extrusion, the volume of which can grow to $56.4 million by 2021 [2].

This technology allows to create (grow) objects by layer-by-layer deposition (extrusion) of the raw material mix in accordance with a three-dimensional digital model [3], [4]. The essence of this method is to extrude a construction mix (sand-cement mortar, fine-grained concrete, gypsum, gypsum-cement-pozzolanic mixtures, etc.) with various mineral, chemical additives and reinforcing fibers through a ‘nozzle’ or an extruder of a 3D printer [5–8]. Each next layer is laid on top of the previous one, which results in a certain structure.

Concrete extrusion can be carried out by various types of 3D printers: portal, with a delta drive working in angular coordinates, based on industrial manipulators [5, 9, 10].

Mukhametrakhimov, R.Kh., Lukmanova, L.V. Structure and properties of mortar printed on a 3D printer. Magazine of Civil Engineering. 2021. 102(2). Article No. 10206. DOI: 10.34910/MCE.102.6

This work is licensed under a CC BY-NC 4.0

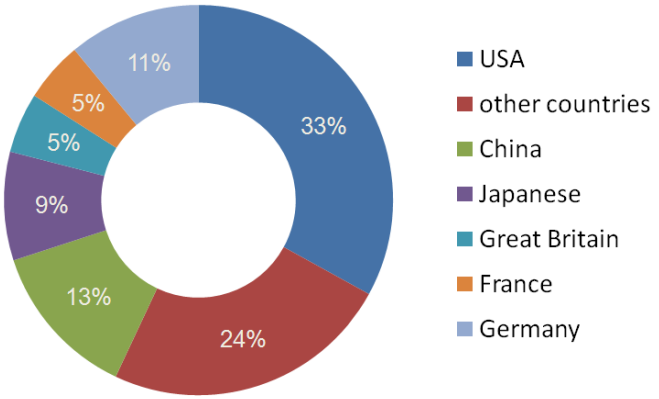

Figure 1. Forecast of the additive manufacturing market structure by 2025 by region. The 'other countries' segment includes India, Latin America, Russia, Australia, Sweden, Italy, Belgium, Spain and the Netherlands [1].

An analysis of the world experience of existing technological solutions for 3D printing in construction performed in [11] made it possible to identify organizations implementing 3D printing technology in construction – 'WinSun' (China), OOO 'SPECAVIA' (Russia), 'ApisCor' (Russia), 'StroyBot' (Rudenko 3D Printer), 'BetAbram' (Slovenia), 'Contour Crafting Corp.' (USA), 'MIT Media Lab' (USA), Loughborough University (Great Britain), 'CyBe Construction' (Holland), 'DUS Architects' (Holland), 'Batiprint 3D' (France), as well as recommendations for concrete mixes used and characteristics of composites based on them. For example, the width of the layer of the extrudable raw mix of different types of 3D printers varies in the range of 20–60 mm, the thickness is 10-40 mm, the average density is 2000–2350 kg/m^3, the bending strength is 6–13 MPa, and the compressive strength is 27.4–110 MPa. It should be noted that the indicators of the properties of construction mixes and hardened compositions based on them, claimed by the listed companies, are often promotional references and they are not always the result of scientific research or certified tests, which does not allow to use these data in the planning of scientific research. The tests performed on some of the proposed compositions in laboratory conditions using a 3D printer confirm this assumption.

An analysis of the quality of construction products printed on a 3D printer shows that the concrete mixes currently used (mainly fine grains) are not adapted for use in extrusion technology (3D printing), which is reflected in the disruption of the geometrical dimensions of the products due to spreading of the underlying layers ruptures, voids and fractures, low crack resistance, high shrinkage deformations, low adhesion of layers caused by not optimal compositions and rheological and technological properties of the mixes, which leads to reduced physical and mechanical characteristics and durability of the products on their basis (Fig. 2-4).

a) b)

Figure 2. Typical 3D printing defects on the example of a residential building by Alex Le Roux (USA) [12]: a), b) disruption of the geometrical dimensions due to spreading of the underlying layers, poor adhesion of the layers.

a) b)

Figure 3. Typical 3D printing defects on the example of residential building by 'Tengda' (China) [12]: a), b) disruption of the geometrical dimensions due to spreading of the underlying layers, surface heterogeneity.

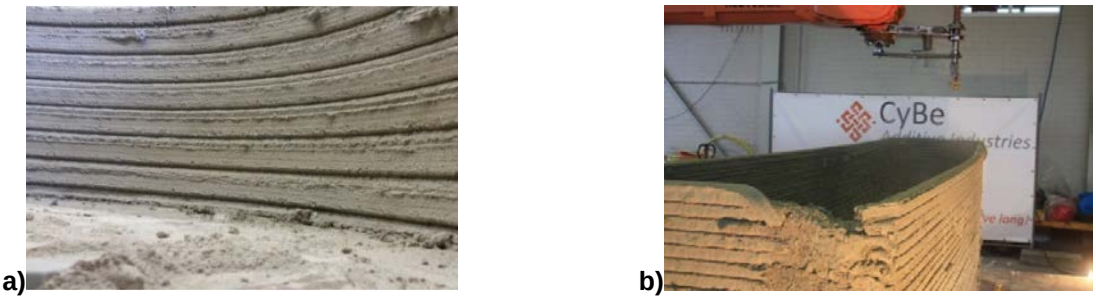

Figure 4. Typical 3D printing defects on the example of concrete wall by 'CyBe Additive Industries' (Holland) [13]: a) disruption of the geometrical dimensions, concrete flows b) destruction of the concrete product due to the low structural strength of the concrete mix.

Molding process furthermore can directly influence on the quality of the molded products along with a composition of the concrete mix. Distinctive features of concrete molding by extrusion from the widely used injection molding method is the absence of formwork (form) resulting in significant open surface module of product and difficulties in curing of concrete; the absence of a technological stage aimed at compaction of the molded concrete mix after its extrusion, difficulties in realizing a full-fledged traditional core reinforcement using flat grids, volume frames, etc. (although there are some positive results in this area [14–17]).

As a result of our experimental studies and literature data, the main requirements for concrete mixtures in additive manufacturing based on operational, prescription and technological factors were identified. It should be noted that this is consistent with the results. At the stage of molding and hardening the mix, the main requirements should include: rheological and technological properties [18, 19] (formability or workability, the ability to transport through pipes, plastic strength [20], thixotropy), dispersion, adhesive properties (tight adhesion of the layers), the absence of fractures of the mixture, the absence of cracking, low shrinkage, uniformity hardening (setting), high setting rate after extrusion. The finished products are required to provide the necessary strength, high uniformity and stability of properties, low density and thermal conductivity, high adhesion strength, frost resistance [21]. M.Y. Elisrtatkin at al. [22] established links between the process factors and properties of molding components; principles of their practical implementation are proposed.

There are a number of works aimed at developing new compositions of raw mixes adapted for the 3D printing by extrusion, as well as methods for controlling their properties [23]. G.S. Slavcheva at al. [24, 25] established that the W/C-ratio defining the concentration of solid phase particles in the system is the main factor of structuring and strengthening of cement paste for 3D construction printing. R.A. Buswell at al. [26] explored the relationship between raw material mix and geometry of the created hardened composite (mortar and concrete). Based on the obtained data, a matrix of issues has been created that identifies the spectrum of future research exploration in this emerging field. Y. Zhang at al. [27] propose to use recycled pieces of glass as a fine aggregate, which makes it possible to control the rheological parameters of the mixture, thus introducing them into the composition increases the mobility of the mix, however, the strength of products made from such concrete is lower compared to conventional concrete.

An alternative way to improve the rheological properties of concrete mixtures for 3D printing is to use active mineral and chemical additives [28, 29]. To reduce the rate of setting concrete mix, authors [30] proposed ultrasonic activation of the binder during the hydration process in the pre-induction period, during which a larger number of ettringite crystals is created, which can significantly increase the speed of 3D printing, while the concrete strength reaches approximately 1 MPa within 20 minutes. In another work [21], to reduce the setting time, it is proposed to introduce a solution of sodium silicate in the amount of 5 and 8 % into the formulation of the raw material mix, which allows reducing the setting time from 90 minutes to 20 and 12 minutes, respectively. To reduce the shrinkage deformation of concrete, the authors [31] propose using silica fume together with a plasticizing additive.

To solve the problems of low strength and fracture toughness of products obtained on a 3D printer by the extrusion, it is proposed to use dispersed reinforcement with various types of fibers: polyvinyl [32, 33], polyethylene [34], polypropylene [35, 36], glass [37], basalt [38]. The introduction of polypropylene fibers in an amount of 1 % [36] has a positive effect on a decrease in the spreadability of printed samples (of seven layers) upon application of a vertical load, which is associated with an increase in the compressive strength of composites to 31 %.

P. Lubin at al. [39] proposed replacing cement paste with clay soil up to 25 %, which leads to a reduction in cost and an increase in printability on a 3D printer with a slight decrease in the strength of the material to 7 %.

One of the ways to control the structure formation of building composites is the use of nanomodifying additives [40–42], including creating construction products using 3D printing [43, 44].

There is no study comparing the properties of building mixtures from the molding method, the influence of 3D printing technology on the appearance of defects and damages, the causes of their occurrence in many works. Solution of these problems allows to determine the main directions of development and optimization of concrete raw mixes adapted for 3D printing, which ultimately will lead to high-quality construction products.

The purpose of this study is to examine the impact of the molding process of a raw mix not adapted for 3D printing on the example of a sand-cement mortar on its structure and properties during the injection method with compaction and extrusion without compaction (3D printing) and, based on the results, to determine directions for improving compositions raw mixes for 3D printing.

2. Materials and Methods

The studies were carried out in the laboratory of additive manufacturing in construction (Kazan State University of Architecture and Engineering, Russia).

The process of creating a sample by extrusion (3D printing) included the following sequence of technological operations:

1. Development of object digital three-dimensional model in ‘AutoCad’ (Autodesk, Inc.);
2. Division of the model into layers in cross section in ‘Sheet Cam’ (Stable Design);
3. Translation the model into G-code, which allows to simulate, generate codes and control a 3D printer by Mach3 (Artsoft founder Art Fenerty);
4. Preparation of a raw mix with specified properties;
5. Transfer of the developed code to the print head-extruder;
6. Extrusion of the raw mix in accordance with a specified digital three-dimensional model;
7. Curing of the raw mix material;
8. Secondary processing: removal of the supporting structure (substrate).

The sample was formed from a sand-cement mix by extrusion in workshop 3D printer ‘AMT S-6044’ OOO ‘SPETSAVIA’ (Yaroslavl, Russia), organized by a portal system (Fig. 5), in accordance with a specified digital three-dimensional model (G-code). Technical specifications of 3D printer ‘AMT-S-6044’ are shown in Table 1.

Table 1. Technical specifications of 3D printer ‘AMT-S-6044’.

Length, mm	4000
Width, mm	4000
Height, mm	2800
Weight, kg	870
Producer	OOO ‘SPETSAVIA’
Manufacturing country	Russia. The equipment is certified in the territory of the Customs Union
Type of drive	Stepper motors with parallel-shaft
Type	S Series Small-format Portal Construction 3D Printer
Assignment	Printing of building elements up to 12.6 m^2, hardscape elements, street furniture, architectural decor, reinforced concrete products. The printer is intended for installation in the workshop
Productivity, m^3/h	0.6
Operational zone, mm	3500×3600×1000
Working power, кВт	1.6
Print layer size, mm (height, width)	10×30

The following materials were used in the research process:

a) sand-cement mix (manufacturer Samara gypsum plant) complying with GOST 28013-98 (Russian standard);

b) modifying additives:

- comprehensive additive ‘Cemfix’ superplasticizer-hardening accelerator based on polymethylene naphthalene sulfonates (C-3) and inorganic sodium salts (‘Cemmix’), conforming to TU 2499-007-90557835-2014;

c) polypropylene fibers with a length of 12 mm (VSM-II), conforming to TU 5458-001-82255741-2008. Technical specifications are shown in Table 2;

d) tap drinking water complying with GOST 23732-2011 (Russian standard).

Table 2. Technical specifications of polypropylene fibers 'VSM-II'.

Name	Index
Fiber diameter, μm	20
Fiber lenght, mm	12
Tensible strength, MPa	550
Lengthening	20 %
Elastic modulus, MPa	no less than 10000
Number of single fiber, million pieces/kg	510-550
Surface fiber area, m^2/kg	150
Temperature of fusion, °C	160

Mixing of the components of the raw materials was carried out in a cyclic concrete mixer 'CMI 46' for 5 minutes 30 seconds until homogeneous mass was obtained.

The mortar mix was characterized by the mobility P_k = 2 conforming to GOST 28013-98 (Russian standard), which corresponds to immersion depth of the etalon cone of 5 cm. The mobility of the mortar mixture was determined to GOST 5802-86 (Russian standard).

Defects of the sand-cement mortar mix and hardened composites based on it, formed by extrusion (3D printing), were determined by the visual and instrumental methods using a measuring metal rule.

Samples were formed in two ways: extrusion without mold (formwork) and compaction of the mix (3D printing) and injection molding with further compaction in the mold 40×40×160 mm.

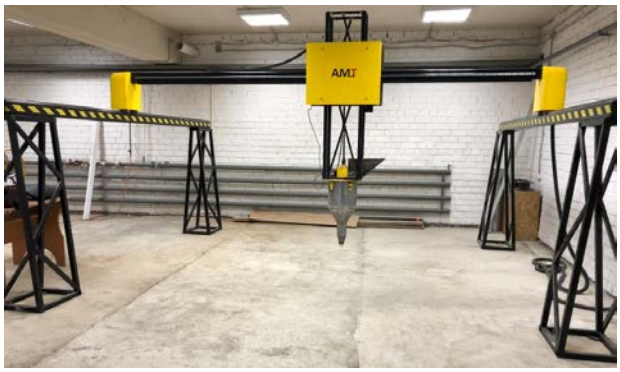

Figure 5. 3D printer 'AMT-S-6044' at the laboratory of additive manufacturing in construction (Kazan State University of Architecture and Engineering, Russia).

The samples were tested after hardening for 28 days in an air-moist environment. Determination of compressive strength was carried out on standard samples of beams with dimensions of 40×40×160 mm by loading them on a press in pure compression mode complying with GOST 310.4-81 (Russian standard).

Water absorption and density of the samples were evaluated according to GOST 5802-86 (Russian standard). Water absorption was defined as the ratio of the difference between the mass of a water-saturated sample and the mass of a dried sample to the mass of a dried sample.

The porosity of the samples of the hardened composite was determined by the results of determining their density, water absorption and sorption moisture according to GOST 12730.4-78 (Russian standard).

Figure 6. 3D concrete printing process.

3. Results and Discussion

According to the results of the first stage of experimental studies, it was found that the molding process of raw mix affects the pore structure parameters and the character of the pore distribution.

Table 3. Effect of molding process on pore structure sand-cement composite.

Molding process	Total pore volume	Volume of open capillary pores	Volume of open non-capillary pores	Volume of conditionally closed pores	Microporosity
Injection molding with further compaction in the mold	30.36	8.38	1.50	20.48	0.85
Extrusion without mold and compaction (3D printing)	33.53	10.24	0.97	22.39	0.92

As can be seen from Table 3, molding process of raw mix affects the pore structure parameters and the character of the pore distribution. Thus, the extrusion molding process (3D printing) leads to an increase in total pore volume by 10 %, volume of open capillary pores – 22 %, volume of conditionally closed pores – 9 %, microporosity – 8 % and it leads to decrease in volume of conditionally closed pores by 65 %.

At the second stage effect of molding process on compressive strength of specimens was investigated (Fig. 7).

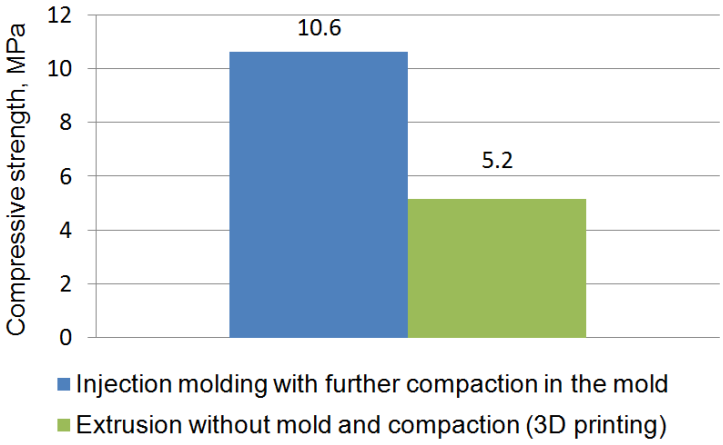

Figure 7. Effect of molding process on compressive strength of sand-cement composite.

As follows from Fig. 7, molding process of raw mix significantly affects the strength of sand-cement composite. Thus, compressive strength of sample formed by extrusion (3D printing) is 5 MPa, which is two times lower than sample formed by injection molding with further compaction. The low compressive strength of a sample formed by extrusion (3D printing) is primarily a consequence of the resulting pore structure of hardened composites, poor adhesion of the printed layers.

Water absorption of sand-cement mortar formed by extrusion (3D printing) and injection molding with further compaction is shown in Fig. 8.

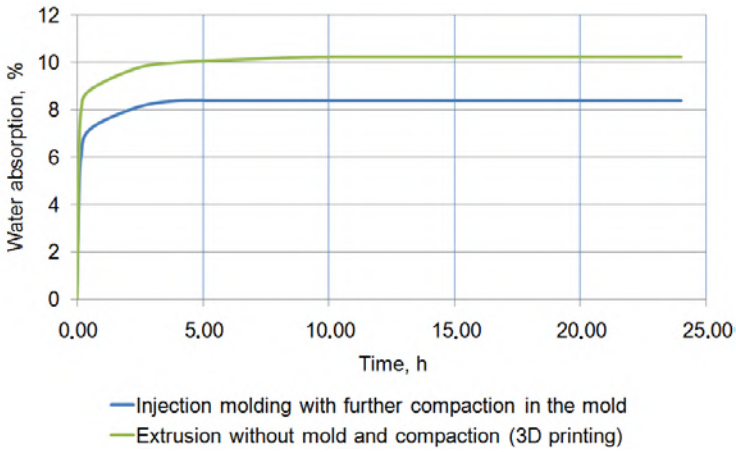

Figure 8. Effect of molding process on water absorption of sand-cement composite.

As follows from Fig. 8, specimen formed by extrusion (3D printing) has the highest water absorption – 10.2 % owing to high pore structure parameters of hardened composite.

In general, the obtained data on the average density of water absorption of cement mortars are consistent with the data presented in the research [45, 46].

The following defects and damages of specimens formed by extrusion (3D printing) were observed: different layer thickness, crushing of the underlying layers, cracks, skew of the mixture, inhomogeneous structure of the hardened composite, mix spreadability, high porosity. Some of the listed defects were also noted by the authors in the research [26].

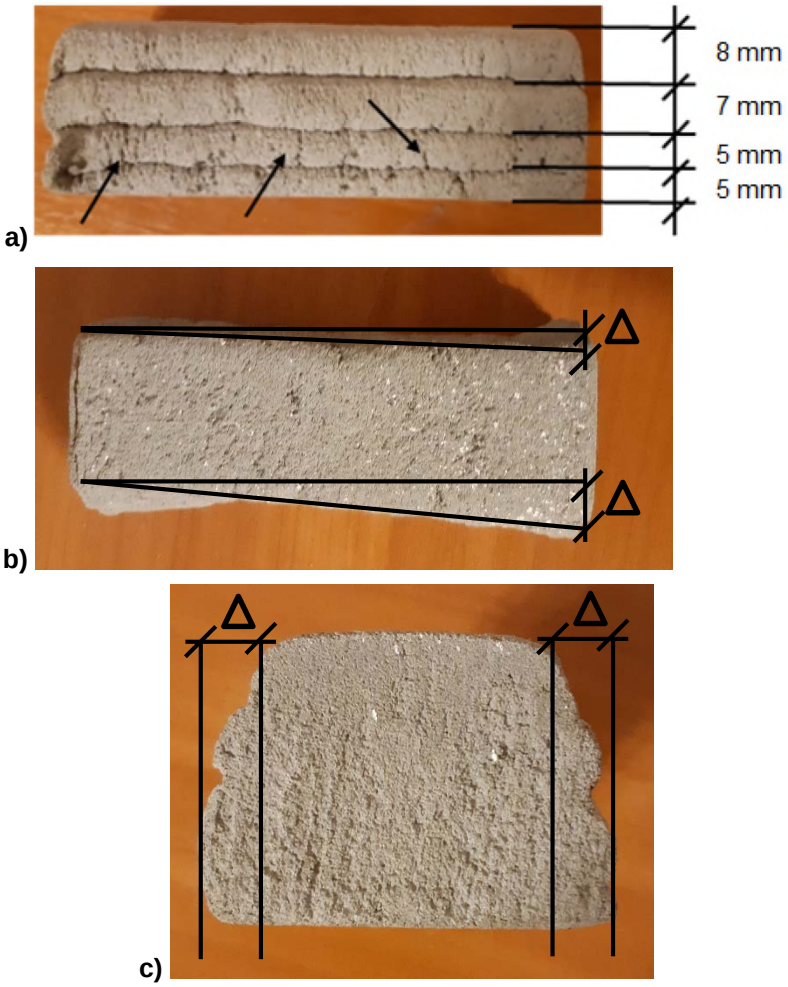

Figure 9. Defects of specimen formed by extrusion (3D printing):
a – different layer thickness (5-8 mm), crushing of the underlying layers, cracks;
b – skew of the mixture, inhomogeneous structure of the hardened composite;
c – mix spreadability, high porosity.

In accordance with the results, the main directions for improving the formulation of fine-grained concrete for extrusion (3D printing) are determined:

- imparting a denser and more uniform structure to fine-grained concrete mix, for example, by introducing the optimal type and amount of active and inert mineral additives;
- imparting required rheological properties to fine-grained concrete mix, accelerating the kinetics of the initial structure formation and hardening of the raw material mix and the strength properties of the hardened composite, for example, by introducing the optimal type and amount of plasticizing additive and hardening accelerator additive;
- imparting increased crack resistance and strength to fine-grained concrete, for example, by reinforcing with fibers of an optimal form and content;
- imparting increased water resistance, frost resistance and other indicators of durability to fine-grained concrete, for example, by introducing a water-repellent additive.

4. Conclusions

1. Concrete mixes currently used are not adapted for extrusion (3D printing), as reflected in the appearance of various defects – disruption of the geometrical dimensions due to spreading of the underlying layers ruptures, voids and fractures, low crack resistance, high shrinkage deformations, low adhesion of layers caused by not optimal compositions and rheological and technological properties of the mixes which leads to reduced physical and mechanical characteristics and durability of the products on their basis.

2. It has been established that the extrusion molding process (3D printing) of sand-cement mortar leads to an increase in total pore volume by 10 %, volume of open capillary pores – 22 %, volume of conditionally closed pores – 9 %, and microporosity – 8 %, and it leads to decrease in volume of conditionally closed pores by 65 % compared with the traditional injection molding with further compaction of samples of a similar formulation. This leads to a deterioration in the physical and mechanical characteristics and durability of 3D printing products.

3. It was revealed that the molding of a cement-sand mortar by extrusion (3D printing) leads to a decrease in compressive strength by half compared to the injection molding with further compaction, and an increase in water absorption by 22 %.

4. The results of research confirm that conventional (not adapted) compositions of raw mixes are not effective for use in 3D printing as “ink”, indicating the need for further theoretical and experimental studies on development of raw mixes, primarily based on fine-grained concrete, as the most effective and used in existing 3D printers for extrusion (3D printing).

5. The main directions of improving the composition of fine-grained concrete for extrusion (3D printing) are following: imparting a denser and more uniform structure, the required rheological and technological properties to fine-grained concrete mix, acceleration of the kinetics of the initial structure formation and hardening of the raw material mix and the strength properties of the hardened composite, increased crack resistance , increased water resistance, frost resistance and other indicators of durability, for example, by introducing optimum type and amount of active and inert mineral additives, chemical additives (plasticizing additives, hardening accelerator additives, water-repellent additives) into formulation, fiber reinforcement.

5. Acknowledgements

The authors gratefully acknowledge OOO ‘3D-Stroy’ for this work. This material is based upon work supported by the Council on grants of the President of the Russian Federation (SP-1051.2021.1).

References

1. Volostnov, A. Frost & Sullivan: tekhnologii additivnogo proizvodstva – rynok, tendentsii i perspektivy do 2025 goda [Volostnov, A. Frost & Sullivan: additive manufacturing technologies – market, trends and prospects until 2025] [Online]. URL: https://3dtoday.ru/blogs/news3dtoday/frost-sullivan-additive-manufacturing-technologies-market-trends-and-p/ (reference date: 30.03.2019). (rus)
2. Rynok 3D-pechati betona prevysit 56 millionov dollarov k 2021 godu [3D concrete printing market will exceed $ 56 million by 2021] [Online]. URL: https://www.3dpulse.ru/news/analitika/rynok-3d-pechati-betona-prevysit-56-millionov-dollarov-k-2021-godu/ (reference date: 29.01.2020). (rus)
3. Tay, Y.W.D., Panda, B., Paul, S.C., Noor Mohamed, N.A., Tan, M.J., Leong, K.F. 3D printing trends in building and construction industry: a review. Virtual and Physical Prototyping. 2017. 12(3). Pp. 261–276. DOI: 10.1080/17452759.2017.1326724
4. Tay, Y.W., Panda, B., Paul, S.C., Tan, M.J., Qian, S.Z., Leong, K.F., Chua, C.K. Processing and Properties of Construction Materials for 3D Printing. Materials Science Forum. 2016. Pp. 177–181. DOI: 10.4028/www.scientific.net/msf.861.177
5. Mukhametrakhimov, R.Kh., Vakhitov, I.M. Additivnaya tekhnologiya vozvedeniya zdaniy i sooruzheniy s primeneniyem stroitelnogo 3D-printera [Additive building technology using a 3D building printer]. Izvestiya KGASU. 2017. 4(42). Pp. 350–359. (rus)
6. Marchment, T., Sanjayan, J. Mesh reinforcing method for 3D Concrete Printing. Automation in Construction. 2020. 109(June 2019). Pp. 102992. DOI: 10.1016/j.autcon.2019.102992. URL: https://doi.org/10.1016/j.autcon.2019.102992
7. Lim, J.H., Weng, Y., Pham, Q.C. 3D printing of curved concrete surfaces using Adaptable Membrane Formwork. Construction and Building Materials. 2020. 232. Pp. 117075. DOI: 10.1016/j.conbuildmat.2019.117075
8. Vantyghem, G., De Corte, W., Shakour, E., Amir, O. 3D printing of a post-tensioned concrete girder designed by topology optimization. Automation in Construction. 2020. 112. Pp. 103084. DOI: 10.1016/j.autcon.2020.103084
9. Mustafin, N.Sh., Baryshnikov, A.A. Noveyshiye tekhnologii v stroitelstve. 3D printer [The latest technology in construction. 3D printer] [Online]. URL: https://elibrary.ru/item.asp?id=25732171 (date of application: 25.11.2018). (rus)
10. Vatin, N., Chumadova, L., Goncharov, I., Zykova, V., Karpenya, A., Kim, A., Finashenkov, E. 3D printing in construction. Construction of Unique Buildings and Structures, 2017, 1 (52), Pp. 27–46. (rus)
11. Inozemtsev, A.S., Korolev, Ye.V., Zyong Tkhan Kuy. Analiz sushchestvuyushchikh tekhnologicheskikh resheniy 3D-pechati v stroitelstve [Analysis of existing 3D printing technology solutions in construction] Vestnik MGSU. 2018. 7(118). Pp. 863–876. DOI: 10.22227/1997-0935.2018.7.863-876. (rus)
12. 10 zdaniy, napechatannykh na 3D-printere [10 buildings printed on a 3D printer] [Online]. URL: https://www.3dpulse.ru/news/stroitelstvo/10-zdanii-napechatannyh-na-3d-printere/ (reference date: 28.01.2020). (rus)
13. Novyy gollandskiy robotizirovannyy 3D-printer pechatayet steny iz «zelenogo» betona [New Dutch 3D robotic printer prints green concrete walls] [Online]. URL: https://www.vzavtra.net/stroitelnye-texnologii/novyj-gollandskij-robotizirovannyj-3d-printer-pechataet-steny-iz-zelenogo-betona.html (reference date: 28.01.2020). (rus)
14. Lukmanova, L.V., Mukhametrakhimov, R.Kh. Mnogosloynaya naruzhnaya stena zdaniya, izgotovlennaya na 3D printere [3D multilayer exterior wall of a building]. Patent Russia no.193776. (rus)

15. Reinforcement method of concrete shear wall based on 3D printing. Patent CN 106013529 A. 2016.
16. Middle section structure of flexible house and for 3D (three dimensional) printing. Patent CN 203654462 U. 2014.
17. Zhislen, G.L.-A.K., Orifovich, Ye.T. Sposob vozvedeniya betonnoy steny, rabochiy organ stroitelnogo 3d-printera i stena betonnaya [The method of construction of a concrete wall, the working body of a building 3d printer and a concrete wall]. Patent Russia no.2704995. (rus)
18. Jayathilakage, R., Rajeev, P., Sanjayan, J. Yield stress criteria to assess the buildability of 3D concrete printing. Construction and Building Materials. 2020. 240. Pp. 117989. DOI: 10.1016/j.conbuildmat.2019.117989
19. Kruger, J., Zeranka, S., van Zijl, G. 3D concrete printing: A lower bound analytical model for buildability performance quantification. Automation in Construction. 2019. 106(February). Pp. 102904. DOI: 10.1016/j.autcon.2019.102904
20. Perrot, A., Rangeard, D., Pierre, A. Structural built-up of cement-based materials used for 3D-printing extrusion techniques. Materials and Structures/Materiaux et Constructions. 2016. 49(4). Pp. 1213–1220. DOI: 10.1617/s11527-015-0571-0. URL: http://dx.doi.org/10.1617/s11527-015-0571-0
21. Kopanitsa, N.O., Sorokina, Ye.A. Osobennosti formirovaniya trebovaniy k stroitelno-tekhnicheskim kharakteristikam betonnykh smesey dlya 3D-pechati [Features of the formation of requirements for the construction and technical characteristics of concrete mixtures for 3D printing]. Sbornik dokladov III Mezhdunarodnoy nauchnoy konferentsii 'Molodezh, nauka, tekhnologii: novyye idei i perspektivy' [Proceedings of III International Scientific Conference 'Youth, Science, Technology: New Ideas and Prospects'] 2016. Pp. 407–410. (rus)
22. Elistratkin, M.Y., Lesovik, V.S., Alfimova, N.I., Shurakov, I.M. On the question of mix composition selection for construction 3D printing. Materials Science Forum. 2018. 945 MSF. Pp. 218–225. DOI: 10.4028/www.scientific.net/MSF.945.218
23. Tay, Y.W.D., Qian, Y., Tan, M.J. Printability region for 3D concrete printing using slump and slump flow test. Composites Part B: Engineering. 2019. 174(February). Pp. 106968. DOI: 10.1016/j.compositesb.2019.106968
24. Slavcheva, G.S., Artamonova, O.V. Rheological behavior of 3D printable cement paste : criterial evaluation. Magazine of Civil Engineering. 2018. 8(84). Pp. 97–108. DOI: 10.18720/MCE.84.10
25. Slavcheva, G.S., Artamonova, O.V. Rheological Behavior and Mix Design for 3D Printable Cement Paste | Scientific.Net. Key Engineering Materials. 2019. (799). Pp. 282–287. DOI: 10.4028/www.scientific.net/KEM.799.282
26. Buswell, R.A., Leal De Silva, W.R., Jones, S.Z., Dirrenberger, J. 3D printing using concrete extrusion: A roadmap for research. Cement and Concrete Research. 2018. 112. Pp. 37–49. DOI: 10.1016/j.cemconres.2018.05.006. URL: https://doi.org/10.10-16/j.cemconres.2018.05.006 (date of application: 4.02.2019).
27. Ting, G.H.A., Tay, Y.W.D., Qian, Y., Tan, M.J. Utilization of recycled glass for 3D concrete printing: rheological and mechanical properties. Journal of Material Cycles and Waste Management. 2019. (March). DOI: 10.1007/s10163-019-00857-x
28. Zhang, Y., Zhang, Y., She, W., Yang, L., Liu, G., Yang, Y. Rheological and harden properties of the high-thixotropy 3D printing concrete. Construction and Building Materials. 2019. 201. Pp. 278–285. DOI: 10.1016/j.conbuildmat.2018.12.061
29. Zhang, Y., Zhang, Y., Liu, G., Yang, Y., Wu, M., Pang, B. Fresh properties of a novel 3D printing concrete ink. Construction and Building Materials. 2018. 174. Pp. 263–271. DOI: 10.1016/j.conbuildmat.2018.04.115
30. Vaitkevičius, V., Šerelis, E., Kerševičius, V. Effect of ultra-sonic activation on early hydration process in 3D concrete printing technology. Construction and Building Materials. 2018. 169. Pp. 354–363. DOI: 10.1016/j.conbuildmat.2018.03.007
31. Slavcheva, G.S. Drying and shrinkage of cement paste for 3D printable concrete. IOP Conference Series: Materials Science and Engineering. 2019. 481(1). DOI: 10.1088/1757-899X/481/1/012043
32. Chaves Figueiredo, S., Romero Rodríguez, C., Ahmed, Z.Y., Bos, D.H., Xu, Y., Salet, T.M., Çopuroğlu, O., Schlangen, E., Bos, F.P. An approach to develop printable strain hardening cementitious composites. Materials and Design. 2019. 169. Pp. 107651. DOI: 10.1016/j.matdes.2019.107651. URL: https://doi.org/10.1016/j.matdes.2019.107651
33. Soltan, D.G., Li, V.C. A self-reinforced cementitious composite for building-scale 3D printing. Cement and Concrete Composites. 2018. 90(March). Pp. 1–13. DOI: 10.1016/j.cemconcomp.2018.03.017
34. Nerella, V.N., Ogura, H., Mechtcherine, V. Incorporating reinforcement into digital concrete construction. Proceedings of the IASS Symposium 2018 Creativity in Structural Design 2018.
35. Poluektova, V.A., Shapovalov, N.A., Chernikov, R.O., Yevtushenko, Ye.I. Modifitsirovannyy polimertsementnyy kompozitsionnyy material dlya 3D pechati [Modified polymer-cement composite material for 3D printing]. Patent Russia no. 266-1970. (rus)
36. Pshtiwan, S., Shami, N., Gavin, P. A Study into the Effect of Different Nozzles Shapes and Fibre-Reinforcement in 3D Printed Mortar. Materials. 2019. 12(10). DOI: 10.3390/ma12101708
37. Ma, Yihe. High density glass fiber reinforced cement curved plate and manufacturing method thereof. CN 101985849A. 2011.
38. Klyuev, S.V., Klyuev, A.V., Shorstova, E.S. Fiber concrete for 3-D additive technologies. Materials Science Forum. 2019. 974. Pp. 367–372. DOI: 10.4028/www.scientific.net/MSF.974.367
39. Iubin, P., Zakrevskaya, L. Soil-concrete for use in the 3D printers in the construction of buildings and structures. MATEC Web of Conferences. 2018. 245. DOI: 10.1051/matecconf/201824503002
40. Artamonova, O.V. Sintez nanomodifitsiruyushchikh dobavok dlya tekhnologii stroitelnykh kompozitov [Synthesis of nanomodifying additives for building composites technologies]. Voronezh: Voronezhskiy GASU, 2016. 100 p. (rus)
41. Chernyshov, Ye.M., Artamonova, O.V., Slavcheva, G.S. Nanomodifitsirovaniye sistem tverdeniya v strukture stroitelnykh kompozitov [Nano-modification of hardening systems in the structure of building composites]. Voronezh: Nauchnaya kniga, 2016. 132 p. (rus)
42. Stroganov, V.F., Sagadeev, E.V., Khuzin. A.F., Potapova, L.I., Vahitov. B.R., Stoianov. O.V. Sravnitelnyy analiz vliyaniya nanotrubok razlichnoy strukturyi funktsionalnosti na biostoykost tsementno-peschanykh rastvorov [Comparative analysis of the effect of nanotubes of different structure and functionality on the biostability of cement-sand mortars]. Izvestiya KGASU. 2018. 4(46). Pp. 300–308.
43. Bogdanov, S., Sychov, M., Lebedev, L., Mjakin, S., Gravit, M. Core-shell Powders for Additive Manufacturing of Articles for Underground Construction. Procedia Engineering. 2016. 165. Pp. 1579–1586. DOI: 10.1016/j.proeng.2016.11.896
44. Slavcheva, G.A., A.O.V. Reologicheskoye povedeniye dispersnykh sistem dlya stroitelnoy 3D-pechati: problema upravleniya na osnove vozmozhnostey arsenala 'Nano' [Rheological behavior of disperse systems for 3D construction printing: a control problem based on the capabilities of the Nano arsenal]. Nanotekhnologii v stroitelstve: nauchnyy internet-zhurnal. 2018. 3(10). Pp. 107–122. DOI: 10.15828/2075-8545-2018-10-3-107-122. (rus)

45. Di Maio, L., Coppola, B., Courard, L., Michel, F., Incarnato, L., Scarfato, P. Data on thermal conductivity, water vapour permeability and water absorption of a cementitious mortar containing end-of-waste plastic aggregates. Data in Brief. 2018. 18. Pp. 1057–1063. DOI: 10.1016/j.dib.2018.03.128
46. Khomich, V.A., Emralieva, S.A., Tsyguleva, M.V. Nanosilica Modifiers for Cement Mortars. Procedia Engineering. 2016. 152. Pp. 601–607. DOI: 10.1016/j.proeng.2016.07.662

Contacts:

Rustem Mukhametrakhimov, muhametrahimov@mail.ru

Liliya Lukmanova, lilya0503199@gmail.com

© Mukhametrakhimov, R.Kh., Lukmanova, L.V., 2021

Magazine of Civil Engineering

ISSN 2712-8172

journal homepage: http://engstroy.spbstu.ru/

DOI: 10.34910/MCE.102.7

Design parameters of steel fiber concrete beams

T.M.D. Do, T.Q.K. Lam*
Mien Tay Construction University, Vinh Long city, Vietnam
**E-mail: lamthanhquangkhai@gmail.com*

Keywords: steel fiber concrete, steel fiber content, nonlinear material, crack, stress-strain, numerical simulation

Abstract. In the study of steel fiber concrete beams, there are many design parameters that affecting stress-strain state, cracks formation and cracks development, etc. in beams. Changes of these design parameters will affect bearing capacity, displacement and cracks in beams. ANSYS can simulate the work of beams when design parameters be changed. Therefore, in this paper, the authors used ANSYS numerical simulation method to simulate design parameters of beams which be changed, to bearing capacity such as: steel fiber content in concrete, shear steel stirrups spacing at the ends of the beam, number of tensile steel bars, diameter of tensile steel bars, considering the nonlinear element of the materials, etc to consider the cracks formation and cracks development in beams from the beginning of loading to the damaged beams and then build the load and stress relationship, load and vertical displacement relationship in steel fiber concrete beams. Beam simulation results show that changes of these design parameters have affected the bearing capacity, stress-strain state, cracks formation and cracks development of beams, with the beams when increasing the content of steel fibers in concrete, increasing the number of tensile steel bars, increasing the diameter of tensile steel etc., making the beams reduce cracks, increase the bearing capacity, etc. for the beams. Simulation results were also compared with experimental methods. So, the study of these design parameters helps the design of steel fiber concrete beam structures to withstand impact loads and limit cracks in beams.

1. Introduction

Fiber concrete has been researched and widely applied in many types of constructions such as civil works, bridges, underground constructions, etc., with many different types of structures such as: basalt fiber concrete [1], crumb rubber in steel fiber beam [2], steel fiber concrete [3], steel fiber concrete of curved shells [4–6], nano concrete or high-performance concrete with steel fiber [7–10], self-compacting geopolymer concrete with and without GGBFS and steel fiber [11], etc. In particular, steel fiber concrete has been researched and widely applied, especially in steel fiber concrete beams. The studies go from analyzing static problems [12], abradability of steel fiber concrete [13], shear behavior, bending resistance, failure mechanisms, etc., [14–16] to use experimental method and numerical simulation on steel-reinforced concrete beams [17–19].

In the steel fiber concrete beams analyzed above, many authors have considered the factors affecting to shear strength of beams [20–21], to flexural behavior [22], to the strength of concrete [23–24], to fracture characteristics [25–26], to improve the quality of mass concrete [27], in study of numerical simulation and experiment on steel fiber concrete beams [28] investigated the effect of 0 %, 4 % and 8 % steel fiber content on stress, deformation and displacement in steel fiber concrete beams, or some another studies [29–34], etc.

In order to determine the stress-strain state and cracks in beams when design parameters be changed, it is necessary to study design parameters such as: steel fiber content in concrete, shear steel stirrups spacing at the ends of the beam, number of tensile steel bars, diameter of tensile steel bars, considering the nonlinear element analysis of the material, etc. To solve the mentioned main problems above, this paper presented ANSYS numerical simulation method to consider the cracks formation and cracks development in beams from the beginning of loading to the damaged beams and then build the load and stress relationship, load and vertical displacement relationship in steel fiber concrete beams with beam section 150×200×2200 mm and simulation results were compared with experimental methods.

Do, T.M.D, Lam, T.Q.K. Design parameters of steel fiber concrete beams. Magazine of Civil Engineering. 2021. 102(2). Article No. 10207. DOI: 10.34910/MCE.102.7

This work is licensed under a CC BY-NC 4.0

2. Materials and methods

2.1. Parameters in model

Beam of 150×200×2200 mm size, shear steel stirrups spacing at the ends of the beam, ∅6, changed from 50 mm to 100 mm, shear steel stirrups spacing at the middle of the beam, ∅6a200, constant. Tensile steel diameter changed from ∅12 to ∅20 and ∅25, number of tensile steel bars changed from 2 bars to 3 bars and 4 bars. Fixed compression steel bars are ∅10.

Concrete B20, all beams, fiber steel content were studied with 0 % to 4 % and 8 % by volume. Fiber steel content with 0 % that means normal reinforced concrete beams without steel fibers, in order to consider the impact of steel fiber content on normal reinforced concrete beams.

Load P is applied to the steel plate 140×140×6 mm, increased from 0 kN until the beam is damaged, each load level is increased by 5 kN, shown in Fig. 1.

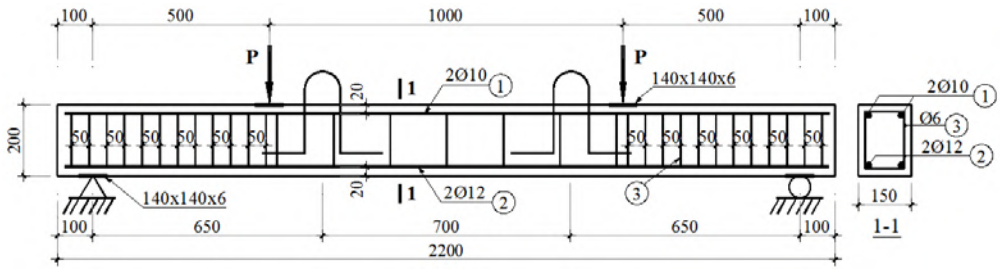

Figure 1. Reinforced concrete beam in the study.

2.2. Input parameters in ANSYS

Select the model of steel fiber dispersion in concrete: To model steel fiber in concrete, three models are used: smeared model, embedded model and discrete model. In this study, steel fibers that are dispersed in concrete should use a smeared model.

Select cracking model in concrete: Currently cracks in concrete are modeled in two basic forms: discrete model and smeared model. In this study, we are interested in the behavior relationship between load and displacement without being too concerned about crack shape, local stress. So in this study choose the smeared model for cracks in concrete.

Constructing a finite element model for beams:

- Concrete simulation element: SOLID65 element, which is a specialized simulation of concrete materials, can simulate reinforcement in concrete with the phenomenon of cracking and compression, nonlinear material definition. This is a 3D element with 8 buttons. In SOLID65, it is allowed to declare steel fiber content through concrete reinforcement constant as a percentage.
- Steel bars element: used beam 188 element: is an element used to model the reinforcement in beams, used as a basis for Timosenko beams, the element consists of 2 nodes with 6 degrees of freedom at each node.

Material model: stress-strain model of concrete when tensile and compression: we have a model of Hognestad, a model of Todeschini, a model of Kent and Park, a model of Kachlakev, etc. Based on the survey of stress-strain models of compressive concrete presented above, we choose concrete model under compression according to Kachlakev model. Model of stress-strain of concrete under tensile stress, this model has been predefined in ANSYS.

Destructive standards: Willam and Warnke's destructive standard is used in this study and are defined in ANSYS.

Meshing for models, boundary conditions and loads: due to the simple beam structure, meshing (VSWEEP, ALL) with mesh shapes is divided by 3D blocks available in ANSYS and optimized element size, shown in Fig. 2.

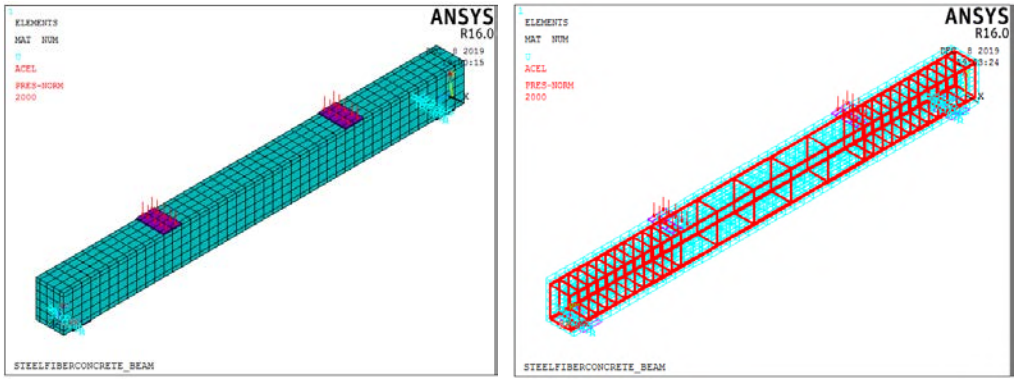

a) Reinforced concrete beam model **b) Steel bar model and loads**

Figure 2. Model, meshing, boundary conditions and loads applied to the beam.

Input parameters for the model: In ANSYS to enter the input parameters for SOLID65 concrete element, we must enter the following 8 basic parameters:

1. Shear force transmission coefficient when the crack is opened (β_0)
2. Shear force transmission coefficient when cracking is closed (β_C)
3. Cracking stress when tensile (f_r)
4. Compression stress $(f_C^{'})$
5. Weak reduction coefficient due to cracking when tensile
6. Modulus (E_C)
7. Poisson's coefficient: v
8. Stress-atrain relationship curve of concrete, considered the nonlinearity of the material.

3. Results and Discussion

3.1. Survey of steel fiber content in concrete

Tensile steel bars are 2⌀12, shear steel stirrups spacing at the ends of the beam is 50 mm, linear material. Steel fiber content in concrete are changed from μ = 0 % to 4 % and 8 %.

The color spectrum will help us to observe changed values, with the color spectrum of vertical displacement and the color spectrum of stresses in beams are shown in the Fig. 3.

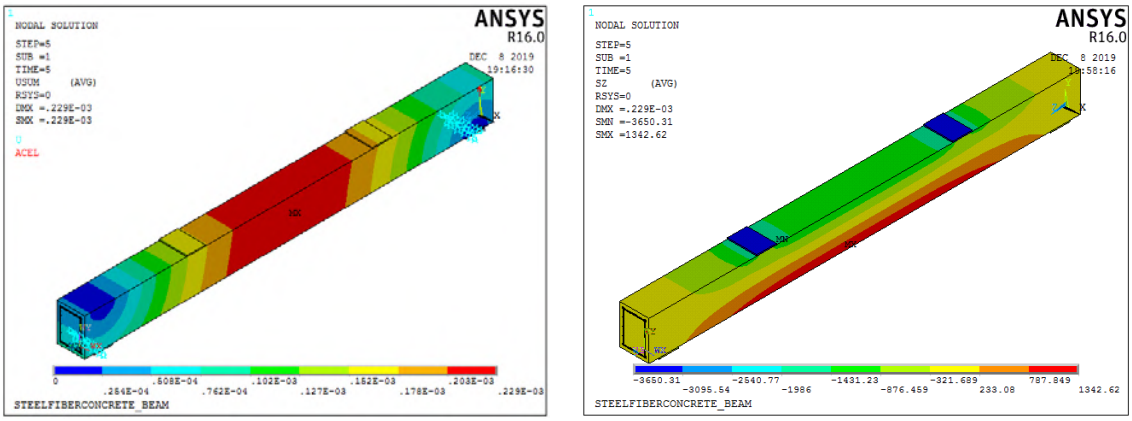

a) Color spectrum of vertical displacement **b) Color spectrum of stresses**

Figure 3. Color spectrum of vertical displacement and stresses values on beam.

The beams begin to appear cracks when the steel fiber content are changed, are shown in Fig. 4.

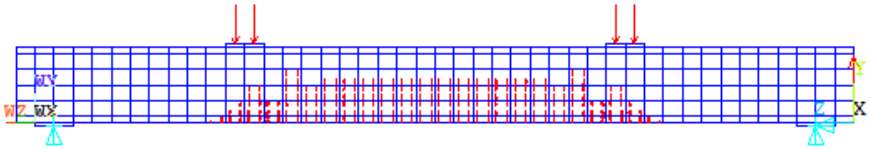

a) Steel fiber content is 0 % (P_{carck} = 6 kN)

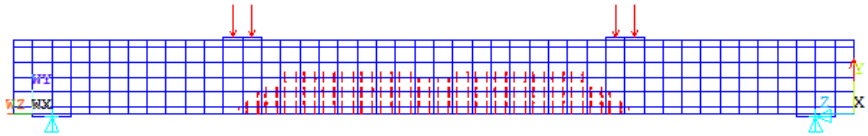

b) Steel fiber content is 4 % (P_{carck} = 6 kN)

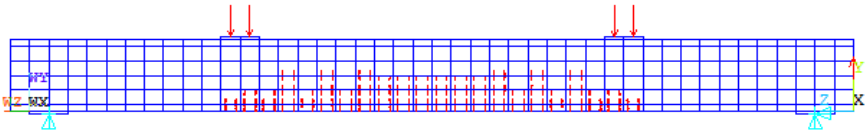

c) Steel fiber content is 8 % (P_{carck} = 5 kN)

Figure 4. Beams begin to appear cracks when the steel fiber content are changed.

The beams begin to be damaged when the steel fiber content are changed, are shown in Fig. 5.

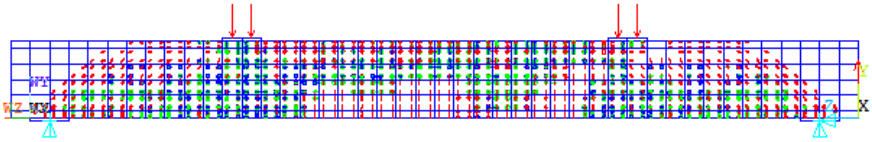

a) Steel fiber content is 0 % (P_{max} = 34 kN)

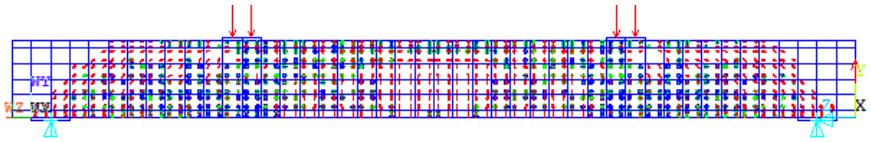

b) Steel fiber content is 4 % (P_{max} = 43 kN)

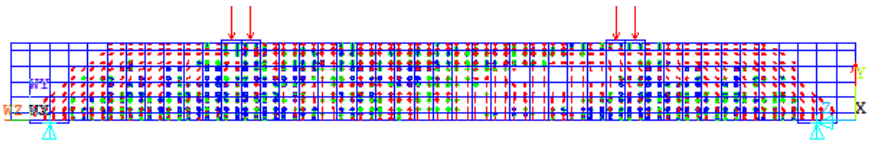

c) Steel fiber content is 8 % (P_{max} = 41 kN)

Figure 5. Beams begin to be damaged when the steel fiber content are changed.

Load and tensile stress relationship, load and compressive stress relationship when the steel fiber content are changed, shown in Fig. 6.

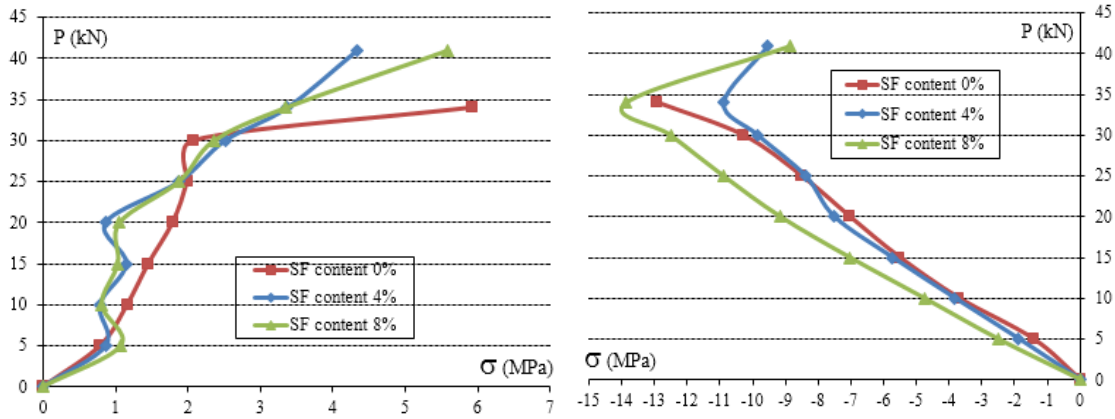

a) Load and tensile stress **b) Load and compressive stress**

Figure 6. Load and stresses relationship when the steel fiber content are changed.

With: SF content is steel fiber content.

Load and vertical displacement relationship at middle and at P forces of beams when the steel fiber content are changed, are shown in Fig. 7.

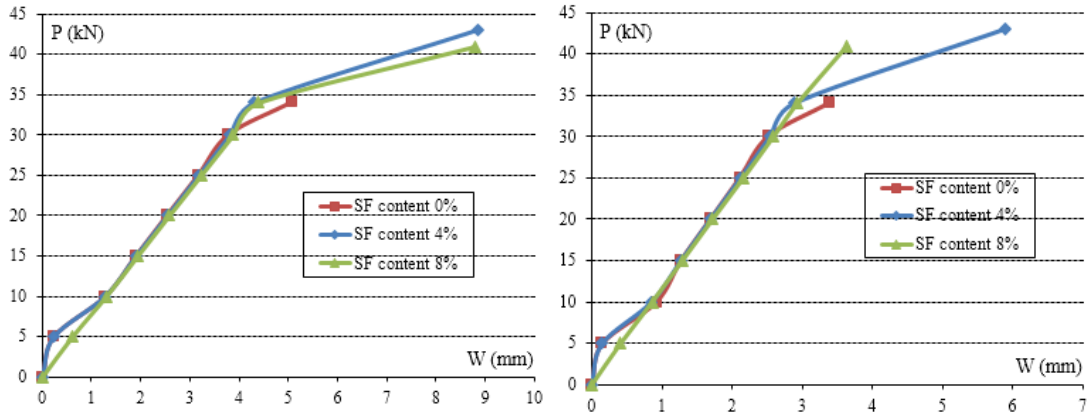

a) at middle of beams **b) at P forces of beams**

Figure 7. Load and vertical displacement relationship when the steel fiber content are changed.

Comment: In Fig. 4, the beams with the steel fiber content in concrete are μ = 0 % and μ = 4 %, all start cracking at the load level P = 6 kN, μ = 8 % cracking earlier and starting to crack at load P = 5 kN. When the beams are damaged, μ = 0 % is damaged at the load of 34 kN, μ = 4 % is damaged at the load of 43 kN, and μ = 8 % is damaged earlier and the damaged at P = 41 kN (Fig. 5). It can be seen that when the steel fiber content is large, surpassing the permissible limit content of steel fibers in concrete, the bearing capacity decreases, in published studies, the steel fiber content ranges from 0.1 % to 4 % according to volume, meaning the beams are brittle. Therefore, do not increase the steel fiber content too high and exceed the permissible limits of steel fibers in concrete.

Load and stresses relationship in beams (Fig. 6), we see in the tensile zone, the steel fiber concrete beams have a tensile stress smaller than normal concrete beams. In contrast, in the compression region, with the participation of steel fibers, the steel fibers have played a role of increasing the bearing capacity for concrete. In relation to the load and vertical displacement in the beams, the steel fibers in the beams did not significantly change the displacement problem, all 3 beams had no significant change (Fig. 7).

3.2. Survey with shear steel stirrups spacing at the ends of the beam

In this survey, fixed steel fiber content is μ = 4 %, tensile steel diameter 2⌀12 and linear material. Shear steel stirrups spacing at the ends of the beams changed from 50 mm to 100 mm.

The beams begin to appear cracks and the beams begin to be damaged, are shown in Fig. 8.

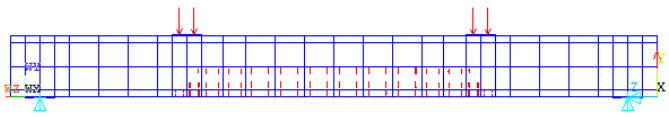

a) The beams begin to appear cracks, P_{crack} = 6 kN

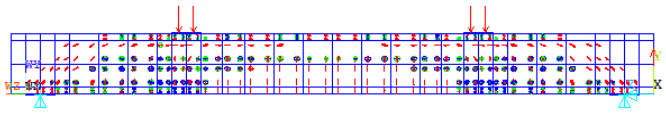

b) the beams begin to be damaged, P_{max} = 45 kN

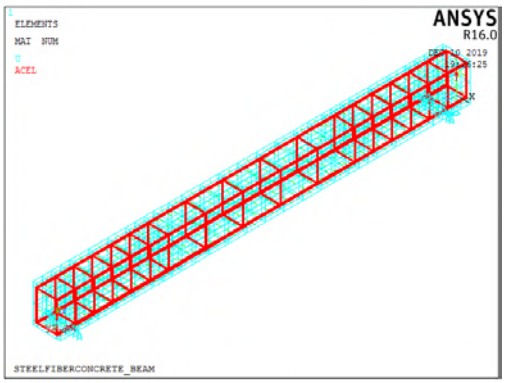

c) shear steel stirrups spacing is 100 mm

Figure 8. Cracks in beams and shear steel stirrups spacing changed to 100 mm.

Load and tensile stress relationship, load and compressive stress relationship when shear steel stirrups spacing changed to 100 mm, are shown in Fig. 9.

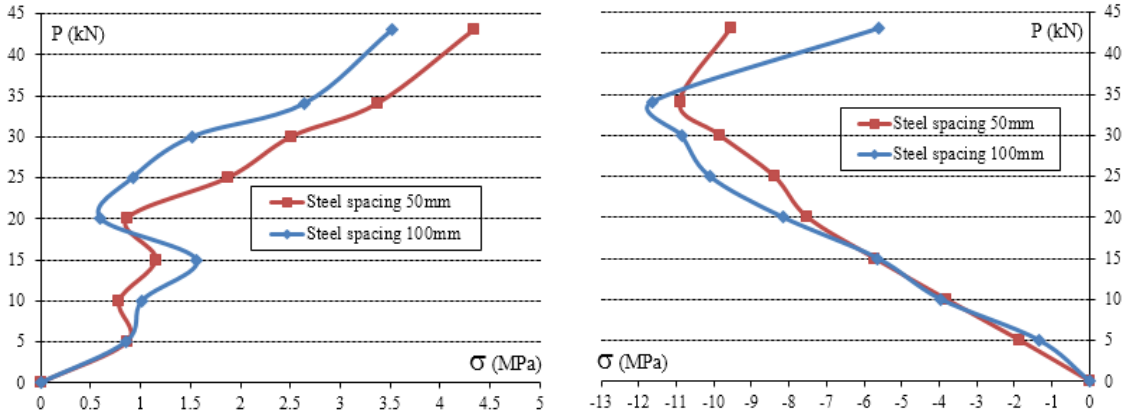

a) Load and tensile stress relationship **b) Load and compressive stress relationship**

Figure 9. Load and stresses relationship when shear steel stirrups spacing changed.

Load and displacement relationship at middle and at P forces of beams when shear steel stirrups spacing changed to 100 mm, are shown in Fig. 10.

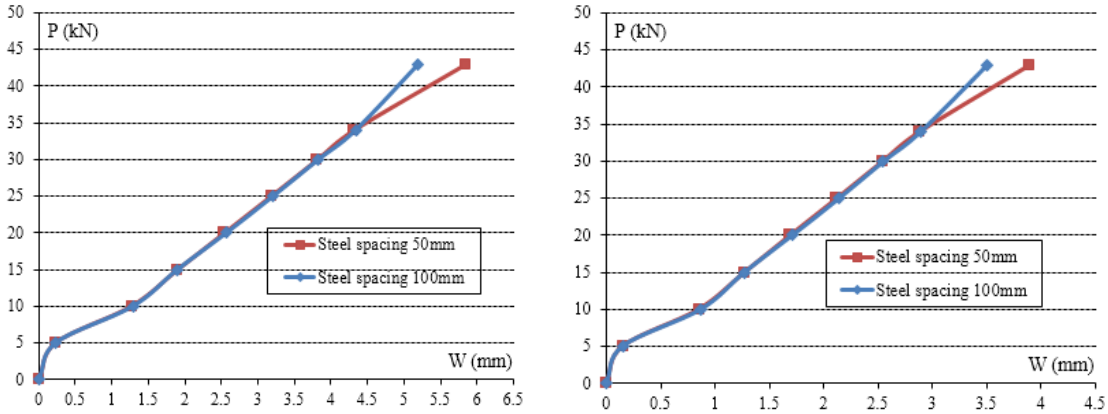

a) at middle of beams **b) at P forces of beams**

Figure 10. Load and displacement relationship of beams when shear steel stirrups spacing changed.

Comment: When shear steel stirrups spacing changed from 50 mm to 100 mm, beams start to crack at P = 6 kN, damaged at P = 45 kN, are shown in Fig. 8, compared to Fig. 4b and Fig. 5b with shear steel stirrups spacing is 50 mm, the cracks start to appear at the same time, but it is damaged later at P = 45 kN. However, the number of cracks decreases. When the content of steel fibers in concrete is still within the limit of steel fiber content in concrete, the stress in the beam will play a role of bearing as well as limiting cracks, stress value changes greatly when passing load level P = 20 kN (Fig. 9). Displacement in beams are not changed much and start to change when the beams pass the P = 35 kN load level (Fig. 10). This is similar to the case when increasing the fiber content exceeds the steel content limit in concrete. Thereby, we should not increase the distance of shear steel too thick.

3.3. Survey of the change in the number of tensile steel bars

This case still does not change the steel fiber content in concrete beams, μ = 4 %, shear steel stirrups spacing at the ends of beams are 50 mm, linear material. However, this case changed the number of tensile steel bars that increased from 2⌀12 to 3⌀12 and 4⌀12, are shown in Fig. 11.

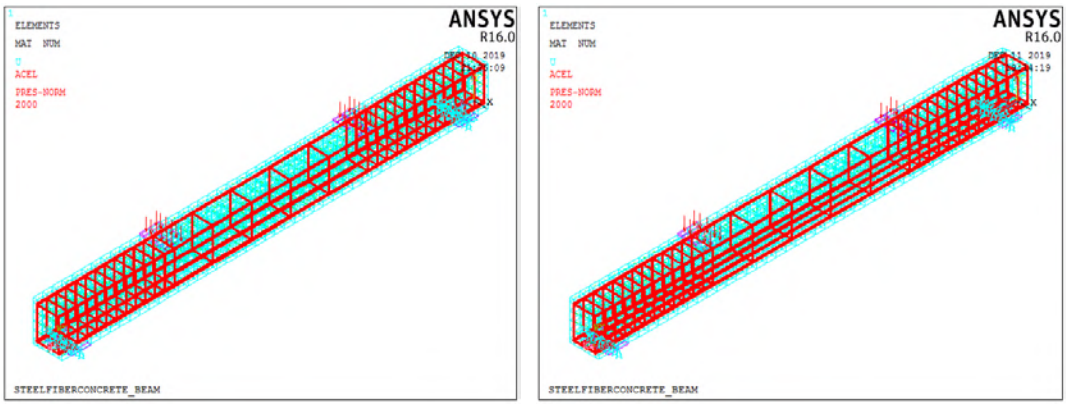

a) Beam model with 3ø12 **b) Beam model with 4ø12**

Figure 11. Beams model with change in the number of tensile steel bars.

Beams start to crack when increasing the number of tensile steel bars, are shown in Fig. 12.

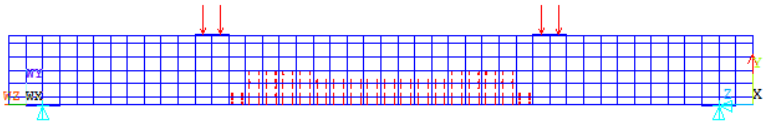

a) Beam model with 3ø12, P_{crack} = 6 kN

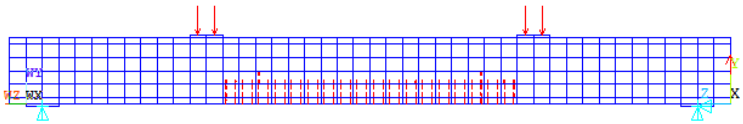

b) Beam model with 4ø12, P_{crack} = 7 kN

Figure 12. Beams start to crack when increasing the number of tensile steel bars.

Beams are damaged by increasing the number of tensile steel bars, are shown in Fig. 13.

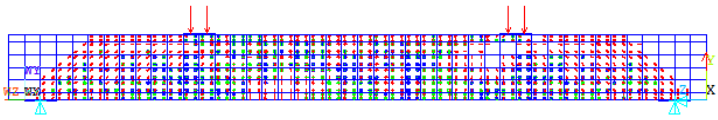

a) Beam model with 3ø12, P_{max} = 43 kN

b) Beam model with 4ø12, P_{max} = 46 kN

Figure 13. Beams are damaged by increasing the number of tensile steel bars.

Load and tensile stress relationship, load and compressive stress relationship when increasing the number of tensile steel bars, are shown in Fig. 14.

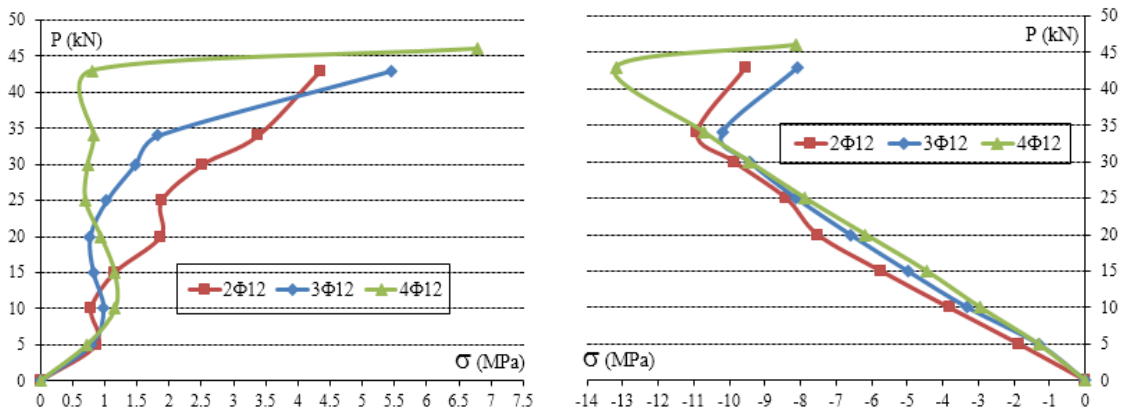

a) Load and tensile stress **b) Load and compressive stress**

Figure 14. Load and stress relationship when increasing the number of tensile steel bars.

Load and displacement relationship at middle and at P forces of beams when increasing the number of tensile steel bars, are shown in Fig. 15.

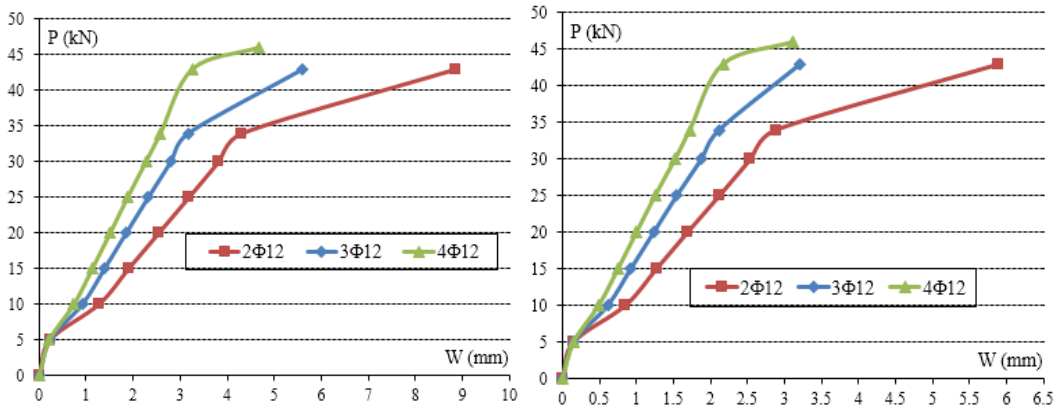

a) at middle of beams **b) at P forces of beams**

Figure 15. Load and displacement relationship when increasing the number of tensile steel bars.

Comment: when increasing the number of tensile steel bars, fixed μ = 4 %, with 2 beams have 2⌀12 and 3⌀12, crack at P = 6 kN, damaged at P = 43 kN. Beam with 4⌀12, Crack at P = 7 kN (Fig. 12) and damaged at P = 46 kN (Fig. 13). This means that with the increasing in the number of tensile steel bars, the working ability of the beams also increases, so increasing the number of tensile steel bars will increase the bearing capacity of the beam and are shown in (Fig. 14), (Fig. 15). In Fig. 14b, when changing the number of tensile steel bars, the relationship of load and tensile stress will change significantly when passing the P = 15 kN load level.

3.4. Survey the affect of diameter of tensile steel bars

This case still does not change the steel fiber content in concrete, μ = 4 %, steel stirrups spacing at the ends of beams are 50 mm, linear material. Diameter of tensile steel bars is changed from 2⌀12 to 2⌀20 and 2⌀25.

Beams begin to crack when increasing the diameter of the tensile steel bars, are shown in Fig. 16.

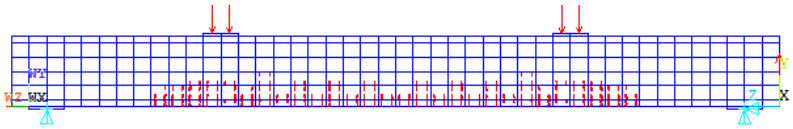

a) Beam model with 2⌀20, P_{crack} = 10 kN

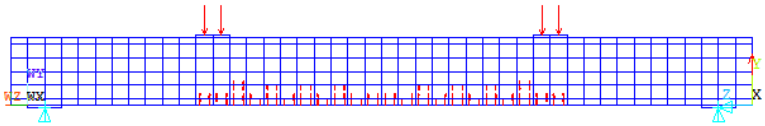

b) Beam model with 2⌀25, P_{crack} = 10 kN

Figure 16. Beams begin to crack when increasing the diameter of the tensile steel bars.

Beams begin to be damaged by increasing the diameter of the tensile steel bars, shown in Fig. 17.

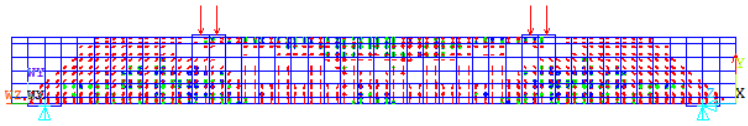

a) Beam model with 2⌀20, P_{max} = 48 kN

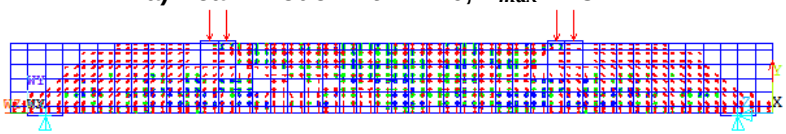

b) Beam model with 2⌀25, P_{max} = 53 kN

Figure 17. Beams begin to be damaged by increasing the diameter of the tensile steel bars.

Load and tensile stress relationship, load and compressive stress relationship when increasing the diameter of the tensile steel bars, are shown in Fig. 18.

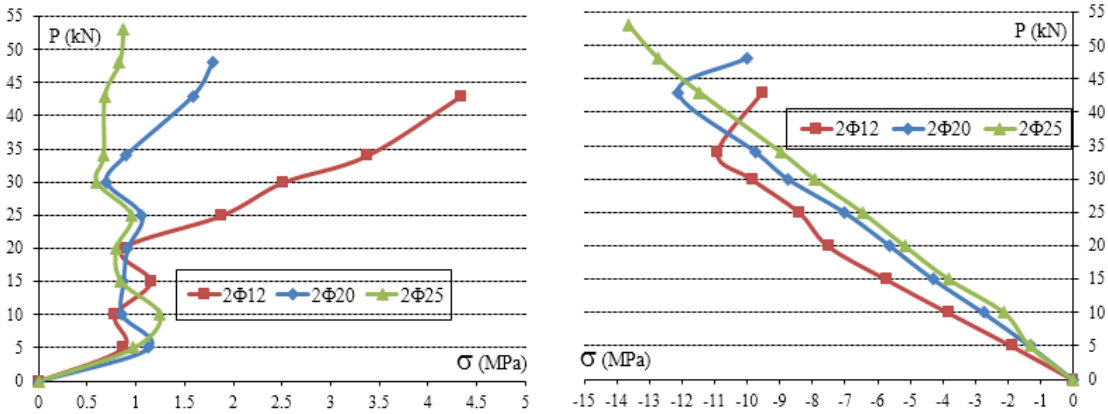

a) Load and tensile stress **b) Load and compressive stress**

Figure 18. Load and stresses relationship when increasing the diameter of the tensile steel bars.

Load and displacement relationship at middle and at P forces of beams when increasing the diameter of the tensile steel bars, are shown in Fig. 19.

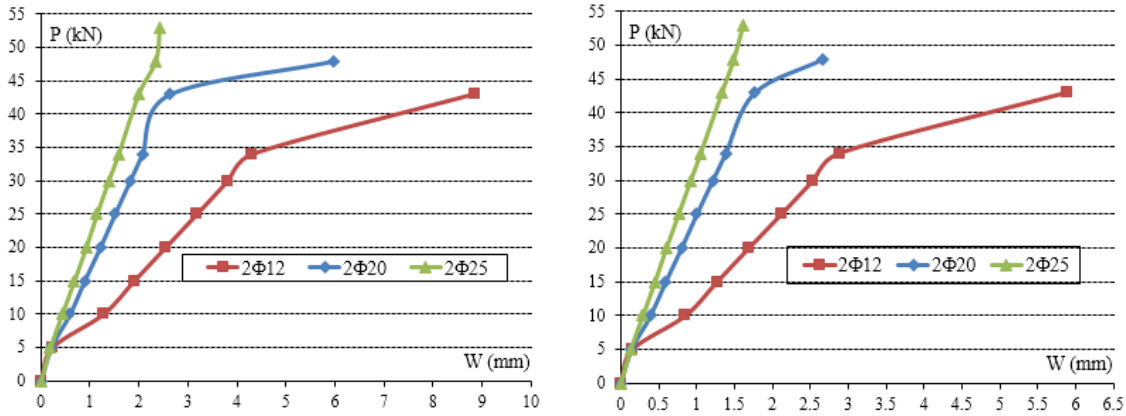

a) at middle of beams **b) at P forces of beams**

Figure 19. Load and displacement relationship when increasing the diameter of the tensile steel bars.

Comment: when increasing the diameter of the tensile steel bars from ⌀20 to ⌀25, all beams crack at P = 10 kN (Fig. 16), damaged at 48 kN of ⌀20 and 53 kN of ⌀25 (Fig. 17). In Fig. 16, beams appear cracks at the same load level but the number of cracks as the diameter of the tensile bar increases, the cracks decrease and is similar to the number of bars increased. Therefore, when increasing the number of tensile steel bars and increasing the diameter of tensile steel, it will make the beams quickly increase bearing capacity and quickly reduce cracks in the beams and load and tensile stress relationship be changed when the loads exceed the P = 20 kN load level (Fig. 18a).

3.5. Surveying the effect of nonlinear material analysis

When increasing the content of steel fibers, increasing the diameter of tensile steel, increasing the number of tensile steel bars, etc., will help the beams reduce cracks, enhance the bearing capacity of the beams. However, nonlinear materials need to be analyzed, in order to use effectively.

This case still does not change the steel fiber content, μ = 4 %, steel stirrups spacing at the ends of beams are 50 mm, tensile steel bars 2⌀12. However, this case analyzes nonlinear material.

Beams start to crack and be damaged by nonlinear material analysis, are shown in Fig. 20.

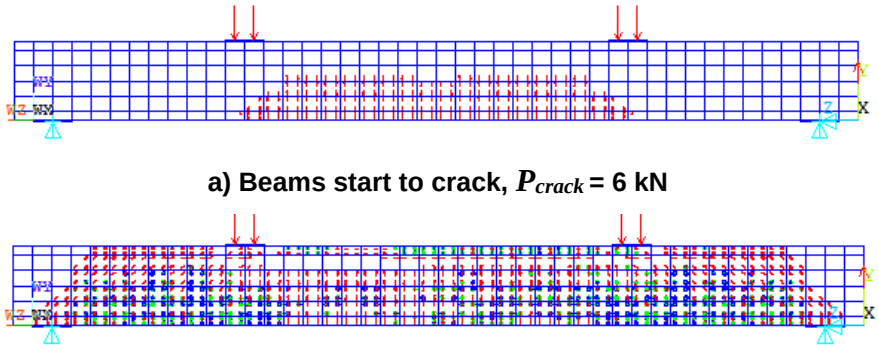

a) Beams start to crack, P_{crack} = 6 kN

b) Beams start to be damaged, P_{max} = 48 kN

Figure 20. Beams start to crack and be damaged by nonlinear material analysis.

Load and tensile stress relationship, load and compressive stress relationship when nonlinear material analysis, are shown in Fig. 21.

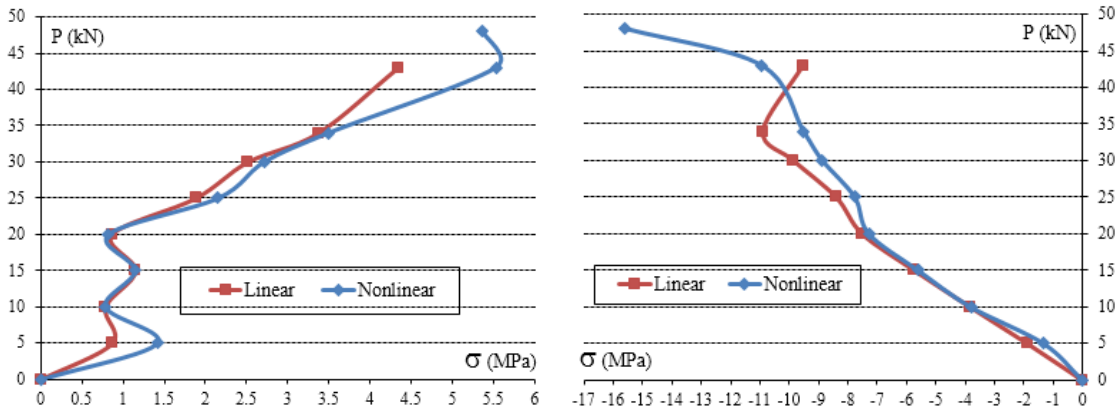

a) Load and tensile stress **b) Load and compressive stress**

Figure 21. Load and stresses relationship when nonlinear material analysis.

Load and displacement relationship at middle and at P forces of beams when nonlinear material analysis, shown in Fig. 22**.**

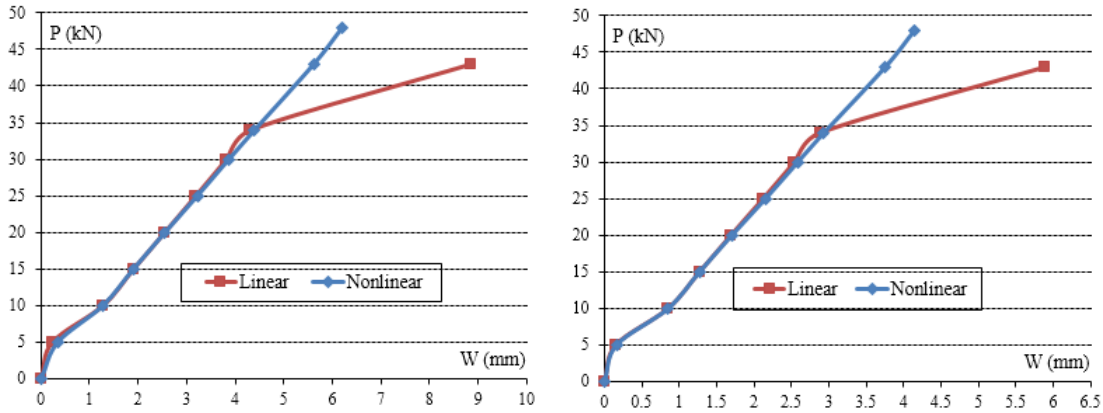

a) at middle of beams **b) at P forces of beams**

Figure 22. Load and vertical displacement relationship when nonlinear material analysis.

Comment: When considering linear and non-linear material analysis, beams begin to crack at load P = 6 kN, in nonlinear material analysis, beams are damaged later at 48 kN (Fig. 20). In Fig. 21 and Fig. 22 at the near destructive stage, the effect of nonlinear material analysis consideration, after the P = 35 kN load level, the difference in stresses and vertical displacements are growing. Therefore, in structural analysis, it is necessary to analyze nonlinear materials.

3.6. Case studies are influenced by many factors

Consider the following 3 cases: Case 1: μ = 0 %, shear steel stirrups spacing at the ends of beams are 50 mm, tensile steel bars 2⌀12 and linear material analysis. Case 2: μ = 4 %, shear steel stirrups spacing at the ends of beams are 50 mm, tensile steel bars 2ϕ20 and nonlinear material analysis. Case 3: μ = 8 %, shear steel stirrups spacing at the ends of beams are 50 mm, tensile steel bars 2⌀25 and nonlinear material analysis.

Beams start to crack and be damaged with many factors considered, are shown in Fig. 23.

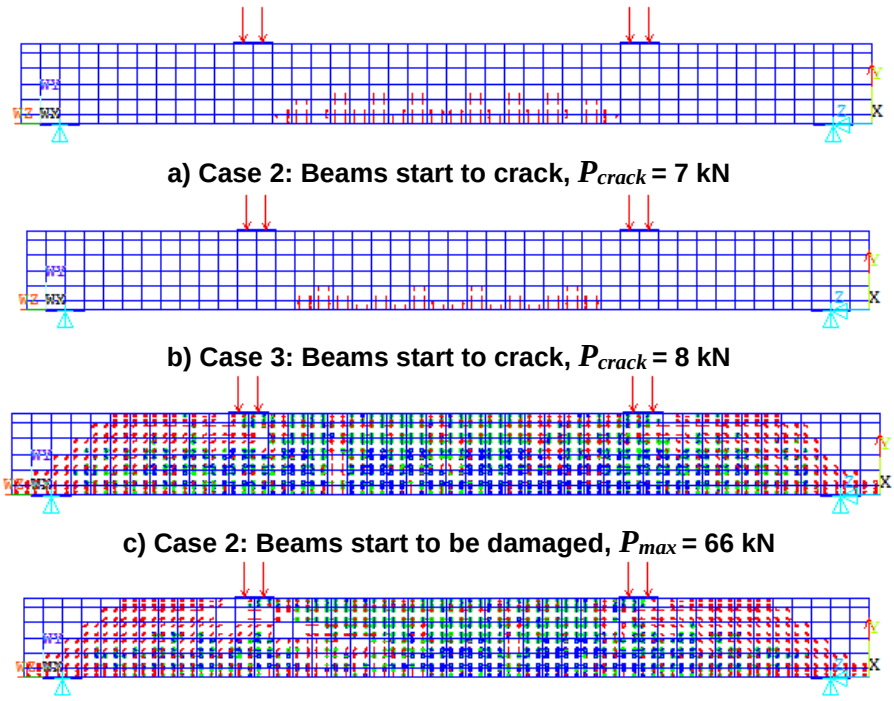

a) Case 2: Beams start to crack, P_{crack} = 7 kN

b) Case 3: Beams start to crack, P_{crack} = 8 kN

c) Case 2: Beams start to be damaged, P_{max} = 66 kN

d) Case 3: Beams start to be damaged, P_{max} = 67 kN

Figure 23. Beams start to crack and be damaged with many factors considered.

Load and tensile stress relationship, load and compressive stress relationship when many factors considered, are shown in Fig. 24.

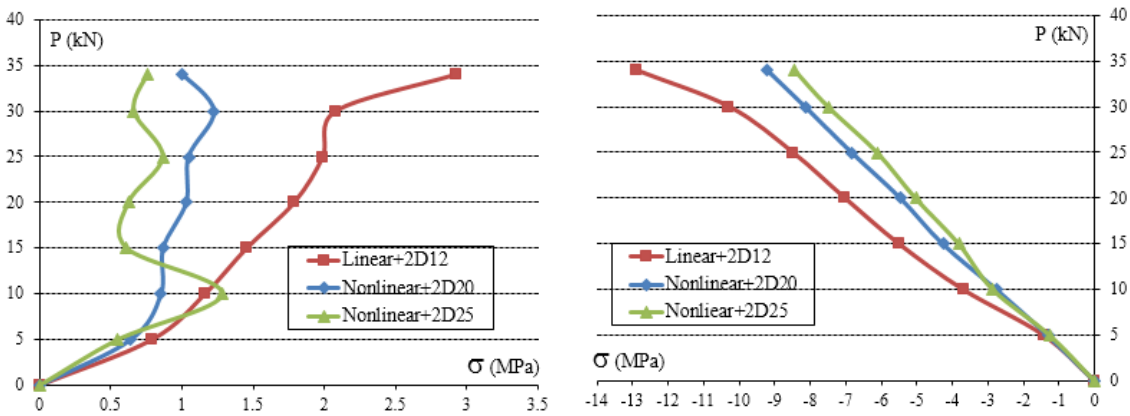

a) Load and tensile stress **b) Load and compressive stress**

Figure 24. Load and stresses relationship when many factors considered.

Load and displacement relationship at middle and at P forces of beams when many factors considered, are shown in Fig. 25.

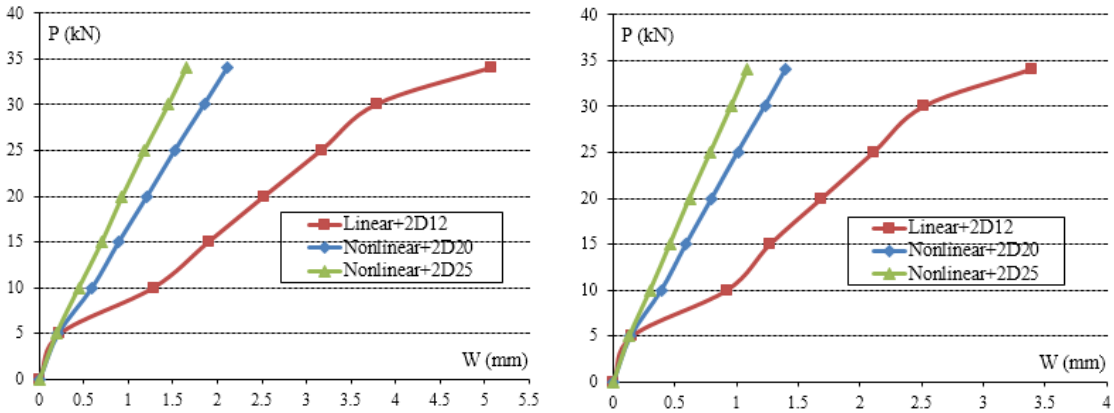

a) at middle of beams **b) at *P* forces of beams**

Figure 25. Load and displacement relationship when many factors considered.

Comment: in case 2, the beams start to crack at 7 kN and damaged at 66 kN, while case 3 starts to crack at 8 kN and damaged at 67 kN (Fig. 23). In case 3 we see that when considering many factors, tensile stress and displacement are significantly reduced (Fig. 24), (Fig. 25).

3.7. Compare with experimental results

The numerical simulation results are compared with experimental results, in the experimental study, we poured concrete for 6 beams of a 150×200×2200 mm size, of which: 2 beams with steel fiber content of 0 %, 2 beams with steel fiber content of 4 % and 2 beams with steel fiber content of 8 % [27].

– The beams were tested with varying steel fiber content, are shown in Fig. 26.

a) Formwork and reinforcement of beams **b) Concreting beams**

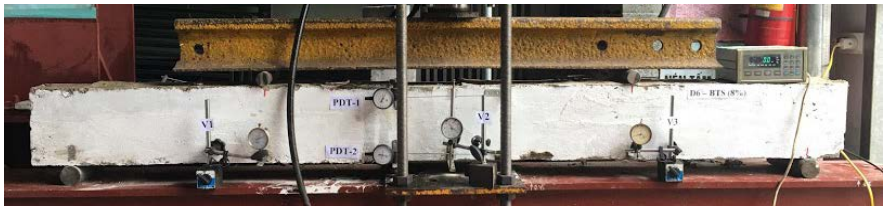

c) Beams with experimental equipments

Figure 26. The beams were tested with varying steel fiber content [27].

– Load and deformation between experiment (EXP) and ANSYS: The simulation results are compared with the test case of 8 % steel fiber content, because in the experiments the authors measured deformation values in beams, in ANSYS, so the authors took deformation values.

Load and deformation between EXP and ANSYS, are shown in Fig. 27.

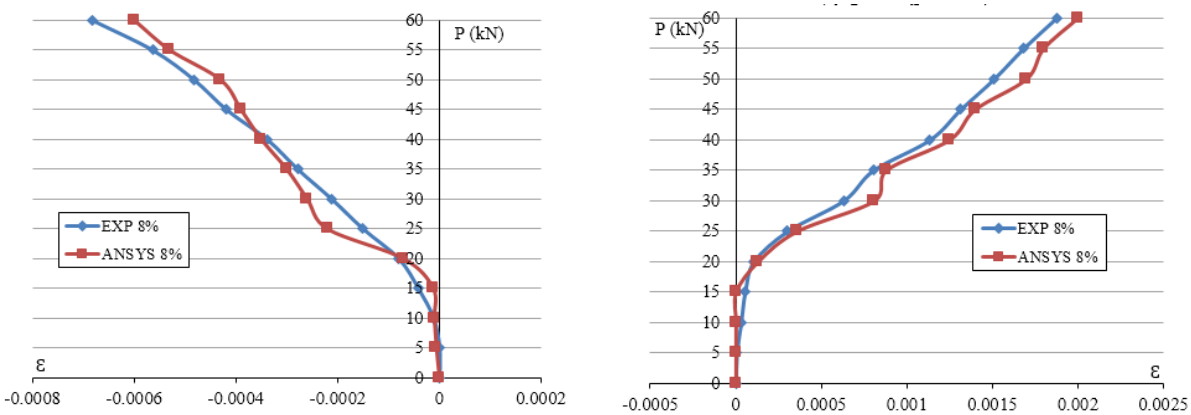

a) Load and tensile deformation **b) Load and compressive deformation**

Figure 27. Load and deformations between EXP and ANSYS, μ = 8 % [27].

Comment: The research results of steel fiber content are suitable for the experiment when μ = 8 %, so the results of the survey of the effects of the above design parameters are reliable. In the study [27], the experiment investigated cracks formation and cracks development by microscopy, so the authors were able to read at the load level of P = 25 kN or higher when cracking appeared. In ANSYS, the program can accurately simulate the position and number of cracks in the beam, so it will show at a smaller level. And this ANSYS program can be used to survey other parameters such as beams cross section, distributed load, etc. With the two simulation and experiment methods above, the difference between the two results is not significant and acceptable.

4. Conclusions

Based on the results of the study lead to the following conclusions:

1. When considering the effect of steel fiber content in concrete, increasing the steel fiber content, the beams reduce cracks, but the stress and displacement do not change much. When the steel fiber content exceeds the allowed steel content in concrete, the beams will be brittle damaged.

2. When shear steel stirrups spacing at the ends of beams too thick, it will affect the working of the beam, so, the content of steel should be sufficient.

3. Considering influencing factors such as the number of tensile steel bars and the diameter of tensile steel bars, the role of steel bars will change stress, vertical displacement and cracks significantly reduced when adding steel fiber content in concrete.

4. When considering the influence of nonlinear materials analysis and considering many factors, steel bars in bending beams have the effect of bearing and reducing obvious cracks.

5. Through studies on steel fiber concrete beams, it is effective to add steel fibers into the concrete, which will make the beams reduce cracks, resist collisions, increase the long life of the works, etc. This shows that the efficiency of steel fiber concrete is not high when using normal concrete. Research is needed on fibers when adding high strength concrete or silica nano concrete.

5. Conflict of interests

The authors declare that there is no conflict of interests regarding the publication of this paper.

References

1. Mehmet, E.G., Mohammed, S.A.J., Adnan, H.A., Twana, A.H., Khamees, N.A., Abdulkadir, C. Rehabilitation of normal and self-compacted steel fiber reinforced concretecorbels via basalt fiber. Advances in Concrete Construction. 2018. 6(5). Pp. 423–463. DOI: 10.12989/acc.2018.6.5.423
2. Ahmed, T.N., Abu, B.B.H., Hazizan, M.A. Influence of Crumb Rubber on Impact Energy of Steel Fiber Concrete Beams. Applied Mechanics and Materials. 2015. 802. Pp. 196–201. DOI: 10.4028/www.scientific.net/AMM.802.196
3. Rakesh, K., Ajeet, K., Manish, K.K. Steel Fiber Reinforced Concrete. IJRASET. 2018. 7. Pp. 2456–2458.
4. Khai, L.T.Q., Dung, D.T.M. Stress-strain in multi-layer reinforced concrete doubly curved shell roof. International Journal of Innovative Technology and Exploring Engineering. 2019. 8(4S2). Pp. 419–424.
5. Lam, T.Q.K., Do, T.M.D. Effect of each shell thickness on deformation stress and the ability for causing the cracks in the multilayer doubly curved shell roof. International Journal of Innovative Technology and Exploring Engineering. 2019. 8(6C2). Pp. 215–220.
6. Lam, T.Q.K., Do, T.M.D. Sliding between layers in 2-layer reinforced concrete beams and shell. International Journal of Engineering and Advanced Technology. 2019. 8(5) (2019). Pp. 1867–1871.

7. Ngo, V.T., Lam, T.Q.K., Do, T.M.D., Nguyen, T.C. Nano concrete aggregation with steel fibers: A problem to enhance the tensile strength of concrete. E3S Web of Conferences. 2019. 135 03001. DOI: 10.1051/e3sconf/201913503001
8. Ngo, V.T., Lam, T.Q.K., Do, T.M.D., Nguyen, T.C. Increased plasticity of nano concrete with steel fibers. Magazine of Civil Engineering. 2020. 93(1). Pp. 27–34. DOI: 10.18720/MCE.93.3
9. Travush, V.I., Konin, D.V., Krylov, A.S. Strength of reinforced concrete beams of high-performance concrete and fiber reinforced concrete. Magazine of Civil Engineering. 20018. 1. Pp. 90–100. DOI: 10.18720/MCE.77.8
10. Ngo, V.T., Bui, T.T., Lam, T.Q.K., Nguyen, T.T.N., Nguyen, V.H. Experimental Evaluation of Nano Silica Effects to High Performance Concrete Strength in Early Age. IOP Conf. Series: Materials Science and Engineering. 2020. 869 032011. DOI: 10.1088/1757-899X/869/3/032011
11. Saad, A., Nildem, T. Performance of self-compacting geopolymer concrete with and without GGBFS and Steel fiber. Advances in Concrete Construction. 2018. 6(4). Pp. 323–344. DOI: 10.12989/acc.2018.6.4.323
12. James, H.H. Static Analysis of Steel Fiber Concrete Beam with Heterosis Finite Elements. ARO-The Scientific Journal of Koya University. 2014. 1. DOI: 10.14500/aro.10041
13. Kiyanets, A.V. Abradability of steel fiber concrete. IOP Conf. Series: Materials Science and Engineering. 2018. 451 012073. DOI: 10.1088/1757-899X/451/1/012073
14. Toshiyuki, K., Yuriko, O., Keisuke, N. Shear behavior of DFRCC coupling beams using PVA and steel fiber. ASEM19. 2019.
15. Duy, H.D., Chinh, H.H., Thanh, B.C. Method of calculating bending resistance of reinforced concrete structure with steel fiber. Journal of Science and Technology Development. 2018. 12(18).
16. Chakrabortty, A., Khennane, A. Failure mechanisms of hybrid FRP-concrete beams with external filament-wound wrapping. Advances in Concrete Construction. 2014. 2(1). Pp. 57–75. DOI: 10.12989/acc.2014.2.1.057
17. Jiajun, T., Changchun, P. Experimental Study on Cracking Resistances of RAC Beams with Polypropylene Fibers and Steel Fibers. IOP Conf. Series: Earth and Environmental Science. 2018. 233. DOI: 10.1088/1755-1315/233/3/032040
18. Khai, L.T.Q. The research working together of steel fiber concrete layer and normal concrete layer in double-layer concrete beams by experiment and by ANSYS. Vietnam Journal of Construction. 2017. 11. Pp. 41–45.
19. Liang, L., Tadepalli, P.R., Mo, Y.L., Hsu, T.T.C. Simulation of prestressed steel fiber concrete beams subjected to shear. International Journal of Concrete Structures and Materials. 2016. 10(3). Pp. 297–306. DOI 10.1007/s40069-016-0153-8
20. Ali, A.H., Mohannad, H.A. Influence of steel fiber on the shear strength of a concrete beam. Civil Engineering Journal. 2018. 4(7). DOI: 10.28991/cej-0309190
21. Juan, A.T., Eva, O.L.L. Influence of fiber content on shear capacity of steel fiber-reinforced concrete beams. Fibers. 2019. 7(12). DOI: 10.3390/fib7120102
22. Yasmin, Z.M., Haneen, M.A. The influence of basalt and steel fibers on the flexural behavior of RC beams. International Journal of Civil and Environmental Engineering. 2019. 13(9). Pp. 548–551. DOI: 10.5281/zenodo.3455747
23. Binh, N.T., Thi, N.H. Influence of concrete strength and steel fiber type on the efficiency of using steel fibers in reinforced concrete. Journal of construction sci and tech. 2011. 3.
24. Viet, T.B., Binh, N.T. Study the effect of fiber direction ratio on the strength of steel fiber concrete. Journal of construction science and technology. 2006. 3.
25. Sivakumar, A., Saiful, I., Roohul, A.K. Effect of steel fiber profile on the fracture characteristics of steel fiber reinforced concrete beams. Journal of Engg. Research. 2019. 7(2). Pp. 105–124.
26. Cuong, H.A., Khoi, P.Q. The influence of dispersed steel fibers in enhancing the shrinkage and cracking resistance of sand-cement concrete. Transport Magazine. 2017. 4.
27. Do, T.M.D., Lam, T.Q.K. Solutions to improve the quality of mass concrete construction in climate conditions of Southern Vietnam. International Journal of Innovative Technology and Exploring Engineering. 2019. 8(6C2). Pp. 188–192.
28. Lam, T.Q.K., Do, T.M.D., Ngo, V.T., Nguyen, T.C., Huynh, T.P. Numerical simulation and experiment on steel fiber concrete beams. J. Phys.: Conf. Ser. 2019. 1425 012007. DOI: 10.1088/1742-6596/1425/1/012007
29. Do, T.M.D., Lam, T.Q.K. Analysis of Risk Problems in Construction by R software. International Journal of Engineering and Advanced Technology. 2019. 8(5). Pp. 1872–1875.
30. Tran, H.Q., Lam, T.Q.K., Do, T.M.D. Model of prefabricated concrete frame in the condition of southern Vietnam. E3S Web of Conferences. 2019. 135 03043. DOI: 10.1051/e3sconf/201913503043
31. Do, T.M.D., Lam, T.Q.K., Ngo, V.T. Analysis of axial stiffness reduction factors in thermal analysis of multistorey buildings. International Journal of Advanced Science and Technology. 2020. 29(8s), Pp. 1378–1390.
32. Do, T.M.D., Lam, T.Q.K. Quality of Construction Works at the Design Phase. Lecture Notes in Civil Engineering, 2020. 70. Pp. 15–24. DOI: 10.1007/978-3-030-42351-3_2
33. Lam, T.Q.K., Do, T.M.D., Truong, C.B. Analysis of Structural Failures and Remedial Measures. International Journal of Advanced Science and Technology, 2020, 29(8s), Pp. 2780–2786.
34. Do, T.M.D., Nguyen, T.C., Lam, T.Q.K. Investigating the effectiveness of insulation for walls of buildings in Vietnamese climatic condition. IOP Conf. Series: Materials Science and Engineering. 2020. 869 032008. DOI: 10.1088/1757-899X/869/3/032008

Contacts:

Thi My Dung Do, dothimydung1983@gmail.com

Thanh Quang Khai Lam, lamthanhquangkhai@gmail.com

© Do, T.M.D, Lam, T.Q.K., 2021

Magazine of Civil Engineering

ISSN 2712-8172

journal homepage: http://engstroy.spbstu.ru/

DOI: 10.34910/MCE.102.8

Numerical investigation of truss-shaped braces in eccentrically braced steel frames

M. Haji, F. Azarhomayun, A.R. Ghiami Azad*
University of Tehran, Tehran, Iran
**E-mail: rghiami@ut.ac.ir*

Keywords: finite element method, cyclic loads, stainless steel, buckling, hysteresis, eccentric brace

Abstract. Eccentrically braced frames are one of the most popular systems in buildings because they provide both high stiffness and ductility to the structure. Other systems such as moment frames and concentrically braced frames do not usually provide desirable stiffness and ductility, respectively. Steel shear walls are also popular systems in steel buildings; however, they can be expensive due to the large amount of steel used in these systems. Therefore, it is of interest to investigate new types of eccentrically braced frames. In this paper a truss-shaped brace is proposed and its behavior under cyclic loading in an eccentrically braced frame is numerically investigated using finite element software. Different cross-sections are implemented in the truss-shaped brace and the effect of the cross-section on the behavior of the frame is studied and compared to the reference specimen with conventional configuration. The results of this study show that hollow square cross-section with 100 mm width and 4 mm thickness had the best performance in terms of strength, absorbed energy and pinching compared to other specimens.

1. Introduction

Among seismic lateral load-bearing systems, moment frames, special moment frames in specific, can be considered as seismic load-bearing systems that have high ductility and low stiffness. On the other hand, concentrically braced frames despite having high stiffness, do not have high ductility. In other words, the displacement criterion usually controls the design of special moment frames, whereas in concentrically braced frames the ability to absorb and dissipate earthquake energy controls the design. Eccentrically braced frames (EBF) are in fact a perfect combination of moment frames and concentrically braced frames, which have sufficient stiffness and ductility properties simultaneously. The stiffness of these systems comes from restraining the lateral displacement by bracing and the ductility of these systems are resulted from using link beams that act as fuses under earthquake loads. A fuse shuts down the current in an electrical circuit when the current becomes more than the capacity of the circuit; therefore, not allowing serious damage to the circuit. This is how a link beam works in EBF systems except that the current in the electrical circuit is in fact the load demand in the building.

Eccentrically braced frames (EBF) were first introduced by Fujimot et al. in 1972 and Tanabashi et al in 1974 [1] in Japan. The major development of this system was due to the ongoing research of Popov and his colleagues from 1977 to 1989 [2] on isolated link beams and other specifications and design criteria of these frames at Berkeley Earthquake Research Center.

In 2005 Richards and Uang [3] studied the rotational capacity of eccentrically braced links by modeling 112 specimens with various widths to thickness ratios of flange. Okazaki et al. (2005) [4] tested various sections and lengths for linked beam under different load protocols to investigate the flange slenderness limit as well as the over strength factor of links.

Berman and Bruneau in 2007 [5], investigated the behavior of tabular links with various thickness, yield strength, and stiffener spacing in eccentrically braced frames experimentally and analytically. They also proposed an equation to prevent buckling of web and flange in tabular link. Berman and Bruneau in 2008 [6] conducted a parametric study on the effect of different geometry and properties of tabular links (web and flange compactness ratios, length of links and stiffener spacing). They also reviewed and developed the design

Haji, M., Azarhomayun, F., Ghiami Azad, A.R. Numerical investigation of truss-shaped braces in eccentrically braced steel frames. Magazine of Civil Engineering. 2021. 102(2). Article No. 10208. DOI: 10.34910/MCE.102.8

This work is licensed under a CC BY-NC 4.0

recommendations for built-up box links located in eccentrically braced frames [7]. In another study by Berman et al. in 2010 [8], the reduced section was applied in links to improve link to column connection ductility. They proposed a design procedure for links with reduced section, and also investigated different geometry and lengths of the reduced section and concluded that the reduced section could reduce the strain of the flange.

Pan et al. in 2011 [9] proposed a new eccentrically braced frame by adding a plate between columns and shear links and investigated its behavior experimentally and numerically. In 2011, Daie et al. [10] used pre-bent strips in a brace as a damper and modeled this device in steel frames with different stories using finite element software in order to investigate its behavior. The results indicated that this system had acceptable stiffness, energy dissipation and deformation capacity. Ohsaki and Nakajima in 2012 [11] optimized the location and thickness of the link member which is used between the beam and eccentrically braced frame by using a heuristic method. They also used the finite element method to obtain the deformation of the link member.

In 2013, Zahrai et al. [12] used a pushover and time-history analysis to evaluate the behavior of an upgraded eccentrically braced frames by adding zipper-struts to the middle of braced span. They concluded that zipper-struts increased the ductility coefficient, displacement, and dissipation capacity. Moreover, this system caused distribution of shear force between shear links by connecting them in all stories and dilation of shear link collapse by increasing the rotational capacity. Irandegani and Narmashiri (2013) [13] used aluminum panels instead of steel in steel braced frame as a vertical link. They modeled the frame in ABAQUS and then modeled 1-, 4-, 8-, and 12-story buildings with different types and shapes of aluminum panels. The aluminum panels increased the energy dissipation. Zahrai and Vosooq in 2013 [14], proposed a new dual system including knee elements at the bottom of the eccentric brace and a new vertical link beams above the eccentric braces. They assessed the behavior of this system and two other systems under monotonic and cyclic loading. The new dual system indicated significant energy dissipation and stable behavior.

Lai and Mahin (2014) [15] examined the seismic behavior of a new strong back system. They concluded that this economic system could decrease the concentration of deformation and damage. Andalib et al. [16] in 2014 studied the effect of different steel rings on ductility and performance of off-center braced frames experimentally and numerically. In 2016, Ashikov et al. [17] investigated a new bolted replaceable active link in the eccentrically braced frame numerically under cyclic loading. They founded that this system increased the rotation capacity and had stable cyclic behavior. Simpson and Mahin in 2017 [18] evaluated a new retrofitting system (strong back) to improve weak story behavior in braced frames. They tested two-story braced frames with two different braces (buckling restrained braces and hollow structural steel braces) in the first story and one hollow structural steel brace in the second story. Their proposed system successfully mitigated the behavior of the weak story. Kafi and Kachooee [19] proposed a new brace with an unbuckled fuse in the middle of brace length and studied its cyclic behavior numerically.

In 2019, Bishay-Girges [20] proposed a new damping system instead of eccentrically braced frames and investigated the effect of this system on the behavior of structures. Naghavi [21] used cables for bracing instead of channels in a steel frame and compared the performance of a cabled frame with a moment frame using the finite element method. The cabled frame considerably increased initial stiffness and load capacity. Mohammadi et al. [22] proposed a new composite buckling restrained fuse and investigated the cyclic behavior of this fuse experimentally and numerically and concluded that this fuse had acceptable ductility and energy absorption. Peng et al. [23] applied finite element modeling to investigate the seismic behavior of eccentric, concentric, and concentric with ring damper braced frames. They concluded that adding ring dampers to concentric braced frame improved the seismic performance such as energy dissipation and load-bearing capacity. Kafi and Nik-Hoosh [24] investigated the geometry of blades in dampers on the behavior of concentric steel frames under static cyclic loading and proposed an optimal length to width ratio for blades.

The main purpose of this study is to investigate the seismic behavior of truss-shaped braces in eccentrically steel braced frames and compare its behavior with conventional braces, which has not been studied so far. Fig. 1 schematically shows the objective of this study. The reason for using truss-shaped braces is that due to the multiplicity and variety of load-bearing elements, the performance (stiffness, stress, pinching, and especially shear strength and energy absorption) of steel frames with such braces can be improved in comparison with conventional braces. Due to the fact that the seismic behavior of this type of braces has not been studied, so in this study, various cross-sections are applied to a new truss-shaped brace and the cyclic behavior of this new brace was investigated and compared to a solid brace. Different parameters, including shear resistance, absorbed energy, stiffness degradation, stress demands, mode of failure and pinching, are obtained and presented for all specimens. In addition, a statistical study is performed to predict absorbed energy, shear capacity and pinching of truss-shaped braces applied in eccentrically steel braced frames with square and circular cross-sections and a reasonably accurate equation is proposed for each case.

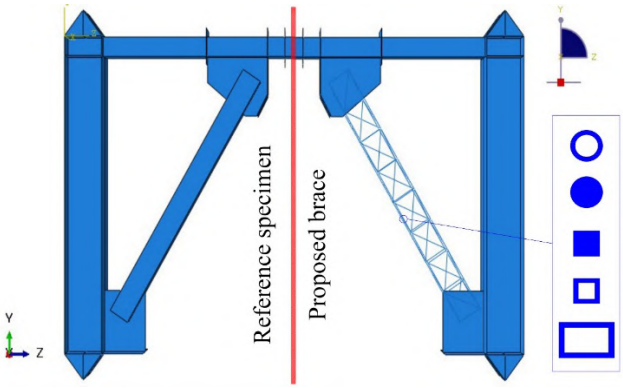

Figure 1. Comparison of the proposed brace comprised of various cross-sections for members with conventional brace.

2. Methods

The use of finite element methods in civil engineering, and especially in the study of concrete and steel structures, has expanded due to its acceptable accuracy and low cost compared to laboratory studies [25]. In this study, the finite element method was used to evaluate the behavior of truss-shaped braces in eccentrically braced steel frames under cyclic loading. First, for the purpose of validation, an experimental frame with an eccentric brace was modeled in ABAQUS software and its results were compared to the experimental specimen. Then the specimens with various brace cross-sections were modeled in ABAQUS and their behavior were studied.

2.1. Model verification

Different eccentric braced frames are presented in Fig. 2 a, b, and c. In this figure, “e” is the length of the link beam. Many experimental studies have been performed on the behavior of eccentric braced steel frames [26–28]. For model verification in finite element software (ABAQUS) [29], a study which was conducted in 2007 by Berman and Bruneau [5], is considered. In the considered frame, the height of the columns is 2460 mm, the length of the beam is 3340 mm, and the length of the braces is 2207 mm. The cross-section of the beam, the column, and the brace are 152×152 mm box, 325×310 wide flange, and 178×178 mm box, respectively. The thickness of the plates used for the flange and the web of columns are 23 and 14 mm, respectively. In addition, the thickness is considered 16 mm, 8 mm, and 11.8 mm for the flange of the beam, the web of the beam, and the braces, respectively. The frame, dimensions and cross-section of the members are shown in Fig. 2d. The thickness of the gusset plates is 13 mm. The modeled gusset plate and its dimensions are shown in Fig. 3.

The frame supports are pinned. In this frame, due to the use of box-shaped cross-sections, the stiffeners are mounted outside the beam to prevent local buckling (Fig. 2d). In order to apply a cyclic lateral load to all specimens, the displacement control method of ASTM E2126-07a [30] was used.

In the study conducted by Berman and Bruneau [5], a hollow rectangular cross-section was applied as link beam in an eccentrically braced frame and the behavior of the frame was investigated. For the purpose of verification, the exact characteristics of the experimental specimen, such as dimensions and cross-sections of the frame and the brace, mechanical properties of steel and the beam to column connection properties were derived from the experimental specimen and were modeled in the finite element software.

The static general analysis in Abaqus was used in this study. The type of elements which were used for meshing the frame, and the proposed brace were shell (S4R), and beam (B31), respectively. The approximate global size of 10 was employed for the mesh size, which was selected based on the accuracy of the results of the verification study. Based on the study by Bruneau and Berman [5], two types of grade 50 steel (elastic-perfectly plastic model) were used for the flange and the web (Fig. 4). The yield stress of steel for the web and the flange material was defined 448 and 393 MPa, respectively. The values of density, young’s modulus and Poisson’s ratio were taken to be 785 kg/m^3, 210000 MPa and 0.3 respectively for both types of steels. The displacement of the frame was measured at a point above the column (U3). Also, the support reaction force (RF3) was obtained in the z-direction for the displacements applied to the specimen. In order to plot the cyclic curve, these values were plotted together.

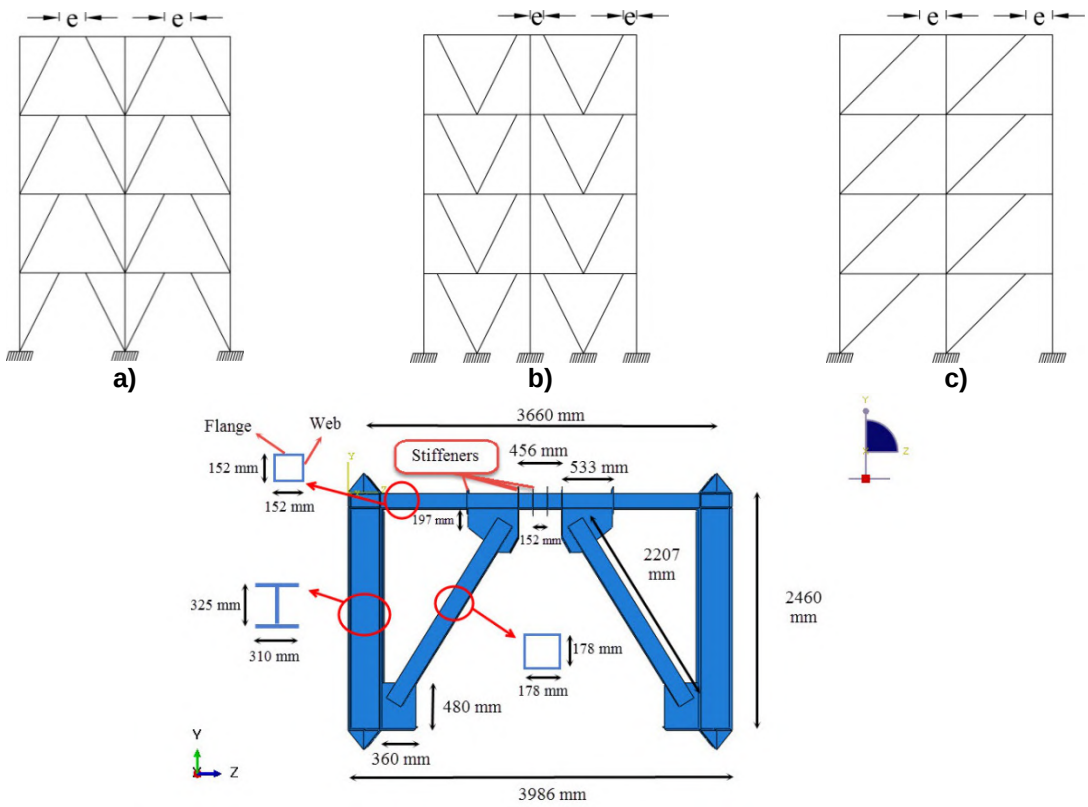

Figure 2. a, b, c) Different types of eccentric braced frames, and d) Dimensions of modeled frame for verification.

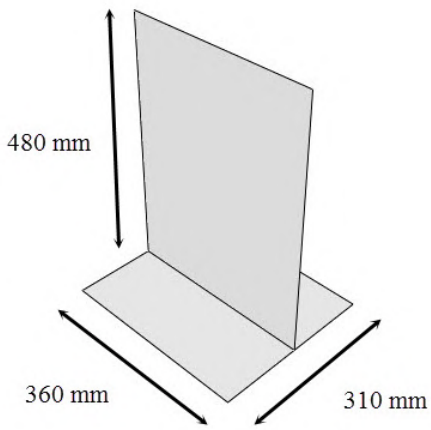

Figure 3. Dimensions of the gusset plate.

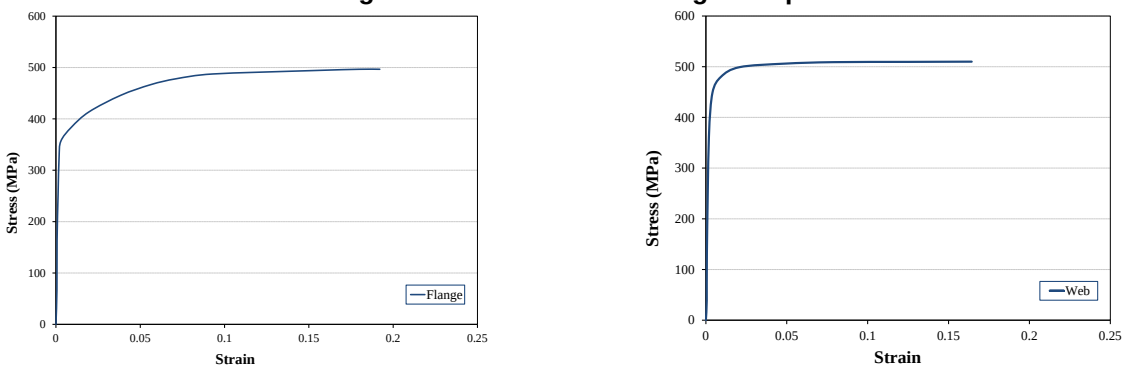

Figure 4. Stress-strain diagrams of steels which were used for a) Flange (type 1), and b) web (type 2) in the experimental study [5].

The ATC-24 [31] loading protocol is used which was used in the Berman and Bruneau study [5]. The rotation of the link beam versus its shear was obtained and was compared to the experimental results. In Fig. 5 the comparison of these two graphs are presented. As shown in this figure, the numerical modeling exhibits reasonable correlation with the experimental results. Although certain correlation between the graphs is observed, some difference is also clearly seen. Differences in experimental and numerical results can be due to two general items: 1. Experimental errors: errors caused by laboratory equipment such as lack of instrumentation calibration, human errors during testing, etc. 2. Errors of numerical methods: these errors can be due to modeling errors, use of simplification hypotheses and techniques (in defining materials, type of connections and supports, and etc.), type of elements, type of analysis, number of degrees of freedom, and etc. Because of all the aforementioned inevitable uncertainties, the difference observed in this study can be acceptable.

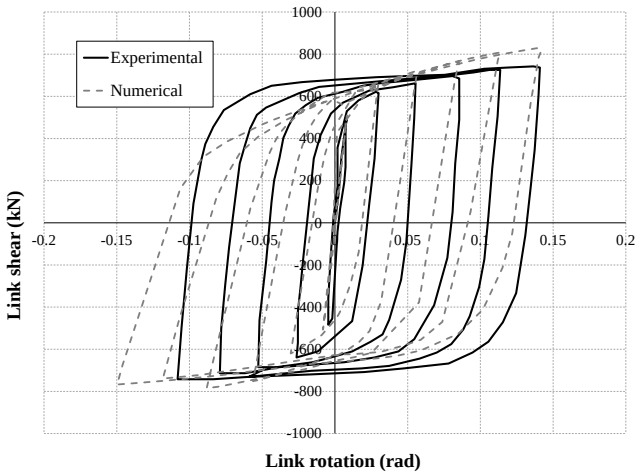

Figure 5. Comparison of experimental results with numerical results.

2.2. Proposed models

In this study, a reference specimen similar to the specimen intended for validation, and 10 specimens similar to the reference specimen but braced with truss-shaped brace (which is shown in Fig. 6) were modeled. Various cross-sections (Table 1) were considered for all the members of truss-shaped brace to investigate the behavior of these braces located in the eccentrically braced steel frame instead of the ordinary brace with a solid section. Six groups of sections including solid and hollow circle, square and rectangle with different dimensions were considered. The mechanical properties of steel (Fig. 4) in all specimens were considered the same as the verified model. For all members, type 1 steel was used except for the web of the beam and column, in which type 2 steel was used.

The geometry of each cross-section, its dimensions, specimen's name, and the moment of inertia of each cross-section are provided in Table 1. Due to the availability of sections in the market, the dimensions of the sections were selected from the Stahl table [32].

Table 1. Cross-sections used in the braces.

Cross-section	Dimensions (cm)	Specimen Name	Moment of Inertia (cm^4)
	r = 1.75	CS1	7.36
	r = 2	CS2	12.56
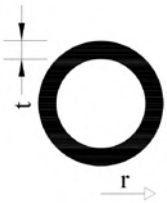	r = 3.8, t = 0.4	CH1	58.78
	r = 4.45, t = 0.6	CH2	135.36

Cross-section	Dimensions (cm)	Specimen Name	Moment of Inertia (cm^4)
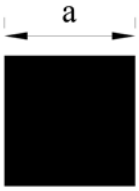	a = 3.2	SS1	8.74
	a = 3.5	SS2	12.5
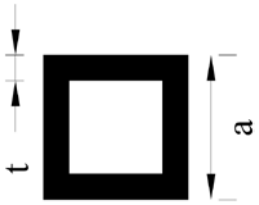	a = 6, t = 0.5	SH1	31.75
	a = 10, t = 0.4	SH2	125.54
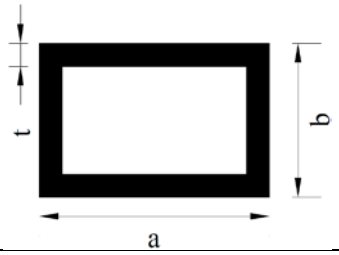	a = 9, b = 5, t = 0.4	RH1	59.93
	a = 12, b = 8, t = 0.4	RH2	163.43

Due to the size of the cross-sections (one relatively smaller dimension compared to other dimensions), all the elements were modeled by shell elements, except for the braces in the reference specimen, which was modeled with beam elements. The Standard reduced integration shell element type (S4R) was selected for mesh element type, which reduced the computation time without significant effect on the results. Furthermore, a beam element was used to mesh the braces. All the members of frame were merged, and tie constraints were used to connect the braces to the frame. In order to take into account the buckling effect in members, the imperfection load was applied to the frame. In Fig. 6 the geometry of the proposed brace and its dimensions are shown. The sections in Table 1 are used for the members of the proposed brace.

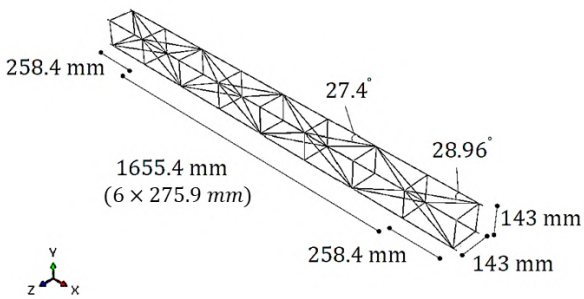

Figure 6. The proposed brace implemented in the steel frame.

3. Results and Discussion

In this section, the results of finite element modeling, such as hysteresis curve, absorbed energy, stiffness degradation, stress, mode of failure and pinching, are presented for all the specimens. The results are compared with each other, as well as with the reference specimen, which is the verified model of the specimen experimentally investigated by Bruneau and Berman [5].

3.1. Hysteresis Curves

To assess the seismic behavior of the proposed braces, a cyclic displacement was applied to the top of the columns. The protocol applied to the specimen includes displacements of 12, 15, 21, 30, 45, 60, 85, 105, 135, 150, 195 mm. In order to consider the buckling effect, an eccentric load was applied to the left side of the link beam. As shown in Fig. 7a, this force generates a very small displacement at the left side of the beam. The hysteresis curves of all specimens are presented in Fig. 8. The displacement value was measured at a point above the column (Fig. 7b).

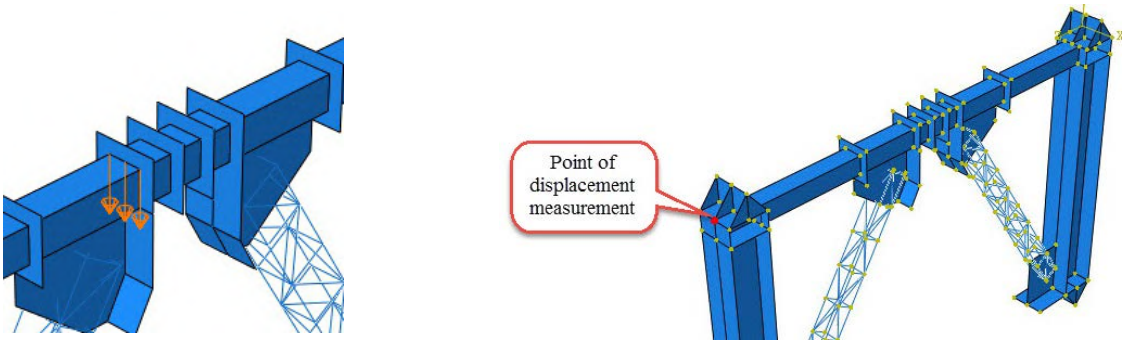

(a) (b)

Figure 7. a) Applying eccentric load, and b) Point of displacement measurement.

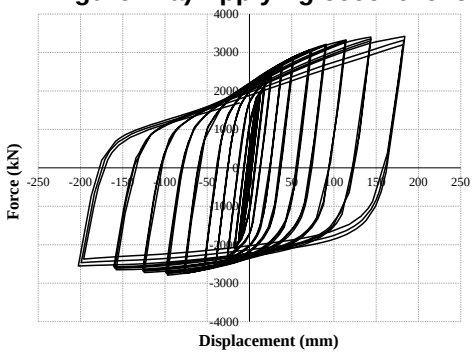

Reference

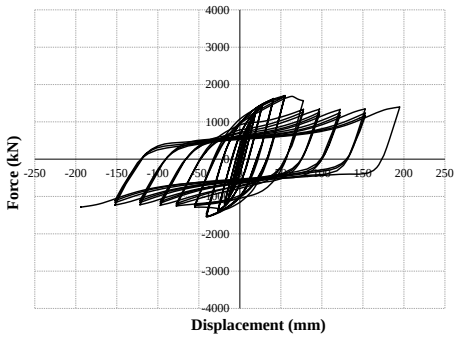

SS1

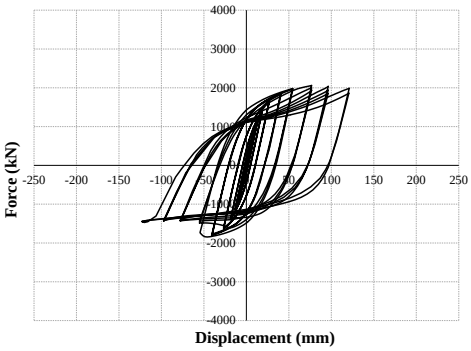

SS2

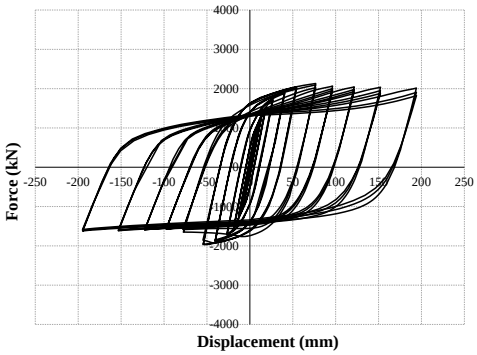

SH1

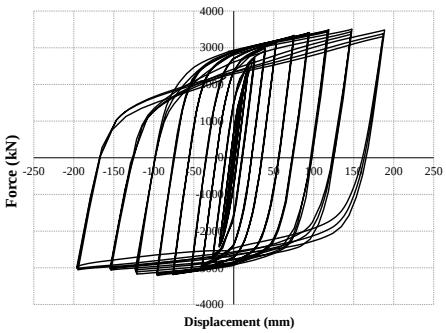

SH2

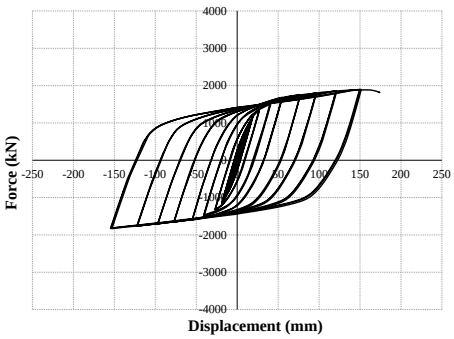

RH1

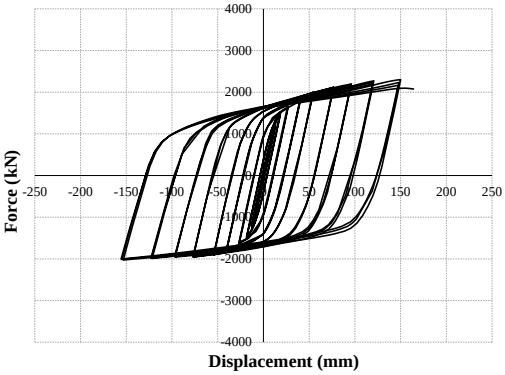

RH2

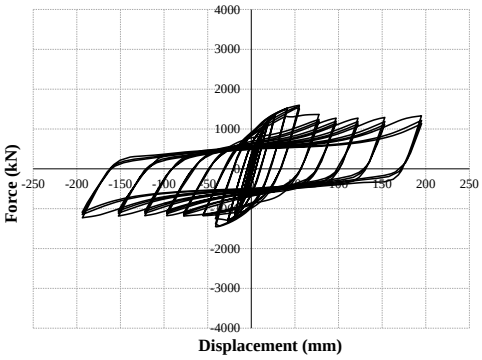

CS1

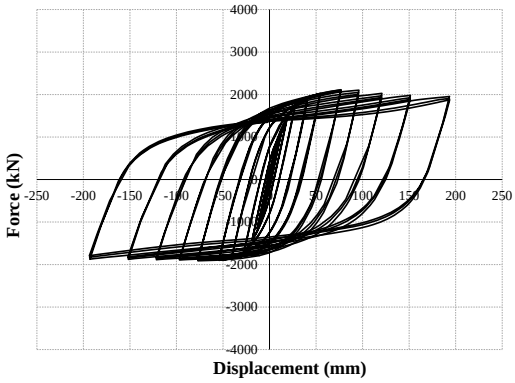

CS2

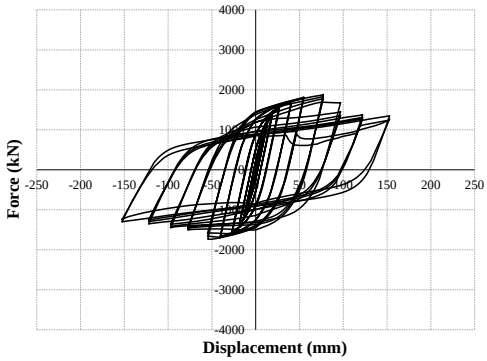

CH1

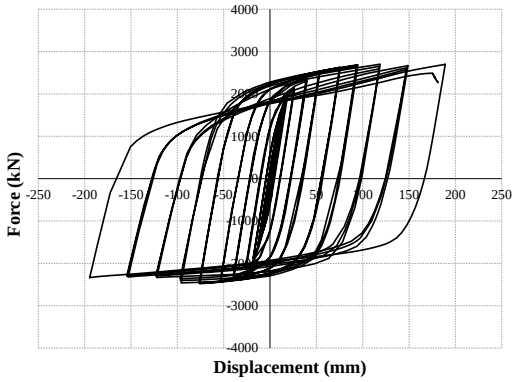

CH2

Figure 8. Hysteresis curves of specimens.

3.2. Absorbed Energy

The meaning of absorbed energy in this section is the area under the force-displacement cyclic curve. In order to compare the absorbed energies in all specimens, this parameter was computed up to the displacement of 150 mm and is present in Table 2. The maximum shear strength tolerated by each specimen is also presented in Table 2. In addition, the difference of absorbed energy and shear strength in all specimens compared to the reference specimen was computed and presented in percent.

Table 2. Comparison of the absorbed energy, and shear strength values of the proposed specimens with those of the reference specimen.

Specimen name	Absorbed Energy (kN.mm)	Difference with the Reference Specimen (%)	Shear Strength (kN)	Difference with Reference Specimen (%)
Reference	1.06E+07	---	3420.11	---
SS1	3.85E+06	63.57	1705.65	50.13
SS2	3.95E+06	62.67	2062.81	39.68
SH1	7.26E+06	31.35	2130.79	37.7
SH2	1.1E+07	-30.71	3510.46	-2.64
RH1	6.71E+06	36.54	1896.92	44.54
RH2	8.35E+06	21.07	2302.31	32.68
CS1	3.60E+06	65.93	1598.85	53.25
CS2	7.52E+06	28.93	2113.55	38.2
CH1	5.24E+06	50.48	1884.48	44.9
CH2	1.05E+07	1.15	2705.13	20.9

In this table the negative sign indicates an increase in the desired parameter compared to the reference specimen. As shown in Table 2, all the specimens showed lower absorbed energy and shear capacity compared to the reference specimen except specimen SH2 with 30.71 % and 2.64 % increase in absorbed energy and shear capacity, respectively. Moreover, in specimen CH2 the results are almost similar to the reference specimen.

In each cross-section with defined geometry, absorbed energy and shear strength increased with increasing cross-section dimensions. The hollow sections indicated acceptable results compared to solid sections such that the hollow square, circle, and rectangular geometries had the top three best responses, respectively. In solid cross-sections, the square cross-section also showed better performance than the circle geometry.

3.3. Stiffness Degradation

The diagram of secant stiffness versus displacement for all the specimens in the positive direction (the direction with the greatest force tolerated) is shown in Fig. 9. To obtain the secant stiffness, the maximum force in three cycles with equal displacement (first cycle) was divided by its corresponding displacement. As indicated in Fig. 9, the reference specimen (indicated by "R" in the figure), SH2, CH2 and CS1 specimens exhibited the highest initial stiffness, respectively. As the displacement increased from 19 mm to 125 mm, specimen SH2 followed by the reference specimen showed the highest stiffness. Moreover, stiffness degraded faster in specimens SS1, CS1 and RH1.

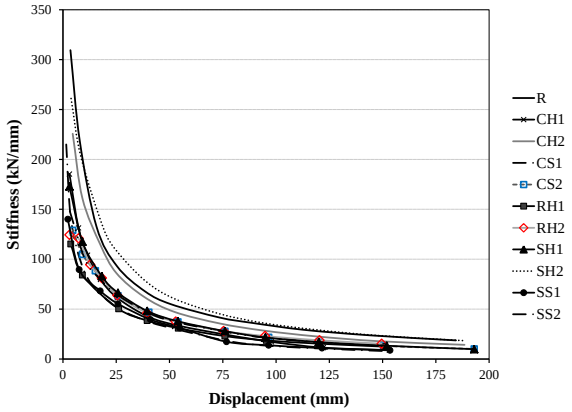

Figure 9. Stiffness degradation versus displacement for all specimens.

3.4. Von Mises Stresses and Modes of Failure

The von Mises stress values in braced frames are presented at the end of loading for all specimens in Fig. 10. The modes of failure can be seen in this figure as well.

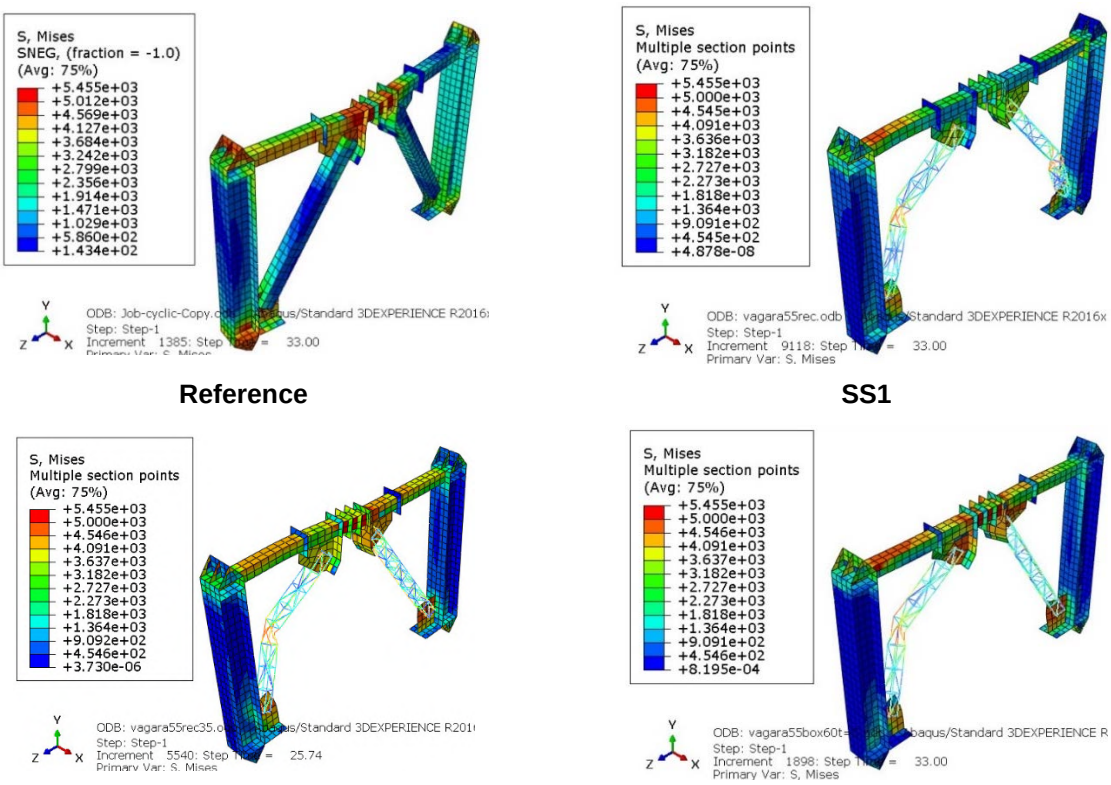

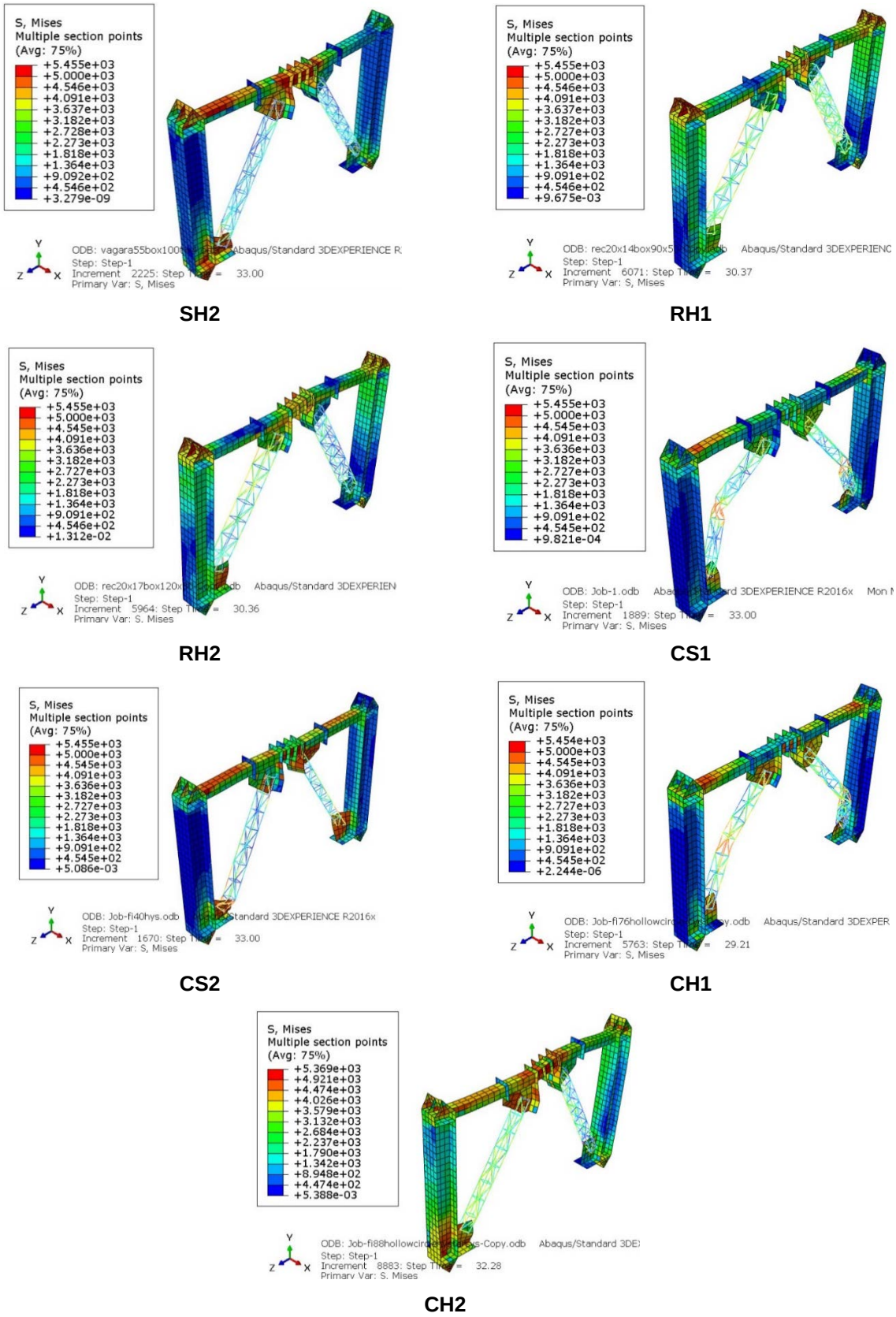

Figure 10. The stresses (kg/cm^2) in all specimens at the end of loading.

As seen in Fig. 10, the maximum stresses in the reference specimen, SS2, SH1, SH2, CS2 and CH2 happened in the linked beam. The stress distribution in specimen SH2 is remarkably close to that of the reference specimen, while specimen RH1 had the lowest stress in the beam compared to other specimens. In specimens SS1, RH1, RH2, and CH2, the stresses in the beam are lower and more stress is tolerated by the braces and gusset plates compared to other specimens. The connections between the beams and columns are fixed to withstand the moment caused by lateral loads (earthquake or wind) in addition to vertical shear stress. If the beam-to-column connection is fixed, the moment tolerated by the beam and the column is greater

that tolerated by the brace. In terms of shear, shear tolerated by the column and the brace is greater than that tolerated by the fixed joint.

The brace buckling occurred in specimens SS1, SS2, SH1, CS1 and CH1 while in other specimens such as SH2, RH1, RH2, CS2, and CH2 the left gusset plate distortion was observed, which is shown in Fig. 11. In cyclic loading, the first force that caused out of plane movement of the braces was considered as the buckling force. The buckling force of these specimens are presented in Table 3. In this table, the buckling load is the load that causes the brace to buckle. The negative sign means that buckling occurred first in the left brace. According to Table 3 the specimens with solid circle (CS1) and hollow square cross-sections (SH1) had the lowest and highest buckling load, respectively, whereas the braces with rectangular cross-sections did not experience buckling in the brace.

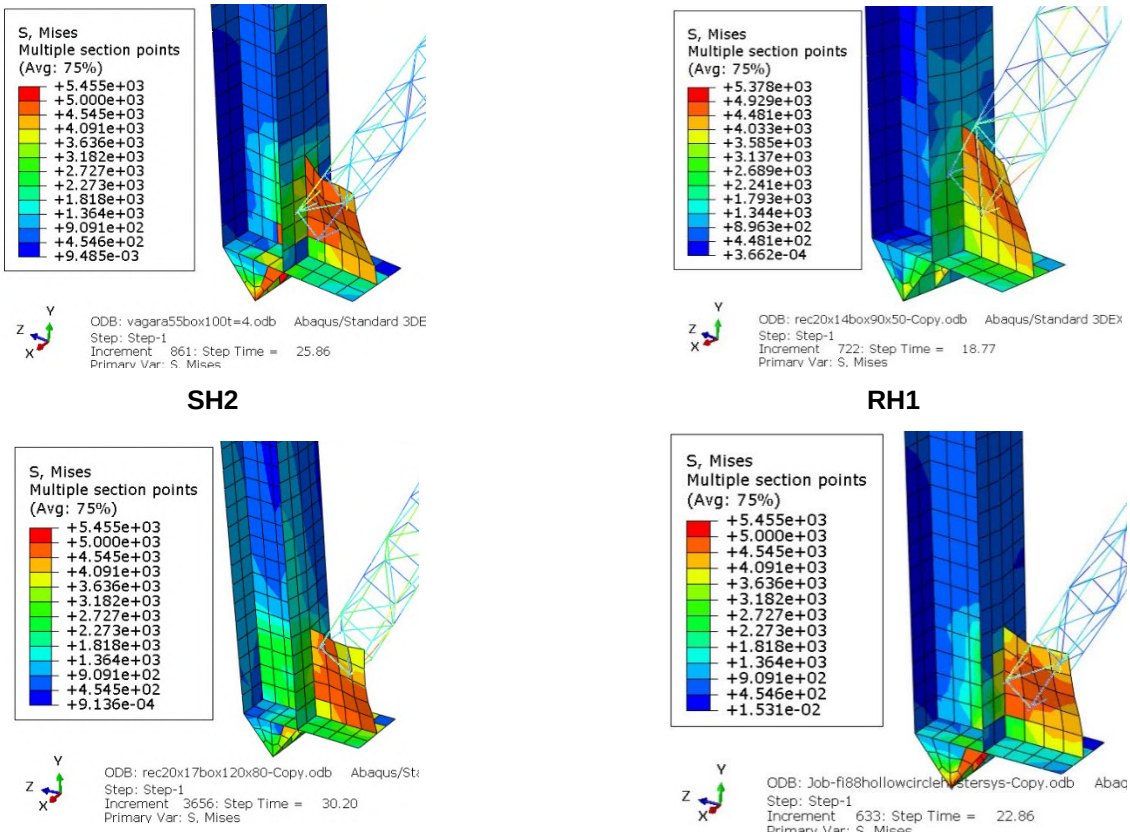

Figure 11. The gusset plate distortion.

Table 3. Buckling loads of specimens.

Specimen	Buckling Load (kN)
SH2	-1544.98
SS2	-1839.41
SH1	-1853.15
CS1	-1116.06
CH1	-1733.94

In the reference specimen, the beam was deflected and moved out of plane (Fig. 12), whereas this deflection was not seen in specimens SH2 and CH2. This may be attributed to the fact that the beam is weaker than the braces in the reference specimen. Therefore, before the braces can withstand much stress, the beam undergoes non-linear and plastic deformation and moves out of its plane.

According to Table 3 the specimens with solid circle (CS1) and hollow square cross-sections (SH1) had the lowest and highest buckling load, respectively, whereas the braces with rectangular cross-sections did not experience buckling in brace.

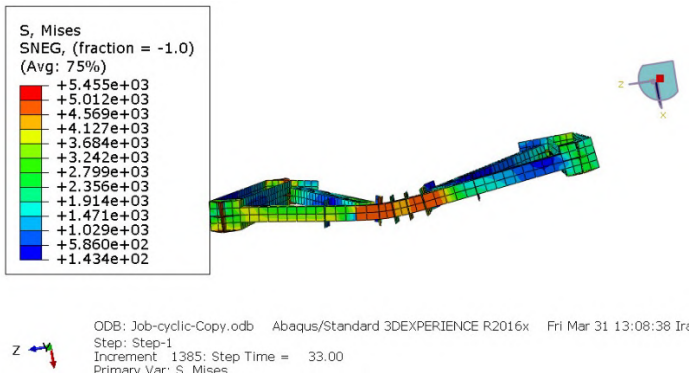

Figure 12. Deviation from the main axis of the beam (out-of-plane displacement) in the reference specimen.

3.5. Pinching

Pinching is the amplitude of the force which corresponds to the maximum force range tolerated by the specimen. The distance between the minimum and maximum force tolerated by the specimen on the vertical part of the cyclic diagram is defined as pinching. Pinching is a measure of the degree of ductility and energy absorption of a specimen. The smaller the amount of pinching is, the more flexible and ductile the behavior of the frame is [33]. Pinching is defined by parameter "X" in Fig. 13. Pinching was calculated for all specimens and is presented in Table 4. To calculate pinching, the distance between maximum and minimum forces in vertical axis was determined and presented. Note that more pinching means that the distance "X" in Fig. 13 is in fact smaller.

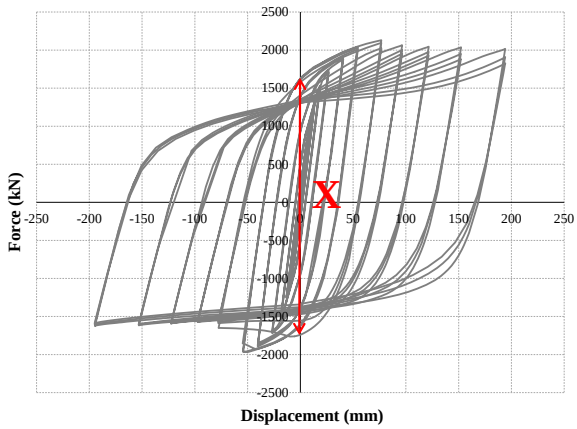

Figure 13. Pinching in hysteresis curve.

Table 4. The amount of pinching for all specimens.

Specimen name	Pinching (kN)
Reference	4579.71
SS1	2235.3
SS2	2930.67
SH1	3407.17
SH2	5915.96
RH1	2867.65
RH2	3382.35
CS1	1949.787
CS2	3413.87
CH1	2966.39
CH2	4588.23

According to Table 4, the amount of parameter "X" in SH2, CH2 and the reference specimen is more than that in other specimens. This means that specimens SH2, CH2 have ductile and flexible behavior.

3.6. Prediction

In this section, prediction means obtaining the values of absorbed energy, shear strength and pinching for frames with truss-shaped braces based on the results obtained in this study. According to the results, as

well as the moments of inertia for each section, the prediction of each result was performed using trend lines. Diagram of absorbed energy, shear strength and pinching changes versus moment of inertia for each section in each group (circle and square) was plotted and the best relationship was obtained for each case using trend lines. These diagrams for the circular and square sections are shown in Fig. 14 and 15, respectively. In these figures, the points are the values obtained by the finite element method and the lines are regression lines. In each diagram, the values of R^2 for the regression lines are provided, which indicates the accuracy of the prediction. In each case, the best type of regression which had a value of R^2 closer to one was selected.

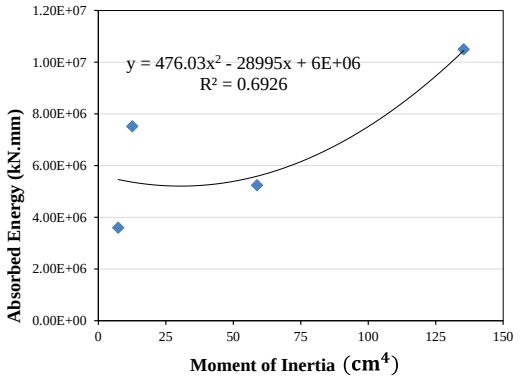

a) Absorbed energy

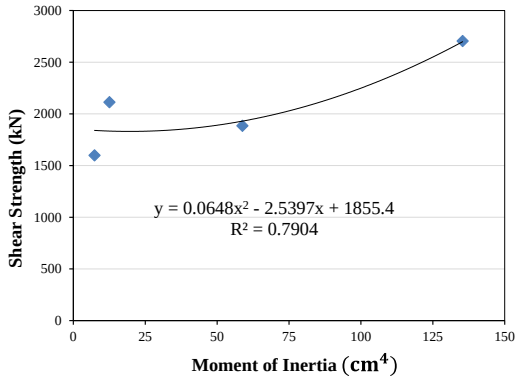

b) Shear strength

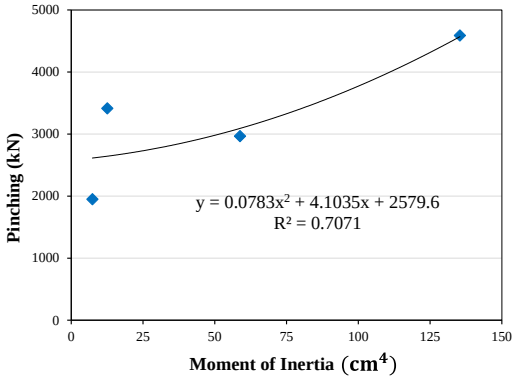

c) Pinching

Figure 14. Regression of results for circular cross-sections.

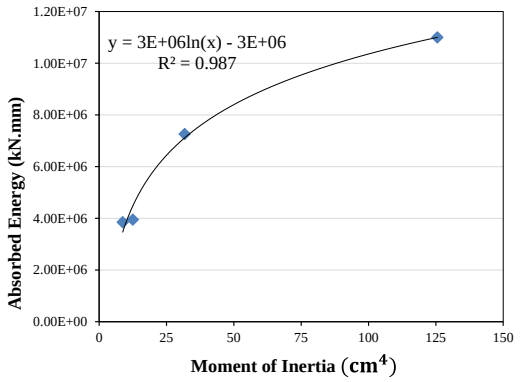

a) Absorbed energy

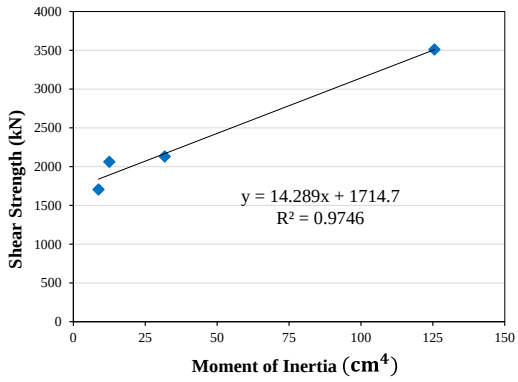

b) Shear strength

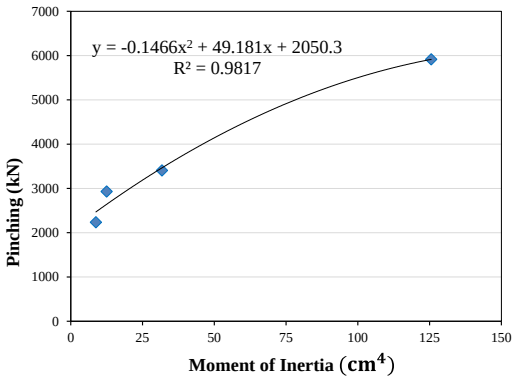

c) Pinching

Figure 15. Regression of results for square cross-sections.

For both circular and square sections, second order polynomial was used as regression type to predict the results. However, a logarithmic function was considered for regression in square sections for absorbed energy. The values of R^2 for the square sections are closer to one than the circular sections, indicating better performance of the considered functions in predicting the results for these sections.

4. Conclusion

In this paper, a new truss-shaped brace was proposed, and the cyclic behavior of this new brace was investigated numerically. The variables in the models included the geometric shapes of the cross-section (solid/hollow and circle/square/rectangular). Nonlinear analysis was performed by finite element software, the results were obtained and some parameters such as shear strength, absorbed energy, stiffness degradation, stress, failure mode and pinching were presented for all specimens and compared to the reference specimen. Also, some equations were presented based on obtained results for the absorbed energy, shear strength, and pinching of circular and square cross-sections versus moment of inertia. The most important results are as follow:

- In terms of absorbed energy, the hollow square section with width and thickness of 100 and 4 mm (SH2), with 30.71 % increase compared to the reference specimen showed the best performance among all specimens. In the brace with hollow circular cross-section with the radius of 44.5 mm and the thickness of 6 mm, the absorbed energy was almost similar to the reference specimen. Also, the same results were obtained for the shear strength, except that the amount of increase in shear strength compared to the reference specimen was 2.64 % in SH2.
- The brace buckling was observed in at least one of each cross-section shapes, expect in the braces with hollow rectangular cross-section. The lowest stresses in the frame due to cyclic loading were also observed in the braces with this kind of cross-section. Among the buckled braces, the braces with solid circular cross-section and hollow square cross-section had the lowest and highest buckling load, respectively.
- Initial stiffness in the reference specimen and SH2 specimens had the highest amounts and the stiffness reduction rate in these two specimens was minimal in comparison with other specimens.
- It can be concluded from the pinching values that the new brace with hollow square cross-section with bigger dimensions (SH2) with 29.18 % increase in pinching compared to the reference specimen showed more ductile behavior than the rest of the specimens.

Finally, by increasing the moment of inertia of the proposed brace cross-section, its performance such as shear capacity, absorbed energy, stiffness degradation, stresses in members, mode of failure and pinching, improves. However, more research is required to better understand the behavior of truss-shaped braces in eccentrically braced frames. Conducting full-scale experiments are highly recommended to further back up the results of this study. In addition, studying this brace in concentrically braced frames is recommended to better understand the behavior of this type of brace.

References

1. Tanabashi, R., Naneta, K., Ishida, T. On the rigidity and ductility of steel bracing assemblage. Proceedings of the 5th World Conference on Earthquake Engineering. Rome, 1974. Pp. 834–840.
2. Popov, E.P., Kasai, K., Engelhardt, M.D. Advances in design of eccentrically braced frames. Earthquake Spectra. 1987. 3(1). Pp. 43–55.
3. Richards, P.W., Uang, C.M. Effect of flange width-thickness ratio on eccentrically braced frames link cyclic rotation capacity. Journal of Structural Engineering. 2005. 131(10). Pp. 1546–1552. DOI: 10.1061/(ASCE)0733-9445(2005)131:10(1546)
4. Okazaki, T., Arce, G., Ryu, H.C., Engelhardt, M.D. Experimental study of local buckling, overstrength, and fracture of links in eccentrically braced frames. Journal of Structural Engineering. 2005. 131(10). Pp. 1526–1535. DOI: 10.1061/(ASCE)0733-9445(2005)131:10(1526)
5. Berman, J.W., Bruneau, M. Experimental and analytical investigation of tubular links for eccentrically braced frames. Engineering Structures. 2007. 29(8). Pp. 1929–1938. DOI: 10.1016/j.engstruct.2006.10.012
6. Berman, J.W., Bruneau, M. Tubular links for eccentrically braced frames. I: Finite element parametric study. Journal of Structural Engineering. 2008. 134(5). Pp. 692–701. DOI: 10.1061/(ASCE)0733-9445(2008)134:5(692)
7. Berman, J.W., Bruneau, M. Overview of the development of design recommendations for eccentrically braced frame links with built-up box sections. Engineering Journal-American Institute of Steel Construction. 2013. 50(1). Pp. 21–31.
8. Berman, J.W., Okazaki, T., Hauksdottir, H.O. Reduced link sections for improving the ductility of eccentrically braced frame link-to-column connections. Journal of Structural Engineering. 2010. 136(5). Pp. 543–553. DOI: 10.1061/(asce)st.1943-541x.0000157
9. Pan, X., Hao, J., Gao, J. Study of adding cover-plate used for the single diagonal eccentrically braced steel frames. Open Civil Engineering Journal. 2011. No. 5. Pp. 143–153.
10. Daie, M., Jalali, A., Suhatril, M., Shariati, M., Arabnejad Khanouki, M.M., Shariati, A., Kazemi-Arbat, P. A new finite element investigation on pre-bent steel strips as damper for vibration control. International Journal of the Physical Sciences. 2011. 6(36). Pp. 8044–8050. DOI: 10.5897/IJPS11.1585
11. Ohsaki, M., Nakajima, T. Optimization of link member of eccentrically braced frames for maximum energy dissipation. Journal of Constructional Steel Research. 2012. No. 75. Pp. 38–44. DOI: 10.1016/j.jcsr.2012.03.008

12. Zahrai, S.M., Pirdavari, M., Momeni Farahani, H. Evaluation of hysteretic behavior of eccentrically braced frames with zipper-strut upgrade. Journal of Constructional Steel Research. 2013. No. 83. Pp. 10–20. DOI: 10.1016/j.jcsr.2012.12.017
13. Irandegani, M.A., Narmashiri, K. Numerical study on aluminum panels used in braced steel frames as energy dissipation systems. International Journal of Physical Sciences. 2012. 7(10). Pp. 1661–1669.
14. Vosooq, A.K., Zahrai, S.M. Study of an innovative two-stage control system: Chevron knee bracing & shear panel in series connection. Structural Engineering and Mechanics. 2013. 47(6). Pp. 881–898. DOI: 10.12989/sem.2013.47.6.881
15. Lai, J.W., Mahin, S.A. Strongback system: a way to reduce damage concentration in steel-braced frames. Journal of Structural Engineering. 2015. 141(9). Pp. 04014223. DOI: 10.1061/(ASCE)ST.1943-541X.0001198
16. Andalib, Z., Kafi, M.A., Kheyroddin, A., Bazzaz, M. Experimental investigation of the ductility and performance of steel rings constructed from plates. Journal of Constructional Steel Research. 2014. 103. Pp. 77–88. DOI: 10.1016/j.jcsr.2014.07.016
17. Ashikov, A., Clifton, G.C., Belev, B. Finite element analysis of eccentrically braced frames with a new type of bolted replaceable active link. New Zealand Society for Earthquake Engineering (NZSEE) Annual Technical Conference. Christchurch, 2016. Pp. 1–9.
18. Simpson, B.G., Mahin, S.A. Experimental and numerical investigation of strongback braced frame system to mitigate weak story behavior. Journal of Structural Engineering. 2018. 144(2). Pp. 04017211. DOI: 10.1061/(ASCE)ST.1943-541X.0001960
19. Kafi, M.A., Kachooee, A. The behavior of concentric brace with bounded fuse. Magazine of Civil Engineering. 2018. 78(2). Pp. 16–29.
20. Bishay-Girges, N.W. An Alternative system for eccentrically braced frames resisting lateral loads. Engineering, Technology & Applied Science Research. 2019. 9(3). Pp. 4281–4286.
21. Naghavi, M.S. Retrofitting steel moment frames using cable bracing. Journal of Building Material Science. 2019. 1(01). Pp. 10–17.
22. Mohammadi, M., Kafi, M.A., Kheyroddin, A., Ronagh, H.R. Experimental and numerical investigation of an innovative buckling-restrained fuse under cyclic loading. Structures. 2019. 22. Pp. 186–199. DOI: 10.1016/j.istruc.2019.07.014
23. Peng, X., Lin, C., Cao, Y., Duan, W. Nonlinear finite element simulation on seismic behavior of steel frame-central brace with ring damper. IOP Conference Series: Materials Science and Engineering. 2019. 472. Pp. 012031. DOI: 10.1088/1757-899X/472/1/012031
24. Kafi, M.A., Nik-Hoosh, K. Geometry of steel slit dampers in a braced steel frame under cyclic loading. Magazine of Civil Engineering. 2019. 87(3). Pp. 3–17.
25. Haji, M., Naderpour, H., Kheyroddin, A. Strengthening of reinforced concrete bridge columns with FRP, using wrapping, near-surface mounted and combined methods. Journal of Transportation Infrastructure Engineering. 2018. 3(4). Pp. 33–48.
26. Popov, E.P., Engelhardt, M.D. Seismic eccentrically braced frames. Journal of Constructional Steel Research. 1988. 10. Pp. 321–354. DOI: 10.1016/0143-974X(88)90034-X
27. Wang, F., Su, M., Hong, M., Guo, Y., Li, S. Cyclic behavior of Y-shaped eccentrically braced frames fabricated with high-strength steel composite. Journal of Constructional Steel Research. 2016. 120. Pp. 176–187. DOI: 10.1016/j.jcsr.2016.01.007
28. Mansour, N., Christopoulos, C., Tremblay, R. Experimental validation of replaceable shear links for eccentrically braced steel frames. Journal of Structural Engineering. 2011. 137(10). Pp. 1141–1152. DOI: 10.1061/(ASCE)ST.1943-541X.0000350
29. HKS. ABAQUS standard user's manual. Hibbitt, Karlsson, and Sorensen, Inc.2001.
30. ASTM. Standard test methods for cyclic (reversed) load test for shear resistance of vertical elements of the lateral force resisting systems for buildings. 2009.
31. ASTM. Standard test methods and definitions for mechanical testing of steel products, A370-03a. ASTM International. 2003.
32. EN 10365 – The European Norm for Structural Sections in Steel. 2017.
33. Haji, M., Naderpour, H., Kheyroddin, A. Experimental study on influence of proposed FRP-strengthening techniques on RC circular short columns considering different types of damage index. Composite Structures. 2019. 209. Pp. 112–128. DOI: 10.1016/j.compstruct.2018.10.088

Contacts:

Mohammad Haji, mohammadhaji@semnan.ac.ir

Fazel Azarhomayun, fazel.azarhomayun@ut.ac.ir

Amir Reza Ghiami Azad, rghiami@ut.ac.ir

© Haji, M., Azarhomayun, F., Ghiami Azad, A.R., 2021

Magazine of Civil Engineering

ISSN 2712-8172

journal homepage: http://engstroy.spbstu.ru/

DOI: 10.34910/MCE.102.9

Setting seismic input characteristics required for designing

S.V. Prokopovich[a]*, A.M. Uzdin[a], T.V. Ivanova[b]
[a] Petersburg State Transport University, St. Petersburg, Russia
[b] B.E. Vedeneev VNIIG", JSC, Saint Petersburg, Russia
**E-mail: spr94@outlook.com*

Keywords: models of seismic input, velocity impulse, characteristics of seismic effects, seismic design, structure damage spectrum, response spectrum of the work of plastic deformation forces

Abstract. The paper is devoted to the analysis of seismic input characteristics from the point of view of their importance for engineers. It is noted that the design input does not need to have an external resemblance to the real one but it must provide for some properties of real actions. The paper considers three groups of seismic input characteristics: kinematic, spectral and energy ones. The stability of the characteristics under consideration is analyzed within the seismic intensity on the MSK scale. Among all characteristics, peak acceleration, peak velocity, harmonicity coefficient, Arias intensity, and absolute cumulative velocity are highlighted. It is noted that the kinematic characteristics significantly depend on the prevailing accelerogram period, and many energy characteristics are stable within the seismic intensity under consideration and can describe it. It is noted that for calculating structures under the design earthquake action, the kinematic characteristics should be fundamental for the engineer, and for calculating structures under the destructive (maximum design) earthquake action, the energy characteristics are fundamental. Two new seismic input characteristics are introduced, which are based on the response spectrum of the work of plastic deformation forces and on the structure damage spectrum.

1. Introduction

Using certain models of seismic input is widely discussed in literature [1–11].

When selecting seismic input models, different authors considered to various characteristics of real actions.

According to widespread opinion, it is the necessary to use a package of past earthquake accelerograms. It is supposed that this way makes it needless to study the properties of seismic effects that define the structure behavior under seismic actions. Hazardous input is assumed to be found in the packet under consideration and if you get a lot of real actions from different places, it is most likely to be there. However, in practice the design action package includes about 60–100 accelerograms and sometimes less, which is not enough, which is a significant drawback of this way. You can get 100 high-frequency accelerograms and draw a wrong conclusion about the high seismic resistance of a weakly damped seismically insulated structure. Therefore, selecting past earthquake accelerograms must be carried out together with engineers, who know what is dangerous for their constructions.

Another, less important, but also significant drawback of this approach is an enormous amount of necessary calculations, though not more than 2–3 inputs from the accelerogram package turn out dangerous. Calculating the structure using other accelerograms will be "redundant." Hence, attempts to specify a limited number of design inputs that should simulate real ones are made. In so doing, the central question to answer is the question of what properties of real actions should be taken into account when modeling design input. In our opinion, we do not have to “copy” the real earthquake functions, but it is necessary to mark out the main features of real actions and to take these features into account in the process of generating input. Such approach has been in fact developed in earthquake engineering over the past 60 years.

The first experts in earthquake engineering used harmonics as an action model.

Prokopovich, S.V., Uzdin, A.M., Ivanova, T.V. Setting seismic input characteristics required for designing. Magazine of Civil Engineering. 2021. 102(2). Article No. 10209. DOI: 10.34910/MCE.102.9

This work is licensed under a CC BY-NC 4.0

The founders of modern earthquake engineering in the USSR used the action model in the form of a damped sinusoid. Furthermore, complex models were used in the form of Berlage polynomial, Puzyrev polynomial, Gelfand polynomial and polynomial proposed by N. Ricker [12].

These models based primarily on specifying peak ground accelerations (PGA) and possible action frequency. In most cases, the authors analyzed the base acceleration, not paying attention to the displacements, so many input processes, except the Berlage polynomial, were unbalanced and led to huge displacements. The second feature of most processes is that all processes are narrowband, i.e. one frequency is dominant.

Working with a linear system, when the system spectrum is known, several narrow-band processes can be used. To use one process, a number of experts proposed a variable frequency input models. They believed that such processes would be broadband. This result is described in some Russian textbooks: the authors showed that they provide only PGA of real actions and do not estimate displacements.

In [9] it was proposed to use well-known models of accelerograms to describe velocigrams. Then the processes become balanced, i.e. the velocity at the end of the process becomes 0, and the residual displacements are limited. However, the processes under consideration are still quite narrowband. As an example, the acceleration spectrum of the Annaev – Uzdin process [9] is given in Fig.1. Accelerograms, seismograms, and characteristics of models are shown above in Tables 1-3.

Table 1. Unbalanced processes.

№	Model name	Model accelerogram	Model seismogram
1	Gelfand's model	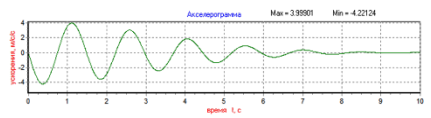	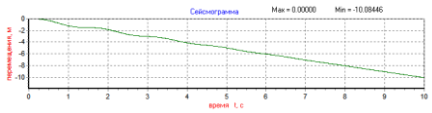
2	Korchinsky's model	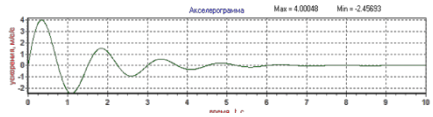	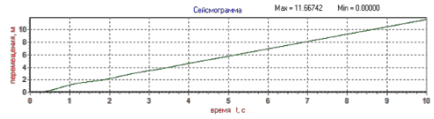
3	Kostyrev-Vetoshkin's model	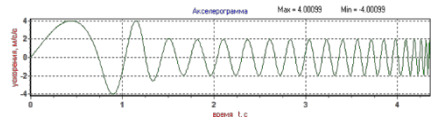	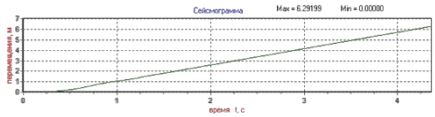
4	Epstein's model	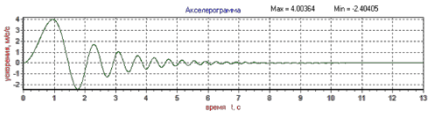	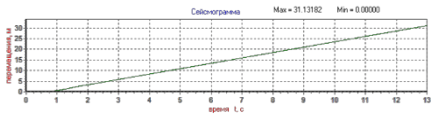

Table 2. Balanced processes.

№	Model name	Model accelerogram	Model seismogram
5	Annaev-Uzdin's model	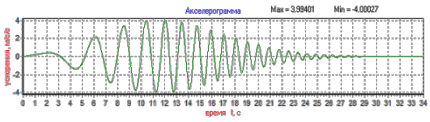	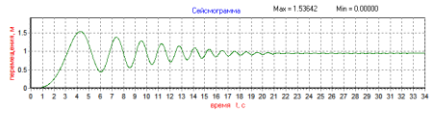
6	Berlage's model	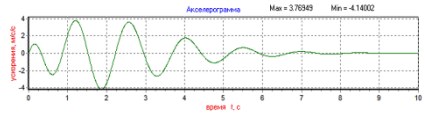	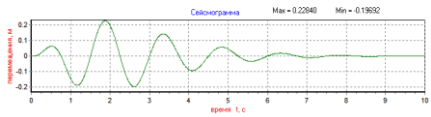
7	Velocity, presented by damped sinusoid	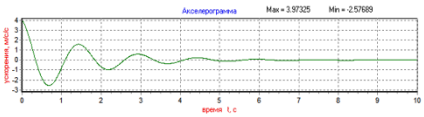	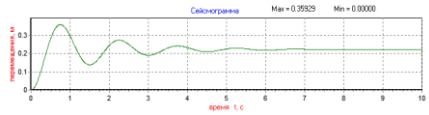
8	Ricker's model	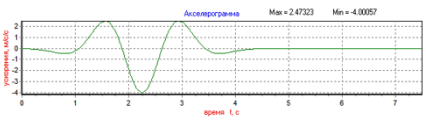	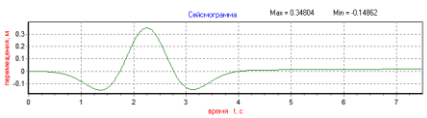

№	Model name	Model accelerogram	Model seismogram
9	Puzyrev's model	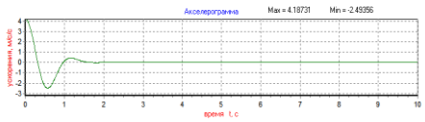	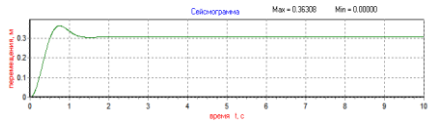
10	Bucharest earthquake	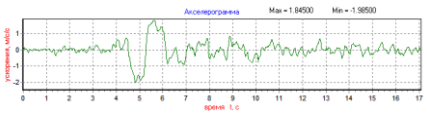	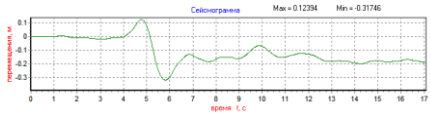
11	Tabass earthquake		

Table 3. Characteristics of processes.

№	Model name	Model function	PGA, m/s^2	PGV, m/s	I_A, m/s	CAV, m/s	κ
1	Gelfand's model	$y = e^{-\beta \cdot t^2} \cdot \sin(\omega \cdot t)$	4.22	1.99	4.08	10.76	10.75
2	Korchinsky's model	$\ddot{y} = e^{-\beta \cdot t} \cdot \sin(\omega \cdot t)$	4.00	1.84	1.52	4.86	13.19
3	Kostyrev-Vetoshkin's model	Discrete input	4.00	1.91	2.59	7.11	6.88
4	Epstein's model	$\ddot{y} = A \cdot e^{-\beta \cdot t} \cdot \sin(\omega(t) \cdot t)$	4.00	3.14	2.05	6.00	12.62
5	Annaev-Uzdin's model	$\dot{y} = A \cdot e^{-\beta \cdot t} \cdot \sin(\omega(t) \cdot t)$	4.00	1.14	11.99	33.07	4.76
6	Berlage's model	$y = t^n \cdot e^{-\beta \cdot t} \cdot \sin(\omega \cdot t)$	4.14	0.93	3.43	9.37	1.10
7	Velocity, presented by damped sinusoid	$\dot{y} = e^{-\beta \cdot t} \cdot \sin(\omega \cdot t)$	3.97	0.76	0.99	3.92	2.50
8	Ricker's model	$y = \left(1 - 2 \cdot \left(\omega \cdot \left(t - \frac{\pi}{\omega}\right)\right)^2\right) \cdot e^{-\left(\omega \cdot \left(t - \frac{\pi}{\omega}\right)\right)^2}$	4	0.93	1.68	4.74	1.6
9	Puzyrev's model	$y = e^{-\left(\frac{\omega}{\pi} \cdot t\right)^2} \cdot \sin(\omega \cdot t)$	4.19	0.81	0.73	1.93	2.31
10	Bucharest earthquake	Discrete input	1.99	0.80	0.74	5.48	1.04
11	Tabass earthquake	Discrete input	8.63	1.00	11.20	33.30	3.29

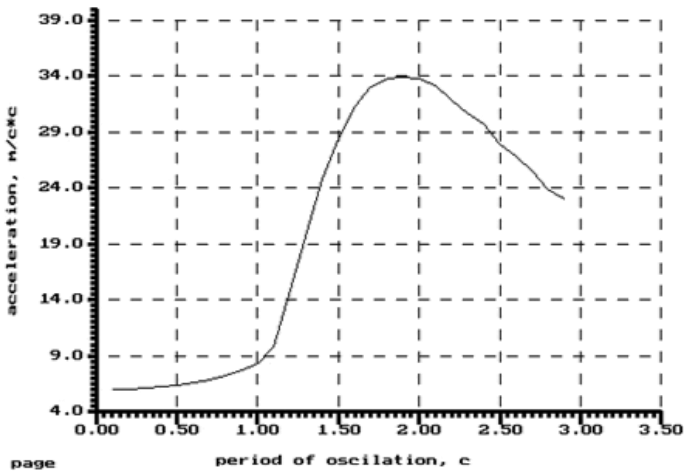

Figure 1. The acceleration spectrum of the Annaev – Uzdin process [9].

Thus, engineers are faced with many models of seismic actions with the same PGA and similar frequencies. In order to give preference to one or another model, it is necessary to know characteristic properties of real actions and the influence of these properties on the behavior of structures during earthquakes. A lot of various characteristics of seismic actions are discussed in literature. Among the most famous ones, in addition to peak accelerations (PGA) one can include the following:

1. Harmonic coefficient

$$\kappa = \frac{\ddot{y}_0^{(\max)} \cdot y_0^{(\max)}}{\left(\dot{y}_0^{(\max)}\right)^2}, \tag{1}$$

where $\ddot{y}_0^{(\max)}$ is the peak acceleration value (PGA); $\dot{y}_0^{(\max)}$ is peak velocity value (PGV); $y_0^{(\max)}$ is peak desplacement value (PGD).

2. Arias intensity I_A and Arias modified intensity I'_A [14], as well as modifications of this intensity [15] $I_{A,std}$ and $I'_{A,std}$:

$$I_A = \frac{\pi}{2 \cdot g} \int_0^{\tau} \ddot{y}^2(t)dt\,; \tag{2}$$

$$I'_A = \int_0^{\tau} \ddot{y}_0(t)^2 dt \tag{3}$$

where $\ddot{y}_0(t)$ is the earthquake accelerogram, τ is its duration.

Note that the Arias intensity has the dimension of velocity.

3. Absolute cumulative velocity, CAV [15]

$$CAV = \int_0^{\tau} |\ddot{y}| dt \tag{4}$$

4. Potential damage index I_{Araya} proposed by R. Araya and widely used to describe seismic impact intensity [16, 17]:

$$I_{Araya} = \frac{I'_A}{\nu_0^2}, \tag{5}$$

where ν is the number of crossing of the time-axe by the process

5. Effective earthquake duration

$$\tau = 2\sqrt{\frac{\int_0^{t_S} (t - t_c)^2 a^2(t)dt}{\int_0^{t_S} \ddot{y}^2(t)dt}} \tag{6}$$

where t_c is the “center of acceleration gravity” along the time axis, t_S is the total accelerogram duration.

6. Root-mean-square (RMS) peak acceleration [18]

$$\sigma_A = \sqrt{\frac{\int_0^{\tau} \ddot{y}_0^2 dt}{\tau}} = \sqrt{\frac{I_{A,\mathrm{mod}}}{\tau}} \tag{7}$$

7. Seismic energy density, SED [13]

$$SED = \int_0^{\tau} \dot{y}^2(t)dt\,; \tag{8}$$

8. RMS peak velocity [18]

$$\sigma_V = \sqrt{\frac{\int_0^{\tau} \dot{y}_0^2 dt}{\tau}} = \sqrt{\frac{SED}{\tau}} \tag{9}$$

These characteristics (except for the harmonic coefficient) are often called energy. Recently, many experts [15] prefer to use the CAV value as an indicator of earthquake intensity.

Tables 1.2 show frequently used seismic input models normalized to 4 m/s^2 and the values of some characteristics of these models. For comparison, Table 2 shows two accelerograms of real impacts of 9 degree on the MSK-scale (Bucharest and Tabas). As can be seen from Table 1, most of the known processes are unbalanced. The harmony indicators of unbalanced processes turn out to be unrealistic due to large parasitic displacements of the process. For processes in which a velocigram is adopted as a basic function, the process is balanced, but at the same time $\ddot{y}_0(0) \neq 0$.

The purpose of this paper is to systematize the known characteristics, consider new indicators of the earthquake intensity, as well as to analyze the significance of the considered parameters when setting design accelerograms.

2. Methods

2.1. Determining the main characteristics of seismic input necessary for an engineer in designing

Some characteristics of seismic input have been considered earlier. In the general case, all characteristics can be divided into three groups: kinematic, spectral and energy ones.

Kinematic characteristics include

- peak ground acceleration (PGA);
- peak ground velocity (PGV);
- peak ground displacement (PGD);
- the harmonic coefficient κ, calculated by the formula (1);
- seismic action duration τ.

The main spectral characteristics are acceleration, velocity and displacement spectra, as well as the Fourier spectra of seismic actions [19]. In addition to these characteristics, the prevailing action period T or the prevailing action frequency ω can be specified. However, it should be borne in mind that these values are different for an accelerogram and a seismogram.

The energy input characteristics are quite diverse. We consider it necessary to mark out the following:

- Arias intensity, I_A, determined by formula (2);
- seismic energy density SED (formula (8)) and the associated root-mean-square velocity σ_V (formula (9));
- absolute cumulative velocity CAV (formula (4));
- the work of plastic deformation forces PFW, when an earthquake acts on an elastoplastic pendulum

$$PWF = \int_0^{\tau_{eq}} (R(y, \dot{y}) \cdot \dot{y})dt\,, \tag{10}$$

In formula (10), $y(t)$ is pendulum displacement, $R(y, \dot{y})$ is pendulum response to seismic action.

Now the PGA mainly used in engineering calculations. The PGD value becomes necessary to be additionally used in calculating bridges to estimate the movable bearing travel [20]. Other action characteristics are used in generating design accelerograms [21].

Specifying action characteristics correctly seems to be very important and this question is still far from being sold finally. However, results obtained on questions of specifying these characteristics should be taken into account in calculations.

First, the PGA decreases with increasing the prevailing action period. Prof. O.A.Savinov drew attention to this phenomenon. The data on this question are given in the monograph [20]. A.A. Dolgaya obtained the

dependence of the PGA on the earthquake prevailing period T_{eq} based on the records of 240 earthquakes with intensity 8 on the MSK-scale [7]. The corresponding dependence is shown in Fig. 1. Further, such dependence was confirmed in the analysis of about 100 records of earthquakes with intensity 9 on the MSK-scale [28, 29].

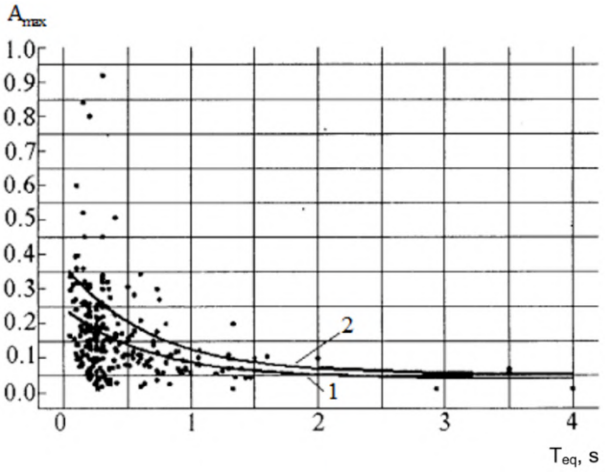

Figure 2. Regression dependencies (for I = 8 on the MSK-scale).
1 – $\bar{A}_{\max}(T_з)$; 2 – $\bar{A}_{\max}(T_з)+\sigma_A(T_з)$.

Secondly, such an important indicator as the harmonic coefficient, just like the PGA, depends on the prevailing action period. In the Guidelines for calculating nuclear power plants (USA), this coefficient is recommended to be set equal to 5 [23]. In 2000 A.A. Dolgaya and O.A. Sakharov [11] found the dependence $\kappa(T_{eq})$. In later studies [28, 29] this dependence was confirmed. Fig. 2 shows such a dependence according to [29].

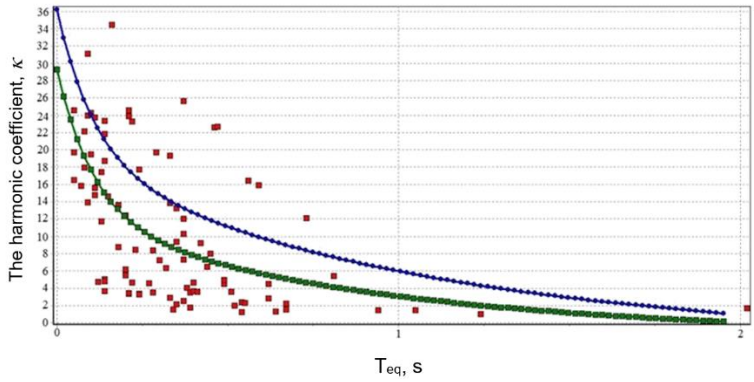

Figure 3. Dependence of the harmonic coefficient κ on the prevailing input period T_{eq}.

Thirdly, energy characteristics may also depend on the prevailing action period. Studies available [22, 24] show that the Arias intensity and the CAV are independent of the prevailing period of action on the accelerogram. This allows one to use them as a universal action characteristic. In particular, the USA experts analyzed more than 500 earthquakes recorded in the USA and came to the conclusion that the most stable energy action characteristic is the CAV value [15]. The values of the I_A value for earthquakes of intensity 9 on the MSK-scale for different exceedance probability P are shown in Table 4.

Table 4. The Arias intensity values of a given exceedance probability.

	I_A values depending on the probability of their exceeding		
P, %	70	80	90
I_A	42.528	52.601	68.389

2.2. Additional characteristics of seismic input important in multi-level designing

In our opinion, the characteristics considered poorly describe the strong earthquake intensity. The intensity of destructive earthquakes is determined by the degree of building and structures damages. Generally in order to damage the structure, it is necessary to do some mechanical work and to do this, it is necessary to have energy. For this reason, the above-mentioned energy action characteristics were introduced. They

indirectly characterize the energy transmitted by the earthquake to the structure. In the literature attempts to link energy with the mentioned characteristics [13].

However, these attempts give very rough estimates of energy transmitted by the earthquake to the structure. In this regard, the authors tried to introduce additional action characteristics directly related to the energy and structure damage. For this, we considered two models of structure damage accumulation. The first model is elastoplastic, and the second is adaptive with degrading stiffness.

In the first case, an elastoplastic pendulum with a Prandtl diagram is considered (Fig. 4). The diagram is characterized by the inclination angle α for the first section of the diagram and by the elastic limit F_{el} with the ultimate displacement u_{el}. The rigidity of the system is $C = tg\alpha$, and the oscillation period in the absence of sliding is $T = 2\pi / k$; where $k^2 = C / m$; m is the system mass; the elastic limit is conveniently expressed in terms of the conditional coefficient of friction $f = F_{el} / (m \cdot g)$. During the loading process, the forces of plastic deformation work only in the second section of the diagram.

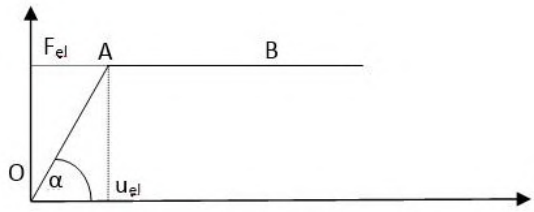

Figure 4. Diagram "force-displacement" of the system used for assessing the earthquake intensity.

To construct the spectrum of the work of plastic deformation forces $W(T)$, we consider the equations

1. for the OA section

$$\ddot{y} + \gamma \cdot k \cdot \dot{y} + k^2 \cdot y = -\ddot{y}_o \tag{11}$$

2. for the AB section

$$\ddot{y} + g \cdot f \cdot \mathrm{s}ign(\dot{y}) = -\ddot{y}_o \tag{12}$$

Equation (11) includes the force of internal friction in the material, characterized by the coefficient of inelastic resistance γ. The value of γ influences the value of W. For objects of mass building constructions, the value of γ varies from 0.08 to 0.2. The lower boundary refers to metal and monolithic reinforced concrete structures on rocky soils. The upper boundary refers to rigid structures on highly compressible soils. To assess the strength of the earthquake, the authors propose using a representative structure with $\gamma = 0.1$.

Solutions of equations (11, 12) have a standard form and are written analytically within the frame of an integration step. Integration begins at the OA section (equation 10), and the transition to the AB section occurs if the elastic force C_y exceeds the elastic limit F_{el}. The return from section AB to section OA occurs when the sign of the mass velocity relative to the base changes. Fig. 5 and 6 show accelerograms of two earthquakes: Bucharest (1977) and Tabass (1978). Earthquakes intensity for both earthquakes is equal to 9 on the MSK scale, but they have completely different characteristics. These characteristics are shown in Table 4. In addition to the characteristics noted above, a harmonic index is included in Table 4.

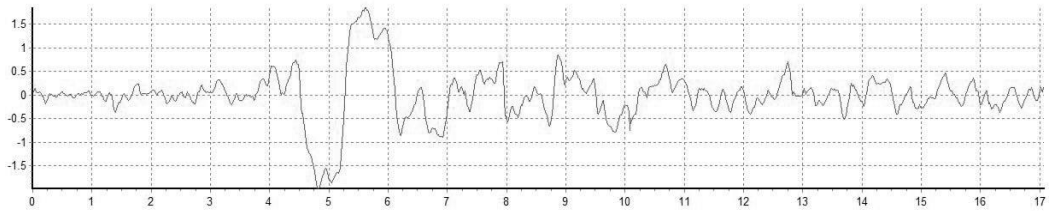

Figure 5. Accelerogram of Bucharest (1977) earthquake.

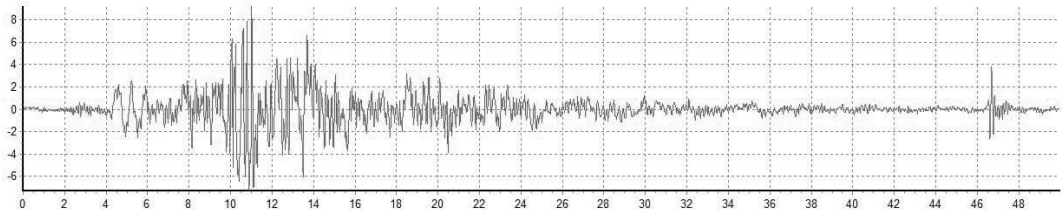

Figure 6. Accelerogram of Tabass (1978) earthquake.

Table 5. Characteristics of Bucharest (1977) and Tabass (1978) earthquakes.

	PGA, $\ddot{y}_o$, m/s²	Arias intensity I_A, m/s	Absolute cumulative velocity, CAV, m/s	Harmonic index, κ
Bucharest earthquake	2	0.74	5.48	1.035
Tabass earthquake	8.63	11.2	33.3	3.286

The spectra of plastic deformation forces for the two considered earthquakes are shown in Fig. 7, 8. With large differences in the seismic impact characteristics used, the $W(T)$ dependences for the considered earthquakes turn out to be close.

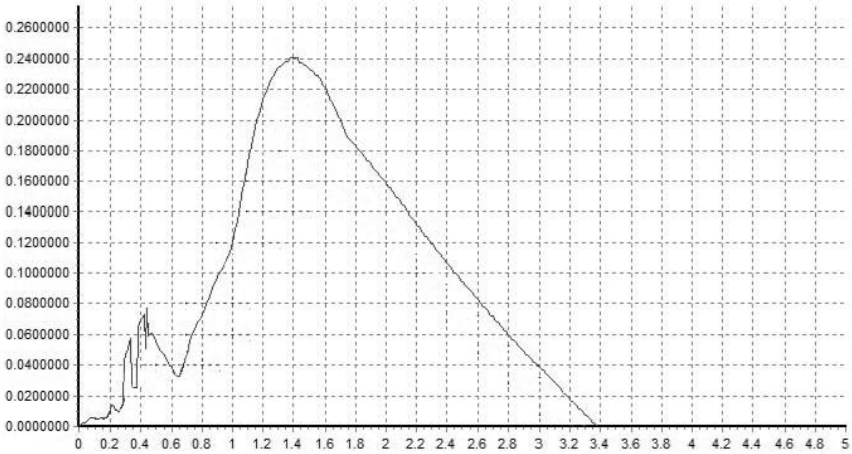

Figure 7. The spectrum of the work of plastic deformation forces for the Bucharest earthquake with a peak acceleration equal to 0.2 g, $\gamma = 0.1$.

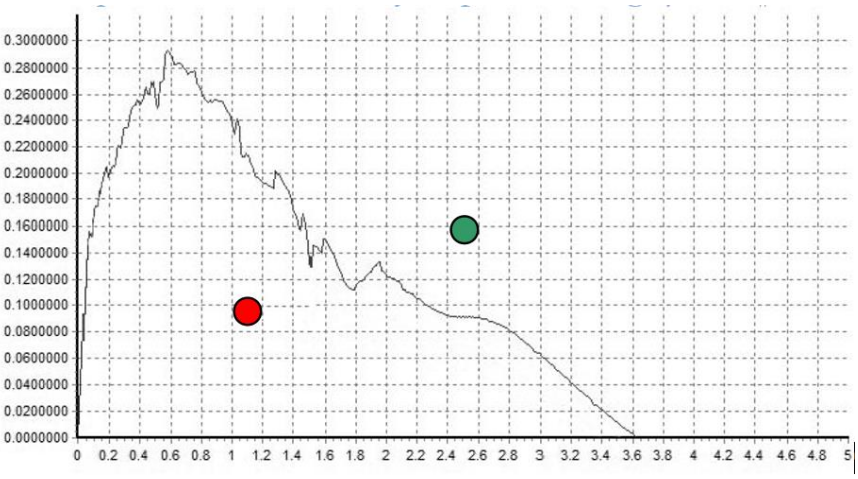

Figure 8. The spectrum of the work of plastic deformation forces for the Tabas earthquake with a peak acceleration equal to 0.863 g, $\gamma = 0.1$. The red and green dots indicate the possible values of the monotonous loading in emergency (red dot) and admissible (green dot) cases.

The work of plastic deformation forces does not depend only on the system oscillations period, but also on its elastic limit F_{el}. In order to assess the possible earthquake potential, it is necessary to find a structure that the earthquake can destroy. To do this, the dependences $W(T)$ should be constructed for various

characteristics f. In the general case, one should work with the two-dimensional spectrum $W(T, f)$. Fig. 9 shows such a two-dimensional dependence for the El Centro earthquake in isoclines.

The potential destructive ability of an earthquake can be estimated by the volume of the figure formed by the surface $W(T, f)$. If we designate this indicator as PFW (Plastic forces work), we can write:

$$PFW = \int_0^{T_{\max}} \int_0^{f_{\max}} W(T, f) df dT \tag{13}$$

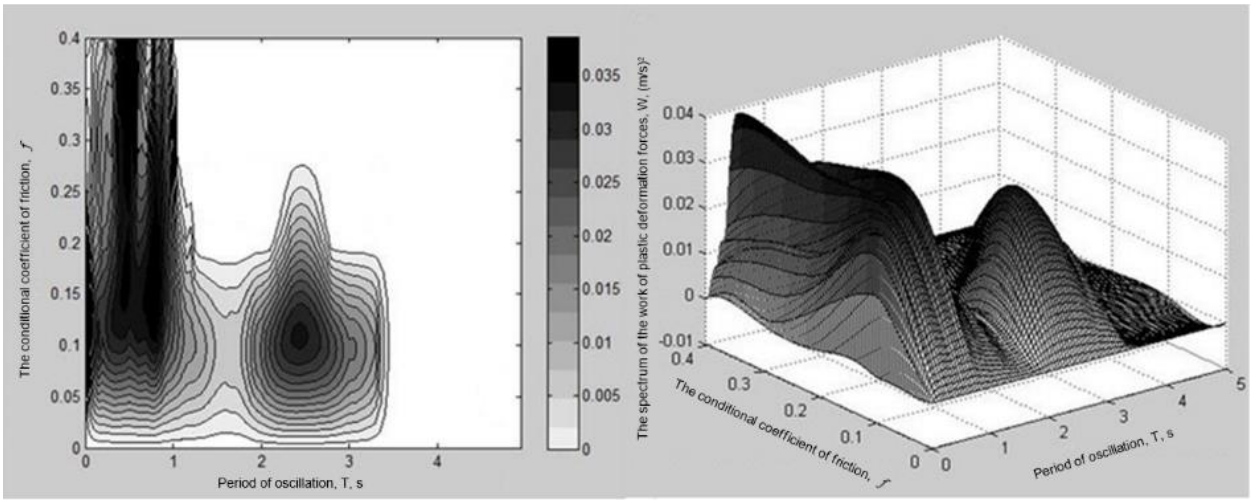

Figure 9. A two-dimensional dependence for the El Centro earthquake in isoclines.

The proposed indicator for assessing earthquake intensity reflects the physical meaning of a macroseismic damage analysis and does not require any expert agreement about the earthquake duration. Singling “safe” sections out of the earthquake process occurs automatically depending on the structure properties. In addition, the proposed indicator gives more information about the earthquake than a macroseismic analysis. For example, a high-frequency earthquake in a territory built up with flexible structures does not result in a large amount of damages and is characterized as weak or moderate. At the same time, in the territory built up with low-rise rigid buildings, the same earthquake would cause a large amount of damage and must be described as strong. When using the proposed indicator of the earthquake intensity is used, the earthquake itself will find objects that it can destroy, which makes it possible to evaluate its strength objectively.

The proposed criterion is conveniently used in assessing the earthquake resistance of structures under strong impacts in accordance with [25].

To this end, the point of monotonous destruction of the structure under consideration is put on the spectrum of work of the forces of plastic deformation. If the point is inside the graph (red dot in Fig. 7), the system will collapse due to low-cycle fatigue or progressive collapse. Otherwise, (green dot in Fig. 7) the system will adapt to the loading program.

For adaptive systems with degrading stiffness, as a criterion for damage accumulation (earthquake intensity), one can use the damage index χ and the current period of the structure fundamental vibration tone T. It is assumed that as the damage accumulates, the rigidity of the system will decrease, and the period of the fundamental vibration tone will increase. At the time of collapse, the rigidity comes down to 0. The concept of damage was introduced by L.M. Kachanov [29] and Yu.N. Robotnov [30] and is characterized by the area of the cross-section part occupied by the crack. At the beginning of the oscillations $\chi = 0$, and at the time of collapse $\chi = 1$.

To describe the structure behavior, the authors used the Kirikov – Amankulov model of the damage accumulation [31]. In accordance with this model, the damage index χ increases linearly, and the oscillation period decreases linearly with an increase of the maximum system displacement u_{max} over the loading history.

For this type of damage accumulation, the restoring force is described by the equation

$$R(y) = \frac{r(u)y}{1 + \kappa(u)y^2} \tag{14}$$

where y is the structure displacement; u is the maximum structure displacement over the history of loading; κ is the nonlinearity parameter.

The system rigidity is constant until the displacement u is less than the elastic limit u_{app}. When the elastic limit is exceeded, the stiffness begins to fall linearly with an increase of the maximum value of the system displacement over the loading process history. The displacement corresponding to the zero rigidity of the system is called the conditional displacement of destruction u_{cond}. In fact, the displacement at which the destruction of the structure takes place is considered the displacement u_{distr} at which the reaction of the system reaches its maximum value. The dependences $R(u)$ and $\gamma(u)$ are shown in Fig. 9.

Systems with the type of nonlinearity under consideration are among the adaptive systems that, due to the increase of damages, are detuned from resonance. Ya.M. Eisenberg introduced the concept of a system state spectrum [31] for such structures. The system adapts itself to the loading program if the state spectrum crosses the response spectrum at some point.

Oscillations of a system with degrading rigidity are described by the equation:

$$m\ddot{u} + \gamma\sqrt{rm}\dot{u} + R(u) = -m\ddot{y}_0 \quad , \tag{15}$$

where $u, \dot{u}, \ddot{u}$ are the movement, velocity and acceleration of the structure, respectively; m is the structure mass; $\gamma(u_{max})$ is the coefficient of inelastic resistance; $R(u,u_{max})$ is the system rigidity; $\ddot{y}_0(t)$ is the accelerogram of base vibrations.

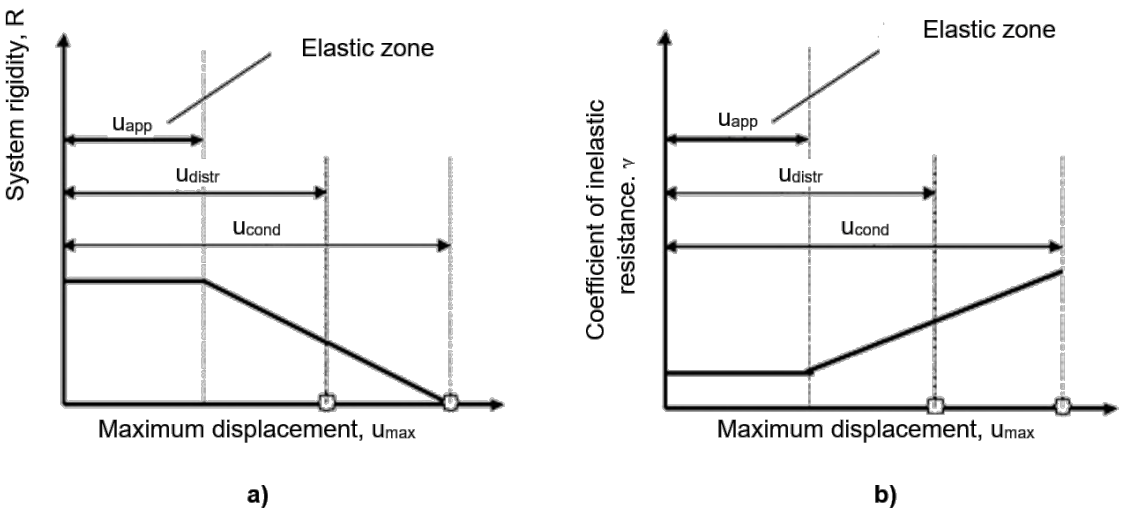

Figure 9. Dependence of the structure rigidity (a) and the coefficient of inelastic resistance of the structure (b) on the maximum displacement over the structure loading history.

The integration of equation (15) has been carried out by standard methods. If the characteristics of the system change within the integration step, its parameters change in accordance with the change in these characteristics. As a result, it is possible to obtain the dependences of the final (after seismic impact) period and the system damage coefficient on the initial period of its oscillations, i.e. period and damage spectra of the system. Fig. 10 and 11 show examples of such spectra for the Bucharest and Tabas earthquakes.

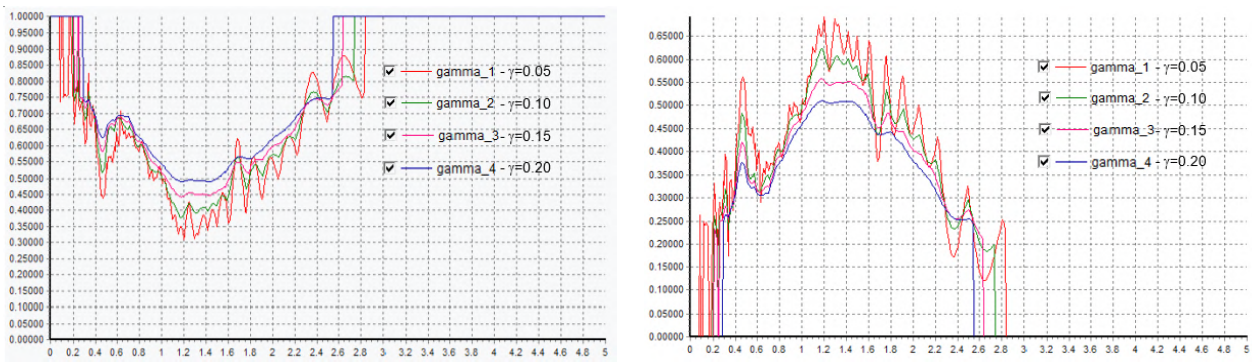

Figure 10. Spectrum of periods (left) and damage spectrum (right) for the Bucharest earthquake for f = 0.25.

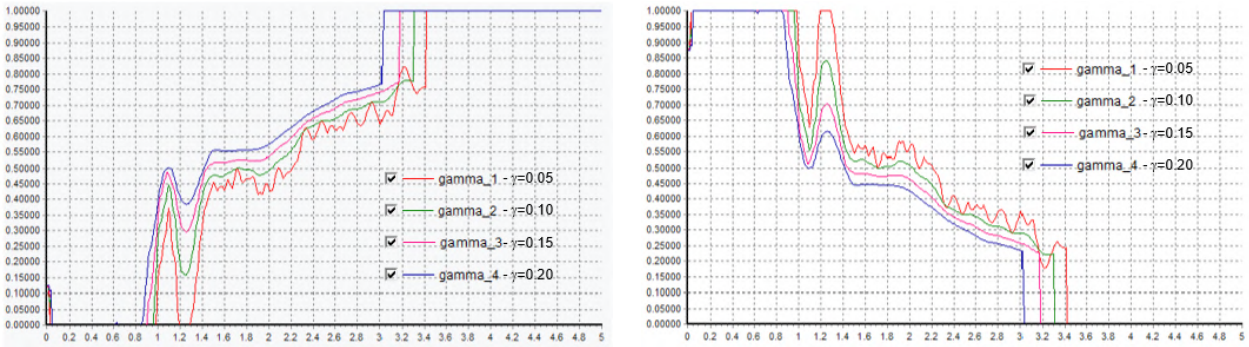

Figure 11. Spectrum of periods (left) and damage spectrum (right) for the Tabas earthquake for *f* = 0.25.

As can be seen from the figures, the systems under consideration with the accepted characteristics of damage accumulation must survive the Bucharest earthquake without collaps, and in the case of the Tabass earthquake, all structures with periods ranging from 0.05 to 1 s must be destroyed.

3. Results and Discussion

When modeling seismic impacts, it is necessary to take into account their characteristics discussed above. The importance of certain characteristics is determined by the adopted limit state. As it is known, the transition to multi-level designing is currently underway. As minimum, two levels of ultimate state and two levels of seismic input are considered. The first limit state is a violation of normal operation, which is referred to as SLS (Serviceability Limit State). It is allowed once every 50–300 years and after it the structure keeps working as usual. The corresponding earthquake is called a design one (DE).

The second limit state is damage accumulation, incompatible with further operation – ULS (Ultimate Limit State). It is allowed with repeatability once every 500–5000 years. It corresponds to the maximum design earthquake (MDE). The requirements for multi-level designing are available in Eurocode-8. In a number of countries, for example, in Italy and France, these requirements are detailed. They provide for four limit states (4 action levels). The first limit state is the complete absence of damage (DLS (Damaged Limited State)), which can take place once every 21 years. The second limit state is SLS which can take place once every 60 years.

The third limit state is ULS with a repeatability of once every 500 years. And the fourth limit state is CLS (Collapsed Limited State) with a repeatability of once every 700 years.

For each limit state and its corresponding actions, different factors are important. For calculating structures using the DLS and SLS, the PGA value should be decisive. The larger the PGA, the greater the structure strains. It goes without saying, the model action should be resonant, i.e. the prevailing action frequency should coincide with the peak of the amplitude-frequency characteristics of the structure. If the system is non-linear, for example, a seismically isolated building on kinematic supports, the PGA value is to correspond with the oscillation period according to the technique proposed in [26].

In all cases, it is necessary to take into account the significant dependence of the PGA and κ on the prevailing input period, which decreases 3–5 times with an increase in the oscillation period from 0.2 to 2 seconds. As damage accumulates, the role of the PGA decreases and energy performance becomes important. Here, from the authors' point of view, preference should be given to I_A and CAV parameters, since they do not depend on the prevailing input period. Values such as, for example, SED, significantly depend on the prevailing input period, which at the input generation it should be adjusted to the fundamental period of the structure oscillation. However, during the accumulation of damages, the period of oscillation falls, and the question of tuning for the period becomes problematic. In our opinion, the problem can be sold using the spectra of plastic deformation forces and the damage. The choice of spectrum depends on the mechanism of structure damage accumulation. For metal structures and other structures that are characterized by plastic work, the tuning is based on the work of plastic deformation forces. For stone and reinforced concrete structures, crack formation and damage accumulation according to the Kirikov-Amankulov model are typical. In these cases, the prevailing input period should correspond.

4. Conclusion

The analysis of seismic action properties allows us to conclude the following:

1. It seems possible to use the simplest seismic impact models for typical designing and calculating mass construction objects.

Such models are also useful at the preliminary design stage, when the required amount of seismological data is not available yet. These impact models may be unlike the real ones, but they must ensure that the basic characteristics of the calculated models and the real impacts are consistent each other.

2. In structure calculating under the action of DE, when the structure has no damages, the most important characteristics are kinematic ones.

For most structures, first of all it is necessary to consider the values of PGA and harmonic coefficient. They determine seismic loads on the structure. In this case, the resonant actions should be chosen for the structure. The most important requirement is the observance of the dependence of both PGA and κ on the prevailing period. The larger the period, the lower the PGA and κ values. Dependences PGA (T) are available in both scientific and educational literature; the dependence $\kappa(T)$ is given in this paper.

3. In calculating the action of moderate earthquake or MDE, when damages appear in the structure and the deformation diagram becomes non-linear, the energy characteristics of the impact become important. The authors believe that in these cases the most convenient are Arias intensity and cumulative absolute velocity (CAV), since these characteristics are independent of the prevailing input period.

4. The authors propose two characteristics important, in their opinion: they are the spectrum of the work of plastic deformation forces and the damage spectrum. Peaks in the spectra of the model input should correspond to the fundamental periods of the structure oscillations.

5. Acknowledgments

The work was carried out with the support of the grant of the Russian Foundation for Basic Research No 19-35-90111.

References

1. Erteleva, O., Aptikaev, F., Baruah, S., Baruah, S., Deb, S.K., Kayal, J.R. Seismic treatment for a maximal credible earthquake in Guwahati city area of northeast India region. Natural Hazards. 2014. 70(1). Pp. 733–753. DOI: 10.1007/s11069-013-0843-3
2. Albert, Y.U., Dolgaya, A.A., Ivanova, T. V., Nesterova, O.P., Uzdin, A.M., Guan, J., Ivashintzov, D.A., Voronkov, O.K., Shtilman, V.B., Shulman, S.G., Khrapkov, A.A. Seismic input models for tuned mass damper designing. Magazine of Civil Engineering. 2017. 76(8). Pp. 98–105. DOI: 10.18720/MCE.76.9
3. Valentini, A., Pace, B., Boncio, P., Visini, F., Pagliaroli, A., Pergalani, F. Definition of Seismic Input From Fault-Based PSHA: Remarks After the 2016 Central Italy Earthquake Sequence. Tectonics. 2019. 38(2). Pp. 595–620. DOI: 10.1029/2018TC005086
4. Rezaeian, S., Petersen, M.D., Moschetti, M.P. Ground Motion Models Used in the 2014 U.S. National Seismic Hazard Maps. Earthquake Spectra. 2015. 31(1_suppl). Pp. S59–S84. DOI: 10.1193/111714EQS194M
5. Dindar, A.A., Yalçın, C., Yüksel, E., Özkaynak, H., Büyüköztürk, O. Development of Earthquake Energy Demand Spectra. Earthquake Spectra. 2015. 31(3). Pp. 1667–1689. DOI: 10.1193/011212EQS010M
6. Kojima, K., Fujita, K., Takewaki, I. Critical Double Impulse Input and Bound of Earthquake Input Energy to Building Structure. Frontiers in Built Environment. 2015. 1. Pp. 5. DOI: 10.3389/fbuil.2015.00005
7. Uzdin, A., Prokopovich, S. Some principles of generating seismic input for calculating structures. E3S Web of Conferences. 2020. 157. Pp. 9. DOI: 10.1051/e3sconf/202015706021
8. Ivanova, T.V., Guan, Y., Nesterova, O.P., Prokopovich, S.V., Smirnova, L.N., Uzdin, A.M., Ivashintzov, D.A. Modeling the design seismic input in conditions of limiting seismological information. Magazine of Civil Engineering. 2017. 75(7). Pp. 129–138. DOI: 10.18720/MCE.75.13
9. Annaev, G., Ilyasov, I.B., Zhgutova, T.V., Sakharov, O.A., Uzdin, A.M. Simplified model of earthquake input for structure dynamic calculations. Natural and Technological Risks. Building Safety. 2014. (1). Pp. 24–27. URL: http://ptrbs.ru/files/20-14/1/PTrBS_2014_01-prostaja model.pdf
10. Nesterova, O.P., Tkachenko, A.S., Uzdin, A.M., Dolgaya, A.A., Smirnova, L.N., Guan, Y. On setting the level of seismic input in seismic intensity scales and design standards. Problems of engineering seismology. 2018. 45(1). Pp. 73–80. DOI: 10.21455/VIS2018.1-7
11. Bogdanova, M.A., Dolgaya, A.A., Ivanova, J.V., Sakharov, O.A., Uzdin, A.M. The Model of Seismic Impact as a Short Temporary Process for Calculating of the Seismoisolated Systems. 12th World Conference on Earthquake Engineering 2000. URL: https://www.iitk.ac.in/nicee/wcee/article/1358.pdf
12. Ricker, N. The form and laws of propagation of seismic wavelets. Geophysics. 1953 18(1) P.10. DOI: 10.1190/1.1437843
13. Shiwua, A.J., Rutman, Y. Assessment of Seismic Input Energy by Means of New Definition and the Application to Earthquake Resistant Design. Architecture and Engineering. 2016. 1(4). Pp. 26–35. DOI: 10.23968/2500-0055-2016-1-4-26-35
14. Arias, A. A measure of earthquake intensity. Seismic Design for Nuclear Power Plants. Hansen RJ (Ed.), MIT Press, Cambridge, 1970. Pp. 438–483.
15. Campbell, K.W., Bozorgnia, Y. Cumulative Absolute Velocity (CAV) and Seismic Intensity Based on the PEER-NGA Database. Earthquake Spectra. 2012. 28(2). Pp. 457–485. DOI: 10.1193/1.4000012
16. Rodriguez, M.E. Damage Index for Different Structural Systems Subjected to Recorded Earthquake Ground Motions. Eartquake Spectra. 2018 34(2) Pp. 773–793. DOI: 10.1193/021117EQS027M
17. Massumi, A., Gholami, F. The influence of seismic intensity parameters on structural damage of RC buildings using principal components analysis. Applied Mathematical Modelling. 2016 40(3) Pp. 2161–2176. DOI: 10.1016/j.apm.2015.09.043
18. Ozmen, H.B., Inel, M. Damage potential of earthquake records for RC building stock. Earthquakes and Structures. 2016. 10(6). Pp. 1315–1330. DOI: 10.12989/eas.2016.10.6.1315

19. Kurbatskiy Ye.N. Spektry Furye i spektry otvetov na zemletryaseniya – teoriya i prilozheniya [Fourier Transform and Response Spectra. Hands-on Seismic Design]. Moskva: Srosekspertiza, 2018. 155 s.
20. Uzdin, A.M., Kuznetsova, I.O. Seysmostoykost mostov [Seismic Stability of Bridges]. Palmarium. Saarbryuken (Germaniya), 2014. 456 p.
21. Smirnova, L.N., Uzdin, A.M., Prokopovich, S.V. Some Features of Modeling Design Accelerograms. Earthquake engineering. Constructions safety. 2019. (1). Pp. 33–41. URL: http://seismoconstruction.ru/pdf/pdf.php?IBLOCK_ID=2&ID=1204
22. Prokopovich, S.V., Uzdin, A.M. Dependence of Aryas Intensitivity on the Predominant Earthquake Period. Natural and technogenic risks. Safety of buildings. 2018. 3(34). Pp. 27–30. URL: http://ptrbs.ru/3-2018.html
23. Birbrayer, A.N. Raschet konstruktsiy na seysmostoykost [Seismic Analysis of Structures]. Nauka. SPb. 1998. 254 p.
24. Prokopovich, S.V. Absolute Sumulative Velocity as a Measurement of Earthquake Strength. Earthquake engineering. Constructions safety. 2019. (5). Pp. 41–44. URL: http://seismoconstruction.ru/pdf/pdf.php?IBLOCK_ID=2&ID=1279
25. Moskvitin, V.V. Tsiklicheskiye nagruzheniya elementov konstruktsiy [Cyclic Loading of Structural Elements]. Nauka. M. 1981. 344 p.
26. Durseneva, N.V., Indeykin, A.V., Kuznetsova, I.O., Uzdin, A.M., Fedorova, M.Y. Peculiarities of Calculating Bridges with Seismic Isolation Including Spherical Bearings and Hydraulic Dampers in Russia. Journal of Civil Engineering and Architecture. 2015. 9(4). Pp. 401–409. DOI: 10.17265/1934-7359/2015.04.004
27. Bogdanova, M.A., Nesterova, O.P., Nikonova, N.V., Tkachenko, A.S., Uzdin, A.M., Rakhmanova, M., Azayev, T.M., Zaynulabidova, K.R. Numerical characteristics of seismic input. Science and world. 2017. 1(3). Pp. 49–55. URL: http://scienceph.ru/f/science_and_world_no_3_43_march_vol_i.pdf
28. Uzdin, A.M., Nesterova, O.P., Prokopovich, S.V., Dolgaya, A.A., Zhang, Y., Guan, Y., Wan, H. Earthquake Input Modeling for Dynamic Calculation of Buildings and Structures. Rossiysko-kitayskiy nauchnyy zhurnal «Sodruzhestvo». Yezhemesyachnyy nauchnyy zhurnal nauchno-prakticheskoy konferentsii. 2017. 1(20). Pp. 59–66. URL: https://rf-china-science.ru/wp-content/uploads/2017/12/RF-China_noyabr_zhurnal_1_chast-23.pdf
29. Kachanov, L.M. Fundamentals of the Theory of Plasticity. Dover Publications. New York, 2004. 482 p.
30. Rabotnov, Y.N. Creep Problems in Structural Members. North-Holland Publishing Company. Amsterdam, 1969. 822 p.
31. Uzdin, A.M., Nazarova, Sh.Sh., Prokopovich, S.V. Once Again on Setting the Design Seismic Input. Natural and Technological Risks. Building Safety. 2019. (6). Pp. 39–48. URL: http://www.ptrbs.ru/2019_6.php

Contacts:

Sergei Prokopovich, spr94@outlook.com
Alexander Uzdin, uzdin@mail.ru
Tatiana Ivanova, IvanovaTV@vniig.ru

© Prokopovich, S.V., Uzdin, A.M., Ivanova, T.V., 2021

Magazine of Civil Engineering

ISSN 2712-8172

journal homepage: http://engstroy.spbstu.ru/

DOI: 10.34910/MCE.102.10

Heat release and thermal conductivity of expanded-clay concrete for 3D printer

K. Usanova[a]*, Yu.G. Barabanshchikov[a], L. Pakrastins[b], S.V. Akimov[a], S.V. Belyaeva[a]

[a] Peter the Great St. Petersburg Polytechnic University, St. Petersburg, Russia

[b] Riga Technical University, Riga, Latvia

**E-mail: plml@mail.ru*

Keywords: claydite concrete, expanded-clay concrete, cement, superplasticizer, heat release, heat of hydration, thermal conductivity, permeability of heat, thermal transmittance, 3D printer, regression analysis, furnace slag, silica fume

Abstract. The subject of research is expanded-clay concrete with additives of ground granulated blast-furnace slag, silica fume, superplasticizer admixture and air-entraining admixture for 3D printing. The heat release of concrete and thermal conductivity of concrete are investigated depending on the concrete composition (cement, water cement ratio, expanded-clay), additives (slag, silica fume) and admixtures (superplasticizer, air-entraining agent). The thermal conductivity of concrete depends primarily on the expanded clay gravel content and depends less on the cement content. If both factors increase, the thermal conductivity decreases. This is due to the replacement of dense sand grains with a more porous cement paste. The influence of air-entraining admixture on the thermal conductivity of expanded-clay concrete was not detected due to the high scattering of the experimental points. It was confirmed that the cement content and water cement ratio have an impact on the integral value of the heat release per unit mass of cement ($q = Q/C$). This value decreases with increasing cement content. The reason for this is that the total heat generated by concrete Q, with constant W/C and other equal conditions, increases linearly with increasing the cement content. The air-entraining admixture increases the heat generation by concrete. This is due to the chemical interaction between the admixture and cement hydration products with the formation of thermodynamically more stable compounds.

1. Introduction

The technology of 3D printing is gradually becoming an integral part of construction industry. Using construction 3D printers automates the manufacturing process of building products and the construction.

3D printers create of an object by adding material to the object layer by layer. The physical object is usually based on a digital 3D model [1–2]. In the construction industry, 3D printing can be used over a wide range: from the creation of hardscape elements [3] to the creation of large structures such as walls and domes [4].

3D printing in construction industry makes it possible to realize not only simple rectangular buildings, but also structures more complex in their geometry [5]. In addition, the positive effects are the opportunity to reduce the cost of the created objects, increase the accuracy of their manufacture and reduce the construction period [6], [7].

The properties of concrete mix for 3D printing technology makes many demands [8]. The mixture must have a certain viscosity and moldability to maintain the required shape during printing. In addition, the mixture must have workability for extrusion [9]. It should also be fast setting, so as not to lose shape without formwork [10–11]. If it is necessary for concrete to have greater strength, steel reinforcement, fiber or glass-fiber are added to the mixture [12–16]. Possible flexural strength is up to 30 MPa and compressive strength is up to 80 MPa in the case of using carbon, glass and basalt fibers with a size of 3–6 mm [17–18]. It is possible to use lightweight steel concrete structures consisting of monolithic concrete, profiled steel and fiber-cement sheets [19–20].

Usanova, K., Barabanshchikov, Yu.G., Pakrastins, L., Akimov, S.V., Belyaeva, S.V. Heat release and thermal conductivity of expanded-clay concrete for 3D printer. Magazine of Civil Engineering. 2021. 102(2). Article No. 10210. DOI: 10.34910/MCE.102.10

This work is licensed under a CC BY-NC 4.0

Other additives may be included in the mixture to improve certain characteristics of the concrete mix or concrete structures [21].

Experimental studies [22–23] showed that the addition of silica and nanoclay improved the formability of the fresh printing mixture, while a slight improvement was observed as a result of the addition of polypropylene fiber [24]. It is possible to use cement with clay soil and additives. The test results [25] shows the possibility of replacing cement paste with clay soil up to 25 % which leads to a reduction in the cost and an increase in printability with a slight decrease in the strength of the obtained material to 7 %. Other mineral admixture (fly ash, blast furnace slag, limestone, silica, silica fume, nanosilica, granite, perlite, vermiculite, etc.) also improved the properties of concrete [26–28].

The study [29] investigated adhesion between the layers of 3D printed concrete. It was found that the adhesion between the layers decreased with increasing time interval between lay-up. The interlayer bonds can be strengthened with cement paste at the interface [30]. This solution minimized voids and increased the adhesion area.

Good extrudability and buildability were achieved when the yield strength of the material was in the range of 1.5–2.5 kPa [31]. The material did not have enough strength for maintain shape if the yield strength was below this range. Nevertheless, the material extrudability was difficult if the yield strength was above this range.

For additive technologies due to the absence of form work, the rheological properties of the concrete mixture and green strength are also significant [9, 32]. As for example, the green strength can be up to 9.5 kPa in 30 min after mortar extrusion and up to 45 kPa in 150 min after mortar extrusion [32]. In this paper, rheological properties and green strength are not considered.

In addition to the above concrete properties, which play an important role for 3D printing, it is the heat release of concrete [33]. Cracks appear in hardening concrete because of the heat of hydration of cement. These cracks are caused by uneven and moderate temperature deformations [34], [35]. There are different technical solutions for controlling the thermal conditions of hardening concrete and reducing temperature differences [36], [37], [38].

Another important property of any types of concrete is its thermal conductivity [39]. The thermal conductivity significantly affects the thermotechnical characteristics of the building and its energy performance [40–41].

In study [42], concrete containing cement, fly ash and hydrophobic aerogel granules was investigated. This type of composite could be used as 3D printing of wall elements with low thermal conductivity.

Another way to reduce the thermal conductivity was to use the extrudable foamed concrete [43–44]. Study [43] showed that the obtained green and early age strength made this material potentially suitable for 3D printing. Relatively high compressive strengths of this concrete was above 10 MPa [44]. Therefore, it fulfilled the requirements for building materials used for load-bearing wall elements in multi-story houses. This type of concrete was suitable for 3D-printing applications, while fulfilling both load-carrying and insulating functions. Besides the foamed concrete could be used foamed fly ash-based geopolymer matrices. This material for 3D printing was investigated in [45].

Large scale building elements could be made on 3D printer by depositing fresh wood chip concrete [46].

Fiber-reinforced concrete was investigated in [47] to optimize the mechanical and heat transfer characteristics of building components. Structures made of this type of concrete showed less thermal conductivity compared to reinforced concrete.

However, the heat release of concrete and the thermal conductivity of concrete has not yet been purposefully investigated for construction 3D printing. Which makes this research relevant.

The subject of research is expanded-clay concrete with additives of ground granulated blast-furnace slag, silica fume, superplasticizer admixture and air-entraining admixture for 3D printing.

The objectives of the work is analysis of expanded-clay concrete composition influence on the heat release and the thermal conductivity of concrete.

2. Materials and Methods

2.1. Materials

The Fly ash aggregate was tested in Peter the Great St. Petersburg Polytechnic University (Russia).

Consistency of experimental mixtures was not tested for 3D printing. The rheological parameters for suitability can be achieved using admixtures after selecting a mixture according to the criteria of heat release and thermal conductivity.

Concrete mixture consisted of:

1. Portland cement PC 500-D0-N produced by OJSC MORDOVCEMENT (Mordovia, Russia). Fineness of the cement is 97.1 %. Mineralogical composition of the cement are presented in Table 1.

Table 1. Mineralogical composition of the cement [%].

C_3S	C_2S	C_3A	C_4AF
60.8	16.6	5.8	12.8

2. Natural sand. The sand has fineness modulus from 2 to 2.5.

3. Expanded clay gravel produced by OOO SUOR (Novocheboksarsk, Russia). Size fraction is 0–20 mm, bulk density is 800 kg/m^3 and cylinder strength is from 5.5 to 6.5 MPa.

4. Silica fume MKU-85 produced by Yurga division of Kuznetskie Ferrosplavy (Yurga, Russia). Specific surface area is 15 m^2/g. Content of SiO_2 is 91.2 %.

5. Ground granulated blast furnace slag produced by PJSC Mechel (Russia). Chemical composition of the slag is presented in Table 2.

Table 2. Chemical composition of the ground granulated blast furnace slag.

S	K	SiO_2	CaO	MnO	Al_2O_3	MgO	TiO_2	FeO
0.710	1.54	38.90	40.50	0.57	10.50	7.50	0.73	0.63

6. Superplasticizer Sika ViscoCrete E78 RC/A on the base of polycarboxylate.

7. Air-entraining admixture Sika AER 200-C on the base of synthetic surface-active agent.

2.2. Thermal conductivity measurement

The thermal conductivity λ was determined by thermal conductivity meter ITP-MG4 “250” according to Russian State Standard GOST 7076-99 “Building materials and products. Method of determination of steady-state thermal conductivity and thermal resistance”. Samples in the form of plates were made with dimensions of 250×250×30 mm. Form removal was carried out 2 days after the manufacture of the samples. After that, the samples were stored under normal conditions at a temperature of 20 ± 2 °C and a relative air humidity of at least 96 %. After 28 days, the samples were removed from the moisture chamber and dried to constant weight. The test results are presented in Table 3.

2.3. Heat release measurement

Heat release Q was determined according to EN 196-9:2010. The heat release of concrete was determined by the thermos method at an initial temperature of 20 ºC. After that, the heat release of concrete was recalculated to the isothermal hardening mode at a temperature of 20 ºC.

In accordance with hypothesis [48] the ratio of the heat release rates and corresponding terms τ_2 and τ_1 remains constant at moments of equal heat release at $Q_1 = Q_2$:

$$\frac{(\partial Q/\partial \tau)_1}{(\partial Q/\partial \tau)_2} = \frac{\tau_2}{\tau_1} = f_t = \text{const} \tag{1}$$

The temperature function f_t was calculated by the formula:

$$f_t = 2^{\frac{t_1 - t_2}{\varepsilon}}, \tag{2}$$

where ε is the characteristically temperature difference. If t_1-t_2 = ε, when $f_t = 2$. This means if the temperature rises by ε degrees, the rate of heat release will double.

Three identical samples of each concrete mix were tested. The readings of the temperature sensors were recorded by the data logger every 30 minutes. Heat release per unit mass of cement $q = Q/C$ in tested mixes was characterized by two parameters of the I.D. Zaporozhets’s equation (3): $q_{max} = Q_{max}/C$, kJ/kg and A_{20}, d^{-1}. The parameter m was accepted constant and equal to 2.2 [49].

$$Q = Q_{\max}\left[1-(1+A_t\tau)^{-\frac{1}{m-1}}\right], \quad (3)$$

where A_t is the heat release rate coefficient that characterizes the heat release rate at a given constant temperature t (in this case t = 20 ºC and $A_t = A_{20}$); m is the order of the cement hydration reaction. The order of the cement hydration reaction for portland cement is between 2 and 2.3.

The values of q_{max} and A_{20} were determined by experimental data.

3. Results and Discussion

3.1. Experimental data of heat release and thermal conductivity

The heat release data and the thermal conductivity data of expanded-clay concrete are presented in Table 3.

Table 3. Mixture proportions, the heat release and the thermal conductivity of expanded-clay concrete.

Cement (C) [kg/m³]	W/C	Expanded clay gravel [kg/m³]	Sika VC E78 [kg/m³]	Sika AER 200-C [kg/m³]	Silica fume [kg/m³]	Slag [kg/m³]	λ [W/(m·°C)]	q_{max} [kJ/kg]	A_{20} [d⁻¹]
X_1	X_2	X_3	X_4	X_5	X_6	X_7	Y_1	Y_2	Y_3
375	0.445	0	4.5	1	0	60	1.352	400	1.45
375	0.45	0	5.25	0	0	60	1.378	380	1.65
430	0.43	130	4.5	1.45	43	70	1.215	392	1.45
435	0.425	276	4.34	1.53	44	70	1.071	420	1.23
440	0.461	347	3.96	1.38	44	70	0.983	423	0.8
450	0.438	115	4.32	1	45	80	1.191	393	1.25
450	0.511	520	4.05	1	45	70	0.791	395	0.9
460	0.374	267	4.15	1	46	80	1.018	360	2
460	0.439	185	4.4	0.8	46	70	1.184	420	1.25
465	0.35	545	3.75	0.75	40	0	0.751	335	0.9
465	0.443	295	4.9	1.4	46	70	0.994	430	1.15
465	0.35	545	3.75	0.75	40	0	0.855	330	1.1
470	0.483	270	4.23	1.4	47	69	0.954	420	1.05
475	0.309	602	5	0.55	44	0	0.842	355	1.5
475	0.314	502	4.5	0	44	0	0.788	350	1.7
475	0.34	0	3.7	0	45	0	0.918	320	1.33
475	0.319	502	5	0	44	0	0.848	360	1.3
475	0.318	602	5.5	0.55	44	0	0.885	360	1.3
475	0.34	560	3.7	0	45	0	0.901	317	1.4
480	0.429	430	4.35	0.85	50	70	0.94	330	0.86
485	0.404	530	6	0	45	110	0.867	380	2.5
490	0.414	351	5.8	1	48	68	0.878	370	1.35
520	0.296	486	7.6	1.25	50	60	0.83	345	1.1
520	0.337	504	6.7	0	50	100	0.858	325	3.3
520	0.379	400	7.5	0	45	60	0.906	350	1.3
520	0.404	556	6.4	0	50	50	0.86	330	2.8
520	0.41	428	4.9	1.5	50	70	0.791	358	1.55
550	0.351	512	6.25	0	50	50	0.77	310	1.05

3.2. Thermal conductivity dependence on concrete composition

The influence of independent composition parameters (X_1 ... X_7) on the thermal conductivity parameters (Y_1) is determined by multivariate analysis based on linear regression.

Linear regression $Y_1 = f(X_1 \ldots X_7)$ is appropriate according to the F-test, which is 4.32E-12 with a statistical value of 60.7. A determination coefficient R^2 is 0.9550. The regression coefficients and their significance are given in Table. 4.

Table 4. Parameters of linear regression for the thermal conductivity dependence on concrete composition.

Variables	coefficients	Standard error	t-statistics	*P*-value	Limits of confidence 95 %	
					Upper	Lower
X_1	-0.00176	0.000610	-2.88	0.00916	-0.00303	-0.000487
X_2	-0.154	0.270	-0.569	0.576	-0.717	0.410
X_3	-7.79E-04	6.55E-05	-11.9	1.59E-10	-9.15E-04	-6.42E-04
X_4	0.0125	0.0148	0.847	0.407	-0.0183	0.0433
X_5	-0.0448	0.0198	-2.26	0.0349	-0.0861	-0.00352
X_6	0.00126	0.00164	0.766	0.453	-0.00217	0.00468
X_7	0.000546	0.000472	1.16	0.261	-0.000439	0.00153
Y_1 interaction	2.02	0.239	8.44	5.02E-08	1.52	2.52

Size of a region meets the condition $P < 0.05$ for three of seven factors. These factors are X_1 (cement content), X_3 (expanded-clay gravel content) and X_5 (air-entraining admixture content). Moreover, all three coefficients are negative, that is, an increase in the content of each of these components reduces the value of thermal conductivity of concrete. However, the results of dual regression analysis shows that coefficient of X_5 is positive, which contradicts the physical meaning, and the coefficient of determination is very small, $R^2 = 0.0292$. Linear regression plots for significant factors X_1 and X_3 are shown in Fig. 1.

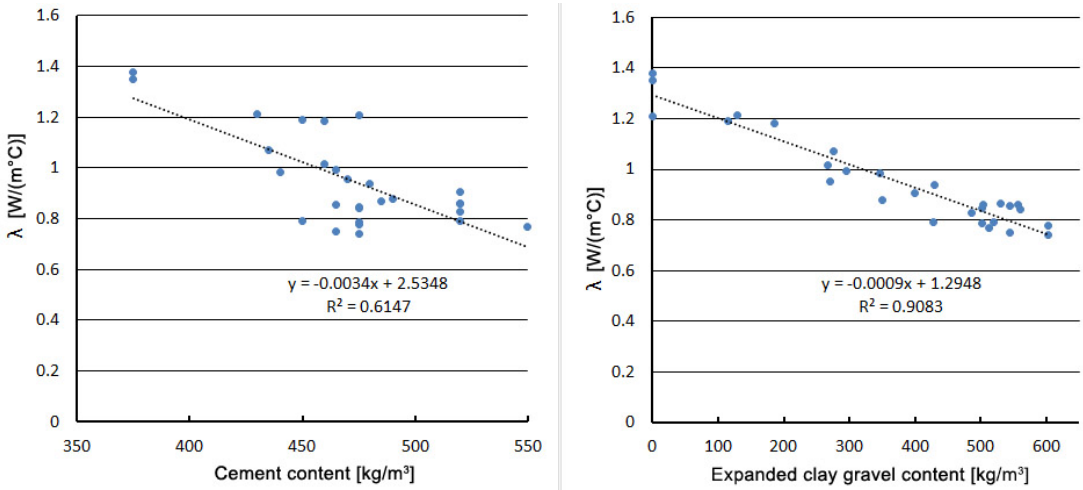

Figure 1. Dual regression plots for the dependence of thermal conductivity versus cement content, and expanded clay gravel content.

3.3. Heat release dependence on concrete composition

The influence of independent composition parameters (X_1 ... X_7) on the heat release parameters (Y_2 and Y_3) was determined by multivariate analysis based on linear regression. Importance factors are presented in Table 5.

Table 5. Linear hypothesis factors of the multifactorial regression.

Regression	F-statistics	*F*-value	R^2
$q_{max} = Y_2 = f(X_1 \ldots X_7)$	9.70	2.95E-05	0.7725
$A_{20} = Y_3 = f(X_1 \ldots X_7)$	3.63	0.0109	0.5598

Linear regression graphs for the most significant factors X_1, X_2, and X_5 of the response function $Y_2 = q_{max}$ are shown in Fig. 2.

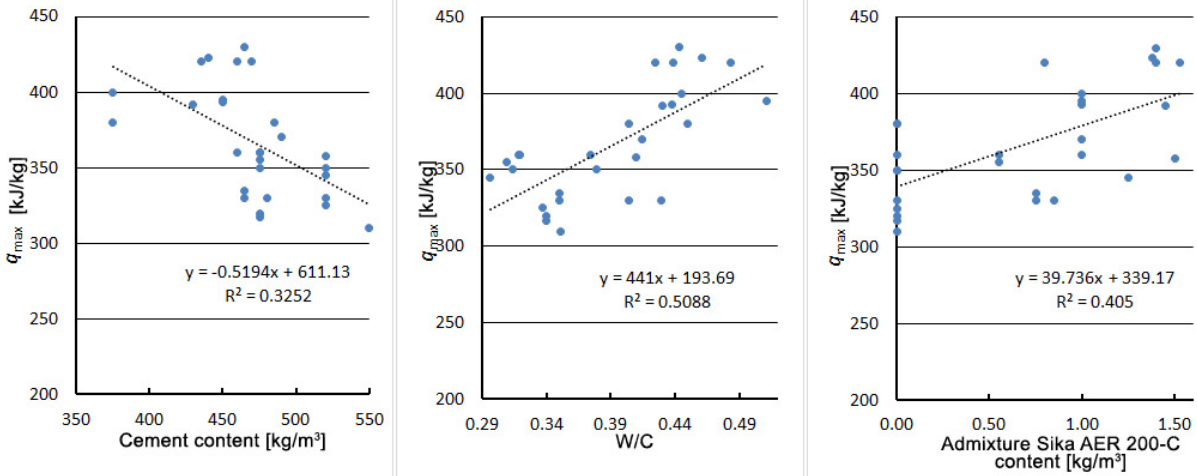

Figure 2. Dual regression plots for the dependence of q_{max} versus cement content, water-cement ratio and admixture Sika AER 200-C content.

Function $Y_3 = A_{20}$ has very low coefficients of determination for the dual regression and represents hundredths and thousandths of a unit.

3.4. Correlation between the concrete parameters

The results of regression analysis on the influence of seven factors on the thermal conductivity *(Y_1)* shows that only two factors have significant statistical value. The thermal conductivity decreases with increasing the expanded clay gravel content (factor X_3), which is characterized by a relatively small scattering of points and a high coefficient of determination of R^2 = 0.9083. The influence of another significant factor – cement content (X_1) – is difficult to explain. If the cement content increases, the thermal conductivity decreases. Two more dual regressions of dependencies could explain this fact. They are concrete density versus cement content and thermal conductivity versus concrete density (Fig. 3).

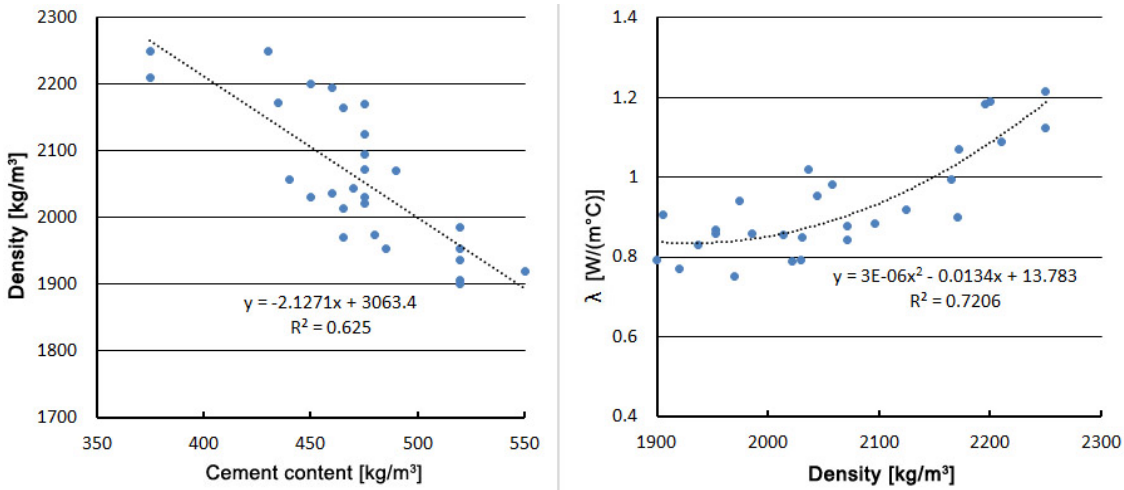

Figure 3. Dual regressions of dependencies: concrete density versus cement content and thermal conductivity versus concrete density.

As shown in Fig. 3, the effect of cement content (factor X_1) on the thermal conductivity (Y_1) is associated with a decrease in the concrete density. Authors assume that this is the result of replacement of fine aggregate with a more porous cement paste. In this case, the usual correlation between λ and the concrete density is satisfactorily described by a second degree polynomial with a determination coefficient of R^2 = 0.721.

As a regression analysis has shown, the total integral value of the heat release per unit mass of cement q_{max} (Y_2) depends on three factors: the cement content (X_1), the water cement ratio (X_2) and the admixture Sika AER 200-C content (X_5). Fig. 2 shows a significant scattering of experimental points, but a certain tendency is observed. The decrease in the heat release per unit mass of cement $q = Q/C$ with an increase in cement content is a well-known position. The heat Q produced by concrete, with constant W/C and other

equal conditions, increases linearly with an increase in the cement content C [50], [51]. This explains the law of mass action from chemical kinetics.

4. Conclusions

A multivariate analysis of experimental data on the influence of seven factors of concrete mixture (cement, water cement ratio, expanded clay, ground granulated blast-furnace slag, silica fume, superplasticizer, air-entraining admixture) on the thermal conductivity and the heat release of concrete was carried out. The results obtained lead to the following conclusions:

1. The thermal conductivity of concrete depends primarily on the expanded clay gravel content and depends less on the cement content. If both factors increase, the thermal conductivity decreases. This is due to the replacement of dense sand grains with a more porous cement paste. The influence of air-entraining admixture on the thermal conductivity of expanded-clay concrete was not detected due to the high scattering of the experimental points.
2. The cement content and water cement ratio impact on the integral value of the heat release per unit mass of cement. This value $q = Q/C$ decreases with increasing cement content. The reason for this is that the heat Q generated by concrete, with constant W/C and other equal conditions, increases linearly with increasing the cement content C. W/C has a positive effect on the heat release of concrete. This explains the law of mass action from chemical kinetics.
3. The influence of these seven factors on the rate of heat release, and, consequently, on the hydration of cement has not been established.

Further research on this topic may be experimental studies of cold-bonded fly ash aggregate concrete for 3D printer. Fly ash can be used as an additive in the mix [52] or as a large aggregate [53]. If presoaked aggregate is added to the concrete mix, this will create “internal curing” for the concrete and reduce cracks caused by the heat release [54].

5. Acknowledgements

The research is funded by the Ministry of Science and Higher Education of the Russian Federation as part of World-class Research Center program: Advanced Digital Technologies (contract No. 075-15-2020-934 dated 17.11.2020).

References

1. Ngo, T.D., Kashani, A., Imbalzano, G., Nguyen, K.T.Q., Hui, D. Additive manufacturing (3D printing): A review of materials, methods, applications and challenges. Compos. Part B Eng. 2018. 143. Pp. 172–196. DOI: 10.1016/j.compo-sitesb.2018.02.012.
2. Vatin, N.I., Usanova, K.Y. BIM end-to-end training: From school to graduate school. Adv. Trends Eng. Sci. Technol. III- Proc. 3rd Int. Conf. Eng. Sci. Technol. ESaT 2018. 2019. Pp. 651–656. DOI: 10.1201/9780429021596-102
3. Lowke, D., Dini, E., Perrot, A., Weger, D., Gehlen, C., Dillenburger, B. Particle-bed 3D printing in concrete construction – Possibilities and challenges. Cem. Concr. Res. 2018. 112. Pp. 50–65. DOI: 10.1016/j.cemconres.2018.05.018.
4. Lim, S., Buswell, R.A., Valentine, P.J., Piker, D., Austin, S.A., De Kestelier, X. Modelling curved-layered printing paths for fabricating large-scale construction components. Addit. Manuf. 2016. 12. Pp. 216–230. DOI: 10.1016/j.addma.20-16.06.004
5. Gosselin, C., Duballet, R., Roux, P., Gaudillière, N., Dirrenberger, J., Morel, P. Large-scale 3D printing of ultra-high performance concrete – a new processing route for architects and builders. Mater. Des. 2016. 100. Pp. 102–109. DOI: 10.1016/j.matdes.2016.03.097
6. Akulova, I., Slavcheva, G. Methodical Approach to Calculation of the Maintenance Cost for 3D Built Printing Equipment. IOP Conf. Ser. Mater. Sci. Eng. 2020. 753. DOI: 10.1088/1757-899X/753/5/052056
7. Tay, Y.W.D., Panda, B., Paul, S.C., Noor Mohamed, N.A., Tan, M.J., Leong, K.F. 3D printing trends in building and construction industry: a review. Virtual Phys. Prototyp. 2017. 12. Pp. 261–276. DOI: 10.1080/17452759.2017.1326724
8. Elistratkin, M.Y., Lesovik, V.S., Alfimova, N.I., Shurakov, I.M. On the question of mix composition selection for construction 3D printing. Mater. Sci. Forum. 945 MSF. 2018. Pp. 218–225. DOI: 10.4028/www.scientific.net/MSF.945.218
9. Slavcheva, G.S., Artamonova, O.V. Rheological behavior and mix design for 3D printable cement paste. Key Eng. Mater. 799 KEM. 2019. Pp. 282–287. DOI: 10.4028/www.scientific.net/KEM.799.282
10. Bos, F., Wolfs, R., Ahmed, Z., Salet, T. Additive manufacturing of concrete in construction: potentials and challenges of 3D concrete printing. Virtual Phys. Prototyp. 2016. 11. Pp. 209–225. DOI: 10.1080/17452759.2016.1209867
11. De Schutter, G., Lesage, K., Mechtcherine, V., Nerella, V.N., Habert, G., Agusti-Juan, I. Vision of 3D printing with concrete – Technical, economic and environmental potentials. Cem. Concr. Res. 2018. 112. Pp. 25–36. DOI: 10.1016/j.cem-conres.2018.06.001
12. Paul, S.C., van Zijl, G.P.A.G., Gibson, I. A review of 3D concrete printing systems and materials properties: current status and future research prospects. Rapid Prototyp. J. 2018. 24. Pp. 784–798. DOI: 10.1108/RPJ-09-2016-0154
13. Bos, F.P., Ahmed, Z.Y., Wolfs, R.J.M., Salet, T.A.M. 3D printing concrete with reinforcement. High Tech Concr. Where Technol. Eng. Meet – Proc. 2017 fib Symp. 2017. Pp. 2484–2493. DOI: 10.1007/978-3-319-59471-2_283
14. Klyuev, S.V., Klyuev, A.V., Shorstova, E.S. Fiber concrete for 3-D additive technologies. Mater. Sci. Forum. 2019. 974. Pp. 367–372. DOI: 10.4028/www.scientific.net/MSF.974.367
15. Klyuev, S.V., Klyuev, A.V., Vatin, N.I. Fiber concrete for the construction industry. Magazine of Civil Engineering. 2018. 84. Pp. 41–47. DOI: 10.18720/MCE.84.4

16. Murali, G., Fediuk, R. A Taguchi approach for study on impact response of ultra-high-performance polypropylene fibrous cementitious composite. J. Build. Eng. 2020. 30. DOI: 10.1016/j.jobe.2020.101301
17. Hambach, M., Volkmer, D. Properties of 3D-printed fiber-reinforced Portland cement paste. Cem. Concr. Compos. 2017. DOI: 10.1016/j.cemconcomp.2017.02.001
18. Ibragimov, R.A., Izotov, V.S. Effect of carbon nanotubes on the structure and properties of cement composites. Inorg. Mater. 2015. 51. Pp. 834–839. DOI: 10.1134/S0020168515080087
19. Rybakov, V., Seliverstov, A., Petrov, D., Smirnov, A., Volkova, A. Lightweight steel concrete structures slab panels load-bearing capacity. MATEC Web Conf. 2018. 245. DOI: 10.1051/matecconf/201824508008
20. Rybakov, V.A., Ananeva, I.A., Pichugin, E.D., Garifullin, M. Heat protective properties of enclosure structure from thin-wall profiles with foamed concrete. Magazine of Civil Engineering. 2020. 94(2). Pp. 11–20. DOI: 10.18720/MCE.94.2
21. Soltan, D.G., Li, V.C. A self-reinforced cementitious composite for building-scale 3D printing. Cem. Concr. Compos. 2018. DOI: 10.1016/j.cemconcomp.2018.03.017
22. Zareiyan, B., Khoshnevis, B. Effects of interlocking on interlayer adhesion and strength of structures in 3D printing of concrete. Autom. Constr. 2017. 83. Pp. 212–221. DOI: 10.1016/j.autcon.2017.08.019
23. Zareiyan, B., Khoshnevis, B. Effects of mixture ingredients on interlayer adhesion of concrete in Contour Crafting. Rapid Prototyp. J. 2018. 24. Pp. 584–592. DOI: 10.1108/RPJ-02-2017-0029
24. Kazemian, A., Yuan, X., Cochran, E., Khoshnevis, B. Cementitious materials for construction-scale 3D printing: Laboratory testing of fresh printing mixture. Constr. Build. Mater. 2017. DOI: 10.1016/j.conbuildmat.2017.04.015
25. Iubin, P., Zakrevskaya, L. Soil-concrete for use in the 3D printers in the construction of buildings and structures. In: MATEC Web of Conferences. EDP Sciences. 2018. DOI: 10.1051/matecconf/201824503002
26. Klyuev, S.V., Klyuev, A.V., Shorstova, E.S. The micro silicon additive effects on the fine-grassed concrete properties for 3-D additive technologies. Mater. Sci. Forum. 2019. 974. Pp. 131–135. DOI: 10.4028/www.scientific.net/MSF.974.131
27. Ma, G., Wang, L. A critical review of preparation design and workability measurement of concrete material for largescale 3D printing. Front. Struct. Civ. Eng. 2018. 12. Pp. 382–400. DOI: 10.1007/s11709-017-0430-x
28. Rybakov, V., Seliverstov, A., Petrov, D., Smirnov, A., Volkova, A. Strength characteristics of foam concrete samples with various additives. MATEC Web Conf. 2018. 245. DOI: 10.1051/matecconf/201824503015
29. Wolfs, R.J.M., Bos, F.P., Salet, T.A.M. Hardened properties of 3D printed concrete: The influence of process parameters on interlayer adhesion. Cem. Concr. Res. 2019. 119. Pp. 132–140. DOI: 10.1016/j.cemconres.2019.02.017
30. Marchment, T., Sanjayan, J., Xia, M. Method of enhancing interlayer bond strength in construction scale 3D printing with mortar by effective bond area amplification. Mater. Des. 2019. 169. DOI: 10.1016/j.matdes.2019.107684
31. Rahul, A.V., Santhanam, M., Meena, H., Ghani, Z. 3D printable concrete: Mixture design and test methods. Cem. Concr. Compos. 2019. 97. Pp. 13–23. DOI: 10.1016/j.cemconcomp.2018.12.014
32. Ding, T., Xiao, J., Qin, F., Duan, Z. Mechanical behavior of 3D printed mortar with recycled sand at early ages. Constr. Build. Mater. 2020. 248. DOI: 10.1016/j.conbuildmat.2020.118654
33. Shanahan, N., Tran, V., Zayed, A. Heat of hydration prediction for blended cements. J. Therm. Anal. Calorim. 2017. 128. Pp. 1279–1291. DOI: 10.1007/s10973-016-6059-5
34. Klemczak, B., Batog, M., Pilch, M., Zmij, A. Analysis of Cracking Risk in Early Age Mass Concrete with Different Aggregate Types. Procedia Eng. 2017. 193. Pp. 234–241. DOI: 10.1016/j.proeng.2017.06.209
35. Shaibakova, A., Semenov, K., Barabanshchikov, Y. Thermal cracking resistance of stacking concrete blocks. MATEC Web Conf. 2018. 245. DOI: 10.1051/matecconf/201824508005
36. Singh, P.R., Rai, D.C. Effect of piped water cooling on thermal stress in mass concrete at early ages. J. Eng. Mech. 2018. 144. DOI: 10.1061/(ASCE) EM.1943-7889.0001418
37. Azenha, M., Lameiras, R., de Sousa, C., Barros, J. Application of air cooled pipes for reduction of early age cracking risk in a massive RC wall. Eng. Struct. 2014. 62–63. Pp. 148–163. DOI: 10.1016/j.engstruct.2014.01.018
38. Seo, T.S., Kim, S.S., Lim, C.K. Experimental study on hydration heat control of mass concrete by vertical pipe cooling method. J. Asian Archit. Build. Eng. 2015. 14. Pp. 657–662. DOI: 10.3130/jaabe.14.657
39. Baghban, M.H. Thermal insulating cementitious composite containing aerogel and phosphate-based binder. IOP Conf. Ser. Mater. Sci. Eng. 2019. 609. DOI: 10.1088/1757-899X/609/6/062024
40. Gorshkov, A., Vatin, N., Nemova, D., Shabaldin, A., Melnikova, L., Kirill, P. Using life-cycle analysis to assess energy savings delivered by building insulation. Procedia Eng. 2015. 117. Pp. 1080–1089. DOI: 10.1016/j.proeng.2015.08.240
41. Gorshkov, A.S., Vatin, N.I., Rymkevich, P.P., Kydrevich, O.O. Payback period of investments in energy saving. Magazine of Civil Engineering. 2018. No. 78(2). Pp. 65–75. DOI: 10.18720/MCE.78.5
42. Baghban, M.H., Javadabadi, M.T. Effect of hydrophobic aerogel granules on thermomechanical properties of cementitious composites. Mater. Sci. Forum. 971 MSF. 2019. Pp. 114–118. DOI: 10.4028/www.scientific.net/MSF.971.114
43. Falliano, D., Gugliandolo, E., De Domenico, D., Ricciardi, G. Experimental investigation on the mechanical strength and thermal conductivity of extrudable foamed concrete and preliminary views on its potential application in 3D printed multilayer insulating panels. RILEM Bookseries. 2019. 19. Pp. 277–286. DOI: 10.1007/978-3-319-99519-9_26
44. Markin, V., Nerella, V.N., Schröfl, C., Guseynova, G., Mechtcherine, V. Material design and performance evaluation of foam concrete for digital fabrication. Materials (Basel). 2019. 12. DOI: 10.3390/ma12152433
45. Alghamdi, H., Neithalath, N. Synthesis and characterization of 3D-printable geopolymeric foams for thermally efficient building envelope materials. Cem. Concr. Compos. 2019. 104. DOI: 10.1016/j.cemconcomp.2019.103377
46. Henke, K., Talke, D., Winter, S. Additive manufacturing of building elements by extrusion of wood concrete. WCTE 2016 – World Conf. Timber Eng. 2016.
47. Vantyghem, G., Boel, V., De Corte, W., Steeman, M. Compliance, stress-based and multi-physics topology optimization for 3D-printed concrete structures. In: RILEM Bookseries. Pp. 323–332. Springer Netherlands, 2019. DOI: 10.1007/978-3-319-99519-9_30
48. Zaporozhets, I.D., Okorokov, S.D., Pariyskiy, A.A. Heat Liberation by concrete. Stroyizdat, Moscow (1966).
49. Makeeva, A., Amelina, A., Semenov, K., Barabanshchikov, Y. Temperature action in analysis of thermal stressed state of massive concrete and reinforced concrete structures. MATEC Web Conf. 245. 2018. DOI: 10.1051/matecconf/201824503016

50. Yang, K.H., Moon, G.D., Jeon, Y.S. Implementing ternary supplementary cementing binder for reduction of the heat of hydration of concrete. J. Clean. Prod. 2016. 112. Pp. 845–852. DOI: 10.1016/j.jclepro.2015.06.022
51. Bohloli, B., Skjølsvold, O., Justnes, H., Olsson, R., Grøv, E., Aarset, A. Cements for tunnel grouting – Rheology and flow properties tested at different temperatures. Tunn. Undergr. Sp. Technol. 2019. 91. DOI: 10.1016/j.tust.2019.103011
52. Fediuk, R.S., Yushin, A.M. The use of fly ash the thermal power plants in the construction. IOP Conf. Ser. Mater. Sci. Eng. 2015. 93. DOI: 10.1088/1757-899X/93/1/012070
53. Usanova, K.Y., Barabanshchikov, Y.G., Kostyrya, S.A., Fedorenko, Y.P. Cold-bonded fly ash aggregate as a coarse aggregate of concrete. Constr. Unique Build. Struct. 2018. 72. Pp. 1–16.
54. Barabanshchikov, Y., Fedorenko, I., Kostyrya, S., Usanova, K. Cold-Bonded Fly Ash Lightweight Aggregate Concretes with Low Thermal Transmittance: Review. Adv. Intell. Syst. Comput. 2019. 983. Pp. 858–866. DOI: 10.1007/978-3-030-19868-8_84

Contacts:

Kseniia Usanova, plml@mail.ru
Yuriy Barabanshchikov, ugb@mail.ru
Leonids Pakrastins, leonids.pakrastins@rtu.lv
Stanislav Akimov, akimov_sv@spbstu.ru
Svetlana Belyaeva, belyaeva_sv@spbstu.ru

© Usanova, K., Barabanshchikov, Yu.G., Pakrastins, L., Akimov, S.V., Belyaeva, S.V., 2021

Magazine of Civil Engineering

ISSN 2712-8172

journal homepage: http://engstroy.spbstu.ru/

DOI: 10.34910/MCE.102.11

Analytical calculation of deflection of a planar truss with a triple lattice

M.N. Kirsanov
National Research University "Moscow Power Engineering Institute", Moscow, Russia
E-mail: c216@ya.ru

Keywords: structural design, truss, deflection, Maple, asymptotics, exact solution, induction, stability

Abstract. We propose a scheme of a statically determinate truss with straight chord s and four supports, one of which is a fixed hinge, the other movable hinges. The task is to obtain the dependence of the deflection of the middle span of the structure on the number of panels. The problem is solved by induction using operators of the Maple computer mathematics system. The deflection is determined by the Maxwell – Mohr's formula, the forces in the rods are found from the solution of the joint system of the equation of equilibrium of nodes, the unknowns of which include the reaction of the supports. of nodes, whose unknowns include the reaction of the supports. The inclusion of support reactions in the system of equilibrium equations allows us to reveal the external static indeterminability of the structure. Generalizing a number of solutions for trusses with a consistently increasing number of panels, the desired dependence is obtained. To do this, we create recurrent equations that satisfy the terms of the sequences of coefficients in the deflection formula. The resulting homogeneous linear recurrent equations have a degree no higher than the eighth in the case of a problem with a load distributed over the upper chord and the sixth for a concentrated load in the middle of the span. Solving these equations in the Maple environment using the rsolve operator gives expressions of the dependence of the coefficients of the desired formula on the number of panels. The asymptotics of solutions are found. The dependence of the horizontal shift of the mobile support on the action of distributed and concentrated load is also obtained. Formulas are derived for the dependence on the number of panels of forces in some elements in the middle of the span. The obtained solutions can be used for preliminary evaluation of the designed structure and for evaluating the accuracy of numerical solutions.

1. Introduction

Rod structures that carry loads or perform fencing or decorative functions are widely used in construction [1–6]. The most common planar schemes of such structures, consisting of pivotally connected rods that experience only compression or tension (trusses). On the basis of such models, more complex schemes with arbitrary (rigid or elastic) nodal connections are also built. Among all truss schemes, statically determinate ones are singled out separately, the forces in which are found from the static equations. Trusses differ in the shape of chords and the grid pattern. Despite a fairly large variety of schemes for statically determinate planar trusses, the search for new designs continues. This search is not an end in itself. Different working conditions of structures suggest different schemes. In some cases, a well-chosen scheme gives an advantage in terms of structural rigidity, where this is especially important, for example, in railway bridges or industrial buildings with suspended crane equipment. In other cases, the truss is used as a decorative element and must have a non-standard architectural expression. In [7], spatial periodic hinge – rod structures are developed for modeling materials with a cellular structure. Very often, the structure requires more strength than rigidity. In all these variants, you can not do with one simple scheme, for example, a truss with parallel chords and a triangular lattice. A variety of schemes is required. In 2005, Hutchinson and Fleck even called the search for new statically determinate schemes "hunting" [8, 9]. In the future, the direction of studying the features of calculating regular plane and spatial structures is continued [10, 11]. Statically determinate regular schemes of arch-type trusses were proposed and analytically calculated in [12–18]. More than 70 schemes of regular trusses with formulas for the deflection dependence on the number of panels are contained in the reference [19]. The relevance of this research is determined by the need to have a reliable alternative method

Kirsanov, M.N. Analytical calculation of deflection of a planar truss with a triple lattice. Magazine of Civil Engineering. 2021. 102(2). Article No. 10211. DOI: 10.34910/MCE.102.11

This work is licensed under a CC BY-NC 4.0

of obtaining a solution for numerical calculations of building structures. This method is the analytical method used in this paper. In addition, analytical solutions can be used for truss optimization problems [20–24].

The first paper aim is the task of developing a new architectural and expressive scheme of a statically determinate truss in order to expand the class of statically determinate schemes of regular type trusses, and second – the analysis of this scheme and obtaining an analytical solution for the deflection of the structure, whose parameters include the number of panels, which significantly expands the applicability of the desired formula.

The paper proposes a scheme of an externally statically indeterminate truss with straight belts and four supports, one of which is a fixed hinge, the other three are movable hinges. Triple lattice of parallel struts and resemble in structure members of a cable-stayed bridge Harp design or a Bolman truss with an additional lower chord. The task is to get a formula for calculating the dependence of the deflection of the middle span of the truss on the number of panels, the load and the size of the structure. The problem is solved by induction using operators of the Maple computer mathematics system.

The main novelty of the work consists in the proposed scheme of a statically determinate regular truss scheme, for which a simple analytical solution obtained by the induction method is admissible.

2. Methods

2.1. The calculation of the forces in the members

A distinctive feature of the structure under consideration is its external static indeterminate, defined by four supports, one of which is pivotally fixed, the other ones pivotally movable. However, this scheme is not only statically determinate, but also allows an analytical solution of the deflection problem for an arbitrary number of panels. The total length of all truss rods with n panels is $2(4n-1)a+3hn+12cn$, where $c=\sqrt{a^2+h^2}$. Each panel consists of six braces, three struts h high each, and six upper chord rods a long. Adjacent panels intersect with each other along two common members of the upper chord and are connected along the lower chord by a rod of length $4a$. Thus, shorter rods are located in the upper chord that is subject to compression, and the lower stretched chord contains long members. The truss consists of $m=14n+6$ rods, including five rods that model supports.

The truss is externally statically indeterminate, which means that the standard calculation scheme with independent determination of support reactions does not pass here. The reactions of the supports can only be determined from solving the joint system of equilibrium equations of all nodes together with the forces in the rods.

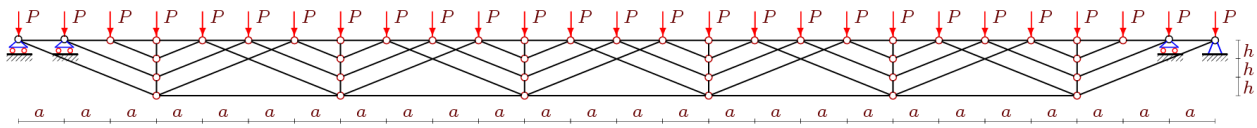

Figure 1. Load distributed over the upper chord, *n* = 6.

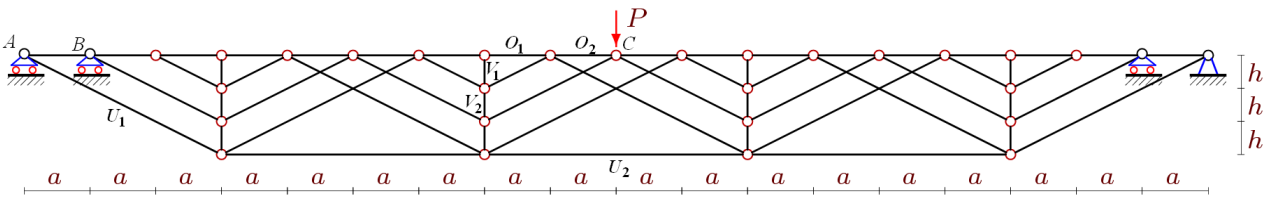

Figure 2. Concentrated force, *n* = 4.

Since the goal is to derive a formula for deflection, the forces in the rods must also be found in symbolic form. In [12, 14], an algorithm for calculating forces in planar truss rods in the Maple computer mathematics system is proposed. Nodes and rods of the truss are numbered (Fig. 3). The program code for the values of the coordinates of the nodes of the structure:

$$x_i=a(i-1),\ y_i=0,\ i=1,\dots,4n+3,$$
$$x_{i+4n+3j}=x_{4j},\ \ y_{i+4n+3j}=-hi,\ i=1,2,3,\ j=1,\dots,n. \tag{1}$$

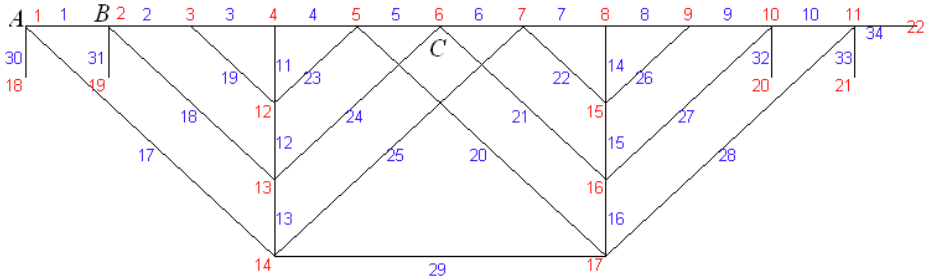

Figure 3. Numbering of nodes and rods, *n* = 2.

Each element is assigned an ordered list of end numbers. For upper chord, for example, these lists have the form: $N_i = [i, i+1],\ i = 1,\ldots,4n+2.$ For the lower chord:

$$N_{13n+2+i} = [3i+3+4n, 3i+6+4n],\ i = 1,\ldots,n-1. \tag{2}$$

The matrix of the system G of node equilibrium equations consists of guide cosines of forces, which are calculated through projections of members $l_{1,i} = x_{N_{2,i}} - x_{N_{1,i}},\ l_{2,i} = y_{N_{2,i}} - y_{N_{1,i}},\ i = 1,\ldots,m,$ and their lengths $l_i = \sqrt{l_{1,i}^{\ 2} + l_{2,i}^{\ 2}}$. Even (j = 2) rows of the matrix contain guide cosines with a horizontal x axis, and odd (j = 1) rows contain guide cosines with a vertical y axis:

$$\begin{gathered} G_{k,i} = -l_{j,i} / l_i,\ k = 2N_{i,2} - 2 + j,\ \ k \le m,\ j = 1,2,\ i = 1,\ldots,m, \\ G_{k,i} = l_{j,i} / l_i,\ \ k = 2N_{i,1} - 2 + j,\ \ k \le m,\ \ j = 1,2,\ i = 1,\ldots,m. \end{gathered} \tag{3}$$

Solving a system of equilibrium equations using standard operators of the Maple system gives forces in the rods. The scheme of distribution of forces in the rods in the case of a distributed load (Fig. 1) is shown in Fig. 4

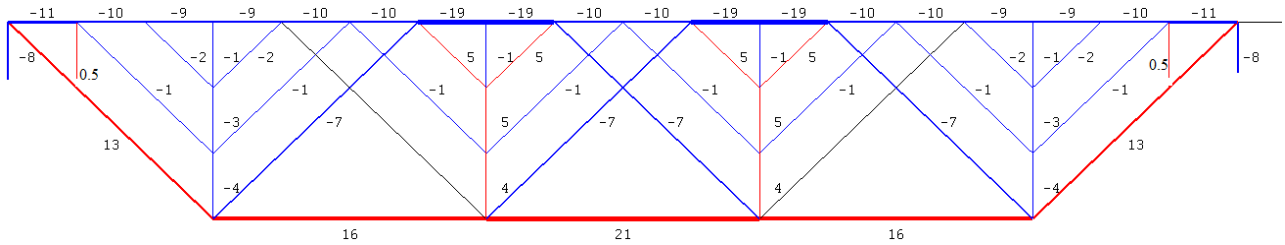

Figure 4. Forces in the rods in the case of distributed load action, *n* = 4, *a* = 4m, *h* = 3m.

Compressed members are marked in blue, and tension members are marked in red. The upper chord is compressed, the lower chord is stretched. It is significant that the extreme racks of the truss are compressed, the lower middle ones are stretched. The thickness of the line is proportional to the modules of forces related to the load P. In the case of concentrated force, not all members of the upper chord are compressed (Fig. 5), and many members, including side extensions, are not loaded.

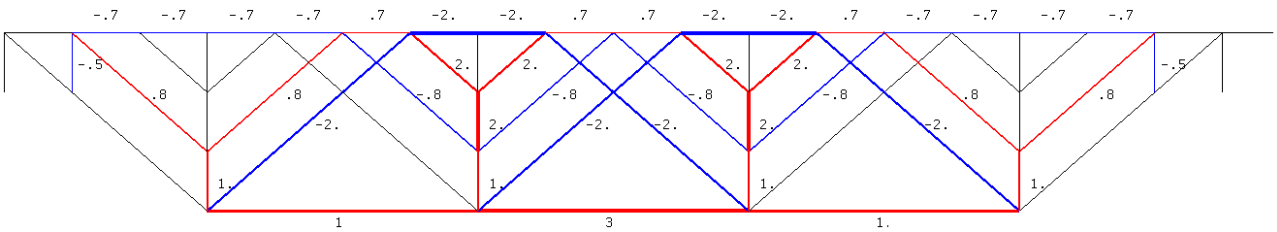

Figure 5. Forces in the rods under the action of a concentrated load, *n* = 4, *a* = 4m, *h* = 3m.

It is noted that for an odd number of panels, the determinant of the system of equilibrium equations turns to zero. This indicates the kinematic variability of the system. This is confirmed by the diagram of possible node velocity. For n = 1 it is given in Fig. 6:

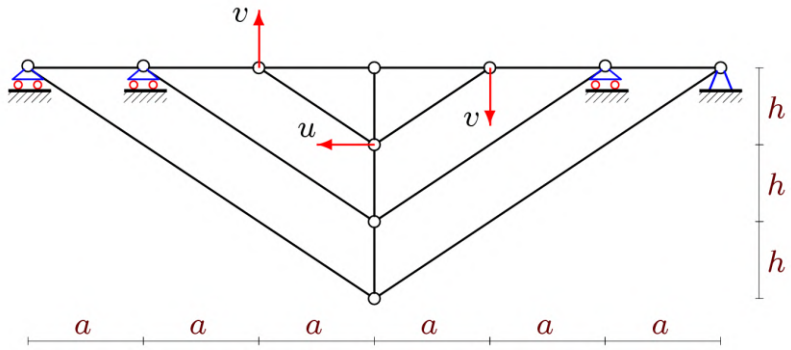

Figure 6. Diagram of possible velocity of nodes for instantly changeable truss, *n* = 1, *v/a* = *u/h*.

If the calculations are made not in analytical form, but numerically, then due to rounding errors, the effect of turning the determinant of the system to zero may not be noticed. Consider trusses with an even number of panels $n = 2k$.

2.2. Calculation of deflection

The deflection of the middle of the truss is calculated using the Maxwell – Mohr's formula

$$\Delta = \sum_{j=1}^{m-5} \frac{S_j \tilde{s}_j l_j}{EF}, \tag{4}$$

where E and F are the elastic modulus of the members and their cross-sectional area, l_j and S_j are the length and force in the j-th element from the action of a given load, $\tilde{s}_j$ is the force from the unit load applied to the upper chord nodes in the middle of the span.

Calculations show that the deflection of the truss for any number of panels has the form

$$\Delta = P(C_{1,k}a^3 + C_{2,k}c^3 + C_{3,k}h^3)/(h^2 EF), \tag{5}$$

where the coefficients $C_{j,k}$, $j = 1,2,3$ depend only on the number k. The main task at this stage is to find these dependencies. Sequential calculation of trusses with increasing number k = 1,2,... gives the sequence of coefficients. Common terms of these sequences can be found by composing recurrent equations for sequence members using the rgf_findrecur operator. To determine the coefficient $C_{1,k}$, it was necessary to consistently find the deflection of 16 trusses at k = 1,2,..., 16 and obtain a linear homogeneous equation of the eighth order:

$$C_{1,k} = 2C_{1,k-1} + 2C_{1,k-2} - 6C_{1,k-3} + 6C_{1,k-5} - 2C_{1,k-6} - 2C_{1,k-7} + C_{1,k-8}. \tag{6}$$

The solution of the equation is given by the rsolve operator:

$$C_{1,k} = (40k^4 + 2(9 - 8(-1)^k)k^2 + ((-1)^k - 1)(2k-1))/2. \tag{7}$$

The other coefficients are determined in the same way:

$$\begin{aligned} C_{2,k} &= (40k^4 + 16(2(-1)^k - 5)k^3 + 2(37 - 24(-1)^k)k^2 + (1-(-1)^k)(38k+15))/6, \\ C_{3,k} &= (40k^4 + 16(2(-1)^k - 5)k^3 + 2(7 - 24(-1)^k)k^2 + (1-(-1)^k)(26k+3))/6. \end{aligned} \tag{8}$$

Coefficients $C_{2,k}$ and $C_{3,k}$ differ only in a few terms. Formula (5) with these coefficients is the main solution of the problem. It can be supplemented by calculating the truss for other loads and by output formulas for the forces in some of the most critical rods in the relation to the stability and strength of the rods. So, for the case of the action of a concentrated force (Fig. 2), we have the following coefficients, obtained also by induction

$$C_{1,k} = 4k^3 + 2(2-(-1)^k)k + (-1)^k - 1,$$
$$C_{2,k} = (4k^3 + 6((-1)^k - 1)k^2 + (20 - 6(-1)^k)k - 3(-1)^k + 3)/3, \quad (9)$$
$$C_{3,k} = 2k(2k^2 + 3((-1)^k - 1)k - 3(-1)^k + 4)/3.$$

In the case of a load distributed over the nodes of the lower chord (Fig. 7), the coefficients of the solution (3) have the form

$$C_{1,k} = 5k^4 + (3 - 2(-1)^k)k^2,$$
$$C_{2,k} = (10k^4 + 4(2(-1)^k - 5)k^3 + 4(5 - 3(-1)^k)k^2 + 8(1-(-1)^k)k - 3(-1)^k + 3)/6, \quad (10)$$
$$C_{3,k} = k(5k^3 + 2(2(-1)^k - 5)k^2 + (7 - 6(-1)^k)k + 2((-1)^k - 1))/3.$$

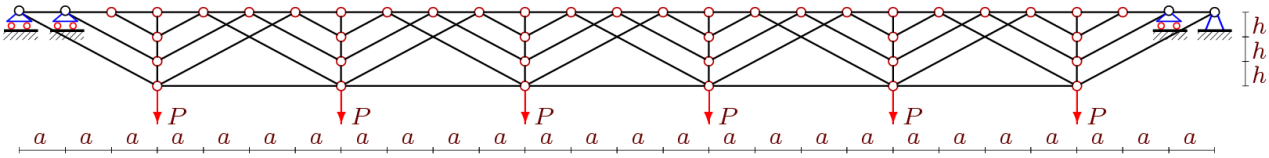

Figure 7. Load distributed over the lower chord, *n* = 6.

2.3. The forces in the members

In the process of calculating the deflection in analytical form, formulas for the forces in all rods and supports were obtained. We will write out only the most interesting results related to the most compressed and stretched rods (Fig. 2). For a distributed load, we have the following expressions:

$$O_1 = -Pa(8k^2 - 3)/(2h),\ O_2 = -Pa(8k-1)/(2h),$$
$$U_1 = 4Pck/h,\ \ U_2 = 4Pak^2/h,\ V_1 = -P,\ V_2 = P(2k+1)(2k-3). \quad (11)$$

At $k > 1$, the most compressed rod has a force of O_1. To approximate the stability of the structure, we can use Euler's formula, taking the coefficient of reduced length equal to 1:

$$Pa(8k^2 - 3)/(2h) = \pi^2 EJ/a^2, \quad (12)$$

where J is the moment of inertia of the cross section.

Reactions of supports of an externally statically indeterminate structure have the form:

$$Y_A = 4Pk,\ Y_B = -P/2. \quad (13)$$

It is interesting to note that the reaction of support B does not depend on the number of panels or the size of the structure. Judging by the sign, the reaction of this support is directed downward, the support does not support the structure from below, but holds it. In the case of a concentrated load for the same rods and support reactions the formulas are obtained:

$$O_1 = -Pa(2k-1)/(2h),\ O_2 = Pa(-1)^k/(2h),$$
$$U_1 = -Pc((-1)^k - 1)/(2h),\ \ U_2 = Pak/h,\ V_1 = 0,\ V_2 = P(2k + (-1)^k - 1)/2, \quad (14)$$
$$Y_A = P(1-(-1)^k)/2,\ Y_B = P(-1)^k/2.$$

Here the signs of reactions and some forces depend on the parity of the number of panels in the half span.

2.4. Shifting of the movable support

In addition to the deflection of the middle of the span, an equally important operational characteristic of the truss is the shift of the movable supports under the influence of an external vertical load. Of course, in girder trusses, this value is not as large as in arched or frame trusses, but to calculate the support structures, the engineer must have an estimate of the amount of support shift under load. When calculating the horizontal

displacement in the Maxwell – Mohr's formula (4), $\tilde{s}_j$ it is the forces from the action of the horizontal unit force on the movable support *A*. Omitting the intermediate calculations, we present the results of an inductive generalization of solutions. In the case of distributed load action the offset of the support *A* has the following formula depending on the number of panels:

$$\delta = 16Pa^2k(k+1)(2k+1)/(3EFh). \tag{15}$$

For the case of a concentrated load, this dependence has the form:

$$\delta = 2Pa^2k(1+k-(-1)^k)/(EFh). \tag{16}$$

For the case of a load distributed over the lower belt, the dependence of the shift of the movable support on the number of panels has the form:

$$\delta = 2Pa^2k(4k^2+6k+5)/(3EFh). \tag{17}$$

3. Results and Discussion

The features of the obtained solution in the case of distributed load are studied on the graphs of the dependence of the dimensionless deflection $\Delta' = \Delta EF/(P_{sum}L)$, where $P_{sum} = (4n-1)P$ is the total load on the structure. Let us assume that the span length is fixed $L = 2(2n+1)a$. As the number of panels increases, the length of each panel decreases, and the relative deflection increases (Fig. 8). Note that this growth is uneven and strongly depends on the height h. The intersection of curves shows that for different heights, but the same number of panels in this setting, the relative deflection can be the same. The deflection – height ratio also depends on the number of panels. At the beginning of the graph, for small k, the order of the curves is natural. The higher the height of the truss, the smaller the deflection. Starting from a certain value of k, the curves are reversed. Note that the effect of self-intersection of the curves on the graph and the alternation of their order is associated with the nonlinearity of the problem and the accepted assumption about the constancy of the load and the span length. If the deflection is attributed not to the total load and the panel size rather than the span is fixed, then the self-intersection effect disappears.

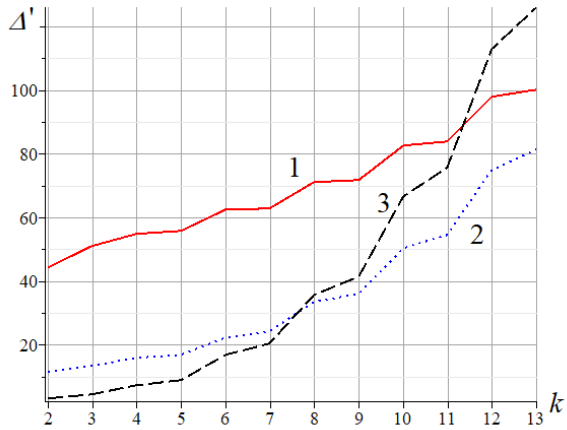

Figure 8. Dependence of dimensionless deflection on the number of panels,

1 – *h* = 1 m; 2 – *h* = 2 m; 3 – *h* = 4 m; *L* = 100 m.

Curves of deflection dependence on the number of panels are non-monotonic. The presence of jumps in such curves is typical for trusses with a complex lattice [14]. Trusses with a lattice consisting of triangles, these curves are smooth and have no jumps [15, 16].

In the case of a load applied to the lower belt, the curves are almost the same with the same effects of intersecting the curves and changing their order.

The asymptotics of the solution turns out to be nonlinear. By means of Maple system, we get that the deflection dependence on the number of panels with increasing k tends to be cubic:

$$\lim_{k\to\infty} \Delta'/k^3 = 5h/(3L). \tag{18}$$

The same order is obtained for a concentrated load: $\lim_{k\to\infty} \Delta'/k^3 = 8h/(3L)$. The cubic character of the deflection growth with an increase in the number of panels is also found in the arch-type truss [14]. However, the deflection growth in this problem is much slower. The growth factor is $5h/(384L)$.

The dependence of the deflection on the height reveals a minimum (Fig. 9). As the number of panels increases, the extreme point on the h axis shifts to lower values. The presence of a minimum deflection with a change in height is very typical for such problems [14–16] and is associated with the form of the solution. The quantity h in (5) has the second degree in the denominator and cubic in the numerator. Functions of this kind usually have a minimum. A less obvious minimum is found in a similar statement of the problem for the arch [14]. In [8–11] such curves were not constructed.

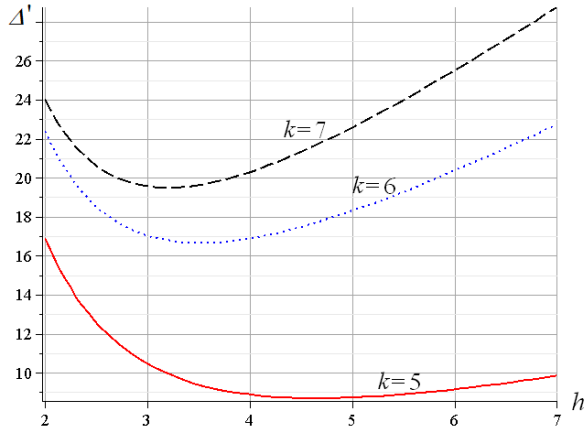

Figure 9. Dependence of the deflection on the height of the truss, L = 100 m.

In addition to the usual calculations of forces and deflections in truss problems, this paper reveals a somewhat unexpected feature of the proposed scheme – kinematic degeneration of the structure. This is shown in the degeneration of the matrix of the system of equilibrium equations for certain values of the panel numbers. This effect was not found in [1–3, 8–11], where regular trusses were also studied. The effect of kinematic degeneration of many regular truss schemes with a complex lattice at a certain number of panels was previously noted in the reference [19].

4. Conclusions

- A new scheme of a statically determinate truss is proposed and its mathematical model is constructed, which allows calculating the forces in the members and obtaining the deflection dependence on the number of panels in an analytical form.
- Kinematic degeneration of the structure was found for an odd number of panels. The result is confirmed by a picture of the distribution of virtual node velocities.
- By generalizing a series of solutions for trusses with a successively increasing number of panels, a formula is obtained for the dependence of the deflection and forces in some rods on the truss size, load and number of panels. Formulas have the form of polynomials in the number of panels of degree no higher than the fourth.
- The dependence of the horizontal displacement of the mobile support under the action of three types of loads is found. An asymptotic analysis of the solution of the deflection problem was performed, which revealed the cubic character of the deflection growth with an increase in the number of panels.
- The solution graphs constructed for specific dimensions of the structure showed the presence of a minimum deflection depending on the height of the truss and a jumpy, non-monotonous increase in the deflection with an increase in the number of panels.

5. Acknowledgements

The investigation was carried out within the framework of the project “Dynamics of light rod structures of manipulators” with the support of a grant from NRU "MPEI" for implementation of scientific research programs "Energy", "Electronics, Radio Engineering and IT", and “Industry 4.0, Technologies for Industry and Robotics in 2020-2022” and supported by the Interdisciplinary Scientific and Educational School of Moscow University “Fundamental and Applied Space Research”.

References

1. Marutyan, A.S. Optimizatsiya fermennykh konstruktsiy so stoykami i poluraskosami v treugol'nykh reshetkakh [Optimization of truss structures with uprights and half-rake in triangular lattices]. Stroitelnaya mekhanika i raschet sooruzheniy. 2016. No. 4 (267). Pp. 60–68. (rus)
2. Marutyan, A.S., Pavlenko, Yu.I. Priblizhennyy raschet perekrestnykh sistem na staticheskiye vozdeystviya [An approximate calculation of the cross-systems on static exposure]. Stroitelnaya mekhanika i raschet sooruzheniy.2009. No. 4. Pp. 14–20. (rus)
3. Marutyan, A.S., Abovyan, A.G. Raschet optimal'nykh parametrov ploskooval'nykh trub dlya fermennykh konstruktsiy [Calculation of optimal parameters of flat oval pipes for truss structures] Stroitelnaya mekhanika i raschet sooruzheniy. 2017. No. 4 (273). Pp. 17–22. (rus)
4. Buka-Vaivade, K., Serdjuks, D., Goremikins, V., Pakrastins, L., Vatin, N.I. Suspension structure with cross-laminated timber deck panels. Magazine of Civil Engineering. 2018. 83 (7). Pp. 126–135. DOI: 10.18720/MCE.83.12
5. Murnieks, J., Serdjuks, D., Buka-Vaivade, K. Load-Carrying Capacity Increase of Arch-Type Timber Roof. Proceedings of the 12th International Scientific and Practical Conference: Environment. Technology Resources. Rezekne, Latvia. 2019. 1. Pp. 175–179. DOI: 10.17770/etr2019vol1.4056
6. Lalin, V.V., Rybakov, V.A., Morozov, S.A. Issledovaniye konechnykh elementov dlya rascheta tonkostennykh sterzhnevykh sistem [The study of finite members for the calculation of thin-walled bar systems]. Magazine of Civil Engineering. 2012. Vol. 27. No. 1. Pp. 53–73. DOI: 10.5862/MCE.27.7. (rus)
7. Dong, L. Mechanical responses of snap-fit Ti-6Al-4V warren-truss lattice structures. International Journal of Mechanical Sciences. 2020. Vol. 173. Pp. 105460. https://doi.org/10.1016/j.ijmecsci.2020.105460
8. Hutchinson, R.G., Fleck, N.A. Microarchitectured cellular solids – the hunt for statically determinate periodic trusses. ZAMM Z. Angew. Math. Mech. 2005. Vol. 85. No. 9. Pp. 607–617. DOI 10.1002/zamm.200410208
9. Hutchinson, R.G., Fleck, N.A. The structural performance of the periodic truss. Journal of the Mechanics and Physics of Solids. 2006. Vol. 54. No. 4. Pp. 756–782. DOI: 10.1016/j.jmps.2005.10.008
10. Zok, F.W., Latture, R.M., Begley, M.R. Periodic truss structures. Journal of the Mechanics and Physics of Solids. 2016. Vol. 96. Pp. 184–203. https://doi.org/10.1016/j.jmps.2016.07.007
11. Latture, R. M., Begley, M. R., Zok, F. W. Design and mechanical properties of elastically isotropic trusses. Journal of Materials Research. 2018. 33 (03). Pp. 249–263. DOI: 10.1557/jmr.2018.2
12. Kirsanov, M.N. Sravnitel'nyy analiz zhestkosti dvukh skhem arochnoy fermy [A comparative stiffness analysis of two schemes arched truss] .Construction of unique buildings and structures. 2015. No. 9 (36). Pp. 44–55. DOI: 10.18720/CUBS.36.4. (rus)
13. Chao, Dou, Yu-Fei, Guo, Zi-Qin, Jiang, Wei Gao, Yong-Li, n Pi. In-plane buckling and design of steel tubular truss arches. Thin-Walled Structures. 2018. Vol. 130. Pp. 613–621. https://doi.org/10.1016/j.tws.2018.06.024
14. Kirsanov, M.N. Formuly dlya rascheta deformatsiy arochnoy fermy s proizvol'nym chislom paneley [The formula for calculating the deformations of the arched truss with arbitrary number of panels] Construction of unique buildings and structures. 2018. No. 4 (67). Pp. 86–94. DOI: 10.18720/CUBS.67.7. (rus)
15. Bolotina, T.D. The deflection of the flat arch truss with a triangular lattice depending on the number of panels. Bulletin of Scientific Conferences. 2016. No. 4-3 (8). Pp. 7–8. DOI: 10.17117/cn.2016.04.03
16. Kazmiruk, I.Yu. On the arch truss deformation under the action of lateral load. Science Almanac. 2016. No. 3-3 (17). Pp. 75–78. DOI: 10.17117/na.2016.03.03.075
17. Rakhmatulina, A.R., Smirnova, A.A. The dependence of the deflection of the arched truss loaded on the upper belt, on the number of panels. Scientific Almanac. 2017. No. 2-3 (28). Pp. 268–271.
18. Voropay, R.A., Domanov, E.V. Analytical solution of the problem of shifting a movable support of a truss of arch type in the Maple system. Postulat. 2019. No. 1.
19. Kirsanov, M. Planar Trusses: Schemes and Formulas. Newcastle upon Tyne, United Kingdom, Cambridge Scholars Publishing, 2019. 198 p.
20. Degertekin, S.O., Lamberti, L., Ugur, I. B. Sizing, layout and topology design optimization of truss structures using the Jaya algorithm. Applied Soft Computing. 2017. Vol. 70. September, Pp. 903–928. https://doi.org/10.1016/j.asoc.2017.10.001
21. Tinkov, D.V., Safonov, A.A. Design Optimization of Truss Bridge Structures of Composite Materials. Journal of Machinery Manufacture and Reliability. 2017. Vol. 46. No. 1. Pp. 46–52. DOI: 10.3103/S1052618817010149
22. Serpik, I.N., Alekseytsev, A.V. Optimizatsiya sistemy stal'noy ploskoy ramy i stolbchatykh fundamentov [Optimization of flat steel frame and foundation posts system]. Magazine of Civil Engineering. 2016. No. 1. Pp. 14–24. DOI: 10.5862/MCE.61.2. (rus)
23. Serpik, I.N., Alekseytsev, A.V. Optimizatsiya ramnykh konstruktsiy s uchetom vozmozhnosti zaproyektnykh vozdeystviy [Optimization of frame structures with possibility of emergency actions]. Magazine of Civil Engineering. 2013. No. 9. Pp. 23–29. DOI: 10.5862/MCE.44.3. (rus)
24. Kaveh, A., Laknejadi, K. A hybrid evolutionary graph-based multi-objective algorithm for layout optimization of truss structures. Acta Mechanica. 2013. Vol. 224. No. 2. Pp. 343–364. DOI: 10.1007/s00707-012-0754-5
25. Foroughi, H., Ji, C., Moen, C.D., Schafer, B.W. Experimental determination of stiffness and strength for metal building system rod bracing. Journal of Constructional Steel Research. 2020. Vol. 171. Pp. 106–149. https://doi.org/10.1016/j.jcsr.2020.106149
26. Tinkov, D.V. Sravnitel'nyy analiz analiticheskikh resheniy zadachi o progibe fermennykh konstruktsiy [Comparative analysis of analytical solutions to the problem of truss structure deflection]. Magazine of Civil Engineering. 2015. No. 5(57). Pp. 66–73. DOI: 10.5862/MCE.57.6. (rus)

Contacts:

Mikhail Kirsanov, c216@ya.ru

© Kirsanov, M.N., 2021

Magazine of Civil Engineering

ISSN 2712-8172

journal homepage: http://engstroy.spbstu.ru/

DOI: 10.34910/MCE.102.12

Tendencies in developing structural designs of non-soil seepage-control structures of embankment dams

M.P. Sainov*, F.V. Kotov
Moscow State University of Civil Engineering, Moscow, Russia
**E-mail: mp_sainov@mail.ru*

Keywords: embankment dams, non-soil seepage-control element, cement, diaphragm walls, concrete face, combined dams

Abstract. Introduction. The urgent scientific and practical problem in hydraulic engineering is refinement of structural designs of embankment dams with seepage-control elements (SCE) made of artificial materials. They should conform with the requirements of effectiveness and safety. Different authors make proposals on refinement of structural designs of embankment dams with SCE to be made of materials based on cement and on widening the sphere of their application. Materials and methods. Analyses were made of the spheres of application in hydraulic engineering of the materials based on cement: concrete, clay-cement concrete, soil-cement concrete, soil-cement mixes. With this consideration the analysis was made of SCE structure alternatives. Their classification permitted revealing the main tendencies in development of embankment dam structural designs. Results. The sphere of possible application of SCE different types depends on the dam height. For low-head and medium-head dams the most applicable design solution refers to dams with diaphragms made of clay-cement concrete bore piles. It was already tested in practice. For high-head and ultra-high-head dams the effective and safe solution has not been found yet. Four conceptual ways may be considered, but all of the men visage using structures made of cement-containing materials. The first way is refinement of a concrete face rockfill dam structural design. It may be realized by doubling the seepage control facility with use of geo-synthetic materials. The second way is elaboration of a principally new massive seepage-control structure to be made of material based on cement. The third way is use of combined dams, where the dam safety is enhanced by replacement of a part of an embankment dam by concrete. The fourth way is combination of different types of SCE each of which is arranged at different by height dam sections. Conclusions. Materials based on cement propose wide possibilities for refinement of embankment dam structural designs. Nevertheless, the main tendency in development of high-head embankment dam structural designs is application of SCE complicated structures with use of materials based on cement. By their structure they may be either double (multi-layered) or compound (SCE combination).

1. Introduction

The urgent problem of hydraulic engineering is refinement of structural designs of embankment dams. Structural designs used at present are varied: they differ by type (earthfill, rock-earthfill, rockfill), by structure (core, face, curtain, diaphragm) and by material of a seepage-control element. However, all of them have limitations either in the field of application or do not guarantee the proper level of safety.

Therefore, refinement of embankment dam structural designs envisages solution of at least one of the following tasks:

1. Enhancing effectiveness of dam construction: decreasing the cost, decreasing man-months and construction period;
2. Enhancing reliability and safety of the dam structural design;
3. Widening the field of embankment dam application for higher heads.

Sainov, M.P., Kotov, F.V. Tendencies in developing structural designs of non-soil seepage-control structures of embankment dams. Magazine of Civil Engineering. 2021. 102(2). Article No. 10212. DOI: 10.34910/MCE.102.12

This work is licensed under a CC BY-NC 4.0

At present the only type of dams which may be used actually for any head and conditions is rock- earthfill dam with central core made of clay soil. The highest dam of such type is 300 m high dam of Nurek HPP in Tajikistan.

However, rock-earthfill dams have limitations by application related to the possibility of placing clay soils into the seepage-control core. In severe climatic conditions it is difficult to provide proper quality of clay soil placement which results in decreasing the dam safety level. This is testified by operation experience of the highest in Russia rock-earthfill dam of Kolyma HPP built in Magadan Oblast [1]. As a result of insufficient quality of soil placement, the dam is subject to considerable deformations, and there are zones of increased permeability in the core. Danger of affecting the seepage strength of the soil core is also a characteristic feature for other rock-earthfill dams. The case of complete failure in 1976 of 93 m high Teton rock-earthfill dam (USA) is well known [2]. In literature there described cases of hydraulic fracturing of Balderhead dam cores (England) [3, 4], of Kureika dam [5–7].

Therefore, the urgent problem is search for alternatives of embankment dam structural designs [8]. A number of publications is devoted to this issue. Analysis of these papers shows that the most perspective is use of seepage-control elements (SCE) of non-soil materials in embankment dam structures. This is explained by the quality of artificial materials production and provision of the required level of their strength and water permeability.

A that, the important role is played by the materials based on cement. Based on cement a wide spectrum of different materials may be created and various methodologies may be applied for their production.

This article presents the analysis of proposals on refinement of the existing and elaboration of new structural designs of embankment dams with use of materials based on cement in order to estimate the perspectives of these materials' application.

2. Materials and methods

Analysis of the considered issue is carried out in two stages. At the first stage there was made a review of used materials based on cement in hydraulic engineering. The considered materials are those where cement plays the role of a binding agent. At the second stage there were analyzed the ways of further refinement of embankment dam structural designs as well as the advantages and disadvantages of structures proposed by different authors.

3. Results

3.1. Review of information about the materials developed based on cement

Materials created on the base of cement differ in composition and / or manufacturing technology. They may be classified as follows.

1. First of all, it is traditional concrete and reinforced concrete. However, it should be noted that for the increased level of SCE safety, special solutions can be applied to the design of concrete structures. In particular, instead of traditional concrete reinforcing with steel bars, it is possible to use distributed reinforcement. In particular, the face of the Shuibuya dam was reinforced with geosynthetic fibers to increase tensile strength [9]. It is also proposed to use self-healing concrete.

2. In hydraulic engineering and road construction, so-called roller compacted concrete is widely used. In hydraulic engineering, it has been used since the middle of the 20th century. It is a particularly hard concrete mix with a low cement content and a high content of coarse aggregate. Unlike conventional concrete, it is placed by layers and compacted not by internal vibrators, but by vibration rollers.

3. Further development of roller compacted concrete technology is the "hard fill" technology, which found its application in the 21st century. [10–13]. As a result of its application, a new type of dam was created – the "hard fill". The profile of such dams is trapezoidal, like that of embankment dams, but with steeper slopes (about 0.8). Abroad, a hard soil-cement mix of cement, sand and gravel is called CSG, and in Russia it is called soil-cement concrete. The technology for producing soil-cement-concrete can be various. The already produced CSG mix is placed in the dam and compacted by rollers. It includes not more than 80 kg/m^3 of cement, and sand and gravel in equal proportions. It is also possible to obtain soil cement concrete by pouring coarse soil with cement mortar, the so-called divided technology.

Technologies of roller compacted concrete and "hard fill" are convenient for construction of massive structures, but roller compacted concrete and soil-cement concrete are quite permeable, therefore, they require additional seepage-control structure. For example, the upstream face of CSG dams is covered with a protective layer of concrete.

4. Clay-cement concrete or plastic concrete is used exclusively to create seepage-control structures. It is concrete with the addition of local clay materials. Bentonite clay or similar local clay soils are used as such

additives [14]. Additives are designed to reduce the stiffness of cement stone. The ratio of cement and bentonite in clay-cement concrete mix may be different. For example, clay cement concrete used for construction of Karkhe dam seepage-control wall (Iran) contains 200-220 kg of cement and 30-40 kg of bentonite in 1 m^3 [15], while clay cement concrete of the Kureika dam wall contains 125-156 kg of Portland cement and 120-140 kg of bentonite.

Depending on the ratio in the content of cement and clay, it is possible to obtain clay-cement concrete with the necessary deformability and strength. The modulus of deformation of clay-cement concrete may vary widely: it may be less than 100 MPa or may exceed 1000 MPa [15]. Clay-cement concrete has plastic properties, due to which it can have the ability to self-heal cracks [16], so it is advisable to use it for installation of seepage-control walls. To increase the strength of clay-cement concrete, it is proposed to introduce distributed reinforcement, fiber in its composition in the form of metal wires or in the form of polymer fibers [17, 18].

A separate class of cement-containing materials is composed of various soil-cement mixes. They are soils, binded in one way or another with cement. Depending on the technology of consolidation, several types of soil-cement mixes are distinguished.

5. *Soil cement* is produced by mixing soil with cement directly at the site of placement. It was first used in the USA for protection of the slope against the effects of waves.

Soil-cement mixes can be formed during the development of soil. Recently, such methods of creating seepage-control walls in soils as the mixing method and the jet grouting method have appeared[1]. In these methods, cement and soil are mixed in place, during the execution of the wall. The base soil is not removed, but is part of the cement-soil material. Depending on the content of cement, water and air, the properties of soil-cement mixes can vary greatly.

6. *Soil cemented by injection* of cement-based grouts is produced by injecting the grout into the pores of coarse-grained soil at a pressure of 0.5-6 MPa [19, 20], and after hardening of which a cemented stone is formed.

The material of curtains and walls produced by injection, mixing, and jet grouting is unpredictable in properties, because its composition is determined by the composition of the original soil massif.

Even a brief review shows that the range of cement-based materials used in hydraulic engineering is very wide.

Perspectives of using in embankment dams of new structures of seepage-control elements made of cement-containing materials.

Use of the above cement-containing materials, as well as the technology of their application, allows creating new design solutions for embankment dams.

A peculiarity of scientific and technical progress in hydraulic engineering is that fundamentally new solutions are rarely implemented; more often development is carried out by improving or borrowing already existing technologies. In construction of embankment dams, the main trend is the transfer of technology, that is, the adaptation of those structures and technologies that have previously proven themselves in any field and have proven their effectiveness, reliability, to solve new problems.

Expanding the scope of application of this or that material, technology is limited by technical capabilities and gained experience. Therefore, the ways of developing designs of low-, medium- and high-head technologies differ.

Perspectives of using seepage-control elements made of cement-containing materials in embankment dams of low and medium heights.

Development of structures of low-head and medium-hed embankment dams is aimed at increasing the efficiency of construction, as the problem of providing reliability and safety can be solved by traditional methods. It is proposed to use SCE of cement-containing materials (including concrete) as an alternative to the traditional soil SCE (cores and faces of clay soils).

This is proved by the experience of repairing several rock-earthfill dams, where cracks appeared in seepage-control cores. An example is Balderhead Dam in England [3, 4]. Its repair was carried out in 1968, first by grouting to fill the cracks, and then by creating a trench method of a seepage-control wall made of soil concrete with a thickness of 0.65 m and a depth of up to 45 m [21]. There are other examples of creating new seepage-control diaphragms in the bodies of repaired dams using the trench method, for example, at Navajo dam (USA, 1987) [21].

[1] Broid I.I. Jet geotechnology. – M.: ACB, 2004. – 448 p.; Development of Dam Engineering in the United States. Pergamon Press. Edited by E.B. Kollgaard and W.L. Chadwick, 1988. 1072 p.

Another technology for creating a new seepage-control wall is the technology of bored piles. An example is the dam at the Kureika hydroelectric station, in one of the sections of which in 1992 failure occurred with loss of core tightness [5–7]. The dam repair was proposed to be implemented by creating a new SCE of bored piles [5–7]. It was completed in 1998–1999 and after that the dam continues to operate successfully.

According to the experts of VNIIG named after B.E. Vedeneev, making a diaphragm of bored piles is a promising way to create SCE in low-head embankment dams. This was shown by recent experience in building the dam of the Nizhnyaya-Bureya hydroelectric plant [22, 23]. VNIIG named after B.E. Vedeneeva developed typical designs of dams with diaphragms made of clay-cement concrete for future use[2].

It should be noted that this idea has already been realized abroad. Already in the 1970s –1980s, the diaphragms of a number of embankment dams were made using the “slurry trench cutoff wall” method [24]. For example, at 6.5 meters high Wadi Hawashinah dam (Oman), a 0.6 m thick diaphragm was constructed using a trench method [25]. In the 1970s, 31 m high Formiz dam was built in Germany, the SCE of which was the core of silty sands, and a wall was built in its center [26]. The wall with a thickness of 0.6 m was erected with use of the trench method by 4 m high layers. The material softer than concrete was used as the diaphragm material, i.e. clay-cement concrete.

For medium-head dams, Russian authors propose a new type of dam SCE – a bored pile diaphragm erected by layers [17, 27]. A number of papers published recently have been devoted to the issues of possible use and development of such structures [28–30]. The complexity of using this design is vulnerability of connection of the diaphragm layers [31].

Abroad, there is an experience in creating deep (in one layer) seepage-control diaphragm walls for repair of rock-earthfill dams. These walls are made by the trench method. In 1985–1986 in this way, the Fontenel Dam was repaired in the USA: a 0.65 m thick and 55 m deep concrete wall was constructed in sandy-loamy soil [21, 32, 33]. At the Mud Montain Dam (USA), the depth of the wall, made in a similar way, was 120 m [34]. The wall thickness was 0.85÷1 m [21].

There is experience in application to create a temporary diaphragm wall in the cofferdam and body of the Xianlongdi dam in China [22]. Its total depth (in the dam and foundation) was 52 m. The diameter of the borehole columns was 1.2 m.

In all these cases, SCE arranged by various underground methods in the body of a filled dam, showed their reliability during several years of operation. Thus, the use of diaphragm walls makes it possible to create safe structures of embankment dams.

Perspectives of using seepage-control elements made of cement-containing materials in high-head embankment dams.

For high and ultra-high dams, the problem of SCE safety is the main one, and the issues of construction efficiency are fading into the background. These dams require special design and technological solutions.

Currently, for high-head dams, only one SCE made of artificial materials is used: this is a concrete face. At present, the highest concrete face rockfill dam (CFRD) is Shuibuya Dam in China. Its height is 233 m. Chinese designers suggest using CFRD with even at a height of 300 m [9, 35, 36]. However, as practice shows, the safety of CFRD is not guaranteed. At a number of such dams, the faces were damaged and needed repairs. Dams Campos Novos, Aguamilpa, Tianshengqiao 1, Mohale, Barra Grande [35, 37, 38] may be presented as examples. For the possibility of using SCE of non-soil materials, it is necessary to solve the problem of providing the necessary level of its safety. As experience and research show, of all types of non-soil materials, only cement-based materials are suitable for construction of ultra-high dams.

Two fundamentally different ways of solving the safety problem of high-head dams with non-soil SCE can be distinguished:

- the first way is to improve the applied design of CFRD;
- the second way is development of a fundamentally new dam design.

The first way, enhancing safety of the applied design of CFRD can be realized by duplication of one SCE (concrete face) with another, i.e. by using a multilayer construction. A similar approach is used in the design of sludge collector dams, ash and slag dumps and toxic liquid storage facilities where an increased level of seepage-control protection is required. For example, in them, asphalt concrete and geosynthetic faces are simultaneously performed, between which drainage is arranged to collect and drain filtered water.

Several alternatives for construction of a multilayer SCE structure may be considered. The first alternative is a combination of concrete and geosynthetic faces. This method has proven itself at construction

[2] Company-specific standard STP 310.02.HT-2017. Recommendations for designing, analysis and construction of a seepage-control element made of clay-cement concrete bored piles / edited by Miltzin V.L., Orishuk R.N., Solsky S.V.: JSC «VNIIG named after B.E.Vedeneev», JSC «Lenhydroproject». 2017. 118 p.

of Bovilla dams [39] and repair of concrete face of dams Turimiquire [40], Salt Springs [41] and New Exchequer [42]. Its disadvantage is the possibility of damage to the open geomembrane due to mechanical and thermal effects, as well as by solar radiation.

The second alternative is a combination of concrete and soil-cement concrete face. This idea is promoted by a number of Russian authors – L.N. Rasskazov [43], Yu.P. Lyapichev [44], A.S. Bestuzheva [45]. The idea is not only to increase safety of SCE due to appearance of a second line of seepage-control protection, but also to provide the maintainability of SCE, which is achieved by repairing a soil-cement concrete zone by injecting grouts. The concept of creating a massive SCE of cement-containing materials is debatable, because according to the results of our research [46], this does not increase, but reduces the concrete face efficiency.

The concept of creating a massive SCE of cement-containing materials is debatable, because according to the results of our research [46], this does not increase, but reduces the efficiency of BE.

The second way to improve the design of high-head embankment dams, i.e. elaboration of new designs of ultra-high dams, is even more problematic. A number of publications are devoted to this issue. Several dam designs may be proposed and considered. For example, L.I. Kudoyarov proposed to use steel faces for construction of ultra-high dams [47], however, this alternative of the dam is very costly and difficult for repairs.

More realistic alternatives are also available. As a rule, their idea is based on use of materials based on cement. All the proposed alternatives may be classified as three different concepts.

Concept No. 1 is based on use of a massive SCE made of one of the materials based on cement in the dam design. An injection curtain or a concrete mass (core) may present such a SCE.

Alternative 1 – an *injection core* (curtain) made by binding a gravel-pebble soil with a cement-containing mix (Fig. 1). The advantage of this option is that it has already been put into practice in one form or another. For example, the grout curtain is at the bottom of a series of SCE high embankment dams. These are Atbashinsk [48], Yumaguza [49] dams, dams of Kambarata hydroelectric power plant-2 [50] and Mainskaya hydroelectric power plant [20].

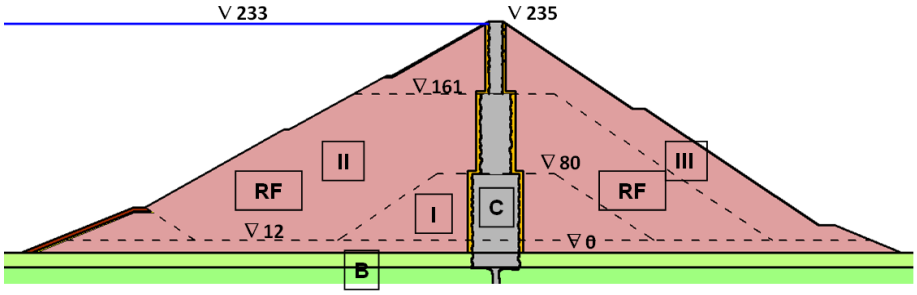

Figure1. Design of rockfill dam with a seepage-control elements grout curtain.
C – grout curtain, RF – rock fill, B – bedrock base, I, II, III – construction project phases.

There are cases of grout curtain in the body of an embankment dam for repair purposes. An example is Orto-Tokoi Dam (Kyrgyzstan), 52 m high, in which clay-cement grout was injected to reduce seepage through the dam body.

Successful experience gained in operating the above dams shows that the grout curtain may be used as the main SCE of an embankment dam. Grout curtains (cores) have several advantages over other types of SCE. Firstly, due to arrangement of a curtain (injection) after completion of the dam construction, SCE will be free from deformations of rockfill of the construction period, which improves its SSS. Secondly, in the event of breaking water tightness, the injection core can be repaired by re-injecting the developed cracks.

However, injection cores have a major drawback: in order to ensure seepage strength, the grout curtain in coarse soil should have a greater thickness, which leads to an increase in the cost of the dam.

Option 2 – a massive concrete core made of roller compacted concrete. One such proposal was put forward by V.F. Korchevsky and V.V. Orekhov [51, 52]. To give the concrete core greater flexibility, it is proposed to cut it height-wise with horizontal joints into separate blocks (Fig. 2), and for greater safety, arrange an asphalt concrete face from the upstream side.

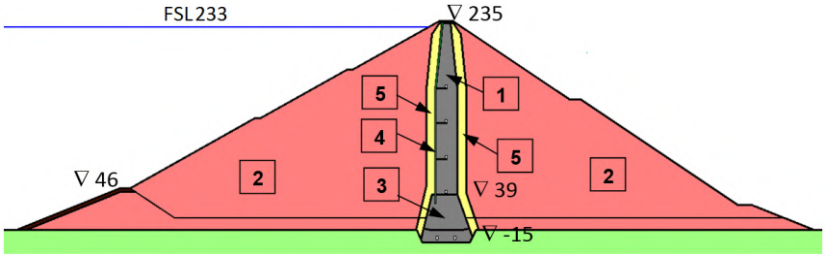

Figure 2. Scheme of arrangement of concrete face rockfill dam 1 – concrete face made of roller compacted concrete, 2 – rockfill shells, 3 – concrete face foundation made of vibrated concrete, 4 – asphalt concrete face, 5 – transition zones.

It was proposed in VNIIG to arrange in the dam body a concrete face enclosing an asphalt concrete diaphragm.

We conducted studies on reliability of the mentioned alternatives [8, 53]. They showed the insufficient level of their reliability. Besides, using massive concrete structures is not feasible because it requires a large volume of both rock excavations and earth moving and concrete work, which is economically unfavorable.

Thus, the concept of elaboration of embankment dam structures based on using massive stiff SCE in most cases is inconsistent. However, analysis of the proposed alternatives permits revealing an important tendency in selection of structural designs of ultra-high embankment dams. It is striving to apply two doubling SCE in one structure.

Concept No.2 is use of combined dams. The dam is called combined when it integrates a concrete dam and an embankment dam. The idea of combined dams is in the fact that in the lower part of an embankment dam a more safe and serviceable concrete structure should be used.

A number of combined dams have already been constructed in the world. They integrate a concrete structure and CFRD. Some of the them are the result of increasing the height of a concrete dam. The example may be 150 m high New Exchequer dam rehabilitated in USA in 1968 [42]. Besides, there known the dams which from the very start were constructed as combined dams. These are 192 m high Sogamoso dam in Columbia [44], 162 m high Yacambu dam in Venezuela.

Other alternatives of combined dam construction may be considered. The example may be 164 m high Quxue dam [54], where a concrete structure is combined with an asphalt concrete diaphragm and Bovilla dam with the face made of geomembrane [39].

Using combined dams seems to be advantageous, however, it also does not guarantee achievement of proper safety level. This is explained by the fact that a concrete and an embankment parts of a dam work actually independently from one another, which may lead to development of decompaction zones at the contact between them. This conclusion is confirmed by technical problems with water tightness at the interface of a concrete face with a concrete structure, which took place during operation of New Exchequer dam [42].

Concept No.3 in development of new structures of ultra-high embankment dams is use of combined non-soil SCE consisting of CSEs of two different types.

Dams with combined non-soil SCE are not principally new; they have been used for a long time in hydraulic engineering. Combination of non-soil SCE appears in case if the dam is rested on a thick layer of soil foundation. In this case in the foundation there arranged a vertical SCE in the form of SCW or a grout curtain which then is continued in the lower part of the dam. Using dams of such design permits increasing effectiveness of their construction. Using in the lower part such SCE as grout curtain, seepage-control wall permits dam construction without performing pit excavation, i.e. without the pit dewatering.

The examples of dams with combined SCE with grout curtain may be At-Bashinsk dam (79 m high, 1970) and the dam of Kambarata HPP-2 (50 m high, 2010) in Kyrgyzstan. At-Bashinsk dam SCE consists of a polyethylene diaphragm (in the upper part) and a grout curtain (in the lower part) [48]. The dam of Kambarata HPP-2 in Kyrgyzstan where SCE consists of a PVC face (in the upper part) and a grout curtain (in the lower part) [50].

The examples of dams with combined SCE with use of a seepage-control wall may be Hengshan dam in China [55] and Arkun dam in Turkey [56, 57]. The first is 70.2 m high, the second is 140 m high. In both cases SCE in the upper part is arranged in a form of a concrete face.

Taking into account this experience at construction of an ultra-high dam it is feasible in the upper part to use SCE as well proven concrete face and in the lower part to use a vertical SCE in the form of a grout curtain or a seepage-control wall. VNIIG specialists proposed to use the design of an ultra-high rockfill dam with combined SCE consisting of a concrete face and a grout curtain [58]. However, till present these dam designs have no analogs; scientific validation is required for their construction.

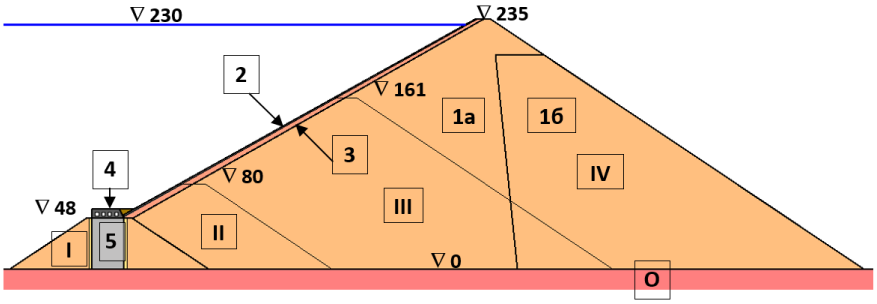

Figure 3. Dam design with combination of seepage-control elements: a concrete face and a grout curtain. 1a, 1b – rockfill, 2 – concrete face, 3 – under-face zone, 4 – concrete gallery, 5 – grout curtain, I, II, III, IV – dam construction stages.

The same may be said about all the proposed new structural solutions of ultra-high rockfill dam with SCE: their possible use will appear in case of thorough scientific validation.

4. Conclusions

1. Due to development of technologies the materials based on cement acquire new properties and become cheaper. All these permits saying about possible widening of application field of these materials based on cement in dam construction. Namely, for low-head and medium-head dams the effective structural solution is arrangement of clay-cement concrete diaphragms.

2. The urgent scientific problem is refinement of structural designs of high embankment dams with use of seepage-control structures made of non-soil materials. Different concepts and alternatives for elaboration of new types of ultra-high dam structures with structures made of materials based on cement are put forward. However, their scientific validation is required for introducing new dam designs.

3. The main tendency in refinement of seepage-control structures of embankment dams is use of complicated structures. The effective ways of enhancing safety of embankment dams is use of doubling each other seepage-control structures as well as use of combined structures. In these structures the important role is played by the materials based on cement.

References

1. Rasskazov, L.N., Aniskin, N.A., Sainov, M.P. Analiz sostoyaniya gruntovoy plotiny Kolymskoy GES [Analysis of the state of the embankmenr dam of the Kolymskaya HPP. Vestnik MGSU. 2009. 2. Pp. 111–118.
2. Sharma, R.P., Kumar, A. Case Histories of Earthen Dam Failures. International Conference on Case Histories in Geotechnical Engineering. 2013. 8. https://scholarsmine.mst.edu/icchge/7icchge/session03/8
3. Vaughan, P.P., Kluth, D.J. et al. Cracking and erosion of the rolled clay core of Balderhead dam and the remedial works adopted for its repair. 10th ICOLD Congress. 1970. 36(5). Pp. 73–93.
4. Nichiporovich, A.A., Teytelbaum, A.I. Otsenka treshchinoobrazovaniya v yadrakh kamenno-zemlyanykh plotin [Assessment of cracking in the cores of rock-earthfill dams]. Gidrotekhnicheskoye stroitelstvo. 1973. 4. Pp. 10–27.
5. Malyshev, L.I., Rasskazov, L.N., Soldatov, P.V. Condition of the Kureika hydroelectric station dam and engineering approaches to its repair. Hydrotechnical Construction. 1999. 33(1). Pp. 33–39.
6. Malyshev, L.I., Shishov, I.N., Kudrin, K.P., Bardjugov, V.G. Tehnicheskie reshenija i rezul'taty rabot po sooruzheniju protivofil'tracionnoj steny v grunte v jadre i osnovanii Kurejskoj GES [Technical solutions and the results of the construction of an seepage-control wall in the soil in the core and base of the Kureyskaya HPP]. Gidrotehnicheskoe stroitel'stvo. 2001. 3. Pp. 31–36.
7. Bardjukov, V.T., Izotov, V.N., Grishin, V.A., Radchenko, V.G., Shishov, I.N. Remont plotiny Kurejskoj GES [Dam repair at Kureyskaya HPP]. Izvestija Vserossijskogo nauchno-issledovatel'skogo instituta gidrotehniki im. B.E. Vedeneeva. 2000. 238. Pp. 92–96.
8. Sainov, M.P., Kotov, F.V. Sravnenie variantov konstrukcii vysokoj kamennoj plotiny v uslovijah Jakutii [Comparison of high rockfill dam design options in Yakutia]. Vestnik MGSU. 2011. 5. Pp. 30–35.
9. Wang, L.-B., Yan, Q. Analyze on development prospects of 300 m level ultra-high CFRD from Shuibuya high CFRD. Asia-Pacific Power and Energy Engineering Conference, APPEEC. 2010. 5448667
10. Glagovskij, V.B., Radchenko, V.G. Novye tendencii v stroitel'stve gruntovyh plotin [New trends in the construction of embankment dams]. Gidrotehnicheskoe stroitel'stvo. 2013. 1. Pp. 2–8.
11. Fujisawa, T. Trapezoidal CSG dam. Dam in Japan. ICOLD. 2012. Pp. 36–61.
12. Fujisawa, T., Sasaki, T. Development of the trapezoidal CSG dam. The International Journal on Hydropower & Dams. 2012. 19(3). Pp. 58–63.
13. Hokkaido Prefecture. Toubetsu dam: an example of the innovative CSG technology. The International Journal on Hydropower & Dams. 2012. 19(3). Pp. 64–67.
14. Derjugin, L.M. Svojstva bentonito-cementnyh lityh betonov dlja konstrukcij tipa “stena v grunte” iz burosekushhihsja svaj [Properties of bentonite-cement cast concrete for wall-in-ground structures made of bored piles]. Gidrotehnicheskoe stroitel'stvo. 2008. 4. Pp. 16–18.
15. Mirghasemi, A.A., Pakzad, M., Shadravan, B. The world’s largest cutoff wall at Karkheh dam. The International Journal on Hydropower & Dams. 2005. 2. Pp. 2–6.

16. Wu, F., Shi, K., Dong, S., Ci, J., Yiziteluopu, N. Experiment on long term seepage corrosion stability of plastic concrete. Nongye Gongcheng Xuebao. Transactions of the Chinese Society of Agricultural Engineering. 2014. 30(22). Pp. 112–119.
17. Koroljov, V.M., Smirnov, O.E., Argal, Je.S., Radzinskij, A.V. Novoe v sozdanii protivofil'tracionnogo jelementa v tele gruntovoj plotiny [New in creating an seepage-control element in the body of a embankment dam]. Gidrotehnicheskoe stroitel'stvo. 2013. 8. Pp. 2–9.
18. Rasskazov, L.N., Radzinskii, A.V., Sainov, M.P. Selection of the Composition of Clay-Cement Concrete for Construction of “Walls-in-the-Ground”. Power Technology and Engineering. 2014. 48(3). Pp. 167–173.
19. Bobrov, R.I. Inyekcionnye zavesy v neskal'nyh porodah [Injection curtains in non-rock formations]. Gidrotehnicheskoe stroitel'stvo. 1963. 7. Pp. 47–56.
20. Zhurkina, N.N. Inyekcionnaja zavesa v osnovanii gruntovoj plotiny Majnskoj GES [Injection curtain at the base of the main dam of the Main HPP]. Gidrotehnicheskoe stroitel'stvo. 1987. 11. Pp. 39–42.
21. Radchenko, V.G., Radchenko, S.V. Primenenie sposoba «stena v grunte» pri stroitel'stve i remonte plotin iz gruntovyh materialov [Application of the “wall in soil” method in the construction and repair of dams from soil materials]. Izvestija VNIIG im. B.E. Vedeneeva. 2010. 258. Pp. 114–127.
22. Radchenko, V.G., Lopatina, M.G., Nikolajchuk, E.V., Radchenko, S.V. Opyt vozvedenija protivofil'tracionnyh ustrojstv iz gruntocementnyh smesej [Experience in the construction of seepage-control devices from soil-cement mixtures]. Gidrotehnicheskoe stroitel'stvo. 2012. 12. Pp. 46–54.
23. Borzunov, V.V., Musaev, A.Sh., Kadushkina, E.A. Optimizacija proektnyh reshenij i usovershenstvovanija konstrukcij osnovnyh sooruzhenij Nizhne-Burejskoj GES [Optimization of design decisions and improvement of structures of the main structures of the Nizhne-Bureyskaya HPP]. Gidrotehnicheskoe stroitel'stvo. 2017. 4. Pp. 2–15.
24. Borzunov, V.V., Denisov, G.V., Kadushkina, E.A., Fedorov, A.V. Opyt proektirovanija i stroitel'stva gruntovoj plotiny Nizhne-Burejskoj GES s primeneniem v kachestve protivofil'tracionnogo ustrojstva diafragmy iz burosekushhihsja svaj [Experience in the design and construction of a soil dam at the Nizhne-Bureyskaya HPP using a diaphragm from boughed sections as an anti-filter device]. Gidrotehnicheskoe stroitel'stvo. 2019. 6. Pp. 2–10.
25. Strobl, T., Shmid, R. Wadi Hawashinah dam. Oman. Groud Water recharge dam to stop salt water instrusion. Strabag. Dam engineering in Kenya, Nigeria, Oman and Turkey. April 1997. Brochure 52. Cologne. Pp. 67–68.
26. Carl, L., Strobl, Th. Dichtungswände aus Zement-Bentonitsuspension. Wasserwirtschaft. 1976. 66(9). Pp. 246–252.
27. Aliev, N.A., Gadzhimagomaev, B.U., Kiseljov, V.N., Nikulin, D.A., Red'kin, V.A., Jurkevich B.N. Gruntovaja plotina [Embankment dam] Patent Russia, No. 2013111020/13, 2013.
28. Orishchuk, R.N. Clay-cement-concrete diaphragm – justifying calculation for new-built constructions. Magazine of Civil Engineering. 2019. 89(5). Pp. 16–25. DOI: 10.18720/MCE.89.2
29. Orishhuk, R.N. Novye konstrukcii gruntovyh plotin s glinocementobetonnymi diafragmami [New designs of embankment dams with cement-concrete diaphragms]. Izvestija VNIIG im. B.E. Vedeneeva. 2019. 292. Pp. 21–29.
30. Prokopovich, V.S., Velichko, A.S., Orishhuk, R.N. Naprjazhenno-deformirovannoe sostojanie zemljanoj plotiny s glinocementobetonnoj diafragmoj (Na primere zemljanoj plotiny Gocatlinskoj GES) [Stress-strain state of an earthen dam with clay-cement-concrete diaphragm (On the example of an earthfill dam of the Gotsatlinskaya HPP)]. Izvestija Vserossijskogo nauchno-issledovatel'skogo instituta gidrotehniki im. B.E. Vedeneeva. 2016. 282. Pp. 87–98.
31. Sainov, M.P., Kotov, F.V. Rabotosposobnost' gruntovoj plotiny s mnogojarusnoj diafragmoj, vypolnennoj metodom «stena v grunte» [Workability of embankment dam with multi-layer diaphragm constructed by «cutoff wall method»]. Vestnik Evrazijskoj nauki. 2018. 10(5). URL: https://esj.today/PDF/03SAVN518.pdf
32. Fenoux, G.Y. Ecrans en paroi realises apres edification des remblais. Nouveaux outillages, nouvelles methods pour travax neufs on travaux de reparation. 16th ICOLD Congress. 1988. Q.61. R.1. Pp. 1–26.
33. Bellport, B.P. Bureau of reclamation experience in stabilizing embankment of Fontenelle earth dam. 9th ICOLD Congress. 1967. Q.32. R.5. Pp. 67–79.
34. Graybeal, K.D., Levallois, F. Construction of a cut off wall with the hydrofraise trough the core of Mud Montain dam. 17th ICOLD Congress. 1991. Q.66. R.49. Pp. 879–908.
35. Ma, H., Chi, F. Technical progress on researches for the safety of high concrete-faced rockfill dams. Engineering. 2016. 2. Pp. 332–339. DOI: 10.1016/J.ENG.2016.03.010
36. Ma, H.Q., Cao, K.M. Key technical problems of extra-high concrete faced rock-fill dam. Science in China. Series E: Technological Sciences. 2007. 50(1). Pp. 20–33. DOI: 10.1007/s11431-007-6007-5
37. Freitas, M.S.Jr. Concepts on CFRDs Leakage Control – Cases and Current Experiences. ISSMGE Bulletin. 2009. 3(4). Pp. 11–18.
38. Sainov M.P., Zatonskih M.A. Povrezhdenie zhelezobetonnyh jekranov kamenno-nabrosnyh plotin: fakty, vozmozhnye prichiny i sposoby predotvrashhenija [Structural cracks initiation in reinforced concrete faces of rockfill dams]. Stroitel'stvo unikal'nyh zdanij i sooruzhenij. 2018. 10(73). Pp. 16–27. DOI: 10.18720/CUBS.73.2
39. Sembenelli, P., Sembenelli, G. and Scuero, A.M. Geosynthetic system for the facing of Bovilla Dam, Proceedings of the 6th International Conference on Geosynthetics, (Edited R. K. Rowe). 1998. Atlanta, Georgia, USA, International Fabrics Association International, Roseville. Minnesota. Pp. 1099–1106.
40. Scuero, A.M., Vaschetti, G.L. Underwater repair of a 113 m high CFRD with a PVC geomembrane: Turimiquire Managing Dams: Challenges in a Time of Change. Proceedings of the 16th Conference of the British Dam Society. 2010. Pp. 474–486.
41. Sembenelli, P., Rodriquez, E. A. Geomembranes for Earth and Earth-Rock Dams: State-of-the-Art Report. Proc. Geosynthetics Applications, Design and Construction. M.B. de Groot, et al., Eds., A.A. Balkema. 1996. Pp. 877–888.
42. Brown, H.M., Kneitz, P.R. Repair of New Exchequer Dam. International Water Power and Dam Construction. 1987. 39(9). Pp. 25–29.
43. Rasskazov, L.N., Sainov, M.P. Numerical Investigation of Reliability of a High Earthen Dam with a Reinforced-concrete Shield and Sub-Shield Zone Formed from Soil-Cement Concrete. Power Technology and Engineering. 2012. 46(2). Pp. 116–120.
44. Ljapichev, Yu.P. Chislennye raschety, proektirovanie i povedenie kamenno-nasypnyh plotin s zhelezobetonnymi jekranami pri sejsmicheskih vozdejstvijah [Numerical analysis, design and behavior of rockfill dams with reinforced concrete faces during seismic actions]. Vestnik MGSU. 2020. 15(4). Pp. 569–584. DOI: 10.22227/1997-0935.2020.4.569-584
45. Bestuzheva, A.S., Gadai, D.V. The Search for Methods of Factor Analysis for an Optimal Design of Earth-Fill Dams with Stone-Concrete Support Zone. Power Technology and Engineering. 2017. 51(4). Pp. 385–389.

46. Sainov, M.P. Ocenka rabotosposobnosti konstrukcij kamenno-nabrosnyh plotin s betonnym jekranom i massivom iz «kamnebetona» [Assessment of workability of concrete faced rockfill dam structure sand mass of stoneconcrete]. Vestnik Evrazijskoj nauki. 2020. 1, https://esj.today/PDF/03SAVN120.pdf
47. Kudojarov, L.I. Osnovnye napravlenija jeffektivnosti stroitel'stva plotin na Severe [The main directions of the effectiveness of the construction of dams in the north regions]. Gidrotehnicheskoe stroitel'stvo. 1983. 7. Pp. 6–11.
48. Loginov, K.A., Kuznecov, V.V. Vozvedenie inyekcionnogo jadra plotiny Atbashinskoj GES (Kirgizskaja SSSR) [Construction of the injection core of the Atbashinskaya Dam (Kyrgyz USSR)]. Gidrotehnicheskoe stroitel'stvo. 1972. 12. Pp. 25–27.
49. Baranov, A.E. Iz opyta proektirovanija i stroitel'stva Jumaguzinskogo gidrouzla na r.Beloj [From experience in the design and construction of the Yumaguzinsky waterworks on the Belaya river]. Vestnik MGSU. 2006. 2. Pp. 112–122.
50. Korchevskij, V.F., Obopol', A.Ju. O proektirovanii i stroitel'stve Kambaratinskih gidrojelektrostancij na r.Naryne v Kirgizskoj Respublike [On the design and construction of Kambarata hydroelectric power plants on the Naryn River in the Kyrgyz Republic]. Gidrotehnicheskoe stroitel'stvo. 2012. 2. Pp. 2–12.
51. Korchevskij, F.V., Malyshev, A.M., Kolichko, A.V., Orehov, V.V. Kankunskaja GES na r.Timpton v Respublike Saha (Jakutija): variant gruntovoj plotiny s jadrom iz ukatannogo betona [Kankunskaya hydroelectric power station on the Timpton River in the Republic of Sakha (Yakutia): a variant of a soil dam with a core of rolled concrete]. Gidrotehnicheskoe stroitel'stvo. 2010. 2. Pp. 11–22.
52. Goncharov, A.V., Korchevskij, V.F., Malyshev, A.M. Gruntovaja plotina [Embankment dam] Patent Russia No. 2013106146/05, 13.02.2013, 2014.
53. Kotov, F.V. Rabotosposobnost' sverhvysokoj kamenno-nabrosnoj plotiny s protivofil'tracionnym jelementom v vide betonnogo jadra [Working efficiency of ultrahigh rockfill dam with a concrete core as a seepage control element]. Internet-zhurnal Naukovedenie. 2017. 9(6). https://naukovedenie.ru/PDF/83TVN617.pdf
54. Radchenko, V.G., Abramova, E.V. Samaja vysokaja v mire kamenno-nabrosnaja plotina s asfal'tobetonnoj diafragmoj [The highest rockfill dam in the world with an asphalt concrete diaphragm]. Gidrotehnika. XXI vek. 2018. 34(2). Pp. 8–11.
55. Tang Ju-shan, Ding Bang-man. Design of concrete face rockfill dam of the expansion project of Hengshan Reservoir. Journal on Water Power. 2002. 28(7). Pp. 35–37.
56. Haselsteiner, R., Kaytan, E., Pamuk, R, Ceri, V. Seepage control design of the Arkun dam in Turkey. Hydropower and Dams. 2012. 1. Pp. 90–96
57. Haselsteiner, R., Kaytan, E., Pamuk, R, Ceri, V. Deformation prediction of a large CFSGD for first impoundment. International symposium on dams in a global environmental challenges. Bali, Indonesia, 2014. 398.
58. Zairova, V.A., Filippova, E.A., Orishhuk, R.N., Sozinov, A.D., Radchenko, S.V. Vybor protivofil'tracionnogo ustrojstva v variantah plotin Kankunskogo gidrouzla [The choice of an seepage-control in the dam options of the Cancun hydroelectric complex]. Gidrotehnicheskoe stroitel'stvo. 2010. 2. Pp. 8–13.

Contacts:

Mikhail Sainov, mp_sainov@mail.ru

Filipp Kotov, filipp_net@mail.ru

© Sainov, M.P., Kotov, F.V., 2021

Magazine of Civil Engineering

ISSN 2712-8172

journal homepage: http://engstroy.spbstu.ru/

DOI: 10.34910/MCE.102.13

Low-heat steaming treatment of concrete with polycarboxylate superplasticizers

O.M. Smirnova
Saint-Petersburg Mining University, St. Petersburg, Russia
**E-mail: smirnovaolgam@rambler.ru*

Keywords: precast prestressed reinforced concrete, precast slabs, railway sleepers, steam-cured concrete, polycarboxylate superplasticizer, heat steaming treatment, transport construction

Abstract. Recommendations for quantity of polycarboxylate water-reducing admixtures, for the properties of Portland cement as well as the curing regimes is presented in order to reduce the Portland cement amount, to improve the transfer and design strength and durability of prefabricated structures. On the basis of experimental studies the parameters of low-heat steaming treatment of concrete with a polycarboxylate superplasticizer were stated: the duration of pre-exposure 2.5–3 hours, the rate of temperature rise 7°C/hour, the temperature of isothermal exposure 40–50 °C. The results obtained can be used in the production of precast prestressed sub-rail structures as well as other reinforced concrete structures with high performance characteristics at concrete plants with double or single mold turnover per day.

1. Introduction

In connection with the increase of requirements for sub-rail structures the issue of using high-strength and durable concretes in their production is relevant [1–4]. Sleepers, half-sleepers, prefabricated slabs of ballastless track of high-speed railway, etc. belong to the reinforced concrete sub-rail structures of factory production [5-7]. Increase of the durability of precast structures is possible through the use of polycarboxylate modifiers and reduction of the temperature of isothermal holding at heat-steaming treatment [4, 8].

At the same time, it is necessary to maintain high productivity of technological equipment for the production of sub-rail structures due to the double turnover of moulds per day. For lines with double turnover of moulds per day, the required transfer strength of concrete at the age of 10–12 hours should be more than 35MPa for B40 strength class and more than 44MPa for B50 strength class.

Water-reducing admixtures based on polycarboxylate esters are used to provide a high strength class of concrete [9–11], to increase concrete early strength [1], to obtain mixtures of high workability [12]. The reduction of water-to-cement ratio and the absence of forced high-heat treatment increase the durability of precast concrete structures [13]. The high temperature of isothermal holding at the heat-steaming treatment leads to the delayed ettringite formation in concrete structure [14–16]. This leads to the presence of high internal tensile stresses and, consequently, to the decrease of concrete strength [17].

According to De Bonte firm their sleepers produced without heat-steaming treatment have minimum service life of 40 years at speeds up to 350 km/h with the axial load of 225kN.

The required transfer strength of concrete for pre-stress release of reinforcement is achieved after 18–24 hours of hardening at normal conditions in a number of technologies of sub-rail structures production, for example, in the technology of large Italian manufacturer PLAN. However, the question of the use of water-reducing admixtures based on polycarboxylates for obtaining concrete with high transfer strength after low-heat steaming treatment of duration of 10–12 hours has not yet been studied. It is necessary to determine the conditions under which the use of method combining the modifier addition and thermal treatment provides the required transfer strength of concrete.

Polycarboxylate-based water-reducing admixtures are widely represented. The range of admixtures grows every year. However, the effect of admixtures on the technological properties of fresh concrete and on

Smirnova, O.M. Low-heat steaming treatment of concrete with polycarboxylate superplasticizers. Magazine of Civil Engineering. 2021. 102(2). Article No. 10213. DOI: 10.34910/MCE.102.13

This work is licensed under a CC BY-NC 4.0

the rate of strength development of hardened concrete is different [12, 18, 19]. Some water-reducing admixtures can significantly slow the growth of concrete strength in the first hours of hardening [20–22]. According to this it is necessary to identify the criterion by which admixture can be selected in order to obtain high-strength concrete after heat-steaming treatment on the example of production of sub-rail structures with double turnover of forms per 24 hours. One can propose the comprehensive approach that considers the use of ordinary raw materials, effective water-reducing modifiers of concrete structure as well as optimal low-temperature modes of heat-steaming treatment.

The aim of the paper is to set the correlation among the concrete strength and the parameters of the mode of low-heat steaming treatment of concrete with admixture namely the duration of pre-exposure, the rate of temperature rise as well as the duration and temperature of isothermal holding. Recommendations on the amounts of water-reducing admixtures on polycarboxylate basis, Portland cement fineness as well as modes of low-heat steaming treatment must be given.

The obtained results can be used for increasing the durability of prefabricated prestressed reinforced sub-rail structures as well as other reinforced concrete structures in the production with double or single turnover of moulds per day.

2. Methods and Materials of research

In transport construction the Portland cement of brand PC500D0-N (normalized composition without mineral additives where C_3A is up to 8 %, R_2O up to 0.6 %) according to Russian State Standard GOST R 55224-2012 "Cements for transport construction" is used for the preparation of concrete mixtures. The consumption of Portland cement in the manufacture of railway sleepers is between 450 and 500 kg/m^3 for concrete of B40 strength class and from 500 kg/m^3 for concrete of B50 strength class. The concrete of B50 strength class is manufactured with the use of superplasticizer.

The high amount of Portland cement is a disadvantage of the compositions since the compositions are designed on the basis of the condition of ensuring the required transfer strength of concrete after heat-steaming treatment at 80°C. The strength at the age of 28 days is provided due to the high consumption of Portland cement. Fresh concrete mixes with water-to-cement ratio up to 0.4 are used to ensure the early strength and durability of concrete according to Russian Application Standard OST 32.152-2000 "Sleepers for the Railways of the track of 1520 mm of the Russian Federation". Studies were performed on the composition of concrete for the production of sleepers with the weight ratio of 1:1.44:2.57 and with mixtures of the same workability. Granite coarse aggregate with the maximum size of 40mm and feldspar sand with the size modulus of 2.1 were used as aggregates.

Water-reducing admixtures must meet the requirements of Russian State Standard GOST 24211 "Admixtures for concrete and mortar." The polycarboxylate-based water-reducing admixtures Stachement 2280 and Stachement 2060 were chosen for the research.

The characteristics of the Portland cements chosen for the study are presented in Tables 1 and 2.

Table 1 Mineralogical composition of clinker.

Designation	Cement	C_3S	C_2S	C_3A	C_4AF
CEM-1	PC500D0-N "Maltsovsky Portland cement"	63.1	14.6	6.3	13.5
CEM-2	PC500D0-N "Volskcement"	63.9	13.0	4.1	16.0

Table 2 Physical and mechanical characteristics of cements.

Desig-nation	Fineness, the rest on sieve No.008, %	Normal consis-tence , %	Setting time of cement paste, hours-min.		Cement activity at normal conditions of hardening at 28 days, MPa	Cement activity after heat-steaming at 80°C *, MPa	Group of cement activity at heat-steaming treatment at 80°C *
			Begin	End			
Cem-1	3.3	27.6	2-30	4-20	51.3	34.1	II
Cem-2	2.3	27.0	2-10	4-20	52.5	40.8	I

*according to method [23]

Comparison of grains quantity of different fractions was made at the evaluation of particle size distribution of Portland cements in Table 3.

Table 3. Particle size distributions of Portland cements.

	The quantity of cement grains smaller than, %							
	2 µm	3 µm	5 µm	10 µm	16 µm	32 µm	50 µm	100 µm
Cem-1	6.3	8.6	14.1	23.7	48.8	68.9	80.2	95.2
Cem-2	11.6	16.6	23.7	38.6	49.2	75.2	90.1	98.7

3. Results and Discussion

3.1. Determination of the optimal amount of admixtures to increase the early strength of cement matrix

The problem of insufficient increase of fluidity of fresh concrete or insufficient reduction of water demand with the addition of superplasticizers due to the influence of chemical and mineralogical composition of Portland cement is known and studied by scientists [24–26]. This problem can rarely occur in the case of the use of Portland cement of brand 500D0-N that has the normalized composition according to standard Russian State Standard GOST R 55224-2012 "Cements for transport construction". However, it should be taken into account that water-reducing admixtures with the increase of their dosage can have a slowing effect on the hydration of cement systems at the early stage due to poor water permeability through the adsorption layers [27–29].

The results obtained in paper [30] at studying inhibitory effect of lignosulfonates lead to the conclusion about the adsorption of a large number of lignosulfonate molecules by the resulting ettringite. This leads to a slower crystallization of ettringite in calcium monosulfoaluminate that reduces the hydration of the C_3A. Hydration of alite also slows down if the concentration of lignosulfonate in the liquid phase remains high. As a result, the cement setting time is extended as well as the set of early strength of cement matrix slows down. The retarding effect of admixtures based on polycarboxylate esters on cement system hydration is also associated with their adsorption on ettringite [31] as well as with the effect of length of the main chain of their molecules [27].

The results of determining the optimal quantity of studied admixtures to produce concrete with high strength at an early age under normal hardening conditions are presented in Figures 1 and 2. The studies were carried out on a cement pastes with the normal consistency. Cubes of size 20×20×20 mm in precise plastic forms were made to determine the kinetics of the strength growth of cement matrix at different amounts of admixtures.

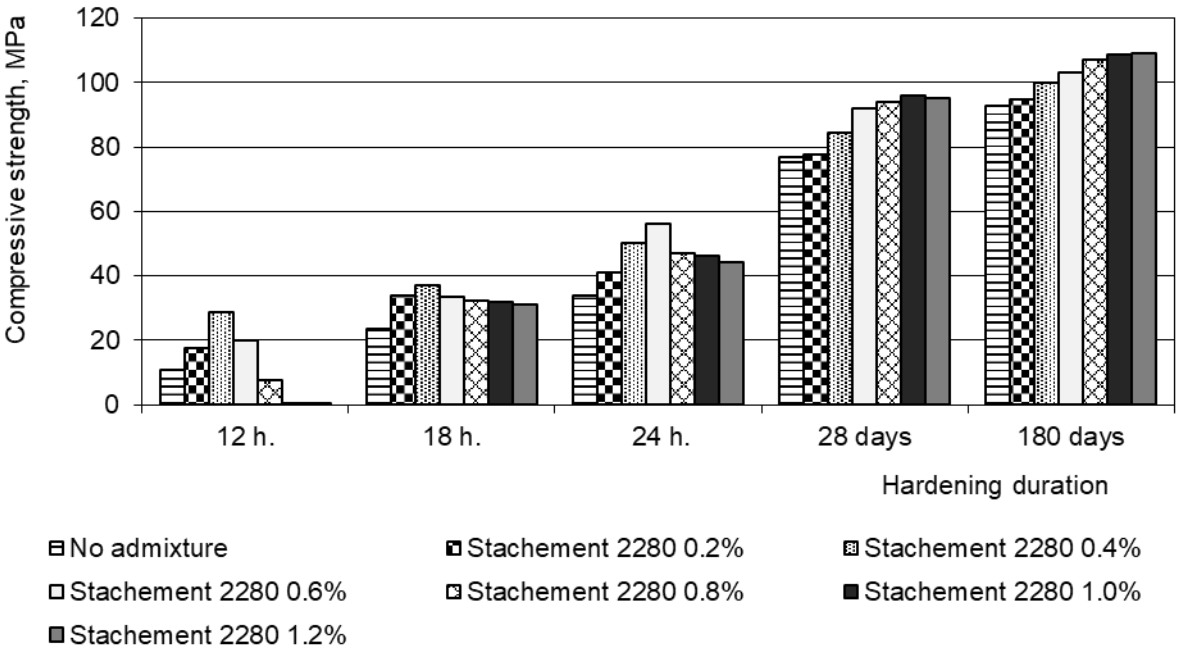

Figure 1. The strength growth of cement matrix at different amounts of Stachement 2280.

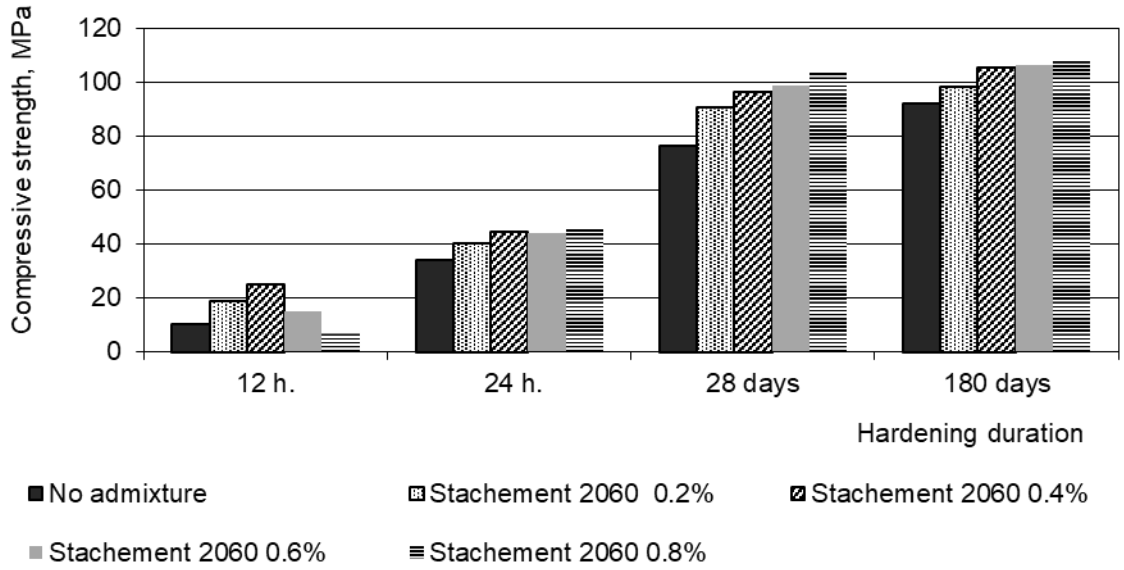

Figure 2. The strength growth of cement matrix at different amounts of Stachement 2060.

The analysis of Figures 1 and 2 has showed that clearly expressed maximum values of the compressive strength at the age of 12, 18 and 24 hours exist at the range of 0.4–0.6 % of Stachement 2280 admixture. The strength of cement matrix at the age of 12 and 18 hours decreases with increasing quantity of admixtures despite the increase of their water-reducing effect.

Thus, the optimal amount of polycarboxylate modifier exists to increase the strength of cement matrix in the early period of hardening, for example 12, 18 and 24 hours.

In the case of superplasticizer quantity less than the optimal one, no increase of early strength was observed due to insufficient water demand reduction. Conversely, the retarding effect of superplasticizer on cement hydration was manifested in the case of admixture quantity greater than the optimal one. The strength of cement matrix at the age of 28 days has increased with increasing quantity of admixtures in the studied range. It should be noted that the increase of strength was insignificant at the age of 180 days at the admixture quantity of more than 0.8 % of Portland cement mass.

3.2. Effective coefficients of strength of cement matrix

A scientifically based approach to determine the effective coefficients of strength of cement matrix taking into account the water-reducing effect of polycarboxylate admixture and the cement activity is proposed in paper [32] for the cement matrix of daily age.

Effective coefficients of strength growth of cement matrix at the age of 12 hours (K_e^{12}) taking into account the water-reducing effect of the admixture are calculated in this paper for the purpose of reasonable choice of admixtures for the studied technologies of production of sub-rail structures:

$$K_e^{12} = W_r \times K_c^{12}, \quad (1)$$

where

$$W_r = (W/C_n)/(W/C_{pl}), \quad (2)$$

Where W_r is water-reducing effect of admixture;

W/C_n is water-to-cement ratio of cement paste without admixture;

W/C_{pl} is water-to-cement ratio of cement paste with admixture.

$$K_c^{12} = R_{pl}^{12} / R_n^{12}, \quad (3)$$

where K_c^{12} is coefficient of relative activity of cement at the age of 12 hours in the presence of admixture;

R_n^{12} is cement matrix strength at the age of 12 hours without admixture;

R_{pl}^{12} is cement matrix strength at the age of 12 hours with admixture.

Similarly, the effective coefficients of cement matrix strength at the age of 18 and 24 hours were calculated in Table 4. It should be noted that the choice of plasticizing admixture and its amount depends on the requirements of precast concrete production technology.

Table 4 Effective coefficients of cement matrix strength.

Admixture	Amount, %	W/C	W_r, %	Compressive strength, MPa			K_c^{12}	K_e^{12}	K_c^{18}	K_e^{18}	K_c^{24}	K_e^{24}
				12 h	18 h	24 h						
No admixture	0	0.255	-	10.6	23.7	34	1.000	-	1.000	-	1.000	-
Stachement 2280	0.2	0.245	1.041	17.6	33.9	41.0	1.660	1.728	1.430	1.489	1.205	1.255
Stachement 2280	0.4	0.225	1.134	28.7	36.9	50.0	2.707	3.070	1.556	1.765	1.470	1.667
Stachement 2280	0.6	0.217	1.175	20.1	33.6	59.9	1.896	2.228	1.417	1.665	1.761	2.070
Stachement 2060	0.2	0.244	1.041	18.8	-	40.1	1.773	1.845	-	-	1.179	1.227
Stachement 2060	0.4	0.224	1.138	24.9	-	44.6	2.349	2.673	-	-	1.312	1.492
Stachement 2060	0.6	0.217	1.175	15.1	-	44.1	1.424	1.673	-	-	1.297	1.524

As one can see from Table 4 the optimal amount of admixture for precast concrete should be assigned not from the condition of its maximum water-reducing effect but from the condition of obtaining the maximum strength of concrete under normal conditions of hardening at the age when the requirements for transfer strength are imposed.

Studies have shown that the admixture amount for concrete with the necessary transfer strength after heat-steaming treatment of duration 10–12 hours should be assigned from the condition of the maximum value of the coefficient of relative activity of cement (K_c^{12}) at the age of 12 hours in the presence of admixtures. The coefficient K_e^{12} provides a more complete assessment of the effectiveness of admixtures since it also takes into account the water-reducing effect of the admixture.

Superplasticizers Stachement 2280 in the amount of 0.4% (K_c^{12} = 2.7; K_e^{12} = 3.07) and Stachement 2060 in the amount of 0.4% (K_c^{12} = 2.35; K_e^{12} = 2.67) were chosen according to the results of determination of the coefficients K_c^{12} and K_e^{12} for the selection of concrete composition to ensure the required transfer strength after heat-steaming treatment of duration up to12 hours.

Thus, the dependences of cement matrix strength on the type and amount of modifiers as well as the duration of hardening under normal conditions are stated. It is shown that the optimal amount of modifier in order to increase the strength at the age of 12, 18 and 24 hours exists for each type of superplasticizer.

The greatest increase of strength at the age of 12 hours was obtained with the addition of water-reducing admixture in the amount of 0.4% compared to the non-admixture composition. The studied admixtures at the amount of less than optimal one have not increase the early strength of concrete due to insufficient water reduction and at the amount higher than optimal one – their slowing effect on cement hydration has prevailed.

3.3. The modes of heat-curing of concrete with polycarboxylate-based admixture

Features of the production of precast reinforced concrete using superplasticizers and heat-curing were studied by many scientists [33–36]. However, obtaining the required strength of concrete after heat-curing was provided either by reducing the temperature of isothermal holding or the duration of heat-curing [37–41] or by reducing the cement quantity [42–46]. In this paper, the author sets the task to simultaneously reduce the Portland cement quantity and the temperature of isothermal holding. The optimal parameter values of low-heat steaming treatment for obtaining the high transfer and design strength as well as durability of precast concrete were stated.

It is shown that the duration of the pre-exposure of concrete before the low-heat steaming treatment is advisable to appoint considering the start of cement paste setting with a polycarboxylate modifier. Cracking was observed in samples with water-reducing admixtures at insufficient duration of pre-exposure or forced modes of heat-curing with the temperature rise rate of more than 10 °C/hour as shown in Figure 3. The width of the cracks was 0.5–1 mm which led to a sharp decrease of concrete strength. Thus, the pre-exposure must be 2.5–3 hours with the modifier of optimum quantity of 0.4 % by weight of Portland cement in contrast to the exposure of 1.5–2 hours used in the production of sub-rail structures (without water-reducing admixtures).

Figure 3. Samples of concrete after low-heat steaming treatment with different duration of preliminary exposure (sample 1 after treatment with mode of 3-3-5-1/40 °C, sample 2 after treatment with mode of 2-3-6-1/40 °C).

Modes with the temperature of isothermal holding of 40 °C and the total duration of 12 hours have differed in the rate of temperature rise as shown in Table 3. These modes were chosen to determine the effect of the rate of temperature rise on the strength of concrete with the optimal amount of admixture. The greatest increase of the concrete strength with admixture compared to the non-admixture concrete is obtained at the temperature of 40 °C as shown in Table 5. For comparison the Portland cements with different quantity of fine fractions were selected.

Table 5 Effect of the temperature rise rate on the concrete strength.

Cement	Admixture	Compressive strength after low-heat steaming treatment, MPa		
		3+1+7+1/40 ºC	3+2+6+1/40 ºC	3+3+5+1/40 ºC
Cem-1	Stachement 2280 0.4%	42.7	44.4	48.3
Cem-2	Stachement 2280 0.4%	44.7	50.6	49.7
Cem-1	Stachement 2060 0.4%	43.0	43.5	50.3
Cem-2	Stachement 2060 0.4%	45.5	51.1	48.4

Table 5 shows that the concrete reaches the greatest strength at the rate of temperature rise of 7–10 °C/hour. At the same time, the temperature rise can be 10 °C/hour for Portland cement with the grain quantity of less than 3 µm in the amount of 17 % (Cem-2).

The Portland cement activity with admixture at low-heat steaming treatment should be considered in addition to the activity of pure Portland cement at low-heat steaming treatment. Studies have shown that the optimal value of the isothermal holding temperature, corresponding to maximum strength, varies and depends on the type of modifier. Determination of the temperature of isothermal holding was performed at the temperature rise rate of 7–8 °C/h according to Table 6.

It is stated that the maximum absolute values of the concrete strength of samples with Stachement 2280 can be obtained at the isothermal holding temperature of 50 °C, with Stachement 2060 – at 40 °C. The maximum increase of strength of concrete with admixtures after low-heat steaming treatment compared with non-admixture concrete is achieved at 40 °C.

Table 6 Effect of the isothermal holding temperature on the concrete strength (Cem-2).

Admixture, %	*W/C*	Compressive strength after low-heat steaming treatment, MPa / in %			
		3+1+7+1/30ºC	3+3+5+1/40ºC	3+4+3+2/50ºC	3+5+2+2/60ºC
0	0.34	28.1/100	33.6/100	37.1/100	37.8/100
Stachement 2060 0.4%	0.30	39.1/138	49.2/145	48.8/130	48.7/128
Stachement 2280 0.4%	0.30	39.8/140	50.8/150	52.2/139	49.8/131

Accordingly, the Portland cement must have a high activity with water-reducing modifier at the optimum temperature of isothermal holding in order to significantly reduce the consumption of Portland cement.

One can propose to simultaneously determine the efficiency coefficient of Portland cement with polycarboxylate modifier after low-heat steaming treatment (for example, at temperatures of 40, 50 and 60 °C) (4) and to choose the optimal temperature of isothermal holding as shown in Table 7:

$$K_{\partial t}=R_{\partial t}/R_c, \quad (4)$$

where $R_{\partial t}$ is activity of Portland cement with polycarboxylate modifier after low-heat steaming treatment at t = 40, 50 and 60 °C;

R_c is activity of Portland cement with polycarboxylate modifier at the age of 28 days.

Table 7 Efficiency coefficient of Portland cement with admixture after low-heating treatment.

Components	Efficiency coefficient of Portland cement at 40 °C*	$R_{\partial 40}$	$R_{\partial 50}$	$R_{\partial 60}$	R_c	$K_{\partial 40}$	$K_{\partial 50}$	$K_{\partial 60}$
Stachement 2060 0.4% Cem-1	0.60	43.2	45.7	42.0	57.5	0.74	0.79	0.72
Stachement 2280 0.4% Cem-2	0.71	46.7	46.8	45.0	56.8	0.81	0.81	0.78

* The efficiency coefficient of cement is determined by the formula 4 without the use of admixtures

The coefficient of efficiency of Portland cement with admixture after low-heating treatment allows setting the optimal temperature of isothermal exposure taking into account the properties of admixture and Portland cement.

Thus, the values of the parameters of curing of precast concrete with polycarboxylate-based admixture were stated: the duration of pre-exposure is 2.5–3 hours; the rate of temperature rise is 7–10 °C/h; the temperature of the isothermal holding is 40–50 °C.

Generalized mathematical dependence of the transfer strength of concrete after low-heat treatment from its duration and temperature of isothermal holding, quantity of Portland cement and water-reducing admixtures was derived (5). To do this, the multifactorial task of finding the dependence of concrete strength (Y) on the following factors is considered: R_d is admixture quantity (0.3; 0.4; 0.5%), R_c is cement quantity (400, 440, 480 kg), t is the duration of low-heat treatment (10, 12, 14 hours), T_{grad} is the temperature of isothermal holding (40 °C, 50 °C, 60 °C). The experimental results are presented in Table 8.

The equation of the regression function Y is represented as the polynomial of the 2nd degree of 4 variables with significant estimates of parameters and the coefficient of multiple determinations R^2 = 95.32 % as:

$$Y = -330.5+445.6\times R_d+1.2\times R_c-395.9\times R_d-0.4\times R_d\times R_c+3.9\times Rd\times t+0.2\times Rd\times Tgrad-0.001\times Rc^2 \quad (5)$$

Table 8. Multi-factor task of finding the dependence of compressive strength.

Matrix of the plan in values		Compressive strength of concrete after heat-steaming treatment with duration								
		at 40 °C			at 50 °C			at 60 °C		
		10 hrs, MPa	12 hrs, MPa	14 hrs, MPa	10 hrs, MPa	12 hrs, MPa	14 hrs, MPa	10 hrs, MPa	12 hrs, MPa	14 hrs, MPa
Admixture quantity, %	Cement, kg	Y_{10}^{40}	Y_{12}^{40}	Y_{14}^{40}	Y_{10}^{50}	Y_{12}^{50}	Y_{14}^{50}	Y_{10}^{60}	Y_{12}^{60}	Y_{14}^{60}
0.5	480	35.4	39.6	44.4	35.8	40.2	45.2	35.9	40.5	46.5
0.5	400	32.2	35.8	39.6	32.8	36.4	40.3	32.7	36.9	40.7
0.3	480	41.2	43.1	45.2	42.3	44.5	45.6	43.5	47.7	48.1
0,3	400	29.8	32.2	34.6	30.7	33.6	34.9	33.4	35.2	36.9
0.5	440	33.9	38.1	42.9	35.0	38.9	43.9	35.3	39.2	42.8
0.3	440	37.9	40.6	42.8	39.1	41.8	44.1	42.8	44.3	45.6
0.4	480	41.3	44.6	47.8	42.8	45.0	49.6	43.6	46.3	49.2
0.4	400	35.9	39.3	41.8	37.2	39.9	42.9	38.9	41.6	43.0
0.4	440	40.1	42.9	45.8	41.5	43.8	47.2	42.6	45.6	47.9

The graph of the regression function of concrete strength is shown in Figure 4.

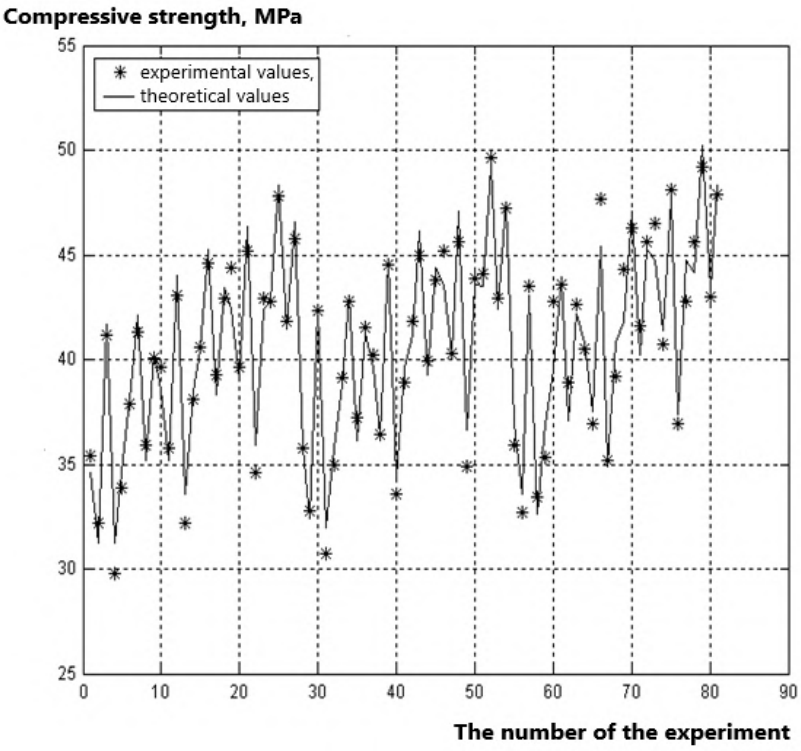

Figure 4. Experimental and, theoretical values of the regression function of concrete strength.

On the basis of the obtained model it was determined that the Portland cement quantity is 400 kg/m^3 in the conditions of application of Portland cement that meet the criteria for activity after low-heat treatment, chemical-mineralogical composition and fineness as well as water-reducing admixture in the optimal amount of 0.4 %. This consumption of Portland cement is 15 % less compared to the consumption in production of precast sleepers of B40 and B50 concrete strength class that are steamed at 80 °C to ensure the required transfer strength.

4. Conclusions

1. Recommendations on the amounts of water-reducing admixtures on polycarboxylate basis, Portland cement fineness as well as modes of low-heat steaming treatment were given in order to increase the strength and durability of prefabricated structures.

2. The optimal amount of polycarboxylate modifier exists to increase the strength of cement matrix in the early period of hardening, for example 12, 18 and 24 hours. In the case of superplasticizer quantity less than the optimal one, no increase of early strength was observed due to insufficient water demand reduction. Conversely, the retarding effect of superplasticizer on cement hydration was manifested in the case of admixture quantity greater than the optimal one. The strength of cement matrix at the age of 28 days has increased with increasing quantity of admixtures in the studied range.

3. Effective coefficients of strength growth of cement matrix at an early age were stated. These coefficients allow choosing the necessary type and quantity of admixture for precast concrete production.

4. The parameters of low-heat steaming treatment of concrete with a polycarboxylate superplasticizer were stated: the duration of pre-exposure 2.5–3 hours, the rate of temperature rise 7 °C/hour, the temperature of isothermal exposure 40–50 °C. The obtained results can be used in the production of precast prestressed reinforced sub-rail structures as well as other reinforced concrete structures with high durability at plants with double or single turnover of moulds per 24 hours.

References

1. Smirnova, O.M. Obtaining the High-performance Concrete for Railway Sleepers in Russia. Procedia Engineering. 2017. No. 172. Pp. 1039–1043. DOI: 10.1016/j.proeng.2017.02.158
2. Kaewunruen, S., Remennikov, A.M. Impact capacity of railway prestressed concrete sleepers. Engineering Failure Analysis. 2009. 16(5). Pp. 1520–1532. DOI: 10.1016/j.engfailanal.2008.09.026
3. Yang, J., Kong, B., Cai, C.S., Wang, J.S. Behavior of High-Speed Railway Ballastless Track Slabs Using Reactive Powder Concrete Materials. Journal of Transportation Engineering. 2016. 142(8). 04016031.
4. Zhu, S., Wang, M., Zhai, W., Cai, C., Zhao, C., Zeng, D., Zhang, J. Mechanical property and damage evolution of concrete interface of ballastless track in high-speed railway: Experiment and simulation. Construction and Building Materials. 2018. 187. Pp. 460–473. DOI: 10.1016/j.conbuildmat.2018.07.163

5. You, R., Li, D., Ngamkhanong, C., Janeliukstis, R., Kaewunruen, S. Fatigue life assessment method for prestressed concrete sleepers. Frontiers in built environment. 2017. 3. Pp. 68–74. DOI: 10.3389/fbuil.2017.00068
6. Tarifa, M., Zhang, X., Ruiz, G., Poveda, E. Full-scale fatigue tests of precast reinforced concrete slabs for railway tracks. Engineering Structures. 2015. 100. Pp. 610–621. DOI: 10.1016/j.engstruct.2015.06.016
7. Su, C., Liu, D., Ding, C., Gong, C., Zhao, P., Liu, X. Experimental study on bond performances of track slab and mortar based on DIC technology. KSCE Journal of Civil Engineering. 2018. 22(9). Pp. 3546–3555. DOI: 10.1007/s12205-018-0848-2
8. Bezgin, N.Ö. An insight into design of prefabricated and prestressed concrete monoblock railway ties for service loads. Challenge. 2018. 4(4). Pp. 126–136. DOI: 10.20528/cjsmec.2018.04.001
9. Barabanshchikov, Y.G., Belyaeva, S.V., Arkhipov, I.E., Antonova, M.V., Shkol'nikova, A.A., Lebedeva, K.S. Influence of superplasticizers on the concrete mix properties. Magazine of Civil Engineering. 2017. 74(6). Pp. 140–146
10. Li, V.C., Herbert, E. Durable railway tie. U.S. Patent Application No. 15/550,304. 2018.
11. Kharitonov, A., Ryabova, A., Pukharenko, Y. Modified GFRC for durable underground construction. Procedia engineering. 2016. 165. Pp. 1152–1161. DOI: 10.1016/j.proeng.2016.11.833
12. Smirnova, O. Concrete mixtures with high-workability for ballastless slab tracks. Journal of King Saud University-Engineering Sciences. 2017. 29(4). Pp. 381–387 DOI: 10.1016/j.jksues.2017.06.004
13. Bezgin, N.Ö. High performance concrete requirements for prefabricated high speed railway sleepers. Construction and Building Materials. 2017. 138. Pp. 340–351. DOI: 10.1016/j.conbuildmat.2017.02.020
14. Amine, Y., Leklou, N., Amiri, O. Effect of supplementary cementitious materials (scm) on delayed ettringite formation in heat-cured concretes. Energy Procedia. 2017. No. 139. Pp. 565–570. DOI: 10.1016/j.egypro.2017.11.254
15. Sato, K., Saito, T., Kikuchi, M., Saeki, T. Relationship Between Expansion Characteristics of Heat-Cured Mortars During Water Curing and Origins of Ettringite Formation. Journal of Advanced Concrete Technology. 2019. 17(5). Pp. 260–268. DOI: 10.3151/jact.17.260
16. Rashidi, M., Paul, A., Kim, J. Y., Jacobs, L. J., Kurtis, K. E. Insights into delayed ettringite formation damage through acoustic nonlinearity. Cement and Concrete Research. 2017. 95. Pp. 1–8. DOI: 10.1016/j.cemconres.2017.02.004
17. Deboucha, W., Leklou, N., Khelidj, A. Blast Furnace Slag Addition Effects on Delayed Ettringite Formation in Heat-cured Mortars. KSCE Journal of Civil Engineering. 2018. 22(9). Pp. 3484–3490. DOI: 10.1007/s12205-017-0642-6
18. Shi, C., Zhang, G., He, T., Li, Y. Effects of superplasticizers on the stability and morphology of ettringite. Construction and Building Materials. 2016. 112. Pp. 261–266. DOI: 10.1016/j.conbuildmat.2016.02.198
19. Mantellato, S., Palacios, M., Flatt, R.J. Relating early hydration, specific surface and flow loss of cement pastes. Materials and Structures. 2019. 52(1). Pp. 5–8. DOI: 10.1617/s11527-018-1304-y
20. Zhang, M.H., Sisomphon, K., Ng, T.S., Sun, D.J. Effect of superplasticizers on workability retention and initial setting time of cement pastes. Construction and Building Materials. 2010. 24(9). Pp. 1700–1707. DOI: 10.1016/j.conbuildmat.2010.02.021
21. Dalas, F., Pourchet, S., Rinaldi, D., Nonat, A., Sabio, S., Mosquet, M. Modification of the rate of formation and surface area of ettringite by polycarboxylate ether superplasticizers during early C3A–CaSO4 hydration. Cement and Concrete Research. 2015. 69. Pp. 105–113. DOI: 10.1016/j.cemconres.2014.12.007
22. Kharitonov, A.M., Tikhonov, Y.M., Belentsov, Y.A. Influence of concrete strength evaluation method accuracy on reliability levels of geotechnical structures. Proceedings of Geotechnics Fundamentals and Applications in Construction: New Materials, Structures, Technologies and Calculations. Saint-Petersburg. Russia, 2019. Pp. 135–138.
23. Smirnova, O. M. Rheologically active microfillers for precast concrete. International Journal of Civil Engineering and Technology. 2018. 9(8). Pp. 1724–1732.
24. Smirnova, O.M. Compatibility of portland cement and polycarboxylate-based superplasticizers in high-strength concrete for precast constructions. Magazine of Civil Engineering. 2016. 66(6). Pp. 12–22. DOI: 10.5862/MCE.66.2
25. Plugin, A., Dedeneva, E., Kostyuk, T., Bondarenko, D., Demina, O. Formation of structure of high-strength composites with account of interactions between liquid phase and disperse particles. Matec Web of Conference. 2017. 116. Pp. 01010. DOI: 10.1051/matecconf/201711601010
26. Sliseris, J., Korjakins, A. Numerical Modeling of the Casting Process and Impact Loading of a Steel-Fiber-Reinforced High-Performance Self-Compacting Concrete. Mechanics of Composite Materials. 2019. 55(1). Pp. 29–40. DOI: 10.1007/s11029-019-09789-x
27. Meier, M.R., Rinkenburger, A., Plank, J. Impact of different types of polycarboxylate superplasticisers on spontaneous crystallisation of ettringite. Advances in Cement Research. 2016. 28(5). Pp. 310–319. DOI: 10.1680/jadcr.15.00114
28. Lange, A., Plank, J. Formation of nano-sized ettringite crystals identified as root cause for cement incompatibility of PCE superplasticizers. In Nanotechnology in Construction. Springer, Cham, 2015. Pp. 55–63. DOI: 10.1007/978-3-319-17088-6_6
29. Schönlein, M., Plank, J. Influence of PCE kind and dosage on ettringite crystallization performed under terrestrial and microgravity conditions. Journal of the American Ceramic Society. 2018. 101(8). Pp. 3575–3584. DOI: 10.1111/jace.15513
30. Ramachandran, V.S. Effect of sugar-free lignosulphonates on cement hydration. Zement-Kalk-Gips. 1978. 31. Pr. 106–111.
31. Plank, J., Hirsch C. Impact of zeta potential of early cement hydration phases on superplasticizer adsorption. Cement and Concrete Research. 2007. 37. Pp. 537–542. DOI: 10.1016/j.cemconres.2007.01.007
32. Bazhenov, Yu.M., Kalashnikov, V.I., Demyanova, V.S. Vysokokachestvennyy beton. Izd-vo ASV. Moskva. 2007. Pp. 555 (rus)
33. Türkel, S., Alabas, V. The effect of excessive steam curing on Portland composite cement concrete. Cement and Concrete Research. 2005. 35(2). Pp. 405-411. DOI: 10.1016/j.cemconres.2004.07.038
34. Ma, K., Long, G., Xie, Y. A real case of steam-cured concrete track slab premature deterioration due to ASR and DEF. Case Studies in Construction Materials. 2017. No. 6. Pp. 63–71. DOI: 10.1016/j.cscm.2016.12.001
35. Shen, P., Lu, L., He, Y., Rao, M., Fu, Z., Wang, F., Hu, S. Experimental investigation on the autogenous shrinkage of steam cured ultra-high performance concrete. Construction and Building Materials. 2018. No. 162. Pp. 512–522. DOI: 10.1016/j.conbuildmat.2017.11.172
36. Xiao, Q.Q., Huang, Z.X., Zu, X.D., Jia, X., Zhu, Q.F., Cai, W. Shaped charge penetration into high-and ultrahigh-strength steel–fiber reactive powder concrete targets. Defence Technology. 2019. DOI: 10.1016/j.dt.2019.04.013
37. Hanif, A., Kim, Y., Lee, K., Park, C., Sim, J. Influence of cement and aggregate type on steam-cured concrete–an experimental study. Magazine of Concrete Research. 2017. 69(13). Pp. 694–702. doi.org/10.1680/jmacr.17.00015

38. Zou, C., Long, G., Ma, C., Xie, Y. Effect of subsequent curing on surface permeability and compressive strength of steam-cured concrete. Construction and Building Materials. 2018. No. 188. Pp. 424–432. DOI: 10.1016/j.conbuildmat.2018.08.076
39. Zeitouni, A. I., Rizos, D.C., Qian, Y. Benefits of high strength reduced modulus (HSRM) concrete railroad ties under center binding support conditions. Construction and Building Materials. 2018. No. 192. Pp. 210–223. DOI: 10.1016/j.conbuildmat.2018.10.124
40. Sharifi, N.P., Chen, S., You, Z., Van Dam, T., Gilbertson, C. A review on the best practices in concrete pavement design and materials in wet-freeze climates similar to Michigan. Journal of Traffic and Transportation Engineering (English Edition). 2019. 6(3). Pp. 245–255. DOI: 10.1016/j.jtte.2018.12.003
41. Baydjanov, D.O., Abdrakhmanova, K.A., Kropachev, R.A., Rakhimova G.M. Modified concrete for producing pile foundations. Magazine of Civil Engineering. 2019. 86(2). Pp. 3–10. DOI: 10.18720/MCE.86.1.
42. Ochkurov, V. I., Vilenskii, M. Y. Comparative evaluation of the saving of binder with fine ground slag. In IOP Conference Series: Materials Science and Engineering. IOP Publishing. 2019. 666(1). Pp. 012026. DOI:10.1088/1757-899X/666/1/012026
43. Samchenko, S., Kozlova, I., Zemskova, O., Potaev, D., Tsakhilova, D. Efficiency of stabilization of slag suspensions by polycarboxylate. In E3S Web of Conferences. EDP Sciences. 2019. 91.Pp. 02039. DOI: org/10.1051/e3sconf/20199102039
44. Sprince, A., Pakrastins, L., Gailitis, R. Long-Term Parameters of New Cement Composites. In International Conference on Application of Superabsorbent Polymers & Other New Admixtures Towards Smart Concrete. Springer, Cham. 2019. Pp. 85–94. DOI: 10.1007/978-3-030-33342-3_10
45. Dvorkin, L.I., Zhitkovsky, V.V. Method of proportioning the cement-water ratio of steam-cured concrete. Magazine of Civil Engineering. 2019. 90(6). Pp. 15–27. DOI: 10.18720/MCE.90.2
46. Koyankin, A.A., Mitasov, V.M., Deordiev, S.V. The compatibility of deformation of the hollow-core slab with beams. Magazine of Civil Engineering. 2019. 87(3). Pp. 93–102. DOI: 10.18720/MCE.87.8

Contacts:

Olga Smirnova, smirnovaolgam@rambler.ru

© Smirnova, O.M., 2020

Magazine of Civil Engineering

ISSN 2712-8172

journal homepage: http://engstroy.spbstu.ru/

DOI: 10.34910/MCE.102.14

Elasto-plastic progressive collapse analysis based on the integration of the equations of motion

S.Yu. Fialko[a]*, O.V. Kabantsev[b], A.V. Perelmuter[c]

[a] *Tadeusz Kościuszko Cracow University of Technology, Kraków, Poland*

[b] *Moscow State University of Civil Engineering, Moscow, Russia*

[c] *Scientific and Production Company «SCAD Soft» Ltd., Kiev, Ukraine*

**E-mail:* sfialko@riad.pk.edu.pl

Keywords: progressive collapse, reinforced concrete structures, numerical analysis, finite element method, nonlinear dynamics

Abstract. This paper considers the progressive collapse analysis of reinforced concrete structures based on the sudden removal of a load-bearing structural element and simulation of the dynamic structural behavior, taking into account the elasto-plastic properties of the material and the degradation of concrete during cracking. A specially developed finite element library is used, which includes triangular and quadrilateral shell finite elements of medium thickness, and a two-node finite element of a spatial frame, which take into account the discrete arrangement of reinforcement and various elasto-plastic material models for concrete and reinforcement. The novelty of the proposed approach lies in the formulation of both: the spatial frame and shell finite elements as a three-dimensional solid body with sequential application of the conventional hypothesis of the for Mindlin-Reissner shells of medium thickness, Timoshenko beams, and the elasto-plastic constitutive models. This makes it possible to achieve sufficiently high reliability of the results for engineering analysis, and on the other hand, a relatively simple implementation, which makes it possible to perform an elasto-plastic dynamic analysis of the entire design model of the structure, and not a separate fragment, in real time from the point of view of practical design. This approach is free from assumptions related to the introduction of a dynamic amplification factor into the quasi-static analysis, which is widely used to solve such problems. The paper provides a numerical example illustrating the effectiveness of using a special structure – an outrigger storey, to prevent progressive collapse, and a comparison of the nonlinear dynamic analysis and the linear one.

1. Introduction

One of the most important problems in the reliability assessment of the entire load-bearing structural system is its resistance evaluation in the case of failure of individual load-bearing structures or in the case of a local defect in the structural system. This problem is sometimes formulated as a structural robustness assessment, which seems to be one of the possible approaches.

Essentially, the problem of resistance evaluation of a load-bearing system in the case of failure of a structural element can be reduced to the analysis of the collapse development in the load-bearing system due to a local cause (failure of an individual structure). This approach corresponds to the modern interpretation of the well-known and commonly used concept of progressive collapse, which is considered as disproportionate collapse due to a failure of the local structure or assembly.

Progressive collapse is a dangerous phenomenon in which the failure of some key load-bearing structural elements leads to the failure of other elements; this in turn leads to a partial or even complete collapse of the structure. This phenomenon attracted much attention in 1968, after the partial collapse of the Ronan Point Building, when an explosion of domestic gas in one of the apartments entailed a chain of collapses throughout the building. This problem, however, became even more acute after the events of 2001, when the twin towers of the World Trade Center (WTC) were destroyed in a terrorist attack, which resulted in a large number of victims and huge economic losses.

Fialko, S.Yu., Kabantsev, O.V., Perelmuter, A.V. Elasto-plastic progressive collapse analysis based on the integration of the equations of motion. Magazine of Civil Engineering. 2021. 102(2). Article No. 10214. DOI: 10.34910/MCE.102.14

This work is licensed under a CC BY-NC 4.0

It is quite obvious that the concept of progressive / disproportionate collapse refers to a phenomenon that needs to be prevented, i.e., the collapse development in a load-bearing system due to a failure of an individual structure should not be allowed. In order to ensure the stability of the load-bearing system in the case of failure of a structural element and to provide the resistance of the load-bearing system, building codes now include the requirements for taking into account a possible progressive collapse and preventive measures, which increases the construction costs. One of the components that significantly affect the cost is the factor of the dynamic response of the construction to the failure of its local part. The nonlinear behavior of the system and the dynamic effect can be taken into account in one of three different analytical procedures, i.e., linear static analysis (LS), nonlinear static analysis (NS) or nonlinear dynamic analysis (ND).

The dynamic effect was usually taken into account in quasi-static analyses by introducing a dynamic amplification factor of $k_{dyn} = 2.0$ into the linear static analysis (LS) regardless of the type and mass distribution of the designed structure.

The simplicity of quasi-static analysis and dissatisfaction with such a rough decision prompted the scientists to refine the values of k_{dyn}, and in 2009 the dynamic amplification factor formulas appeared, which allow to replace the nonlinear dynamic analysis with a quasi-static linear or nonlinear one. These factors were empirically derived by A. McKay [1] based on statistical processing of the results of frame structure analyses for column failures and presented in the report written together with K. Marchand and D. Stevens [2]. In the same year, the proposed formulas were included in UFC 4-023-03: Design of Buildings to Resist Progressive Collapse. They were further refined in the works of M. Liu [3, 4], M. Tsai [5], H. Saffari and J. Mashhadi [6] and others, but they still referred only to simple orthogonal frame structures. More complex designs (with additional bracings, outriggers, etc.) were not considered. Moreover, the quasi-static analysis did not provide sufficient accuracy, and sometimes did not even guarantee a conservative solution, which was noted, for example, in [7, 8]. Therefore, nonlinear dynamic analysis remains a very important problem, which is studied by many researchers [9–12].

This paper is devoted to the same problem. The simulation of the progressive collapse process is based on a nonlinear dynamic analysis of the structure as a whole or of its separate part. Nonlinearity is caused by high stress levels in the material leading to partial and/or complete collapse of structural fragments. Not only does this approach have great computational complexity, but it should also be based on a mechanical-mathematical model that adequately describes the processes occurring in structural elements. Partial and complete collapse of structural elements often leads to poor conditioning of the system of governing equations; therefore, it becomes necessary to use specific approaches that ensure the computational stability of the method. The foregoing emphasizes the difficulties of the considered problem and explains the fact that the vast majority of practical calculations today are based on approximate models using certain simplifications. Therefore, creating a method that uses a nonlinear dynamic analysis based on sufficiently advanced mechanical models of physical nonlinearity to solve the progressive collapse problem is still a relevant task. Solutions obtained on the basis of such an approach could possibly improve simpler approaches — static, linear dynamic, or nonlinear dynamic ones based on simplified nonlinearity models.

In the absence of proven calculation methods that take into account the nonlinear behavior of the entire reinforced concrete structure, some generalized partial criteria for individual elements and assemblies are proposed and justified [13, 14]. This approach should be considered as a solution to the problem at a local level, but it cannot be accepted as a generalized methodology for assessing the progressive collapse stability of reinforced concrete load-bearing systems.

Without reducing the generality of the proposed approach, we will consider only reinforced concrete structures with bar or plate-bar load-bearing systems, whose behavior during progressive collapse is much less studied than the behavior of steel structures. There are many different approaches today to simulating the behavior of concrete at high stress levels. We will consider only the most typical ones.

These or other relations of the theory of plasticity are used in [15–23], and in many other works. Degradation of concrete in the tension area during cracking is described by the descending branch of the $\sigma - \varepsilon$ diagram. Usually, in the absence of reinforcement, a finite element solution becomes mesh-dependent: it diverges when the finite element mesh refines [24, 25]. Different approaches were proposed for dealing with this phenomenon, which, as a rule, involved a significant complication of the design model. A nonlocal continuum approach is presented in [18–20], where exact relations for strains at a given point are replaced by weighted average expressions obtained by the integration over a finite neighborhood of this point.

In [26], as well as in a number of other works, derivatives of the higher order stress tensor components are kept in the continuum equilibrium equations, which makes it possible to stabilize the convergence of the numerical solution within the descending branch of the $\sigma - \varepsilon$ diagram. The disadvantage of such approaches is the fact that it is not clear how to choose the values of constants that appear in constitutive relations.

In [27–29] and other works, linear fracture mechanics methods are used to simulate cracking in concrete. A particle method is proposed in [30], which assumes that only particles uniformly distributed over the volume of concrete can have embedded cracks. If the maximum tensile stress exceeds the tensile strength of the material in a unit volume, a discrete crack is initiated in the nearest particle.

The above works, as a rule, considered individual structural elements (a beam, a flat frame, a slab) in a static formulation. There are rare articles, for example, [31], in which the nonlinear dynamic approach is applied to the entire design model. However, these are usually strongly simplified design models, not design models of real structures.

The novelty of this approach is to study the dynamic behavior of a reinforced concrete structure as a whole in an elasto-plastic formulation using governing equations derived from the three-dimensional equations of solid mechanics, taking into account traditional static and kinematic hypotheses of the Mindlin-Reissner theory for shells of medium thickness, Timoshenko beams, and the elasto-plastic constitutive models.

Also, we use an original formulation of the deformation theory of plasticity in the terms of residual strains, allowing us easy to pass from tensile zone to compression one and vice versa. Unlike most approaches published and implemented in modern software, we take into account the stiffness of reinforcement not only on tension-compression but on transverse shear as well, which helps to avoid geometrical instability or poor conditioning of the problem in cases where the finite elements are in the tension area and concrete has significant damages [32, 34, 35].

In order to prevent the divergence of the numerical solution with mesh refinement after passing the yield point of the $\sigma - \varepsilon$ diagram, a simple engineering idea is used: the reinforcement, whose $\sigma - \varepsilon$ diagram does not have a descending branch, should regularize the numerical solution. It is shown in [32, 34, 35] that if the slope of the descending branch of the $\sigma - \varepsilon$ diagram for concrete in reinforced concrete thin-walled structures does not exceed a certain limit value depending on the ratio of the elastic modules of steel and concrete and the reinforcement ratio, then the curve of equilibrium states is monotonically increasing.

On the one hand, the proposed approach demonstrates the reliability of the results acceptable for engineering purposes, which is confirmed by numerous comparisons with the results of well-designed experiments and with reliable numerical solutions [32–35, 37]. On the other hand, the proposed approach is quite simple, which allows performing an elasto-plastic analysis of the entire design model of the structure, and not a separate fragment, on a desktop computer in real time from the point of view of the designer.

2. Methods

2.1. Finite Element Library

The developed finite element library includes triangular and quadrilateral shell finite elements of medium thickness [32–34] (Figure 1), described by the Mindlin-Reissner equations, and a two-node finite element of a spatial frame based on the Timoshenko beam theory [35] (Figure 2).

The stability of the above finite elements against the shear locking is provided. Reinforcement is smeared in the plane of a shell finite element and forms reinforcement layers. The discrete arrangement of rebar along the thickness of the element remains though. Each reinforcement layer is formed by reinforcing bars of the same direction, cross-section and material. The number of reinforcement layers is not limited. The axes of the reinforcement layers $s_1 - s_4$ can be rotated by any angle with respect to the axes of the local coordinate system $OX_1Y_1Z_1$, which allows us to consider structures of complex geometric shape for any configuration of the finite element mesh. Longitudinal reinforcement is taken into account discretely in bar finite elements (Figure 2).

Constitutive relations are based both on the plastic flow theory and on the deformation theory of plasticity. The test problems considered in [32–34] have shown that the application of the deformation theory of plasticity in the case of non-cyclic loading leads to results closer to the experimental ones than the application of the plastic flow theory. We attribute this to the fact that the deformation theory of plasticity takes into account the nonlinear behavior of concrete from the very beginning of loading, while the plastic flow theory assumes the material behavior to be elastic and linear until the image point reaches the yield surface in the space of principal stresses. Another argument for using the deformation theory of plasticity in the progressive collapse analysis is the fact that most design standards, including the Eurocode, are based on this theory, since they govern the form of the $\sigma - \varepsilon$ diagram, but do not provide any information about the shape of the yield surface. Therefore, in this paper we will consider only the constitutive relations derived from the deformation theory of plasticity.

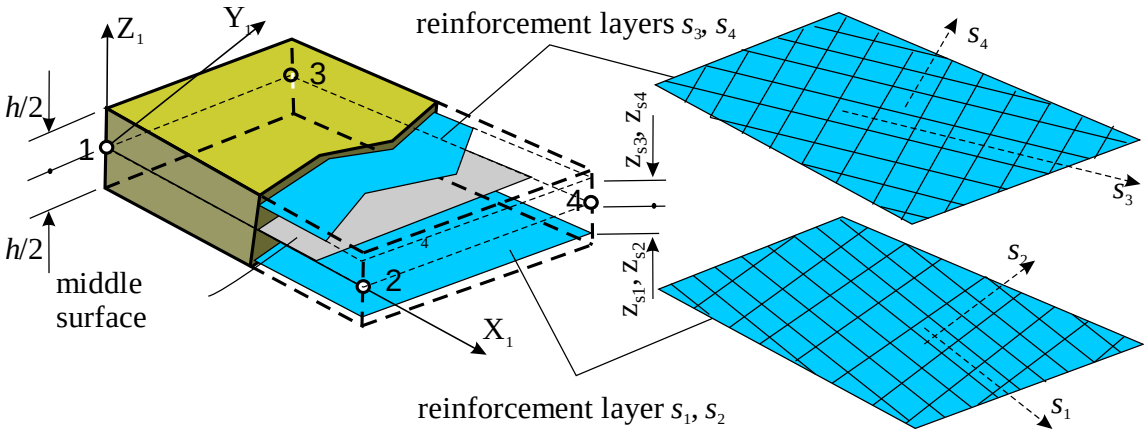

Figure 1. Quadrilateral finite element.

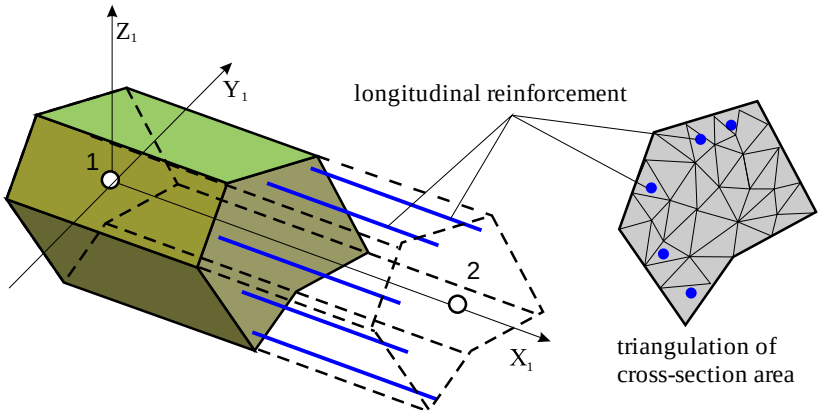

Figure 2. Two-node finite element of a spatial frame.

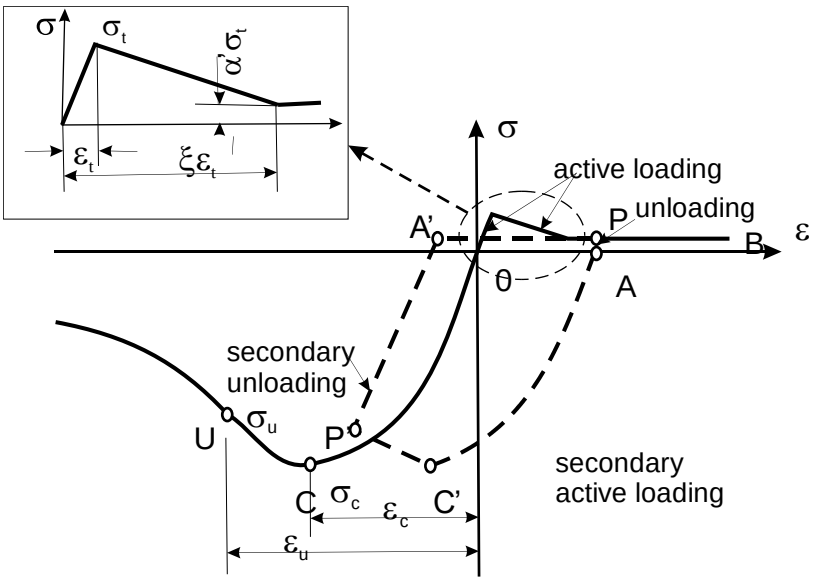

Figure 3. $\sigma - \varepsilon$ diagram for concrete.

We use the $\sigma - \varepsilon$ diagram for concrete proposed in [16] (Figure 3). The stress and strain values in the points C and U (σ_c, ε_c and σ_u, ε_u, respectively), as well as the initial elastic modulus of concrete E define the configuration of the $\sigma - \varepsilon$ curve in the tension area. Here σ_c is the ultimate compressive strength of concrete. A trilinear diagram is used in the tension area, and the descending branch describes the degradation of concrete during cracking. Here σ_t is the ultimate tensile strength of concrete, $\varepsilon_t = \sigma_t/E$, parameter α' defines the residual tensile strength of concrete and is usually equal to zero, and the parameter ξ defines the length of the descending branch and the softening modulus of concrete $E_t = -E/(\xi - 1)$. A distinctive feature of this approach is the fact that the relations of the deformation theory of plasticity are formulated in terms of residual strains [32–34], which allows the transition from the compression area to the tension area and vice versa (Figure 3).

As an example, suppose that from the very beginning there is an active loading in the tension area of the unit volume of concrete – the OP path. Elastic unloading occurs at the point P (the PA path), which then transfers into an active loading in the compression area (the AC´P´ path). The residual strains are calculated at the point A, the origin of the $\sigma - \varepsilon$ diagram is transferred to the point A, and the analysis of the active loading in the compression area begins (the AC´P´ path). The current strain is determined as $\varepsilon - \varepsilon_A$, where ε_A is the residual strain in the point A. It is assumed that concrete with cracks caused by tension can take compressive loads without any damage. Therefore we assume that $\sigma_{C'} = \sigma_C$. Elastic unloading begins at the point P´ (the P´A´ path), the residual strains are determined again at the point A´, the origin of the $\sigma - \varepsilon$ diagram is transferred to this point, and the active loading in the tension area begins. The strains are determined as $\varepsilon - \varepsilon_{A'}$. There are cracks in the tension area of concrete, which formed during the loading stage OP, therefore the stress level is limited by the residual concrete strength $\alpha'\sigma_t$.

The behavior of the reinforcement is also described by the relations of the deformation theory of plasticity formulated in terms of residual strains, and a symmetric bilinear diagram $\sigma - \varepsilon$ with a small hardening is assumed. We denote as E_s the elastic modulus for steel.

2.2. Integration of the Nonlinear Equations of Motion

The problem is solved in three stages. First, a nonlinear static problem is solved for the entire original structure

$$N'\left(\mathbf{u}_0'\right) = \mathbf{f}_{stat}', \tag{1}$$

where $\mathbf{u}_0'$ is a displacement vector corresponding to the solution of the static problem, $N'\left(\mathbf{u}_0'\right)$ is a nonlinear operator that returns the vector of internal forces of the system, $\mathbf{f}_{stat}'$ is the static load, which includes dead and constant live load for the original system.

Second, one of the columns of the first floor is removed, and its action is replaced by the reaction vector $\mathbf{f}_{dyn}$, which is determined by solving the problem (1):

$$N\left(\mathbf{u}_0\right) = \mathbf{f}_{stat} + \mathbf{f}_{dyn}. \tag{2}$$

All the loads here are applied statically, varying in proportion to the same parameter. Removing the column changes the design model, therefore, at the first stage, the values in the equation (1) are written with a prime. As a result, we obtain the stress-strain state of the considered structure equivalent to that obtained in the first stage before removing the column.

Third, the column is suddenly removed ($\mathbf{f}_{dyn} = 0$ when $t \geq t^*$, t is a current time and t^* is a moment when given column is removed) and we obtain a Cauchy problem with inhomogeneous initial conditions defined in the second stage:

$$\begin{cases} \mathbf{M}\ddot{\mathbf{u}} + \mathbf{C}\dot{\mathbf{u}} + N\left(\mathbf{u}\right) = \mathbf{f}_{stat} + \mathbf{f}_{dyn} \\ \mathbf{u}\left(0\right) = \mathbf{u}_0\ ,\ \dot{\mathbf{u}}\left(0\right) = 0 \end{cases}, \tag{3}$$

where $\mathbf{M}$ and $\mathbf{C}$ are mass and dissipation matrices respectively. Proportional damping is used in this paper $\mathbf{C} = \alpha\mathbf{M} + \beta\mathbf{K}_t(\mathbf{u})$, where $\mathbf{K}_t(\mathbf{u}) = \partial N(\mathbf{u})/\partial\mathbf{u}$ is the tangent stiffness matrix. The problem (3) is solved by the method presented in [32, 36]. Thus, the problem of progressive collapse is reduced to the integration of nonlinear equations of motion (3) with inhomogeneous initial conditions.

The presented approach is a special case of a more general method [37], which is used for seismic analysis of structures.

3. Numerical Results and Discussion

Two design models of the structure are considered. The first model (model A) corresponds to a traditional design of a multistorey building which is widely used. The second design model (model B) entails the introduction of a special outrigger storey with elements of high stiffness into the load-bearing system of the building (is shown in red in Figure 4) which must stop the propagation of destructions. After the failure of a vertical load-bearing structure (column) in the lower floor of the building, the outrigger storey structures provide suspension of the entire system of vertical load-bearing elements located above the failed column.

The principle of using outrigger structures as elements ensuring the stability of load-bearing systems in the event of failure of structures in the lower floors was proposed at the beginning of the 21st century and is used in the Russian Federation, Ukraine, Belarus and others countries.

However, even with the widespread use of outrigger structures in the design and construction of reinforced concrete buildings, there is currently no detailed reliability substantiation of such structures, taking into account the nonlinear behavior of reinforced concrete under dynamic loading caused by the sudden failure of a local load-bearing structure.

The design model A is obtained from the design model B by removing the reinforcement of the outrigger storey shown in red. The accidental situation is simulated by removing a corner column of the first floor.

The pitch between the columns in the direction OX and OY is 6 m, and the height of the storey is 3 m.

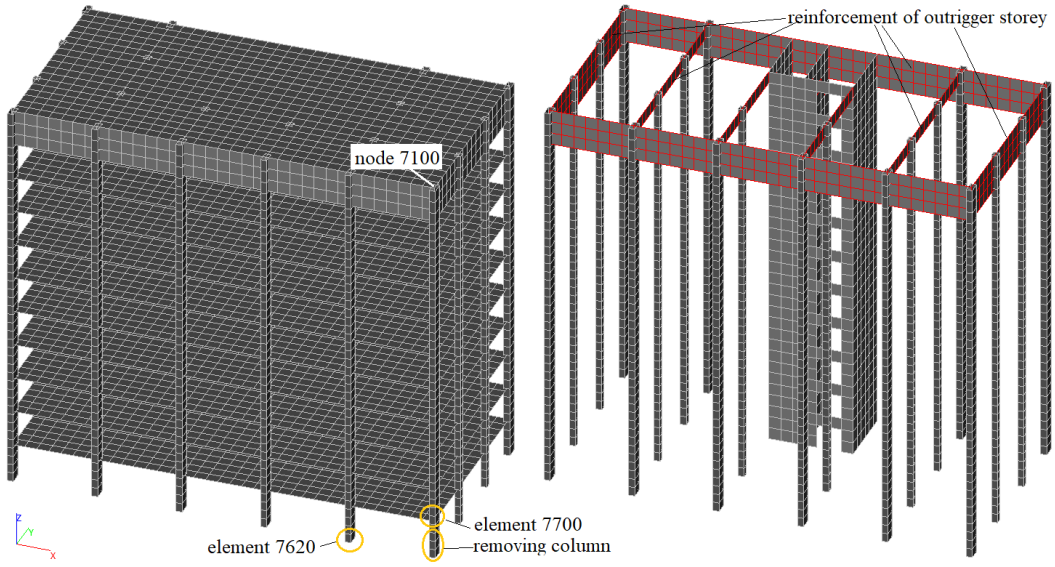

Figure 4. Design model B of a multistorey building with an outrigger storey.

Figure 5 shows the middle column cross-section, and Figure 6 shows the edge column cross-section, the parameter μ denotes the reinforcement ratio. They also show the triangulation mesh necessary for the numerical integration over the volume of the bar finite element to track zones of plasticity, and to calculate the stress and strain tensor components at the centers of gravity of the triangles [32, 35]. 200 mm thick walls are reinforced with Ø22 mm rebar with a spacing of 100 mm, $z_{s1} = z_{s3}$ = 84 mm (vertical reinforcement) and $z_{s2} = z_{s4}$ = 62 mm (horizontal reinforcement) – see Figure 1. The reinforcement ratio both in the vertical and horizontal direction is 2.0%. 200 mm thick floor slabs are reinforced with Ø10 mm rebar with a spacing of 100 mm, $z_{s1} = z_{s3}$ = 90 mm (reinforcement in the direction of the *OX* axis), $z_{s2} = z_{s4}$ = 80 mm (reinforcement in the direction of the *OY* axis). The reinforcement ratio is $\mu_x = \mu_y$ = 0.3%.

The following properties are assumed for concrete: E = 30 018 MPa, ν = 0.2, σ_c = 18.5 MPa, σ_t = 1.55 MPa, ξ = 20 (see Section 2 and Figure 3), and for steel – E_s = 200 000 MPa, ν = 0.3, σ_y = 400 MPa. Here ν is the Poisson's ratio and σ_y is yield stress for steel.

Dissipation parameters α = 0.34 and β = 0.0038 correspond to the modal damping ξ_1 = 0.05 and ξ_2 = 0.1 from the critical value for the frequencies ω_1 = 4 sec^{-1} and ω_2 = 50 sec^{-1}.

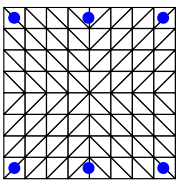

Figure 5. The middle column 50×50 cm, 6Ø32 mm, μ = 1.93 %

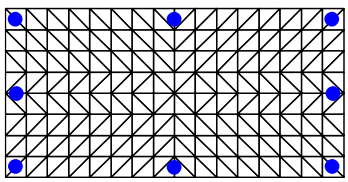

Figure 6. The edge column 100×50 cm, 8Ø40mm, μ = 2.01 %

Figure 7 shows the deformation patterns of models A (left) and B (right), obtained as a result of elasto-plastic (a, b) and elastic (c, d) analysis. Since the displacements of the structural fragment over removed column resulting from the use of nonlinear analysis increase indefinitely in time, and the displacements in linear analysis remain limited in time (Figure 8), displacement scale in Figure 7.c is much

more than displacement scale in Figure 7.a. The deformation schemes of both model A and model B obtained using both linear and nonlinear analysis are generally similar. However, the elasto-plastic analysis of model A shows that the displacements of the structural fragment above the remote column increase unlimitedly (Figure 8, b), which indicates collapse. The analysis was interrupted at a time of 2.4 seconds when the vertical displacement of the node above the remote column reached 9 m. Unlike nonlinear analysis, linear analysis cannot naturally establish the fact of destruction – Figure 8, a. When performing linear analysis, hereinafter, the same approach is used as for nonlinear analysis, but a linear diagram $\sigma - \varepsilon$ is set for both concrete and reinforcement. The exception is the classical linear analysis, which uses finite elements that do not take into account the presence of reinforcement, and concrete is considered as a linear elastic material.

An analysis of the displacements of Model B (Figure 9) confirms the effectiveness of using outrigger structures. The results of the linear analysis do not allow to fully confirm the effectiveness of the reinforcement of the supporting system using the outrigger storey, since the stresses in concrete and reinforcement reach such high values that linear methods of strength analysis become inapplicable. Moreover, the classical linear analysis does not take into account the presence of reinforcement in the finite element, which does not provide even a conservative result of the calculation analysis, which, with the necessary restrictions, could be considered acceptable. Therefore, it is of undoubted interest to compare the results of direct dynamic calculations of model B with the outrigger, performed in a linear and physically nonlinear formulation. The removal of the corner column occurs at time t^* = 0.05 s. If the initial conditions obtained from the solution of the static problem (2) correspond to the given load of the Cauchy problem (3), then the sudden application of all the forces of the problem (2) should not cause oscillations until the column is removed, which is confirmed by the results shown in Figures 9, 10.

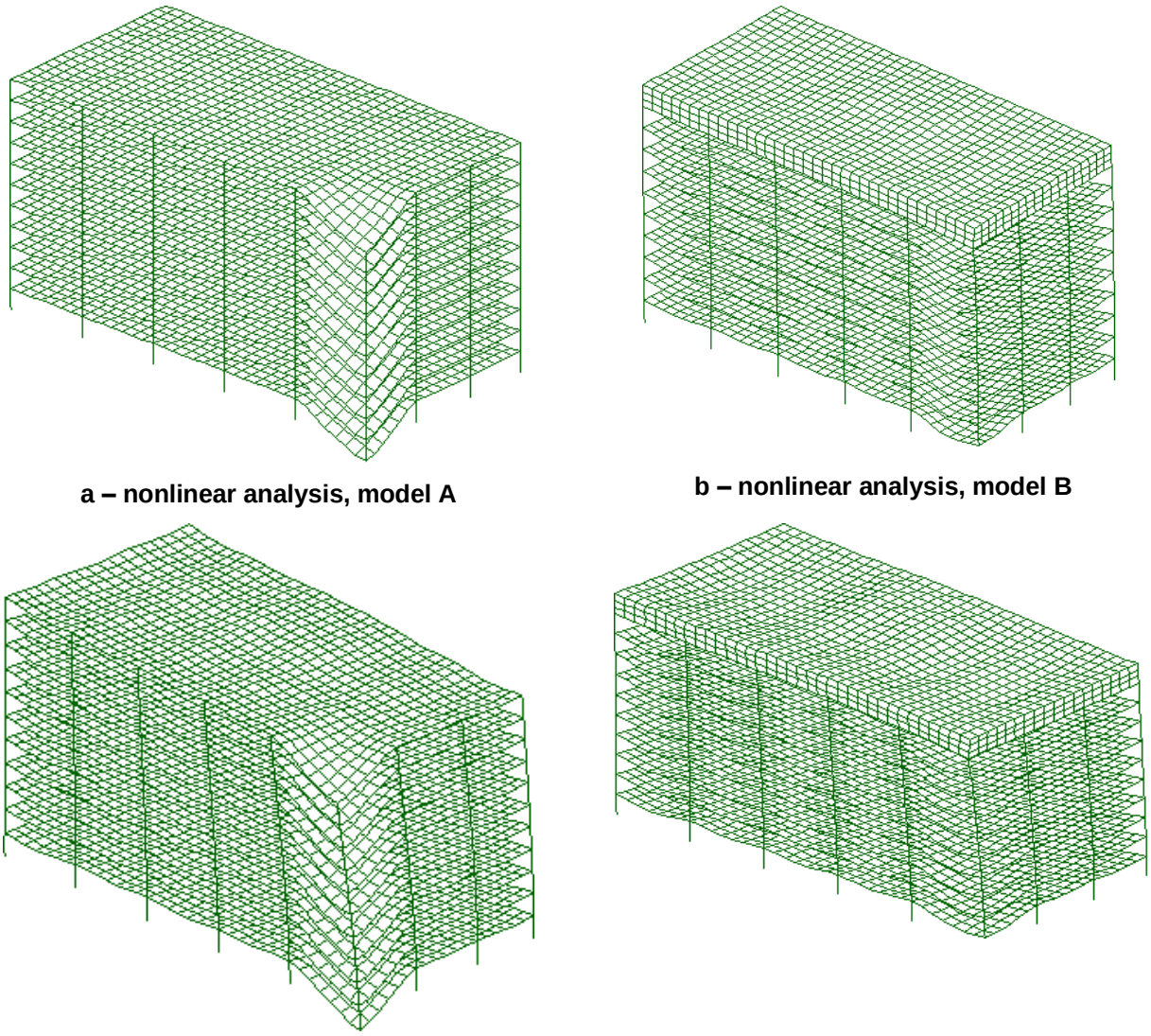

a – nonlinear analysis, model A

b – nonlinear analysis, model B

c – linear analysis, model A

d – linear analysis, model B

Figure 7. The deformed shape after removing of corner column (a – nonlinear analysis, model A; b – nonlinear analysis, model B; c – linear analysis, model A; d – linear analysis, model B).

A comparison of the linear and nonlinear analysis of model B shows:

- the deformation pattern at the initial stage is almost identical, but the magnitude of the extreme displacements is significantly different (Figure 9) 0.0216 m (elasto-plastic analysis) and 0.0123 m (linear analysis);
- the peak value of the longitudinal force in the nearest surviving column (finite element 7620), obtained as a result of nonlinear dynamic analysis, is 24 % less than the corresponding value obtained as a result of linear analysis (Figure 10).
- bearing system behavior after removal of the corner column is oscillatory (Figure 9, 10);
- the displacements obtained with using elasto-plastic analysis turned out to be much larger than the displacements of the elastic analysis, and the period of the fundamental mode for the nonlinear design model is also significantly longer than for elastic;
- the damping of the elasto-plastic design model due to its dissipative nature with the same viscous friction parameters turned out to be much larger than the damping of the elastic model;
- the w 7100 linear static and N 7620 linear static curves (Figure 9, 10) are given to show how much the displacements and efforts of the linear solution of the static problem with the classical approach that does not take into account the presence of reinforcement in concrete differ from the solution of the elasto-plastic dynamic problem in the proposed formulation since traditional methods based on dynamic amplification factors rely on the solution of the linear static problem;
- the dependence of the longitudinal force on time in the finite element 7700 (Figure 4) over the remote column for linear and nonlinear analysis turned out to be close (Figure 11) – the longitudinal force reaches its maximum for a short time interval (0.01 ÷ 0.015 sec), after which its value stabilizes.

Thus, the presented method of elasto-plastic analysis is an effective numerical approach that allows one to identify the features of stress-strain states of reinforced concrete bearing systems, taking into account dynamic effects.

A detailed design analysis using the direct integration of the equations of motion based on the nonlinear behaviour of reinforced concrete structures allowed us to confirm the effectiveness of outrigger storeys as special structures that prevent the progressive collapse of the load-bearing system. The developed method allows performing the analysis of other types of structures designed to protect the load-bearing system in the event of instantaneous failures of vertical load-bearing elements.

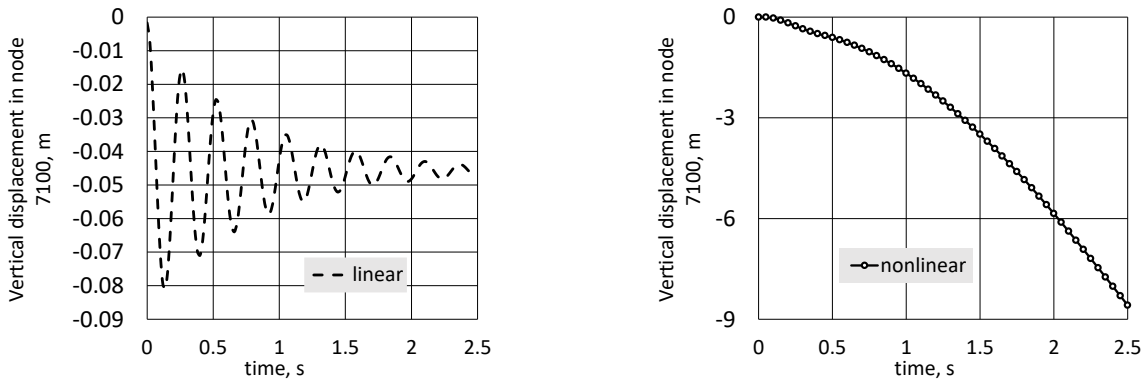

a – linear analysis **b – nonlinear analysis**

Figure 8. Model A. The vertical displacement in node 7100 (a – linear analysis; b – nonlinear analysis)

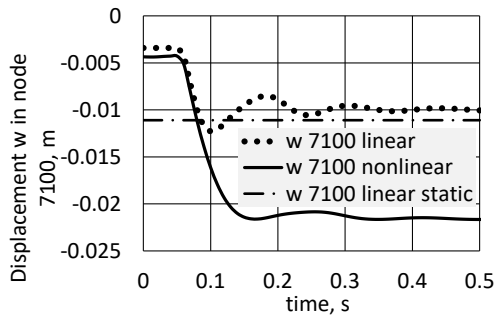

Figure 9. Model B. The vertical displacement in node 7100. Comparison of linear and nonlinear solutions.

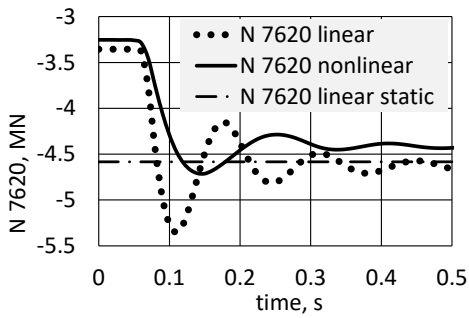

Figure 10. Model B. The longitudinal force in finite element 7620. Comparison of linear and nonlinear solutions.

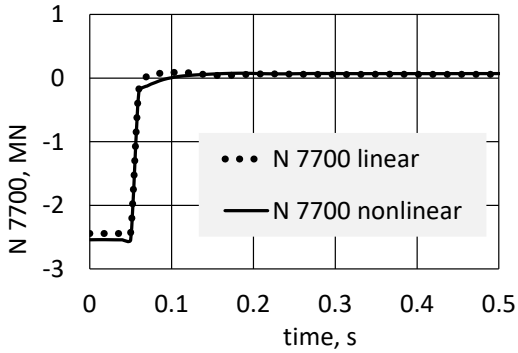

Figure 11. Model B. The longitudinal force in finite element 7700. Comparison of linear and nonlinear solutions.

Discussion. This article presents the results of elasto-plastic dynamic analysis of spatial structure, performed in the accepted formulation of the task of progressive destruction. We have not been able to find any literary source in which, in such a formulation, a large-scale problem for the entire design model would be solved. We know of a few works (for example, [9]), where, in a different formulation (a contact explosion was considered), the dynamic behavior of the entire structure was simulated taking into account the elasto-plastic deformation of its elements. Unfortunately, in the above-mentioned works, data on the impact models or on other parameters of the computational model are not fully presented, which makes it impossible to directly compare our results with the results presented in them. Therefore, the validation of the reliability of the results obtained in this research is based on the solution of individual test problems (benchmarks), producing a comparison of the numerical results obtained by the proposed method with the results of qualitatively performed experiments or high-precision numerical solutions that we trust [32–35, 37].

In a number of works, for individual structural elements, experimental studies on the deformation and destruction of reinforced concrete structures under conditions of support failure have been carried out. However, we are not aware of the publication of the results of experimental studies devoted to the behavior of the supporting system as a whole under conditions of local failure of the supporting structures. Thus, the assessment of the consistency of the results obtained in this work is based on comparison with the results of the general engineering assessment of the consequences of emergency situations associated with structural failures. Analysis of these materials – photographs, descriptions of accidents, etc. - show that the result obtained by us corresponds, in general, to the actual scheme of deformation and damage of reinforced concrete structures under conditions of failure of the supporting elements.

4. Conclusions

Accounting for the dynamic nature of the removal of structural elements allows to perform numerical modeling without using artificially introduced dynamic amplification factors. Taking into account the elasto-plastic properties of the material and the degradation of concrete during cracking leads to a significant increase in displacements and a slight decrease in forces in the structural elements compared to the linear dynamic analysis.

The results of the performed studies demonstrate the effectiveness of the analysis of an entire load-bearing system using the direct integration of the equations of motion taking into account the nonlinear behavior of reinforced concrete. The obtained results also allow to formulate approaches to the justification of deformation criteria for their further use in developing simplified calculation methods for mass application.

References

1. McKay, A. Alternate path method in progressive collapse analysis: Variation of dynamic and non-linear load increase factors. Thesis presented to the graduate faculty of The University of Texas at San Antonio. 2008.
2. Marchand, K., McKay, A., Stevens, D. Development and application of linear and nonlinear static approaches in UFC 4-023-03. Structures Congress 2009. Austin. Texas. April 30-May 2. 2009.
3. Liu, M. A new dynamic increase factor for nonlinear static alternate path analysis of building frames against progressive collapse. Engineering Structures. 2013. Vol. 48. Pp. 666–673.
4. Li, Y., Lu, X., Guan, H., Ye, L. An energy-based assessment on dynamic amplification factor for linear static analysis in progressive collapse design of ductile RC frame structures. Advances in Structural Engineering. 2014. Vol. 17. No. 8. Pp. 1217–1226.
5. Tsai, M.H. Assessment of analytical load and dynamic increase factors for progressive collapse analysis of building frames. Advances in Structural Engineering. 2012. Vol. 15. No. 1. Pp. 41–54.
6. Saffari, H., Mashhadi, J. Assessment of dynamic increase factor for progressive collapse analysis of RC structures. Engineering Failure Analysis. 2018. Vol. 84. Pp. 300–310 https://doi.org/10.1016/j.engfailanal. 2017.11.011.
7. Marjanishvili, S., Agnew, E. Comparison of various procedures for progressive collapse analysis. Journal of Performance of Constructed Facilities. 2006. Vol. 20. No. 4. Pp. 365–374.
8. Perelmuter, A.V., Kabantsev, O.V. About the Problem of Analysis Resistance Bearing Systems in Failure of a Structural Element. International Journal for Computational Civil and Structural Engineering. 2018. Vol. 14. No 3. Pp. 103–113.

9. Yu, J., Rinder, T., Stolz, A., Tan, K.-H. Dynamic Progressive Collapse of an RC Assemblage Induced by Contact Detonation. Journal of Structural Engineering. 2014. Vol. 140. No. 6. https://ascelibrary.org/doi/pdf/10.1061/%28ASCE%29ST.1943-541X.0000959.
10. Pham, A., Tan, K., Yu, J. Numerical investigations on static and dynamic responses of reinforced concrete sub-assemblages under progressive collapse. Engineering Structures. 2016. No. 10. Pp. 1016–1028.
11. Tian, L.-M., Wei, J.-P., Hao, J.-P., Wang, X.-T. Dynamic analysis method for the progressive collapse of long-span spatial grid structures. Steel and Composite Structures. 2017. 23(4). Pp. 435–444. DOI: 10.12989/scs.2017.23.4.435.
12. Wang, T., Zhang, L., Zhao, H., Chen, Q. Analysis on Dynamic Response of Reinforced Concrete Frame for Resisting Progressive Collapse. The Open Construction & Building Technology Journal. 2019. Vol. 13. Pp. 27–38.
13. Kabantsev, O.V., Mitrovich, B. Deformation and power characteristics monolithic reinforced concrete bearing systems in the mode of progressive collapse. VI International Scientific Conference Integration. Partnership and Innovation in Construction Science and Education (IPICSE-2018). MATEC Web Conf.. 2018. Vol. 251. Pp. 1–8. https://doi.org/10.1051/matecconf/201825102047.
14. Kabantsev, O.V., Mitrovich, B. Justification of the special limit state characteristics for monolithic reinforced concrete bearing systems in the progressive collapse mode. IOP Conference Series: Materials Science and Engineering. 2018. Vol. 456. Pp. 1–7. http://iopscience.iop.org/issue/1757-899X/456/1.
15. Geniyev, G.A., Kissyuk, V.N., Tyupin, G.A. Teoriya plastichnosti betona i zhelezobetona [The theory of plasticity of concrete and reinforced concrete]. Moskva: Stroyizdat. 1974. (rus)
16. Bathe, K.J., Walczak, J., Welch, A., Mistry, N. Nonlinear analysis of concrete structures. Computers & Structures. 32. 1989. Pp. 563–590.
17. De Borst, R., Bicanic, N. A note on singularity indicators for Mohr Coulomb type yield criteria. Computers & Structures. 1991. 39. Pp. 219–220. doi: 10.1016/0045-7949(91)90089-5.
18. Bažant, Z. P., Belytschko, T., Chang, T. Continuum theory for strain softening. J. Eng. Mech.. 1984. 110. 12. Pp. 1666–1692.
19. Bažant, Z.P., Pijaudier-Cabot, G. Nonlocal continuum damage. localization instability and convergence. J. Appl. Mech. 1988. 55. 2. Pp. 287–293.
20. Jiràsek, M. Mathematical analysis of strain localization. Rev. Eur. Genie Civil. 2007. 11. 7. Pp. 977–991. DOI: 10.1080/17747120.2007.9692973.
21. Jiang, J.-F., Wu, Y.-F. Identification of material parameters for Drucker-Prager plasticity model for FRP confined circular concrete columns. International Journal of Solids and Structures. 49. 2012. Pp. 445–456. DOI: 10.1016/j.ijsolstr.2011.10.002.
22. Ju, M.H., Li. J.C. Computational plasticity. With emphasis on the application of the unified strength theory. Springer and ZJU Press. London. New York. 2012.
23. Zhang, J., Zhang, Z., Chen, C. Yield criterion plastic-damage models for concrete. Acta Mechanica Solida Sinica. 2010. 23. 3. Pp. 220–230. https://doi.org/10.1016/S0894-9166(10)60024-9 .
24. Kayhan, E. Application of viscous and non-local integral type regularization schemes for softening plasticity. Master's thesis. Manufacturing Engineering Atilim University. 2009.
25. Pietruszczak, S., Mroz, Z. Finite element analysis of deformation of strain-softening materials. Int. J. Numer. Methods Eng. 1981. 17. 3. Pp. 327 – 334. DOI: 10.1002/nme.1620170303.
26. Jouan, G., Kotronis, P., Collin, F. Using a second gradient model to simulate the behavior of concrete structural elements. Finite Elements in Analysis and Design. 2014. 90. Pp. 50 – 60. DOI: 10.1016/j.finel.2014.06.002 .
27. Criesfield, M.A. Non-linear finite element analysis for solids and structures. Volume 2: Advanced topics. John Wiley & Sons Ltd. Chichester New York. 2000.
28. Karpenko, N.I. Teoriya deformirovaniya zhelezobetona s treshchinami [The theory of deformation of reinforced concrete with cracks]. Moskva: Stroyizdat. 1976. (rus)
29. Sukumar, N., Moes, N., Mora, B., Belytschko, T. Extended finite element method for three-dimensional crack modelling. Int. J. Numer. Meth. Engng. 2000. 48. Pp. 1549–1570. DOI: 10.1002/1097-0207(20000820)48:11<1549::AID-NME955>3.0.CO;2-A .
30. Belytschko, T., Rabczuk, T. Application of particle methods to static fracture of reinforced concrete structures. International journal of fracture. 2006. 137. Pp. 19–49.
31. Li J., Hao H. Numerical study of structural progressive collapse using substructure technique. Engineering Structures. 2013. 52. Pp. 101–113. URL http://dx.doi.org/10.1016/j.engstruct.2013.02.016
32. Fialko S.Yu. Primeneniye metoda konechnykh elementov k analizu prochnosti i nesushchey sposobnosti tonkostennykh zhelezobetonnykh konstruktsiy s uchetom fizicheskoy nelineynosti [Application of the finite element method to the analysis of strength and bearing capacity of thin reinforced concrete structures taking into account physical nonlinearity]. Moskva: Izdatelskiy dom ASV, izdatelstvo SCAD SOFT. 2018. (rus)
33. Fialko, S. Quadrilateral finite element for analysis of reinforced concrete floor slabs and foundation plates. Applied Mechanics and Materials. 2015. 725-726. Pp. 820–835. DOI: 10.4028/www.scientific.net/AMM.725-726.820 .
34. Fialko, S., Karpilovskyi, V. Triangular and quadrilateral flat shell finite elements for nonlinear analysis of thin-walled reinforced concrete structures in SCAD software. In W. Pietraszkiewicz & W. Witkowski (Eds.). Shell structures: theory and applications . vol. 4. chapter 83. Pp. 367–370. CRC Press Taylor & Francis Group. London. New York. 2017. DOI: 10.1201/9781315166605-83
35. Fialko, S., Karpilovskyi, V. Spatial thin-walled reinforced concrete structures taking into account physical nonlinearity in SCAD software. Rod finite element. Proceedings of 13th International Conference MODERN BUILDING MATERIALS. STRUCTURES AND TECHNIQUES. 16–17 May 2019. Vilnius. Lithuania eISSN 2029-9915 Vilnius Gediminas Technical University. eISBN 978-609-476-197-3. Pp. 728–735. URL https://www.vgtu.lt/civil-engineering/research-and-innovation/scientific-conferences/modern-building-materials-structures-and-techniques/proceedings/mbmst-2019/314765 . (Last access: 06.02.2020).
36. Hughes, T.J.R., Belytschko, T. Nonlinear finite element analysis. Course Notes. Sept. 4–8. 1995. (Munich. Germany).
37. Fialko, S.Yu. Dynamic analysis of the elasto-plastic behaviour of buildings and structures in the SCAD++ software package. IOP Conf. Series: Journal of Physics: Conf. Series. 2020. 1425 012041. Pp.1–10. DOI: 10.1088/1742-6596/1425/1/012041.

Contacts:

Sergiy Fialko, sfialko@riad.pk.edu.pl
Oleg Kabantsev, ovk531@gmail.com
Anatoly Perelmuter, anatolyperelmuter@gmail.com

© Fialko, S.Yu.,Kabantsev, O.V.,Perelmuter, A.V., 2021

Magazine of Civil Engineering

ISSN 2712-8172

journal homepage: http://engstroy.spbstu.ru/

DOI: 10.34910/MCE.102.15

Dynamic response of structures located in near-field and far-field regions using IDA and MIDA

H.R. Mehdipanah, N. Fanaie*
K.N. Toosi University of Technology, Tehran, Iran
**E-mail: fanaie@kntu.ac.ir*

Keywords: modal incremental dynamic analysis (MIDA), incremental dynamic analysis (IDA), 3D model, irregularity in plan, near-field, far-field

Abstract. In the current research project, an effort is made so as to investigate the capability of the innovative Modal Incremental Dynamic Analysis (MIDA) method considering 3D structural models, the effect of plan irregularities and near-field earthquake records. Therefore, to fulfil this goal, 10 near-field earthquake records in one principal direction of structures as well as 10 far-field earthquake records in two principal directions of structures are applied to 12 structures with 6, 12 and 18-storeys, and 10 %, 20 %, 30 % and 40 % plan irregularities. The study of these parameters reveals that in geometrically regular 3D structures, this innovative method meets all seismic demands parameters just as the IDA method does. Furthermore, it concludes that MIDA method is not capable of obtaining the exact IDA curves in low-rise and medium-rise structures located in near-field regions since it results in noticeable errors. Finally, it is essential to improve the MIDA approach for near-field earthquake records by replacing the drift criterion utilized in this method with a more accurate drift criterion.

1. Introduction

Owing to severe earthquakes, analytical methods for evaluating the capacity of structures have dramatically changed over the years. As a result of exposure to severe earthquakes, structural elements exceed the yield point and enter into the plastic region. To better understand the dynamic behavior of structures, researchers need to evaluate the demand and capacity parameters accurately. For a long time, the behavior of structures had been studied through linear analysis, but this method has its own drawbacks such as overlooking the effect of higher modes and not being dynamic, to name but a few, which results in the structures being overdesigned. Due to special patterns of pushing such as uniform and mode shape based patterns, this method is not capable of meeting the exact demands of structures, when subjected to earthquakes. This problem caused all researchers to accept that nonlinear dynamic “Time-History” analysis can show the realistic behavior of structures. The merit of pushover analysis is that all stages from elastic to plastic behavior of the elements, which leads to instability of structure in the final stage, are monitored. On the other hand, nonlinear time-history dynamic analysis has showed the realistic behavior of structures. As a result, Incremental Dynamic Analysis, which was built based on the clusters of a large number of “Time History” analyses, was invented by Bertero [1]. This method simultaneously combined the advantages of both pushover and nonlinear time-history dynamic analyses. The structures were exposed to different scaled levels of Time-History earthquake records to observe elastic and plastic behavior as well as instability of all structural elements. Therefore, the structure’s capacity is determined in different scaled levels. After Bertero, researchers, including Nassar and Krawinkler [2], Bazzurro and Cornell [3], Sameh Samir Mehanny and Gregory G. Deierlein [4], Gutpa and Kunnath [5] followed him; and in 2002, Vamvatsikos and Cornell [6] carried out invaluable survey on IDA method.

IDA is one of the most accurate methods for evaluating the dynamic behavior of structures. This method has been used by many researchers [7–9]. However, one of the worst drawbacks of this method is that it is time-consuming. For years, this has been a huge problem for researchers. From 1970 to 2000’s there was a dire need for developing a new method to tackle this problem. Therefore, a numerical method named Modal

Mehdipanah, H.R., Fanaie, N. Dynamic response of structures located in near-field and far-field regions using IDA and MIDA. Magazine of Civil Engineering. 2021. 102(2). Article No. 10215. DOI: 10.34910/MCE.102.15

This work is licensed under a CC BY-NC 4.0

Incremental Dynamic Analysis (MIDA) capable of obtaining capacity and demand curves in less time than IDA emerged.

First attempt for solving problems was carried out by Vamvatsikos and Cornell in 2005 [6]. Zarfam and Mofid and Raiesi Fard in 2005 [10] proposed an approximate method named modal incremental nonlinear dynamic analysis. Han and Chopra in 2006 [11], offered a method, which was working on modal pushover based on IDA method. An innovative idea for estimating pushover curves based on error distribution was introduced by Mofid and Zarfam in 2008 [12]. Furthermore, the total input energy applied to SDOF oscillator was used as intensity measure to impose different levels of scaled earthquakes [12]. In another attempt in 2011, Zarfam and Mofid modified this method for those structures in which the elements' materials do not comply with bilinear behavior [13]. In the mentioned field, according to the study done by Jalilkhani and Manafpour, the method proposed by Shafei et al. [14] can confidently be employed as an efficient analysis tool for estimating the median seismic collapse capacity of RC frames [15]. As a last attempt, Mofid et al. modified MIDA in 2017 to investigate the seismic behavior of structures equipped with self-centering viscoelastic damper [16]. In 2017, Incremental Modal Pushover Analysis (IMPA) was proposed by Bergami et al. [17]. They concluded that IMPA approach cannot be considered as an alternative for IDA [17]. In all studies carried out by Mofid et al., they believed that MIDA results were accurate enough [10]. It should be mentioned that all the aforementioned researchers performed their survey on 2D frame using far-field earthquake records [10, 12, 13, 16]. Since real structures are mostly 3D with some irregularities in plan, there is a crucial need to investigate the accuracy of this method on these structures. Since near-field earthquake records feature pulse shape behavior and the frequency content has dramatic impact on the results, it is indispensable to study them.

In this article, the object of research is investigating of MIDA method on 3D models with irregularities in plan. The Subject of this research is dynamic response of these models located in near-field and far-field regions using MIDA Method.

The goal of present work is to investigate the accuracy of MIDA method in comparison to IDA.

2. Methods

Firstly, MIDA method will be reviewed. After that, the modeling and verifications of models will be described. Finally, the procedure of records selection and the way of performing the analysis will be explained.

2.1. Review on MIDA method

In the previous part, it was mentioned that the basic procedure of all surveys was based on the flowcharts presented in 2005 [10] and 2011 [12] by Zarfam and Mofid. This procedure is presented once again herein:

1. Modeling and designing of the structure.
2. Calculating the modes period and participation factor.
3. Performing pushover analysis, and obtaining pushover curve of ith mode.
4. Is there negative hardening in pushover curve? If the answer is negative, construct the bi-linear behavior from obtained pushover curve according to Mofid et al. (2005) [10]; If the answer is positive, construct the trilinear behavior from obtained pushover curve according to Mofid et al. (2011) [12].
5. Modeling a SDOF system as below [10]:
   a. The period of ith mode in multi degree of freedom (MDOF) and SDOF must be even.
   b. The damping of ith mode in MDOF and SDOF must be even.
   c. The yielding strength of ith mode in MDOF and SDOF must have a relation.

$$(F_{yi})_{SDF} = (F_{yi})_{MDF} / (L/M)_i \tag{1}$$

The yielding displacement of ith mode in MDOF and SDOF must have a relation.

$$(D_{yi})_{SDF} = (D_{yi})_{MDF} / [(L/M)_i \phi_{ri}] \tag{2}$$

The strain hardening angle (α) of ith mode in MDOF and SDOF must be even.

$$\alpha_{SDF} = \alpha_{MDF} \tag{3}$$

where F_{yi} is yielding strength of the ith mode of vibration;

D_{yri} is yielding displacement of the roof of the ith mode of vibration;

α is the strain-hardening angle of the material;

ϕ_{ri} is the ith roof mode shape;

And also,

$$L_i = \sum m_j \phi_{ji} \tag{4}$$

$$M_i = \sum m_j \phi_{ji}{}^2 \tag{5}$$

6. Exert n[th] scaled level of earthquake to SDOF system to obtain maximum displacement.

7. Convert the maximum displacement of SDOF to MDOF as mentioned in the work by Zarfam and Mofid (2005) [10].

8. Push MDOF structure to converted maximum displacement and calculate the maximum drift in i[th] mode

9. If the structure is stable, increase one level to scaled level of earthquake, if not, should another mode be considered? If the answer is yes, go to step 1 , If not, go to step 10.

10. Compute the final maximum displacement and maximum drift of applied mode with SRSS method.

11. The MIDA curve is obtained.

2.2. Modeling and the assumptions of the models

In the 2nd type of irregularity mentioned in the table 12.3-1 of ASCE7-10, it is stated that "Reentrant corner irregularity" is defined to exist where both plan projections of the structure beyond a reentrant corner are greater than 15 % of the plan dimension of the structure in the given direction [18]. It means that when $X/L > 0.15$ and $Y/L' > 0.15$ occurred simultaneously, the structure is referred to as irregular. In this article 10 % projection simultaneously in both directions is considered as regular; on the other hand, 20 %, 30 % and 40 % projection in both directions are defined as irregular. In each of the principal directions, three spans with a length of 5 meters were considered. Three types of height, including 6, 12 and 18 stories were considered for the structures. As depicted in Fig. 1, plan of all structures is the same. Moreover, the height of each storey is assumed to be 3 meters, the construction location is in California, USA and the type of soil classification is assumed to be "C". Dead, live, and seismic loading applied to the structures comply with ASCE7.

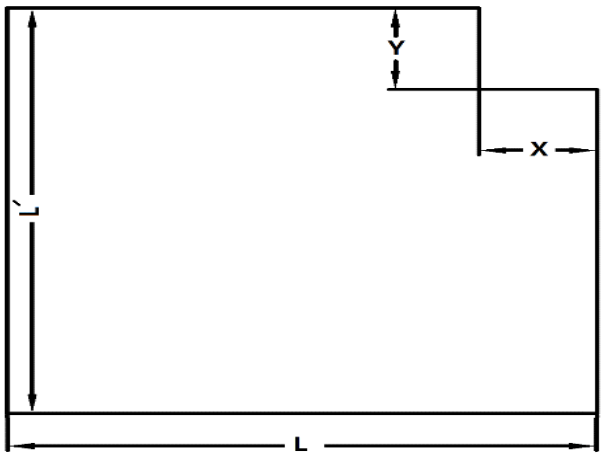

Figure 1. All structure plan.

All 12 structures were designed according to AISC 360-10 [19]. Weak beam-strong column criterion is observed in every single element of structures. All allowable drifts were satisfied in all structures.

Implementing IDA method, all structures need to be modeled in ETABS software and OpenSees. For this purpose, all elements were modeled as nonlinear-beam-column in OpenSees. All cross-sections were constructed by "patch quad" syntax. ST37 in OpenSees were modeled by "Steel02" material behavior. $P-\Delta$ effect was applied in OpenSees by local to global transformation order. All diaphragms and gravity loading were constructed similar to ETABS.

2.3. Verification

In this survey in order to verify the obtained results, two types of verifications were implemented as mentioned below:

2.3.1. Verification with regard to calculated periods

Periods obtained from ETABS and OpenSees must have rational exactness to assure that these two modelings represent the same model. Due to the large number of models, only a few of models have been included in this article. Here, EPeriod is the period obtained from ETABs; and OPeriod is the period obtained from OpenSees.

Table 1. Period verification in 12-story structures.

Irregularity percent	10%				20%			
Mode	EPeriod (s)	OPeriod (s)	Diff (s)	Ratio (%)	EPeriod (s)	OPeriod (s)	Diff(s)	Ratio (%)
1st	1.470	1.383	0.087	5.94	1.292	1.278	0.013	1.04
2nd	1.455	1.339	0.116	7.99	1.254	1.230	0.024	1.88
4th	0.549	0.528	0.021	3.86	0.489	0.495	0.007	1.38
5th	0.545	0.515	0.030	5.51	0.474	0.462	0.011	2.42
7th	0.315	0.309	0.006	1.79	0.276	0.288	0.012	4.33
8th	0.309	0.292	0.017	5.61	0.267	0.264	0.003	1.14
Irregularity percent	30%				40%			
Mode	EPeriod (s)	OPeriod (s)	Diff(s)	Ratio (%)	EPeriod (s)	OPeriod (s)	Diff(s)	Ratio (%)
1st	1.277	1.249	0.027	2.15	1.155	1.127	0.028	2.44
2nd	1.269	1.241	0.028	2.18	1.127	1.111	0.015	1.35
4th	0.487	0.492	0.005	0.94	0.440	0.440	0.000	0.05
5th	0.483	0.483	0.000	0.10	0.434	0.428	0.005	1.19
7th	0.279	0.287	0.007	2.66	0.259	0.265	0.006	2.20
8th	0.278	0.281	0.003	1.12	0.257	0.253	0.003	1.29

Table 2. Period verification in 18-story structures.

Irregularity percent	10%				20%			
Mode	EPeriod (s)	OPeriod (s)	Diff (s)	Ratio (%)	EPeriod (s)	OPeriod (s)	Diff (s)	Ratio (%)
1st	2.181	2.074	0.106	4.88	1.770	1.725	0.045	2.56
2nd	2.164	2.009	0.156	7.20	1.720	1.668	0.052	3.02
4th	0.817	0.834	0.017	2.10	0.637	0.625	0.012	1.91
5th	0.802	0.773	0.029	3.59	0.630	0.603	0.027	4.27
7th	0.478	0.490	0.012	2.40	0.379	0.386	0.007	1.77
8th	0.471	0.460	0.011	2.35	0.372	0.362	0.010	2.71
Irregularity percent	30%				40%			
Mode	EPeriod (s)	OPeriod (s)	Diff (s)	Ratio (%)	EPeriod (s)	OPeriod (s)	Diff(s)	Ratio (%)
1st	1.845	1.839	0.006	0.30	1.752	1.798	0.047	2.65
2nd	1.828	1.815	0.013	0.69	1.695	1.759	0.064	3.79
4th	0.680	0.685	0.004	0.62	0.615	0.620	0.006	0.92
5th	0.678	0.680	0.002	0.33	0.599	0.608	0.009	1.59
7th	0.411	0.417	0.006	1.47	0.363	0.365	0.002	0.65
8th	0.409	0.415	0.006	1.44	0.357	0.356	0.002	0.42

2.3.2. Mode shape verification

To make sure that all the aforementioned 12 structures are accurately built in ETABS, there was a crucial need to verify that all elements were correctly assigned. In period verification, accidental errors may offset each other and make all periods correct, but in essence these structures are different from each other. For this reason, it is essential to implement shape mode verification. By doing this, any mismatches in stiffness or mass in each individual storey would be tackled.

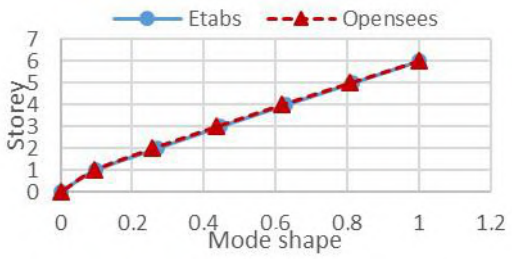

a. Mode shape verification of 6 storey structure with 40% irregularity on the first mode in Y direction

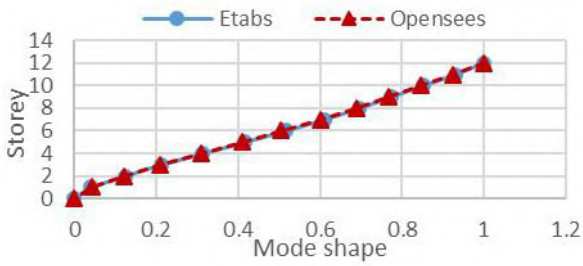

b. Mode shape verification of 12 storey structure with 10% irregularity on the first mode in X direction

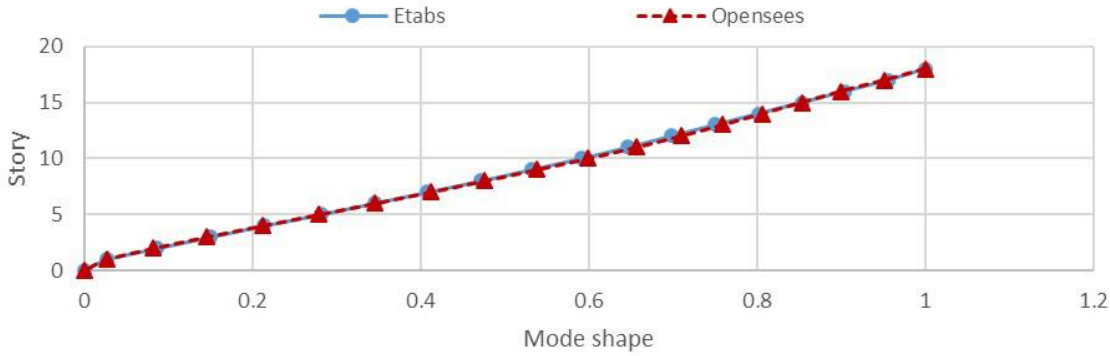

c. Mode shape verification of 18 storey structure with 20% irregularity on the first mode in Y direction

Figure 2. Three samples of mode shapes verifications of structures for better understanding.

Fig. 2(a), (b) and (c) represent overlapping of first mode shape in X direction in 6 storey structure, first mode shape in Y direction in 12 storey structure and first mode shape in Y direction in 18 storey structure, all obtained by ETABS and OpenSees, respectively.

2.4. Record selection

While selecting appropriate records for this study, some recommendations in near-field and far-field region need to be followed.

2.4.1. Selecting near-field records

For selecting near-field records, there are some recommendations provided by FEMA P695, 2009, which is obligatory to comply [20]. These recommendations are outlined below:

1. Soil classification of the records must be the same as the one on which the structures have been modeled.

2. The focal fault mechanism of records must be the same as the one on which the structures have been modeled.

3. The magnitude of records must be equal or higher than 6 Richter to avoid mistakenly selecting an aftershock.

4. Peak ground acceleration must be higher than 0.6g.

5. To select the certifiably near-field records, R_{jb} and R_{rup} must be less than 10 km. R_{jb} is the Joyner-Boore distance which is defined as the closest horizontal distance to the surface projection of the fault plane. Also, R_{rup} is the closest distance to the coseismic rupture plane (km).

6. Pulse behavior should be perceived in velocity versus time graph.

According to the aforementioned recommendations, strike-slip was chosen for focal mechanism and “C” soil type was assumed for selecting records. It should be mentioned that regarding these recommendations, some records were selected from FEMA P695 and the others were obtained from PEER website. The roster of selected records is listed in the following table.

Table 3. Near-field records list.

No.	Earthquake name	Year	Station Name	Mag	Mechanism	R_{jb} (km)	R_{rup} (km)	Vs 30 (m/sec)
1	Morgan Hill	1984	"Coyote Lake Dam - Southwest Abutment"	6.19	strike slip	0.18	0.53	561.43
2	Bam_ Iran	2003	"Bam"	6.6	strike slip	0.05	1.7	487.4
3	Parkfield	1966	Temblor pre-1969	6.19	strike slip	15.96	15.96	527.92
4	San Salvador	1986	"Geotech Investig Center"	5.8	strike slip	2.14	6.3	489.34
5	Mammoth Lakes-06	1980	Long Valley Dam (Upr L Abut)	5.94	strike slip	9.65	16.03	537.16
6	"Chi-Chi_ Taiwan-04"	1999	"CHY074"	6.2	strike slip	6.02	6.2	553.43
7	Coyote Lake	1979	Gilroy Array #6	5.7	strike slip	0.42	3.11	663.31
8	"Parkfield-02_ CA"	2004	"Parkfield - Cholame 3E"	6	strike slip	4.95	5.55	397.36
9	Kocaeli, Turkey	1999	Arcelik	7.51	strike slip	10.56	13.49	523
10	"Darfield_ New Zealand"	2010	"LPCC"	7	strike slip	25.21	25.67	649.67

Records number 1, 4, 5 and 7 are selected from the article of Dimakopoulo et al. (2013) [21]. Record number 3 is selected from Davoodi and Jafari [22]. The other records are selected with the help of recommendation obligated in FEMA P695 [20].

2.4.2. Selecting far-field records

There are also some recommendations for selecting far-field records [20] which are listed below:

1. Soil type of the records must be the same as the one on which structures have been modeled.
2. The focal fault mechanism of records must be the same as the one on which structures have been modeled.
3. To appropriately select the near-field records R_{jb} and R_{rup} must be more than 15 km.

Based on the FEMA P695 recommendations, the far-field records roster is presented in the following table:

Table 4. Far-field records list.

No.	Earthquake Name	Year	Station Name	Mag.	Mechanism	R_{jb} (km)	R_{rup} (km)	Vs30 (m/s)
1	"Big Bear-01"	1992	"Snow Creek"	6.46	strike slip	37.04	38.07	523.59
2	"Tottori_ Japan"	2000	"OKY004"	6.61	strike slip	19.72	19.72	475.8
3	"Darfield_ New Zealand"	2010	"Heathcote Valley Primary School”	7	strike slip	24.36	24.47	422
4	"Victoria_ Mexico"	1980	"Cerro Prieto"	6.33	strike slip	13.8	14.37	471.53
5	"Landers"	1992	"Morongo Valley Fire Station"	7.28	strike slip	17.36	17.36	396.41
6	"Chi-Chi_ Taiwan-04"	1999	"CHY028"	6.2	strike slip	17.63	17.7	542.61

No.	Earthquake Name	Year	Station Name	Mag.	Mechanism	R_{jb} (km)	R_{rup} (km)	Vs30 (m/s)
7	"Chalfant Valley-02"	1986	"Benton"	6.19	strike slip	21.55	21.92	370.94
8	"Joshua Tree_ CA "	1992	"Whitewater Trout Farm"	6.1	strike slip	28.97	29.4	425.02
9	"Imperial Valley-06"	1979	"Cerro Prieto"	6.53	strike slip	15.19	15.19	471.53
10	"Basso Tirreno_ Italy"	1978	"Naso"	6	strike slip	17.15	19.59	620.56

2.5. Performing analysis and obtaining curves

Achieving the purposes of this survey, firstly bilinear curves must be built according to recommendations in part 2. In order to obtain these curves, plastic hinges for performing pushover analysis based on FEMA365 [23] must be assigned to all elements. Then, structures are pushed to the maximum calculated displacement. Subsequently, plastic hinges are formed in beams at first stage; then, plastic hinges at the end of columns, which are rigidly connected to the base, were forged; these two steps of procedure cause structures to be unstable. In all three steps, by monitoring the displacements versus forces, pushover curves were obtained and bilinear curves were built using the procedure discussed in part 2. In this survey, these bilinear curves are specified using the rules of equality of areas above and below the capacity curve of pushover. To solve this problem with good precision, trapezoidal elements were implemented so as to get even areas.

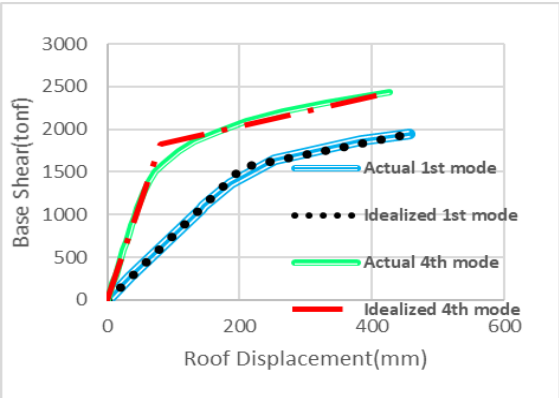

a. 6-storey structure with 20% irregularity

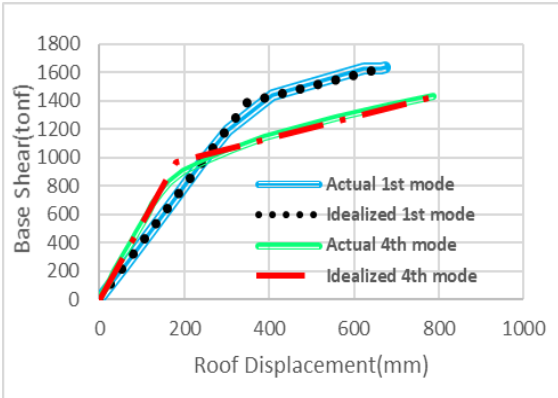

b. 12-storey structure with 10% irregularity

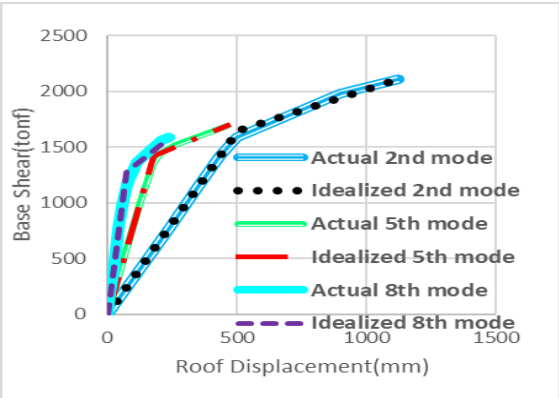

c. 18-storey structure with 20% irregularity

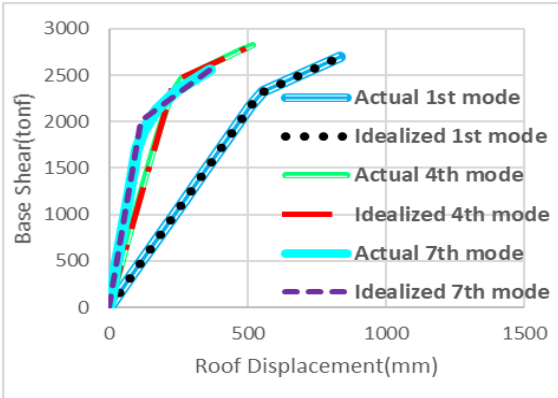

d. 18-storey structure with 40% irregularity

Figure 3. Matching the idealized pushover curve with actual one.

As Fig. 3 illustrates, there is a good conformity between the obtained capacity curves from ETABS and the idealized bilinear graphs revealing that all steps have been correctly employed. Consequently, by utilizing the modal information, these bilinear specifications are converted to the stress-strain diagram for SDOF systems. In the next steps of MIDA, these specifications are exerted for each individual mode of all 12 structures. In addition, all SDOF systems are modeled with complete requirements in OpenSees to perform analysis using near-field and far-field earthquake records. All SDOF systems include one mass and a massless spring, which need to comply with idealized stress-strain diagram specified for individual modes.

Due to the burden of extremely heavy numbers of analyses that need to be performed, the first two transitional modes in each direction for 6 and 12 storey structures are considered. For 18-storey structures, in order to see the effect of higher modes, the first three transitional modes in each direction were considered. All 12 structures are analyzed and subjected to 10 near-field earthquake records in one principal direction and 10 far-field earthquake records in two principal directions. In this survey, maximum displacement should be one of the damage indexes; and the other one, as the procedure dictates, needs to be the maximum roof drift. For better understanding, PGA was selected as intensity index so as to follow the procedure of the pioneers of this method. Then, after performing the analyses, maximum displacement for SDOF system obtained is turned into the maximum displacement of MDOF system to conduct pushover analysis on 3D models by the formulae presented in Zarfam and Mofid article [10]. Then, maximum drifts are obtained as per the procedure presented by Mofid et al. articles [10]; all drifts and displacements obtained from each response to the individual record excitation are gotten SRSS for plotting curves. For IDA and MIDA, 360 analyses were performed individually and respectively.

Due to extremely large number of graphs produced in this survey, the authors have decided to include some of them as well as a few comparison graphs, including graphs of “Morgan Hill” record for near-field region.

3. Results and Discussions

In part 3.1 results with comparison graphs have been presented. In addition, in part 3.2 authors discussed the results.

3.1. Results

Here, the comparison of MIDA and IDA graphs will be presented for far-filed and near field records. In addition, graphs, which demonstrate the effect of structures’ height on MIDA method, will be illustrated at last part.

3.1.1. Comparison of maximum roof displacement and drift versus PGA under near-field records

Because of the extremely large number of graphs that were produced in this survey, the authors have decided to include some of them as well as a few comparison graphs, including graphs of “Morgan Hill” record for near-field region.

3.1.1.1. Comparison of maximum roof displacement and drift versus PGA in “Morgan Hill” record for 6-story structures

Comparison of maximum roof displacement and roof drift versus PGA in “Morgan Hill” record for 6-storey structures with irregularities from 10 % to 40 %.

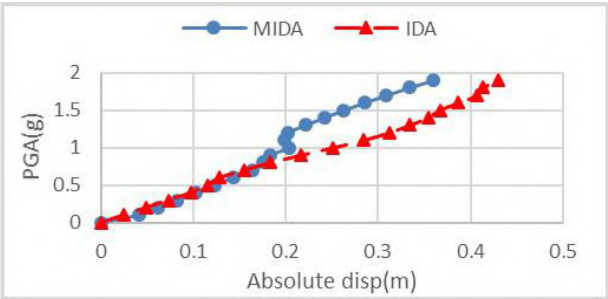

a. with 10% irregularity of plan

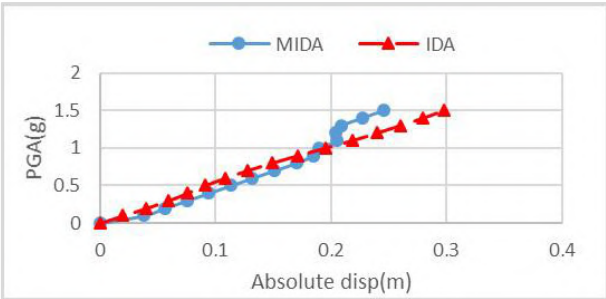

b. with 20% irregularity of plan

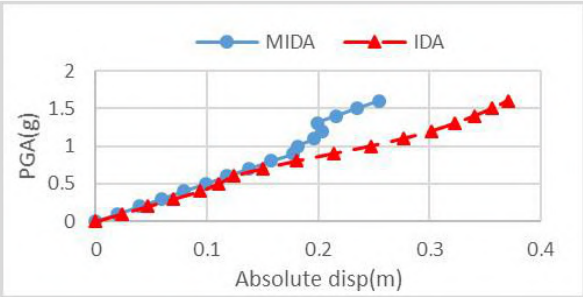

c. with 30% irregularity of plan

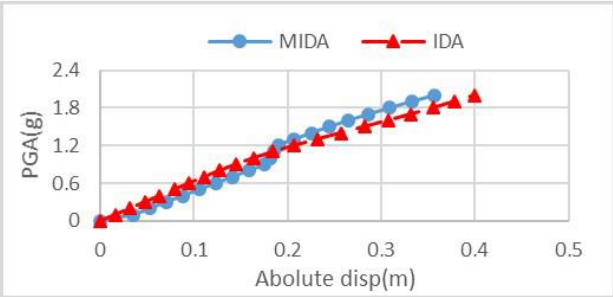

d. with 40% irregularity of plan

Figure 4. Comparison of roof displacement from IDA and MIDA methods in 6-storey structures for record No.1 in near-field records.

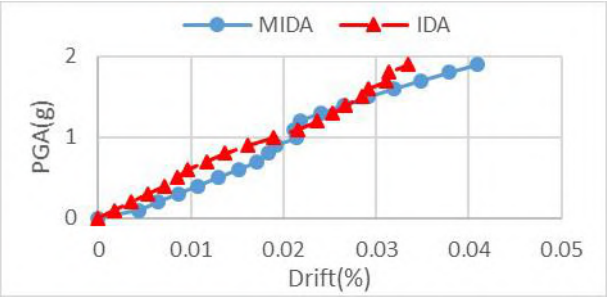

a. with 10% irregularity of plan

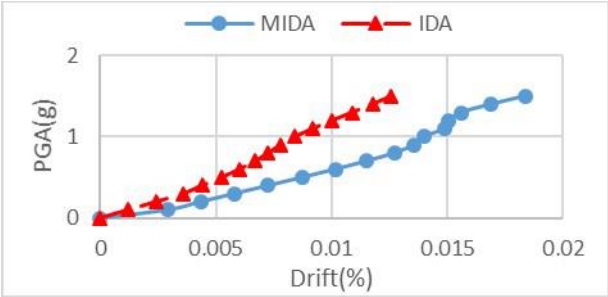

b. with 20% irregularity of plan

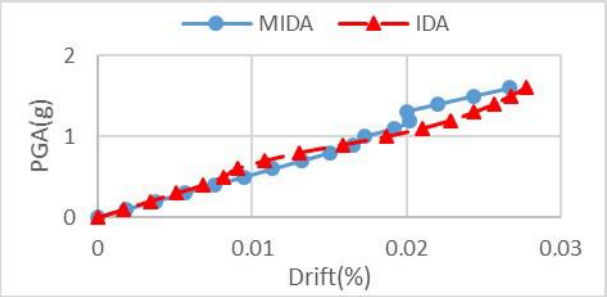

c. with 30% irregularity of plan

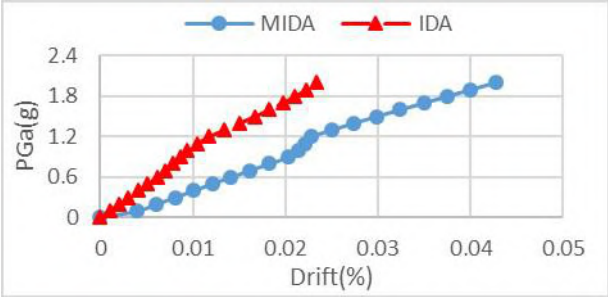

d. with 40% irregularity of plan

Figure 5. Comparison of roof drift from IDA and MIDA methods in 6-storey structures for record No.1 in near filed records.

Comparing the roof displacements obtained from these two methods, it is observed that MIDA is not precise enough in the analysis of low-rise buildings located in near field regions. From the comparison of roof drift in these two methods, it can be concluded that MIDA is not accurate enough in low-rise buildings located in near- field regions neither in elastic region nor in plastic one.

3.1.1.2. Comparison of maximum roof displacement and drift versus PGA in "Morgan Hill" record for 12-storey structures

Comparison of maximum roof displacement and drift versus PGA in "Morgan Hill" record for 12- storey structures with irregularities from 10 % to 40 %.

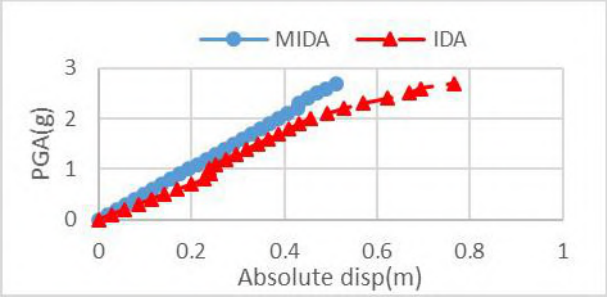

a. with 10% irregularity of plan

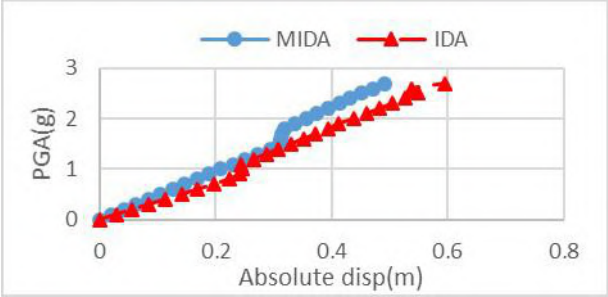

b. with 20% irregularity of plan

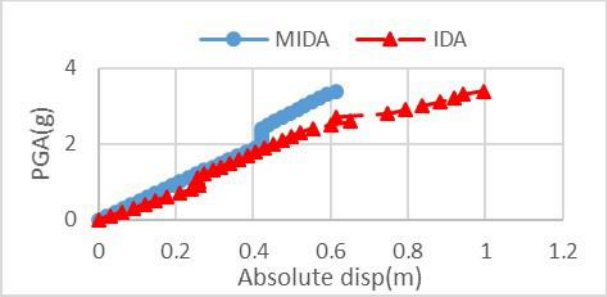

c. with 30% irregularity of plan

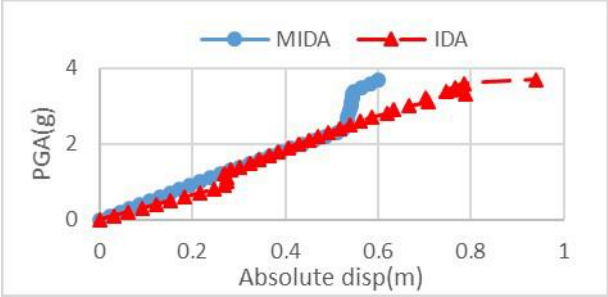

d. with 40% irregularity of plan

Figure 6. Comparison of roof displacement from IDA and MIDA methods in 12-storey structures for record No.1 in near field records.

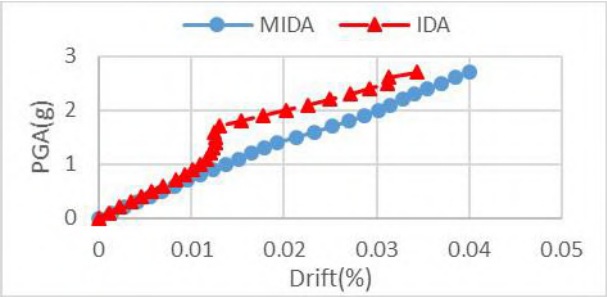

a. with 10% irregularity of plan

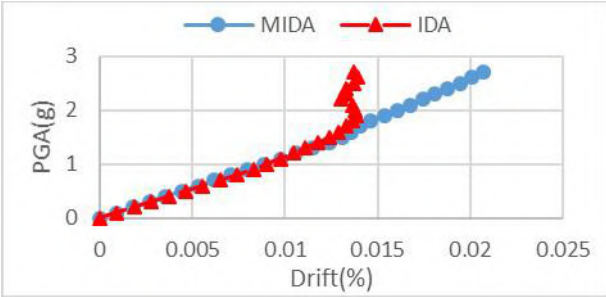

b. with 20% irregularity of plan

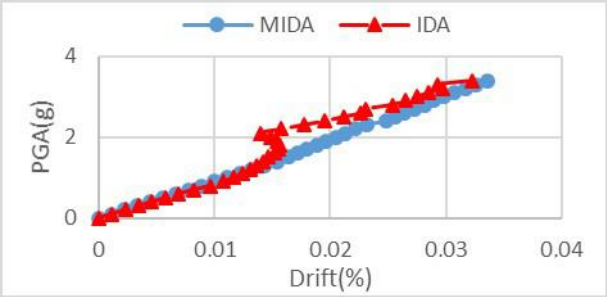

c. with 30% irregularity of plan

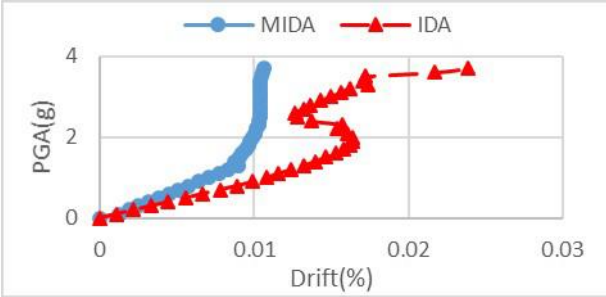

d. with 40% irregularity of plan

Figure 7. Comparison of roof drift from IDA and MIDA methods in 12-storey structures for record No.1 in near field records.

Comparing the roof displacements in these two methods, it can be seen that MIDA is not precise enough in near-field records on medium-rise buildings. From the comparison of roof drift in these two methods, it can be seen that MIDA method is not precise enough in near- field records on medium-rise buildings neither in elastic region nor in plastic one. It can be concluded that the increase in height of structures increases the errors by keeping fixed the number of modes for performing analysis.

3.1.1.3. Comparison of maximum roof displacement and drift versus PGA in "Morgan Hill" record for 18- story structures

Comparison of maximum roof displacement and drift versus PGA in "Morgan Hill" record for 18- storey structures with irregularities from 10% to 40%.

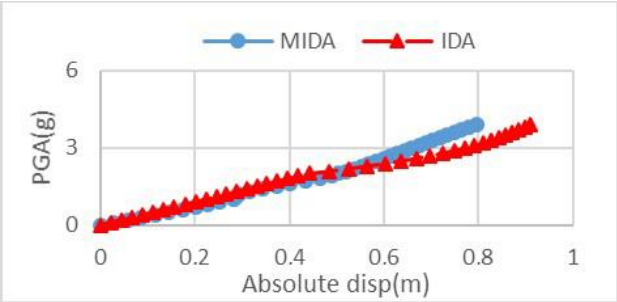

a. with 10% irregularity of plan

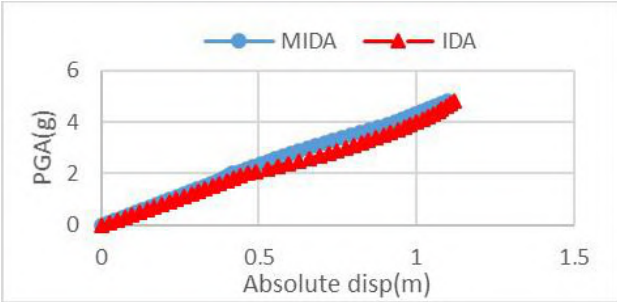

b. with 20% irregularity of plan

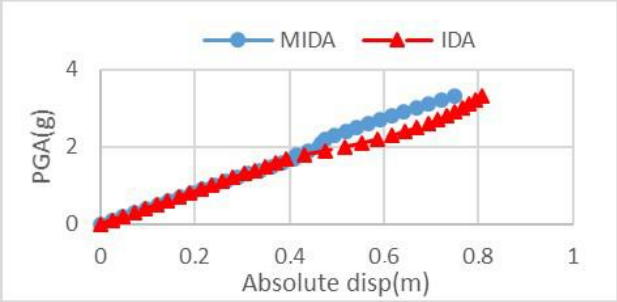

c. with 30% irregularity of plan

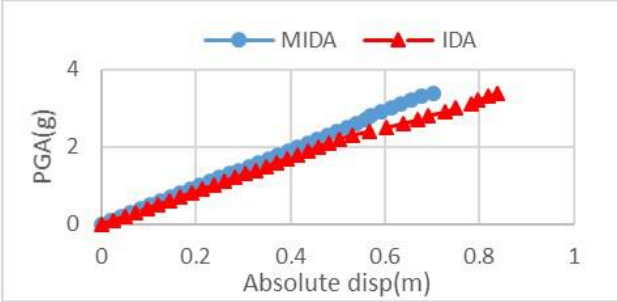

d. with 40% irregularity of plan

Figure 8. Comparison of roof displacement from IDA and MIDA methods in 18-storey structures for record No.1 in near field records.

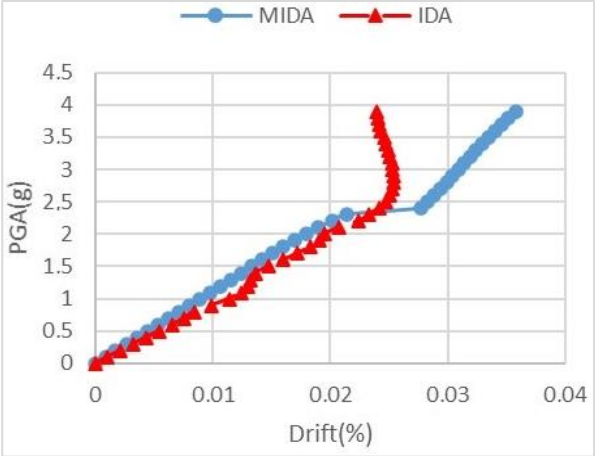

a. with 10% irregularity of plan

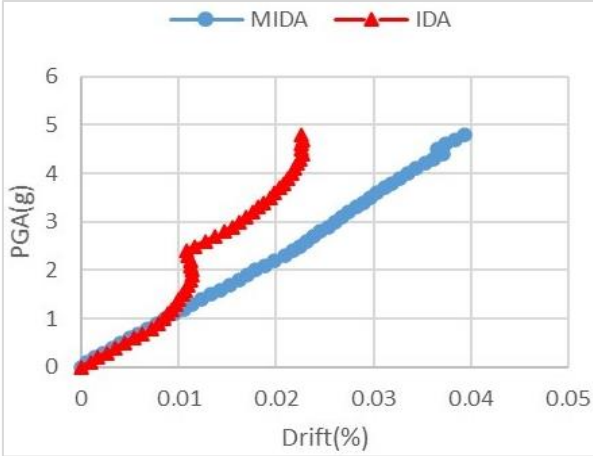

b. with 20% irregularity of plan

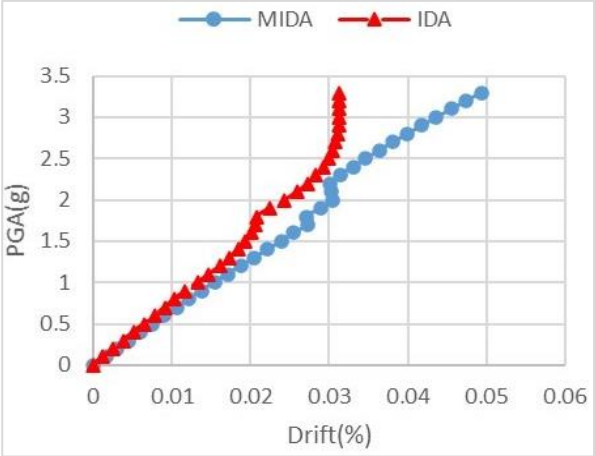

c. with 30% irregularity of plan

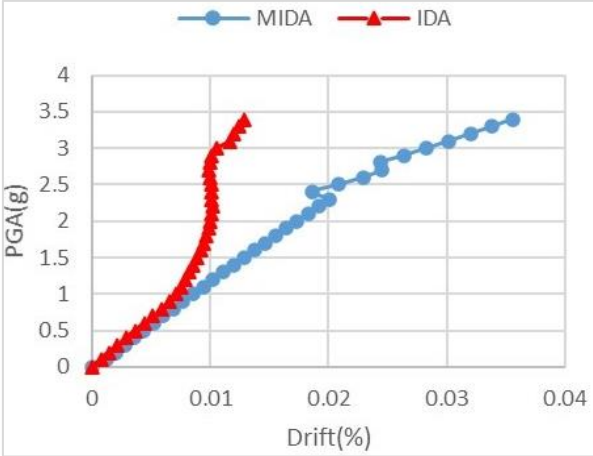

d. with 40% irregularity of plan

Figure 9. Comparison of roof drift from IDA and MIDA methods in 12-storey structures for record No.1 in near field records.

By comparing maximum roof displacement as well as maximum drift in these two methods as shown in Fig. 8 and 9, it can be concluded that the linear region of IDA method in 18-storey structures can be obtained by MIDA method. The reasoning lies in two things. Firstly, according to the survey carried out by Krawinkler et al. in 1999, spectra response of SDOF systems cannot satisfy seismic demands for near-field fault [24]. Secondly, MIDA method was based on SDOF system. Consequently, displacement and drift graph in low-rise and medium- rise structures cannot be obtained correctly and precisely. On the other hand, near-field earthquake records have a huge impact on low-rise and medium-rise structures; but 18-storey structures, as high-rise structures, are less affected by near-field earthquakes; accordingly, IDA and MIDA results match better to each other.

By passing the border of linear region in structural elements, they become plastic elements. Therefore, their stiffness changes result in changes in periods of structure. The validation of SRSS method is up to the point where modes do not interfere with each other. However, when structural elements become plastic and the period changes significantly, SRSS method is not valid anymore. Hence, this is one of the factors creating some errors in this method in inelastic region. In addition, figures illustrate that if the extent of irregularity increases, errors of this method dramatically increase because of the intense torsion of structure. Accumulation of plastic hinges in the reentrant corner of irregularity is the leading cause of this effect. Therefore, applicability of this method narrows down.

3.1.2. Comparison of maximum roof displacement and drift versus PGA in far- field records

Due to the extremely large numbers of graphs produced in this survey, the authors have decided to present comparison graphs of “Darfield _New Zealand” and “Chi- Chi_Tiwan-04” earthquake records for X direction and Y direction respectively in far-field records.

3.1.2.1. Comparison of maximum roof displacement and drift versus PGA for 6-story structures

Comparison of maximum roof displacement and drift versus PGA in “Chi-Chi_Tiwan-04” earthquake record for Y direction in far-field records for 6-storey structures with irregularities from 10 % to 40 %.

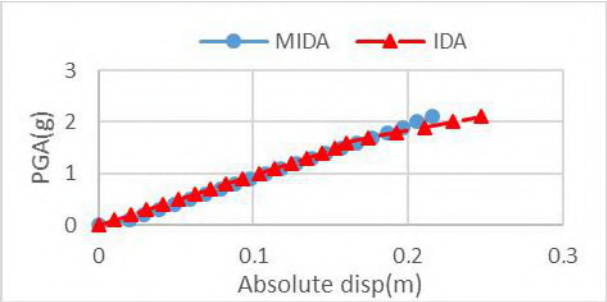

a. with 10% irregularity of plan

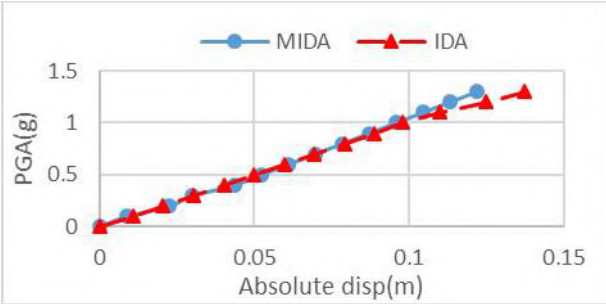

b. with 20% irregularity of plan

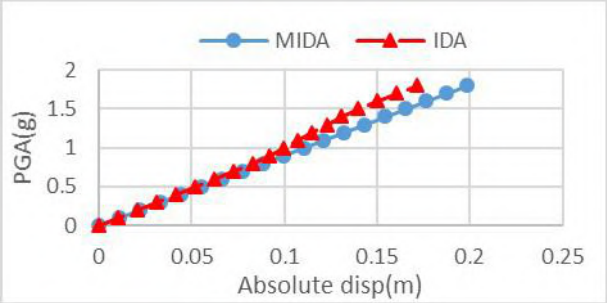

c. with 30% irregularity of plan

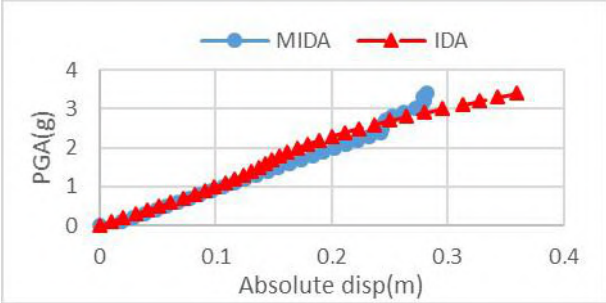

d. with 40% irregularity of plan

Figure 10. Comparison of roof displacement from IDA and MIDA methods in 6-storey structures under record No.3 in far field records Y-Direction.

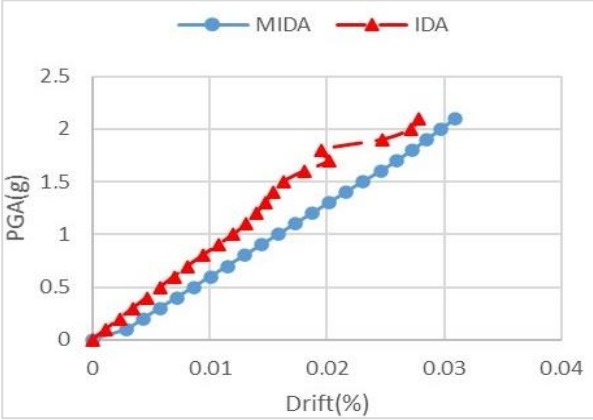

a. with 10% irregularity of plan

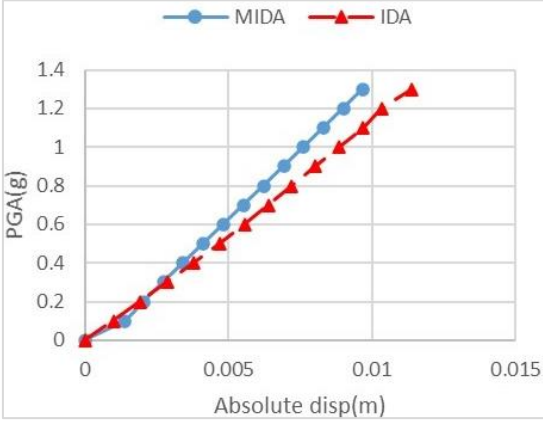

b. with 20% irregularity of plan

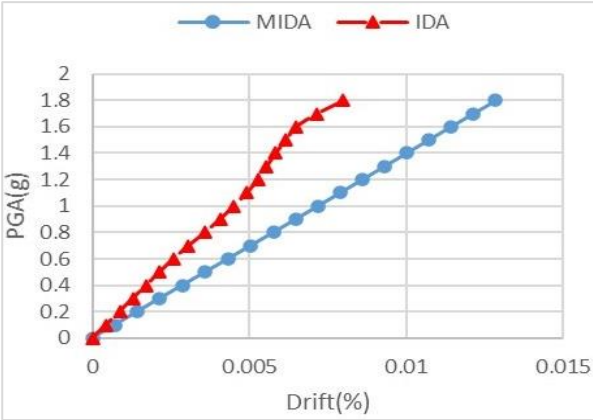

c. with 30% irregularity of plan

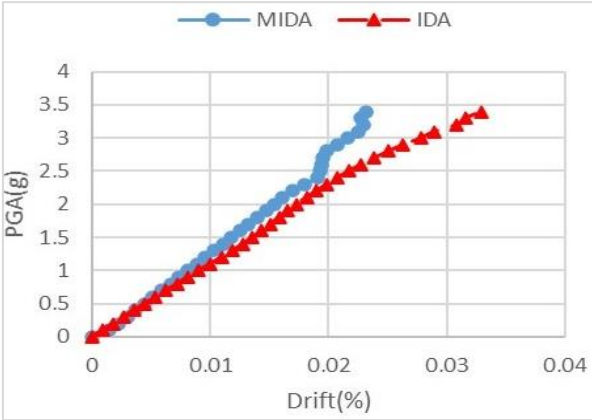

d. with 40% irregularity of plan

Figure 11. Comparison of roof drift from IDA and MIDA methods in 6-storey structures under record No.3 in far field records Y-Direction.

As Fig. 10 to Fig. 11 depict, MIDA method in both maximum roof displacement and maximum roof drift, is capable of extracting the accurate answer in linear region in far-field records. However, in nonlinear region, if the extent of intensity increases, errors of this method slightly increase in 6-storey structures. If the extent of

irregularity increases, errors of this method significantly increase because of the intense torsion of structure. Accumulation of plastic hinges in the reentrant corner of irregularity is the main cause of this effect. Therefore, applicability of this method decreases.

3.1.2.2. Comparison of maximum roof displacement and drift versus PGA 12-storey structures

Comparison of maximum roof displacement and drift versus PGA in "Darfield _New Zealand" earthquake record for X direction in far-field records for 12-storey structures with irregularities from 10 % to 40 %.

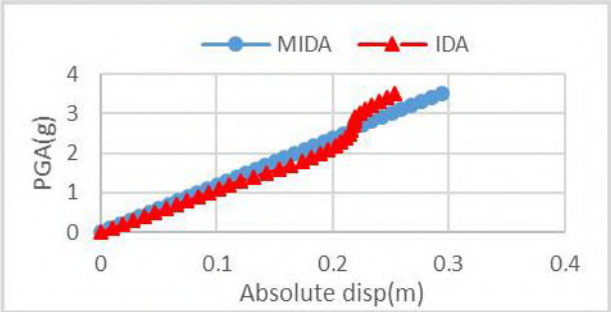

a. with 10% irregularity of plan

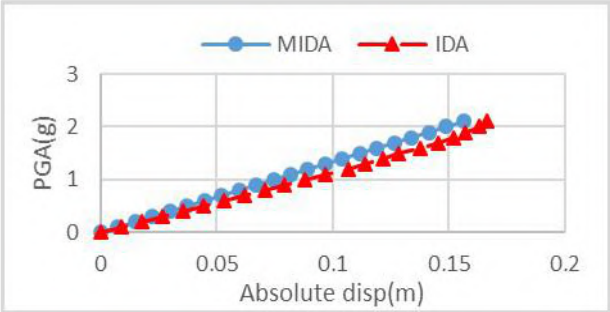

b. with 20% irregularity of plan

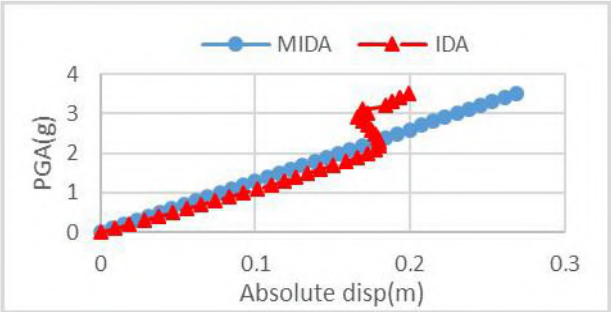

c. with 30% irregularity of plan

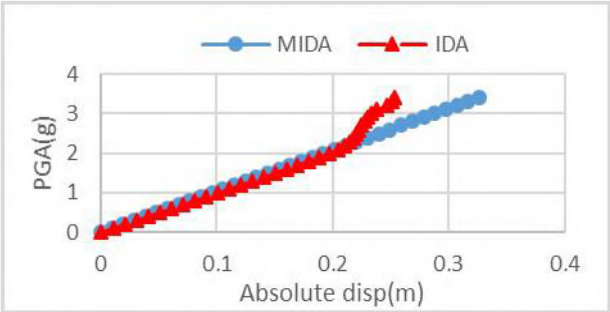

d. with 40% irregularity of plan

Figure 12. Comparison of roof displacement from IDA and MIDA methods in 12-storey structures under record No.3 in far field records X-Direction.

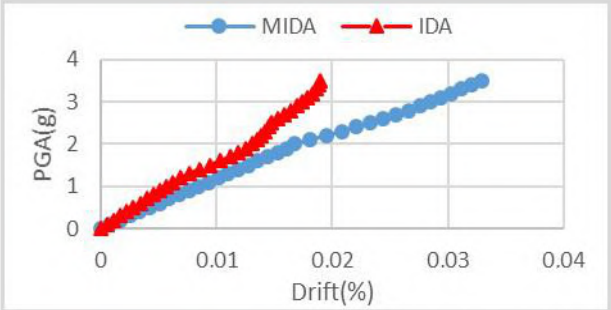

a. with 10% irregularity of plan

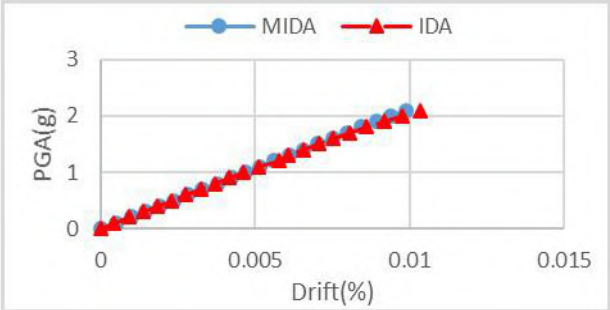

b. with 20% irregularity of plan

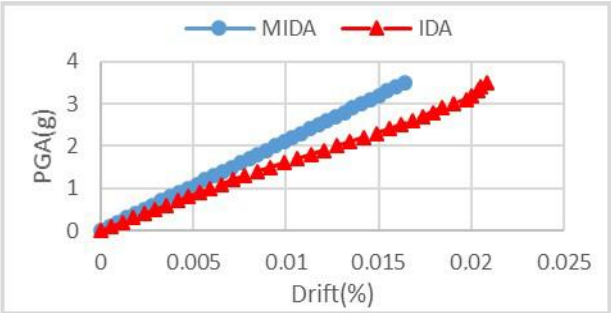

c. with 30% irregularity of plan

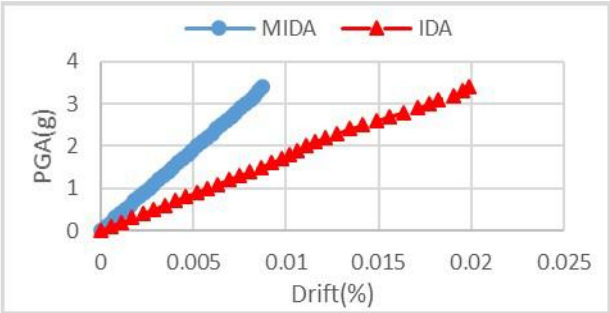

d. with 40% irregularity of plan

Figure 13. Comparison of roof drift from IDA and MIDA methods in 12-storey structures under record No.3 in far field records X-Direction.

As Fig. 12 to Fig. 13 depict, MIDA method, in both maximum roof displacement and maximum roof drift, is capable of extracting the precise answer in linear region in far-field records. However, in nonlinear region, if the extent of intensity increases, errors of this method slightly increase in 12-storey structures. By passing the border of linear region in structural elements, they become plastic elements. Therefore, their stiffness changes; consequently, the periods of structures change as well. The validation of SRSS method is when modes do not have interference with each other. However, when structural elements become plastic and period changes, SRSS method is not feasible anymore. Therefore, this is one of the factors, which brings about some errors in this method in inelastic region. In addition, figures illustrate that if the extent of irregularity increases, errors of this method significantly increase because of the intense torsion of structure. Accumulation of plastic hinges in the reentrant corner of irregularity is the main reason of this effect. Therefore, applicability of this method decreases. In addition, these errors are larger than those calculated in 6-storey structures. It is also mentioned that in 6, 12-storey structures, the number of modes considered for MIDA is the same. Therefore, it can be deduced that when the height of structures increases, the considered modes should increase by at least one more mode in order to decrease the errors in MIDA method.

3.1.2.3. Comparison of maximum roof displacement and drift versus PGA 18-storey structures

Comparison of maximum roof displacement and drift versus PGA in “Chi-Chi_Tiwan-04” earthquake record for Y direction in far-field records for 18-storey structures with irregularities from 10 % to 40 %

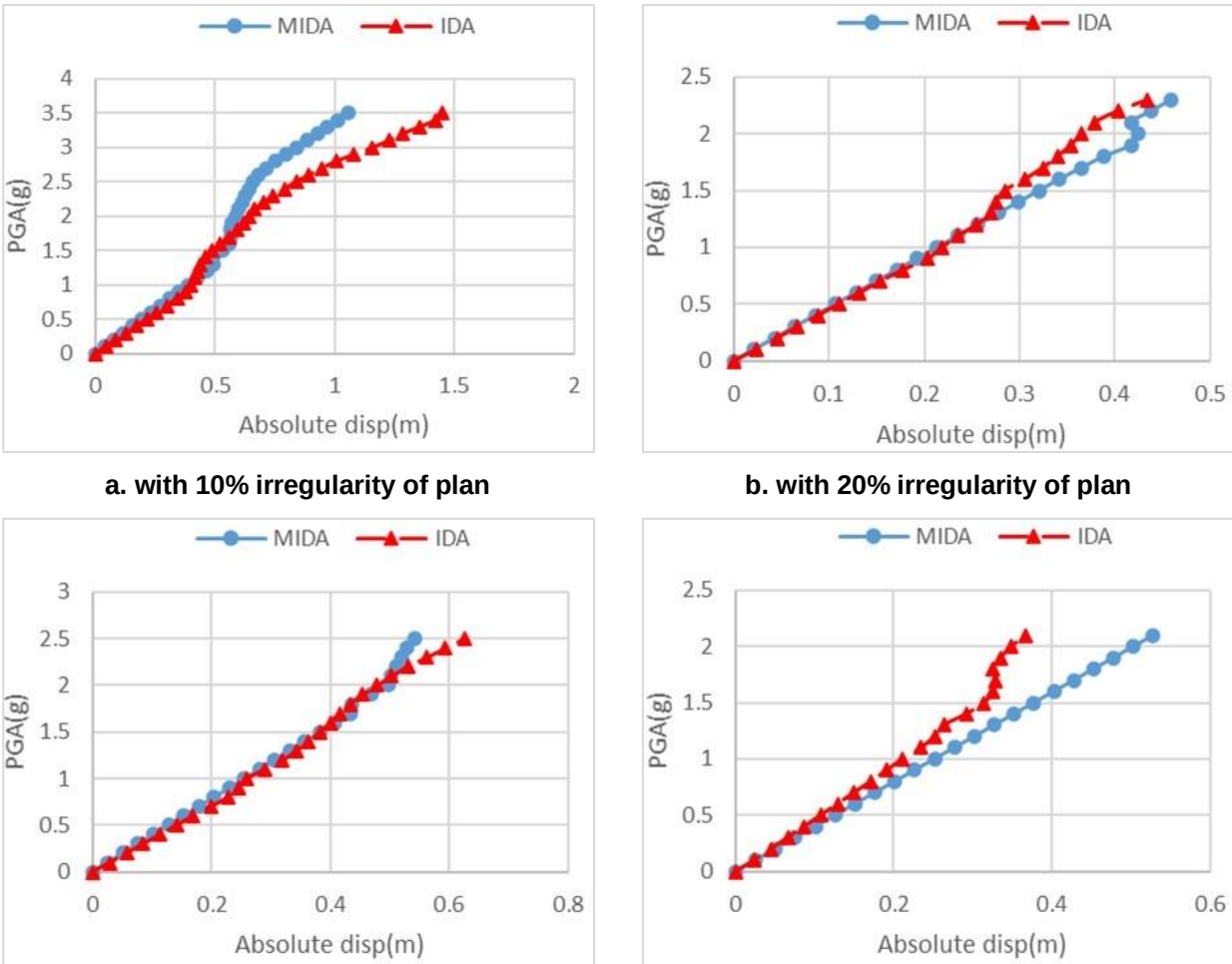

a. with 10% irregularity of plan

b. with 20% irregularity of plan

c. with 30% irregularity of plan

d. with 40% irregularity of plan

Figure 14. Comparison of roof displacement from IDA and MIDA methods in 18-storey structures under record No.3 in far field records Y-Direction.

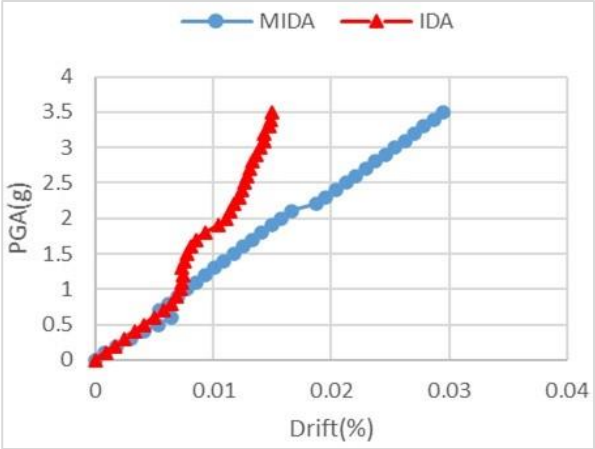

a. with 10% irregularity of plan

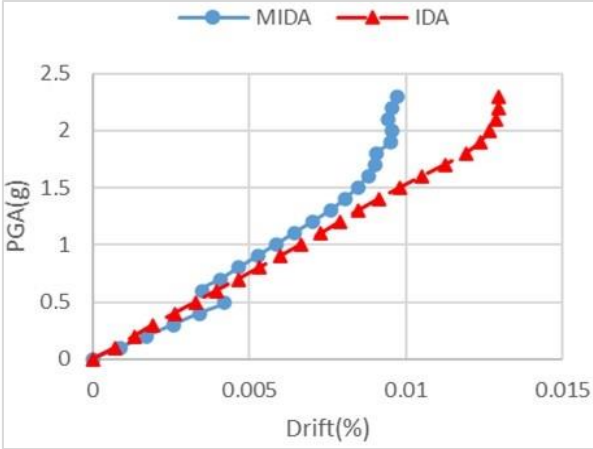

b. with 20% irregularity of plan

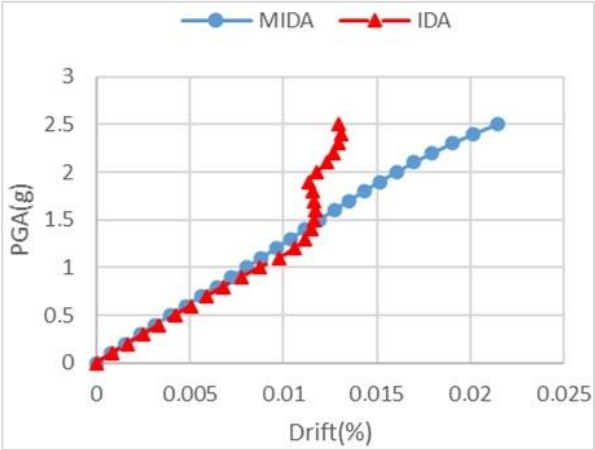

c. with 30% irregularity of plan

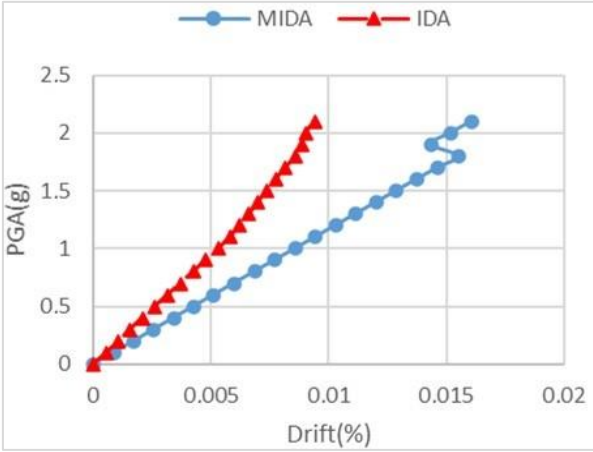

d. with 40% irregularity of plan

Figure 15. Comparison of roof drift from IDA and MIDA methods in 18-storey structures under record No.3 in far field records Y-Direction.

As Fig. 14 to Fig. 15 illustrate, MIDA method, in both maximum roof displacement and maximum roof drift, is capable of extracting the precise answer in linear region in far-field records. However, in nonlinear region, if the extent of intensity increases, errors of this method gradually increase in 18-storey structures. By passing the border of linear region in structural elements, they become plastic elements. Therefore, their stiffness changes; the periods of structures change accordingly. The validation of SRSS method is when modes do not have interference with each other. However, when structural elements become plastic and period changes, SRSS method is not valid anymore. Therefore, this is one of the factors creating some errors in this method in inelastic region. In addition, figures illustrate that if the extent of irregularity increases, errors of this method significantly increase because of the intense torsion of structure. Accumulation of plastic hinges in the reentrant corner of irregularity is the main reason of this effect. Therefore, applicability of this method narrows down.

These errors are larger than those calculated in 6, 12-storey structures. Therefore, it can be deduced that when the height of structures increases, the considered modes should be increased by at least one more modes in order to decrease the errors in MIDA method.

3.1.3. Comparison of the effect of height and modes on maximum roof displacements' error as well as drifts' errors in fixed irregularities

Comparison of the effect of height and modes on maximum roof displacements' error as well as drifts' error Versus PGA for average of structures' responses to 10 near-field records and 10 far-field records in fixed irregularities ranging from 10 % to 40 %.

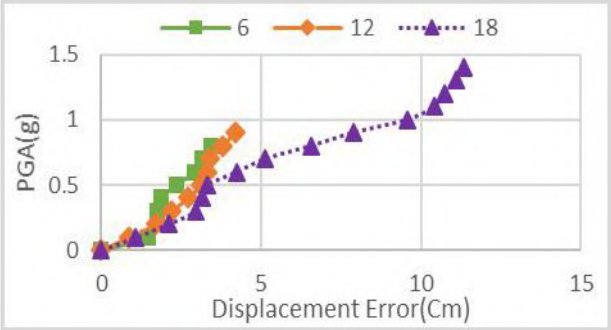

a. In structures with 10% irregularity on X-Direction

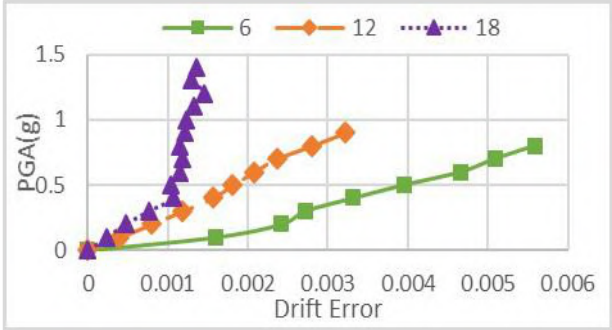

b. In structures with 10% irregularity on X-Direction

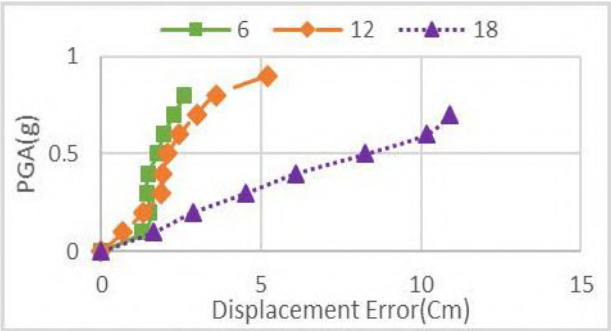

c. In structures with 20% irregularity on Y-Direction

d. In structures with 20% irregularity on Y-Direction

Figure 16. Comparison of the effect of height on roof displacement error and drift error between IDA and MIDA methods under average responses to far field records in structures with 10% and 20% irregularity.

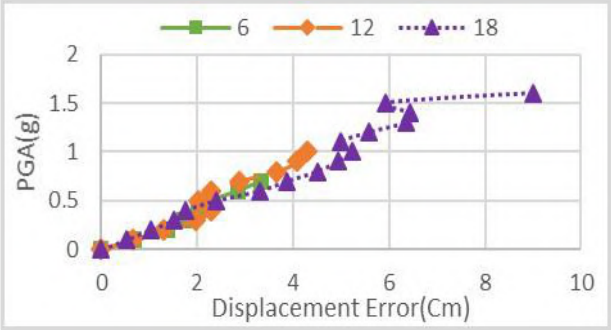

a. In structures with 30% irregularity which were recorded on X-Direction

b. In structures with 30% irregularity which were recorded on X-Direction

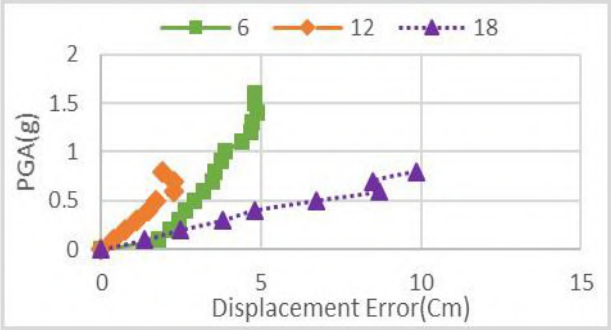

c. In structures with 40% irregularity which were recorded on Y- Direction

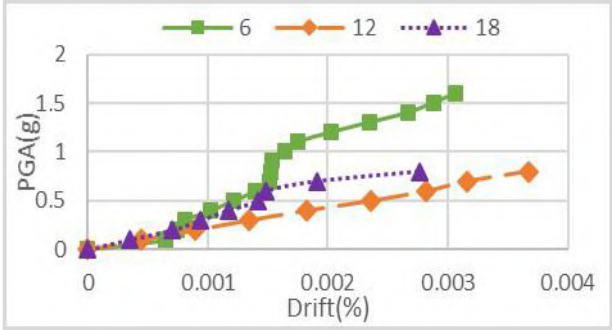

d. In structures with 40% irregularity which were recorded on Y- Direction

Figure 17. Comparison of the effect of height on roof displacement error and drift error between IDA and MIDA methods under average responses to far field records in structures with 30% and 40% irregularity.

Fig. 16(a) illustrates that 18-storey structures with irregularities of 10%, have the most errors in displacement despite considering one more modes in the 6 and 12-storey structures with irregularities of 10 %. However, 6-storey structures with irregularities of 10% have the most errors in drift and 18-storey structures have the least errors, as shown in Fig. 16(b).

Fig. 16(c) illustrates that 18-storey structures with irregularities of 20 %, have the most errors in displacement despite considering one more mode in the 6 and 12-storey structures with irregularities of 20 %. Nevertheless, as depicted in Fig. 16(d)**,** 6-storey structures with irregularities of 10 % have the most errors in drift and 18-storey structures have the least.

3.2. Discussion

In this part, some discussions on results are explained in two main parts.

3.2.1. Discussion of near-field records

Special moment frames should satisfy allowable maximum drifts according to what exactly has been stated on the codes. In these frames, this criterion is dominant in designing structures and determining the dimensions of beams and columns. Therefore, this leads to an increase in beams and columns' cross-sections and consequently an increase in the stiffness of structures. In this type of frame, increasing the stiffness brings about a decrease in ductility; therefore, a decrease in the structures' periods. On the other hand, because these systems are used for their high ductility, they have higher period compared to the other lateral resisting systems. Krawinkler et al. (1999) [24] investigated the effect of specific pulses with the period of T_p on the responses of structures with a fundamental period of T at various performance levels. They found that SDOF spectra are adequate to represent multi-degree-of-freedom system ductility demands in stiff structures with $T/T_p < 1.0$, but are poor in representing the demands in flexible structures with $T/T_p > 1.0$ [24]. It was concluded that SDOF spectra alone are inadequate to represent seismic demands for near field earthquake ground motion [24]. As it is obvious, MIDA is a method based on the analysis of SDOF systems; hence MIDA method complies with what Krawinkler et al. stated in 1999 [24]. Hence, MIDA method is not valid in near-field earthquake records since this phenomenon is intensified in low-rise as well as medium rise structures. In addition, in near-field records movements, both PGA and PGV are very high. Their velocity somehow reaches about $100\ cm/s$ to $200\ cm/s$. One of their characteristics is that they can dissipate huge quantities of energy in a very short period. Near-field records have a huge impact on low-rise structures. It can be inferred that MIDA method is not valid in the linear and nonlinear deformation as well as in low and mid-rise structures; but the results are much better in high-rise building because they get very little effect from near-field records compared to the others.

The pioneers of MIDA hypothesized modes operating separately from each other; but when structural elements pass the yielding point and become plastic, their stiffness decreases causing the interference of modes; therefore, SRSS method is not valid anymore. This is by far the most important factor that produces exceedingly large errors in nonlinear region.

As the extent of irregularity increases, errors of MIDA method dramatically increase owing to the intense torsion of structure. Accumulation of plastic hinges in the reentrant corner of irregularity is the main reason of this effect. Therefore, applicability of this method narrows down.

3.2.2. Discussion of far-field records

In these 12 structures, it is figuratively seen that the first mode has a dramatic direct effect on creation of the structures' displacement and the higher modes have a minor effect on creation of the structures' displacement. On the other hand, the higher modes have an immense direct effect on the creation of the drift and the first mode has a subtle effect on it. Therefore, the increase in considered modes in MIDA method, brings about a decrease in the errors of this method. Because 12-storey structures are higher than 6-storey structures, it is seen that the effect of higher modes on displacements and drifts of 2 stories below the roof are bigger than what is seen in 6-storey structures. Therefore, the errors in drift decrease. In 18-storey structures, by considering one more mode than 6 and 12-storey structures, the errors do not decrease to the expected level. Hence, for the 18-storey structures, it is perhaps better to consider at least two more modes.

3.2.3. Discussion on errors

1. Approximating the roof displacement versus base shear curve with bilinear curves brings about some errors in calculating drift and displacement.

2. The most important factor creating huge errors in nonlinear region is the modes interfering with each other. When structural elements pass the yielding point and become plastic, their stiffness decreases and this results in the interference of modes; therefore, SRSS method is not justifiable anymore. Therefore, the assumption of considering modes operating separately from each other is wrong.

3. Considering just the first two modes in each individual direction is one of the main causes of errors in 6 and 12-storey structures. A better alternative would be to consider more modes.

4. Regarding the errors of MIDA method, it is concluded in general:

- Eigenvector (ϕ_{ji}) is not unique inherently. Therefore, $L_i = \sum m_j \phi_{ji}$ used in $\left(F_{yi}\right)_{SDOF} = \left(F_{yi}\right)_{MDOF} / \left(L/M\right)_i$ can cause this equation to have different answers and this would lead to wrong bilinear curve. Consequently, this can be the cause of errors in MIDA method.
- As the extent of irregularity increases, displacement errors of this method significantly increase because of the intense torsion of structure. Accumulation of plastic hinges in the reentrant corner of irregularity is the main reason of this effect.
- As the extent of irregularity increases, drifts' errors of this method significantly increase because of the intense torsion of structure. Therefore, in order to improve this method, there is a crucial need to introduce new damage index rather than drift in the procedure of MIDA.
- There is no individual rule to figure out how many modes are enough and what optimum is to be considered in the procedure of MIDA.
- In near-field records, low-rise structures are exposed to the effect of these earthquakes more than the others. SDOF spectra alone are inadequate to represent seismic demands for near field earthquake ground motion according to Krawinkler et al. (1999) [24]. It is evident that MIDA is a method based on the analysis of SDOF systems. Hence, MIDA method is not justifiable in near-field records as this phenomenon would cause too many errors in near-field records.

4. Conclusion

The obtained results of this research project are outlined below:

1. MIDA method is capable of calculating the damage indexes just as IDA method is.

2. As the extent of irregularity increases, applicability of this method narrows down.

3. In plan irregularity of structures, drift as damage index is not viable; therefore, there is a crucial need to improve this method through selecting new damage indexes.

4. Considering more modes for calculations in this method causes errors to decrease.

- There is no individual rule to figure out how many modes are enough to be considered as optimum in the procedure of MIDA.
- The speed of calculation in this method on 3D structures was amazing. There is a promising future ahead for future investigation of this method.
- About the MIDA method, it can be said in general:
  - Transformation of 3D MDOF to an equivalent SDOF system reduces the time of calculation as well as CPU usage of computers.
  - Using the concept of pushover analysis in MIDA, all plastic hinges can be traced and the weak point of the structures can be detected in less time than IDA method.
  - Using the MIDA method in far-field records presents no difficulties. Therefore, it is highly recommended to employ this method.

Future researchers can carry out new surveys to consider other irregularities mentioned in ASCE7.

References

1. Bertero, V. Strength and deformation capacities of buildings under extreme environments. Structural Engineering and Structural Mechanics. 1977. 211–5.
2. Nassar, A., Krawinkler, H. Seismic demands for SDF and MDF systems. Report no. 95. p. 62–155: Stanford university: The John A. Blume Earthquake Engineering Center. 1991.
3. Bazzurro, P., Cornell, C. Seismic hazard analysis for non-linear structures. I: methodology. ASCE Journal of Structural Engineering. 1994. 120(11). 3320.
4. Mehanny, S., Deierlein, G. Modeling and assessment of seismic performance of composite frames with reinforced concrete columns and steel beams. Report no. 136: Stanford University: Blume Earthquake Engineering Center. 2000.
5. Gupta, B., Kunnath, S. Adaptive spectra-based pushover procedure for seismic evaluation of structures. Earthquake spectra. 2000. 16(2). Pp. 367–392.
6. Vamvatsikos, D., Cornell, C.A. Direct estimation of seismic demand and capacity of multidegree-of-freedom systems through incremental dynamic analysis of single degree of freedom approximation. Journal of Structural Engineering. 2005. 131(4). Pp. 589–599.

7. Khorami, M., Alvansazyazdi, M., Shariati, M., Zandi, Y., Jalali, A., Tahir, M. Seismic performance evaluation of buckling restrained braced frames (BRBF) using incremental nonlinear dynamic analysis method (IDA). Earthquake and Structures. 2017. 13. Pp. 531–538. DOI: 10.12989/eas.2017.13.6.531
8. Davani, M.R., Hatami, S., Zare, A. Performance-based evaluation of strap-braced cold-formed steel frames using incremental dynamic analysis. Steel and Composite Structures. 2016. Vol. 21. No. 6. Pp. 1369–1388. DOI: 10.12989/scs.2016.21.6.1369
9. Bayat, M., Daneshjoo, F., & Nistico, N. A novel proficient and sufficient intensity measure for probabilistic analysis of skewed highway bridges. Structural Engineering and Mechanics. 2015. 55(6). Pp. 1177–1202. DOI: 10.12989/SEM.2015.55.6.1177
10. Mofid, M., Zarfam, P., Fard, B. On the modal incremental dynamic analysis. The Structural Design of Tall and Special Buildings. 2005. 14. Pp. 315–329.
11. Han, S., Chopra, A. Approximate incremental dynamic analysis using the modal pushover analysis procedure. Engineering Structural Dynamics. 2006. 35(15). Pp. 1853–1873.
12. Zarfam, P., Mofid, M. Evaluation of modal incremental dynamic analysis, using input energy intensity and modified bilinear curve. The Structural Design of Tall and Special Buildings. 2008. 18. Pp. 573–586.
13. Zarfam, P., Mofid, M. On the modal incremental dynamic analysis of reinforced concrete structures, using a trilinear idealization model. Journal of Engineering Structures. 2011. 33. Pp. 1117–1122.
14. Shafei, B., Zareian, F., Lingos, D.G. A simplified method for collapse capacity assessment of moment-resisting frame and shear wall structural systems. Engineering Structures. 2011. 33(4). Pp. 1107–1116. DOI: 10.1016/j.engstruct.2010.12.028
15. Jalilkhani, M., Manafpour, A.R. Evaluation of seismic collapse capacity of regular RC frames using nonlinear static procedure. Structural Engineering and Mechanics. 2018. 68(6). Pp. 647–660. DOI: 10.12989/SEM.2018.68.6.647
16. Zafarkhah, E., Keipour, N., Mofid, M. Exerting Modal Incremental Dynamic Analysis (MIDA) in surveying seismic Behavior of structures Equipped by Self-Centering viscoelastic Damper. Journal of Vibroengineering. 2017. 19(2). Pp. 783–800.
17. Bergami, A.V., Forte, A., Lavorato, D. Proposal of a Incremental Modal Pushover Analysis (IMPA). Earthquakes and Structures. 2017. Vol. 13. No. 6. Pp. 539–549.
18. ASCE07. Minimum design loads for building and other structures. American Society of Civil Engineers: Washington DC, USA. 2010.
19. AISC360. Specification for structural steel buildings,AISC 360. An American National Standard Institute: Washington DC, USA. 2010.
20. FEMAP695. Quantification of Building Seismic Performance Factors. the Applied Technology Council for the Federal Emergency Management Agency: Washington DC, USA. 2009.
21. Dimakopoulou, V., Fragiadakis, M., Spyrakos, C. Influence of modeling parameters on the response of degrading systems to near-field ground motions. Journal of Engineering Structures. 2013. 53. Pp. 10–24.
22. Davoodi, M., Jafari, M., Hadiani, N. Seismic response of embankment dams under near-fault and far-fault ground motion excitation. Journal of Engineering Geology. 2013. 158. Pp. 66–76.
23. FEMA356. Prestandard and Commentary for the Seismic Rehabilitation of Buildings, FEMA 356. Federal Emergency Management Agency; Washington DC, USA. 2000.
24. Gala, K., Ghobarah, A. Effect of near-fault earthquakes on North American nuclear design spectra. Nuclear Engineering and Design, Elsevier. 2006. 236(18). Pp. 1928–1936.

Contacts:

Hamidreza Mehdipanah, hmehdipanah@mail.kntu.ac.ir.

Nader Fanaie, fanaie@kntu.ac.ir

© Mehdipanah, H.R., Fanaie, N., 2021

Федеральное государственное автономное образовательное учреждение высшего образования
Санкт-Петербургский политехнический университет Петра Великого

ПОЛИТЕХ
Санкт-Петербургский политехнический университет Петра Великого

Инженерно-строительный институт
Центр дополнительных профессиональных программ

195251, г. Санкт-Петербург, Политехническая ул., 29, тел/факс: 552-94-60, www.stroikursi.spbstu.ru, stroikursi@mail.ru

Приглашает специалистов проектных и строительных организаций, не имеющих базового профильного высшего образования на курсы профессиональной переподготовки (от 500 часов) по направлению «Строительство» по программам:

П-01 «Промышленное и гражданское строительство»

Программа включает учебные разделы:

- ***Основы строительного дела***
- ***Инженерное оборудование зданий и сооружений***
- ***Технология и контроль качества строительства***
- ***Основы проектирования зданий и сооружений***
- ***Автоматизация проектных работ с использованием AutoCAD***
- ***Автоматизация сметного дела в строительстве***
- ***Управление строительной организацией***
- ***Управление инвестиционно-строительными проектами. Выполнение функций технического заказчика***

П-02 «Экономика и управление в строительстве»

Программа включает учебные разделы:

- ***Основы строительного дела***
- ***Инженерное оборудование зданий и сооружений***
- ***Технология и контроль качества строительства***
- ***Управление инвестиционно-строительными проектами. Выполнение функций технического заказчика и генерального подрядчика***
- ***Управление строительной организацией***
- ***Экономика и ценообразование в строительстве***
- ***Управление строительной организацией***
- ***Организация, управление и планирование в строительстве***
- ***Автоматизация сметного дела в строительстве***

П-03 «Инженерные системы зданий и сооружений»

Программа включает учебные разделы:

- ***Основы механики жидкости и газа***
- ***Инженерное оборудование зданий и сооружений***
- ***Проектирование, монтаж и эксплуатация систем вентиляции и кондиционирования***
- ***Проектирование, монтаж и эксплуатация систем отопления и теплоснабжения***
- ***Проектирование, монтаж и эксплуатация систем водоснабжения и водоотведения***
- ***Автоматизация проектных работ с использованием AutoCAD***
- ***Электроснабжение и электрооборудование объектов***

П-04 «Проектирование и конструирование зданий и сооружений»

Программа включает учебные разделы:

- ***Основы сопротивления материалов и механики стержневых систем***
- ***Проектирование и расчет оснований и фундаментов зданий и сооружений***
- ***Проектирование и расчет железобетонных конструкций***
- ***Проектирование и расчет металлических конструкций***
- ***Проектирование зданий и сооружений с использованием AutoCAD***
- ***Расчет строительных конструкций с использованием SCAD Office***

П-05 «Контроль качества строительства»

Программа включает учебные разделы:

- ***Основы строительного дела***
- ***Инженерное оборудование зданий и сооружений***
- ***Технология и контроль качества строительства***
- ***Проектирование и расчет железобетонных конструкций***
- ***Проектирование и расчет металлических конструкций***
- ***Обследование строительных конструкций зданий и сооружений***
- ***Выполнение функций технического заказчика и генерального подрядчика***

По окончании курса слушателю выдается диплом о профессиональной переподготовке установленного образца, дающий право на ведение профессиональной деятельности